Hierarchical Modeling of Structure and Mechanics of Cement Hydrate

by

Rouzbeh Shahsavari

B.S., Sharif University of Technology (2002)
M.S., McGill University (2004)

Submitted to the Department of Civil and Environmental Engineering
in partial fulfillment of the requirements for the degree of

Doctor of Philosophy

at the

MASSACHUSETTS INSTITUTE OF TECHNOLOGY

February 2011

Signature of Author.....
Department of Civil and Environmental Engineering
December 21, 2010

Certified by.....
Professor of Civil and Environmental Engineering
Thesis Supervisor

Accepted by.....
Heidi Nepf
Chairman, Department of Civil and Environmental Engineering

Hierarchical Modeling of Structure and Mechanics of Cement Hydrate

By

Rouzbeh Shahsavari

Submitted to the Department of Civil and Environmental Engineering on December 21, 2010, in partial fulfillment of the requirements for the degree of Doctor of Philosophy in the field of Civil and Environmental Engineering

Abstract

With an annual production of more than 20 billion tons a year, concrete continues to be the world's dominating manufacturing material for a foreseeable future. However, this ubiquity comes with a large ecological price as concrete stands as the third largest culprit to the torrent of CO_2 after transportation and electricity generation. Despite several decades of studies, fundamental questions are still unsettled on the structure and properties of the smallest building block of concrete, Calcium-Silicate-Hydrate (C-S-H). Given the variable stoichiometry and morphology of C-S-H, no accurate models were ever developed that could link electronic information at one end to the C-S-H molecular properties at the other end.

This thesis develops a new modeling toolbox that enables unraveling the interplay between structure, composition, morphology and mechanical properties of this "liquid stone" gel. First, using *ab-initio* calculations we characterize the structural and mechanical properties of several mineral analogs of C-S-H (tobermorite family and jennite). We show tobermorite as a class of layered materials that unlike the common intuition, is not softest along the interlayer direction. Instead, the mechanically softest directions are two inclined regions forming a hinge mechanism. This feature sheds light on the complex mechanics of the realistic C-S-H layers. It occurs when the electrostatic interlayer interactions become comparable to the iono-covalent intralayer interactions.

Next, to pass information to the next hierarchical level, we start by benchmarking the predictive capabilities of two commonly used force field potentials for C-S-H minerals against *ab-initio* calculations. While both potentials seem to give structural properties in reasonable agreement with the *ab-initio* results, the higher order properties such as elastic constants are more discriminating in comparing potentials with regards to predicting mechanical properties. Based on this finding, we use *ab-initio* structural and elasticity data in tandem to develop a new force field potential, CSH-FF, well customized and substantiated for the C-S-H family. This simple, yet efficient force-field is used in conjunction with statistical mechanics to analyze a series of molecular C-S-H models. Our simulation results predict a range of compositions and corresponding mechanical properties of solid C-S-H molecules that are consistent with real cement paste samples. This confirms our bottom-up multi-scale approach with the model parameters linked to electronic structure calculations. The combination of these techniques and findings paves a path toward a predictive computational design strategy to improve the core properties of cement hydrate while reducing its negative environmental impact.

Thesis Supervisor: Franz-Josef Ulm
Title: Professor of Civil and Environmental Engineering

Contents

List of Figures

Acknowledgments

My doctoral studies at MIT was possible through the support of many people. My deepest gratitude goes to my advisor, Prof. Franz-Josef Ulm, not only for his great technical advice in this project, but for his encouragement, passion and support of my progress at MIT. Working with you continuously inspired me to go beyond the realm of what others may consider sufficient. I greatly enjoyed it and learned more than what I expected. In the same breath, I would like to appreciate my two co-advisors, Prof. Roland Pellenq and Prof. Markus Buehler for their comments and motivations during the past four years towards shaping my professional career. Your extraordinary expertise and your great visions in computational modeling have been always an aspiration for me. In particular, without Prof. Pellenq, this thesis would have not been possible. I am also thankful to other members of my committee, Prof. Sidney Yip and Prof. Krystyn van Vliet for their valuable guidance and discussions over the years of this study.

All my current and former officemates made my study at MIT a truly enjoyable experience. My special thanks to Alberto, Mathieu, Zenzile, Chris, Romain, Benjamin, Jimmy and also to the staff of the CEE department, particularly Donna, Patty Dixon, Patty Glidden, Kris, Denise and Jeanette for their help and kindness. I also want to thank the members of the Laboratory for Atomistic and Molecular Mechanics especially Dipanjan for the technical help and guidance.

Finally, I am indebted to my beloved family for their non-stop support and motivation throughout the completion of my Ph.D. Last but not least, the financial support of the CIMPOR Corporation (Portugal) enabled through MIT-Portugal program is gratefully acknowledged.

Part I

General Presentation

Chapter 1

Introduction

1.1 Industrial Context

Concrete is the most widely used manufacturing material on the planet. The current worldwide concrete production stands at more than 20 billion tons, enough to produce more than one cubic meter of concrete per capita and year. The key strengthening ingredient in concrete is cement, the production of which expends a considerable amount of energy and contributes to 5-10% of anthropogenic CO_2 emissions and significant levels of harmful NO_X worldwide. On the other hand, there is no other bulk material on the horizon that could replace concrete as the backbone material for our societal needs in housing, shelter, infrastructure, and so on. There is thus a need to rethink concrete for the age of global warming to make it part of the sustainable development of our societies.

1.2 Research Motivation

Although concrete is considered to be the third largest climate-change culprit outside of transportation and electricity-generation, it is the only sustainable solution for the construction sector. This is mainly because the concrete raw materials including limestone, sand and aggregate are readily available and affordable practically everywhere. Additionally, its flexible shape, high compressive strength, fire resistance and high thermal mass make concrete most attractive for architects, engineers and end-users. Concrete is a highly heterogeneous material presenting

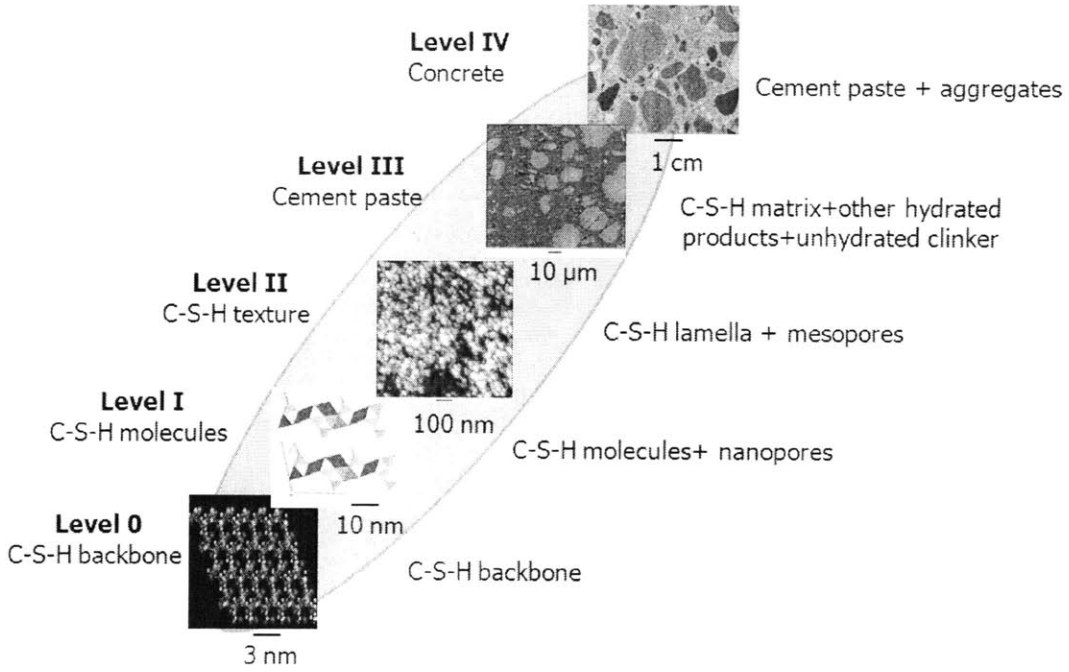

Figure 1-1: Hierarchical structure of concrete. Image credits: level II from [114], level III from [106] and level IV from [81].

different structural features across wide length scales (Fig. 1-1). At a macroscale, concrete is composed of aggregates, cement and water. At a microscale, the cement paste (mix of water and cement) itself is heterogeneous and composed of several hydration products, the principal products being the Calcium-Silicate-Hydrates (C-S-H) phases. At a mesoscale, the different C-S-H phases are a mix of solid particles/lamella and mesopores. At a nanoscale, C-S-H is made of molecules and nanoporosities in between the molecules.

Though concrete has been in widespread use since the Roman Empire, and has become recently the focus of a multibillion-dollar industry under pressure to be eco-friendly, the interplay between the structure, composition and physical properties of its smallest building block, C-S-H, across different scales is essentially unexplored. This complexity is recognized to stem from the lack of reliable structures for C-S-H at the fundamental levels. As an example, the density of C-S-H at the atomistic scale was recently revealed in 2007 [4]. However, the C-S-H structure has been classically investigated at the micro/macro scale for engineering design purposes (see e.g.[153]). The complete chemical processes of C-S-H formation including cement

clinker dissociation, precipitation and setting is still unknown, because there were not neither reliable molecular models of C-S-H nor accurate enough experimental probes at the atomistic level to enable such studies.

We will refer to the backbone of the C-S-H structure and its nanopores at the nano level as *solid* C-S-H. In contrast, at a scale above, we will refer to the spatial organization of the C-S-H molecules and mesopores in between them as the mesotexture of C-S-H. Given the characteristic size of the C-S-H solid (a few Angstroms or nanometers), the classical top-down approach of engineering research is quite daunting if not impossible. In contrast, here, we will use a bottom-up approach to explore and build the C-S-H solid phases, and give perspectives on how to link their structures to the higher scales. This fundamental approach is crucial to explore the heart of cementitious materials and upscale their very properties from the atomistic level into engineering application. For instance, one promising approach derived from analogy to Galileo's analysis of weight-strength relation is to achieve increased specific strength of this material: the weight and CO_2 emissions of cement increase with the volume of required material, whereas the strength increases proportionally to the cross-sectional area. Hence, as one increases the strength of a material by a factor of X, one reduces the environmental footprint by $1\text{-}X^{-1}$ for pure compressive members such as columns, arches and shells, $1\text{-}X^{-2/3}$ for beams in bending, and $1\text{-}X^{-1/2}$ for slabs.

This research aims to answer the following scientific questions: What is the C-S-H backbone structure? And how do elastic, strength and morphological properties of solid C-S-H relate to the electronic properties?

1.3 Research Objectives

A comprehensive bottom-up approach is presented to address the scientific questions. The approach is composed of first-principles calculations, atomistic modeling via Molecular Dynamics and Monte-Carlo methods. The approach is guided by the following three research objectives:

Objective 1: *Develop a benchmark data useful for solid C-S-H via first-principles calculations on known C-S-H minerals.* There are a number of natural minerals that are akin to C-S-H in terms of chemical composition and structure. We shall study their atomistic structure, interlayer

interactions and elastic properties based on accurate first-principles calculations. This study will serve as a benchmark for the next objective to calibrate interatomic interaction for molecular C-S-H phases.

Objective 2: *Develop an accurate and efficient force field potential to predict C-S-H atomistic interactions.* Current force field potentials for C-S-H atomistic interactions are either inaccurate or computationally very expensive to predict C-S-H physical properties. Here, we develop an efficient force field, CSH-FF, which enables decoding the structure and mechanical properties of variety of solid C-S-H phases. This development will serve as the prerequisite for the next objective.

Objective 3: *Develop a bottom-up toolbox to seamlessly link the electronic properties of C-S-H to higher scales.* The ultimate goal of this research is to implement the shift of paradigm in materials science to concrete structures, that is, to pave the path to pass information from electrons to higher scales.

1.4 Industrial and Scientific Benefits

Associated with the research objectives are important industrial and scientific benefits. They include:

- Fundamental understanding of the smallest building block of concrete which lay the foundation for achieving never-seen-before mechanical properties.
- Assessment of upscaling various chemical compositions, which impact energy and environmental footprints of cement.
- Quick insights on stability and mechanics of incorporation of new eco-friendly elements as feedstocks into molecular C-S-H phases.

1.5 Outline of Thesis

This thesis is divided into five Parts. The first Part deals with the presentation of the topic.

Part II deals with a general introduction to cement and modeling and is composed of two Chapters. First, Chapter 2 deals with introducing the hierarchical structure of cement

hydrate. This Chapter discusses various mineral analogs of C-S-H and the challenges ahead for constructing an accurate model that is consistent with the experimental observations at the nano level. Chapter 3 presents an overview of common multi-scale computational modeling techniques by summarizing the theories, fundamentals, hypotheses and equations of several modeling techniques from *ab-inito* calculations to Atomistic Simulations (Molecular Dynamics and Monte-Carlo simulations).

Part III focuses on benchmarking several mineral analogs of C-S-H such as tobermorite family and jennite via first-principles calculations. In Chapter 4, structural, elastic and strength properties of these C-S-H mineral are characterized. Then inter/intra layer competitive interactions are discussed, which may lead to uncommon deformation mechanism and fracture features in C-S-H minerals. Chapter 5 is centred around acoustic tensor analyses of these minerals by which a new statistical averaging scheme for bulk modulus and shear modulus of anisotropic materials is derived.

In contrast to Part III, Part IV is devoted entirely to Statistical Mechanics and Atomistic Simulation methods and is composed of three Chapters. First, Chapter 6 focuses on systematic comparison of common empirical field fields for C-S-H. Based on the *ab-initio* results of Part III, a new simple, yet efficient force-field, CSH-FF, is developed, which is well customized and substantiated for cementitious materials. Next, in Chapter 7, the first consistent molecular model of the C-S-H, cCSH, is proposed that is validated against several experiments at the molecular and atomistic level. Finally, in Chapter 8, the results and concepts of Chapter 6 and 7 are utilized to decode the molecular structure of series of distinct C-S-H phases with realistic Ca/Si ratios and mechanical properties.

The fifth Part, i.e., Chapter 9, summarizes the results of this study and gives perspectives on how to link molecular-scale properties to C-S-H mesotexture.

Part II

Introduction to Cement hydrate and Modeling

Chapter 2

Multi-Scale Model of Cement Hydrate

The aim of Part II is to give a general background on cement hydrate, and computational multi-scale modeling techniques. It is composed of two Chapters: The first reviews the current understanding of hierarchical levels of the cement hydrate and discusses several complexities observed in C-S-H systems. In particular, this Chapter focuses on different atomistic and morphological models postulated for the C-S-H gel at the nano scale. The second Chapter reviews several computational modeling techniques that are each appropriate for different length-scale and physical properties. Together, these two Chapters provide a basis for the comprehensive investigation of the structure and mechanics of C-S-H minerals and the developments of a new force field, which enables tackling larger systems in the forthcoming Chapters.

2.1 Introduction

Portland cement concrete is used more than any other man-made material on the planet. As a consumed material, it is only second after water. On average each person uses more than 3 tons of concrete a year. Concrete is perhaps the oldest construction material used by humankind. The first usage of concrete goes back to Egyptian civilization, which used a mix of mortar in their buildings. But Romans advanced the simple mortar by inventing the first hydraulic cement from fly-ash and lime. The cement modern history started by John Smeaton in 1754

to repair the Eddystone lighthouse in England. However, the first actual patent of Portland cement belongs to Joseph Aspdin who set out the combination of limestone, clay, and their manufacturing process [84].

Nowadays, cementitious materials are the absolute leaders in consumption and investment in the construction sector. As an example, cement production is currently more than 2.4 billion metric tons a year. Cement is an infrastructure key commodity whose production and use is directly correlated with any country's GDP growth. Majority of the cement production is located in the four BRIC countries with half of the world's production in China. Although cement has several advantages such as mass availability, low manufacturing cost, high compressive strength over other construction materials, it is considered to be the third greatest culprit (after transportation and electricity generation) to the climate change by producing 5-10% of global CO_2 emissions and significant levels of NO_x and other harmful particulates. About 60% of these greenhouse gas emissions comes from decarbonation of raw materials and 40% from fuel burning at high temperatures, $\sim 1500\,^{\circ}C$, to produce a so called clinker phase that form cement when mixed with water at room temperature.

Among different types of cement, Ordinary Portland Cement (OPC) is the most common one. It is produced by heating clays and limestone ($CaCO_3$) up to $\sim 1500\,^{\circ}C$, which after a series of chemical transformations result in a coarse phase clinker. A cement clinker contains several crystalline phases, the most prominent being Alite (C_3S), Belite (C_2S) and Tricalcium Aluminate (C_3A). Note that here cement chemistry is used to symbolize S=SiO_2, C=CaO and A=Al_2O_3. When a milled clinker, cement powder, is put in contact with water, a myriad of chemical reactions, phase transformations, and thermodynamic processes takes place whose complete details are quite complex due to the large number of involved variables. The main products of cement hydration are Calcium-Silicate-Hydrate, portlandite, ettringite, monosulphoaluminates [152] (Fig. 2-1).

In contrast to its ubiquity and common availability, and despite the most people belief, cement is a complex heterogenous materials with a hierarchical structure. Thus cement research is, in fact, a multidisciplinary research involving studying the intrinsic nature of chemical reactions of materials to manufacturing process and optimizing the engineering applications. Here, in this report we focus on the most important hydration product, Calcium-Silicate-Hydrate

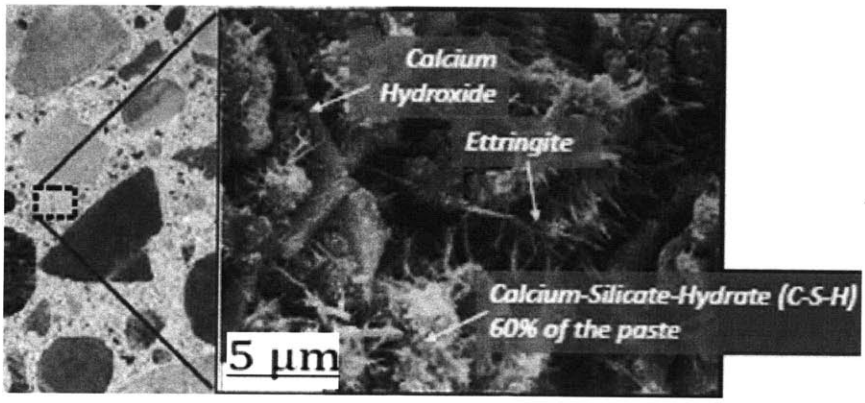

Figure 2-1: A magnified image of major cement hydration products. [Courtesy of Dr. James Beaudoin and Dr. Aalizadeh, National Research Council of Canada].

(C-S-H) that gives cement remarkable mechanical properties.

2.2 Hierarchical Structure of Cement Hydrate

Among concrete ingredients - aggregate, sand, cement and water - cement is the most essential component. Cement paste (cement mixed with water) is a complex, porous, multi-component hierarchical material, which plays the role of a glue to bind all ingredients together. In a cement paste, several crystalline hydration products co-exist with unhydrated clinker particles with different size and shapes, surrounded by the C-S-H gel. Because of the intrinsic heterogeneity from the random distribution and composition of clinker phases, cement hydrate has different levels of organization across different scales. Each scale is a random composite with a characteristic size and pore structure, which together present different structural features.

The multi-scale structure and micormechanical properties of concrete are studied earlier (see e.g. [26], [162]). In this report, we focus on the hierarchical structure of cement hydrate from macro to nano scale.

2.2.1 Macro Scale

At the macro scale ($> 10^{-3}$m), cement hydrate is usually considered as a homogeneous material with bulk physical properties and structural characteristics. At this scale, all hydration products

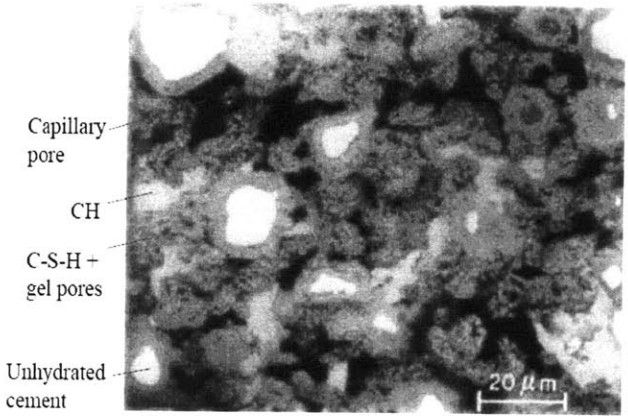

Figure 2-2: A micrograph of a cement paste with different hydratin products co-existing with the unreacted clinker particles and pore distribution (Courtesy of Dr. Hamiln Jennings, Concrete Sustainability Hub, MIT)

and unreacted clinkers particles are present and pores with diameters between 0.1 to 5 mm co-exist. These pores are usually originated from accumulation of trapped air bubbles during the hydration process, and are natural hosts for several chemical attack, which contribute negatively to mechanical properties including strength and durability [101].

2.2.2 Micro scale

At this scale (between 10^{-3} to 10^{-6}m), the heterogeneous structure of cement hydrate manifests itself clearly (Fig 2-2). The most common approach to investigate and study this scale is electron microscopy technique [125]. Among different cement hydration products, the C-S-H gel constitutes more than 60% of the volume. At this scale, C-S-H is an amorphous compound, which encompasses all the other particles/phases. Several morphologies are attempted to describe the C-S-H structure including: needles, foils, honey-comb, flakes and unshaped grains [152]. These morphologies are each based on different initial parameters such as water to cement ratio (w/c) , cement types, hydration stage and available pore size [73],[132].

The most common classification of C-S-H in the light of microscopy images recognizes C-S-H gel as inner and outer products [20],[53],[84],[135],[152]. The inner product grows radially towards inside the unreacted product in contrast to the outer product, which grow away from

the boundaries of the anhydrous clinker phases towards the outer space filled with water. The inner product is denser and more amorphous than the outer product, which form needle types or fiber-like structures fluxing outward from clinker grains. However, both the inner and outer products have similar compositions although a few reports point out otherwise by measuring larger Ca/Si ratio in inner products [134]. Among different crystalline phases, Portlandite, $Ca(OH)_2$, can reach several micrometers in size, hence clearly distinguishing itself at the micro-scale cement hydrate. Portlandite can grow with the outer space and in ideal conditions, its preferred grow direction forms hexagonal plates.

At this scale, the pore structure includes capillary pores or meso pores, which are created as a result of hydration which displaces the initial cement and water with products and empty spaces. The higher the w/c, the more porosity. Thus as the hydration advances, the pore volume decreases and the initial network of connected pores faces a percolation transformation to creates disconnected pores [19],[74],[101]. Although the capillary pores may reach to 5 μm in diameter, in well-cured sample they are usually between 10 nm to 50 nm [101].

Under heating or aging, cement hydrate, which is largely composed of Portlandite, C-S-H gel and reactive SiO_2 entities, all converts to a variety of hydrated Calcium Silicates such as tobermorite, jennite, afwillite, hillebrandite, foshagite, xonotlite, reyerite, gyrolite and truscottite. This family of C-S-H minerals differ in their atomic structure, Ca/Si ratio and the number of OH and H_2O groups [153] and each relates to a real C-S-H phase with different temperature and hydration conditions.

2.2.3 Meso Scale

As the complex cement hydrate structure passes elegantly through scales, we consider an intermediate meso scale, as a bridging scale, which links the nanometers to micrometer features. Thus it ranges from a few tens of nanometers to less than 1 μm. At this scale C-S-H is the most prominent phase controlling the majority of cement hydrate properties. Whether C-S-H is a matrix or a granular particulate material is a controversial subject in cement literature. However, recent experimental techniques such as accurate nanoindentation probing [27] and perhaps small angle neutron scattering measurements (SANS) [4] hint towards a granular particle behavior with (still) unknown shapes, sizes and packing distribution of particles. These

characteristics together with C-S-H particle interactions are still open subjects in the cement community.

2.2.4 Nano Scale

At this scale, ($< 10^{-9}$ m) C-S-H pores are intrinsic to the gel structure (so called gel porosity) and significantly control the high surface area, creep, shrinkage and many other physical processes. But the quantitative characterization of such pore volumes is quite difficult. For instance, water loss measurement by drying the cement paste is flawed by the presence of adsorbed water [31]. Thus characterization of C-S-H at this scale is not straightforward and several experiments including Nuclear Magnetic Resonance (NMR), Scanning Electron Microscopy (SEM), Transmission Electron Microscopy (TEM), Atomic Force Microscopy (AFM), SANS, Small Angle X-ray Spectroscopy (SAXS), and sorption experiments can not fully elucidate the complex details of the C-S-H structure [125]. Even after decades of intensive research, understanding the atomic arrangement of C-S-H gel and properly predicting its mechanical properties is far from satisfactory. Due to the importance of this scale as the next frontier in cement science, we discuss C-S-H gel in length in the next section.

2.3 C-S-H Gel

By mixing water and cement, a so-called gelatious phase, C-S-H (Calcium-Silicate-Hydrate), precipitates as nanoscale clusters of particles which is the primary binding product of cement hydration [153]. Here cement chemistry notation is used for C=CaO, S=SiO_2, H=H_2O. C-S-H is a nonstoichiametric compound and the hyphenated expression refers to different combination of C, S and H. In 1905, le Chatelier suggested CaO.SiO.Aq as a variable composition for the C-S-H gel [86]. C-S-H is considered to be the smallest building block of concrete and it is the principal source of strength and durability in all Portland cement concretes.

As elucidated earlier, due to its complexity, the exact structure of C-S-H gel at the nanoscale is still unresolved. The insufficient accuracy of microscopic techniques can not explore the small sizes of the disordered C-S-H gel. Thus indirect approaches are the only available techniques to investigate the C-S-H. For instance, SANS measurements estimates the average Ca/ Si ratio

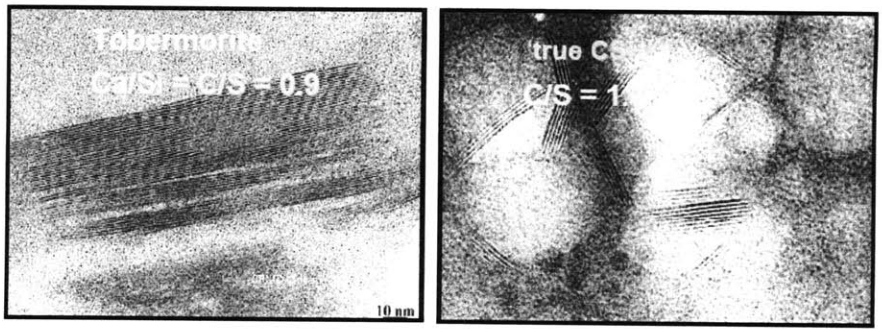

Figure 2-3: TEM images of C-S-H. a) A synthesized C-S-H with Ca/Si=0.9. The layered strucutre is similar to tobermorite (image from [52]), b) True clusters of C-S-H gel with Ca/Si=1.7 [Image credit: courtesy of A. Baronnet, CINaM, CNRS and Marseille Université, France]. Note the difference in Ca/Si ratios and the longer, organized connectivity of the silica chains in the synthesized C-S-H.

in C-S-H to be 1.7 [4], with local values measured by TEM between ~0.6 to ~2.3 [175]. High resolution ^{29}Si and ^{17}O nuclear magnetic resonance (NMR), X-ray adsorption spectroscopy, IR spectroscopy and Raman spectroscopy, nanoindentation and gas sorption reveal important information on C-S-H structures [23],[72],[125]. Figure 2-3 shows a TEM image of the C-S-H gel.

Even though C-S-H gel is amorphous but it has some short-range order at sub-nanometer scales. Much of the findings at this level is obtained through comparison with fully crystalline Calcium-Silicate Hydrate minerals. Different models define C-S-H gel as calcium oxide sheets connected to silicate chains to form a layered structure. The interlayer space is comprised of water molecules and ions such as Ca^{+2} or Na^{+1} [131],[132],[133],[135],[152]. In essence, it is widely accepted that C-S-H has a layered structure akin mostly to that of tobermorite and jennite minerals. Variety of experimental techniques are deployed to characterize these C-S-H layers/chains [125]. Among these methods NMR renders valuable information about the silica chains. These chains are Wollastonite type or Dreierketten with finite lengths of 2,5,8,..,$3n$-1, where n is an integer; hence the minimum length of the repeating unit containing three tetrahedra (Fig. 2-4). Two of tetrahedra share an oxygen in a dome-type pattern and are called

paired tetrahedra while the third tetrahedron, which is in a different chemical site and its vortex points out of the calcium layer, is called bridging tetrahedron [131],[132],[152]. Each repeating unit is an orthosilicic acid group, $Si(OH)_4$, which has polymerized via condensation reactions to form the silica chains [95]. In C-S-H gel, the bridging tetrahedron in a Wollastonite chain does not make a bond (by sharing oxygen on the vortex) with other bridging tetrahedra from an adjacent layer, and thus is called single silica chain. In a young OPC paste, dimers constitute most of the chains but the chain length continue growing. For a 23 year old OPC cement paste, the mean silica chain length is reported 4.8 [139]. Richardson et al, proposed a growth model to explain the discontinuous silica chain lengths (2,5,8, ...) [131], [133], [135], [137]. This model consider chains growth by accumulation of two dimers via a bridging monomer to form a pentamer as apposed to forming a trimer via dimer and monomer and so forth. However, such models are still under development and much of current knowledge on C-S-H at the nanometer scales comes from natural mineral analogs of C-S-H, which we will describe in the next section.

2.4 Mineral Analogs of C-S-H Gel

There are at least thirty crystalline minerals that are similar in composition to C-S-H [136]. For instance at standard conditions, afwillite is a thermodynamically C-S-H phase in equilibrium with water and Portlandite [92]. However, high resolution TEM observations indicate that C-S-H gel contain tobermorite and jennite-like structures [166], [175].

2.4.1 Tobermorite Minerals

The tobermorite natural minerals have structure and crystal chemistry that are not only appealing because of their close similarity to C-S-H phases, but they have also potential application as excellent cation exchangers for nuclear and hazardous waste disposal materials [80]. Tobermorite group are layered structure and can be classified based on their different basal spacing as 9.3 Å, 11.3 Å and 14 Å [100] which are usually referred to as 9 Å, 11 Å and 14 Å [15]. This interlayer spacing distance represents the degree of hydration of tobermorite, which changes by heating. The thermal behavior of tobermorite and their corresponding synthetic minerals are studied by various techniques such as electron diffraction, electron microscopy, X-ray diffrac-

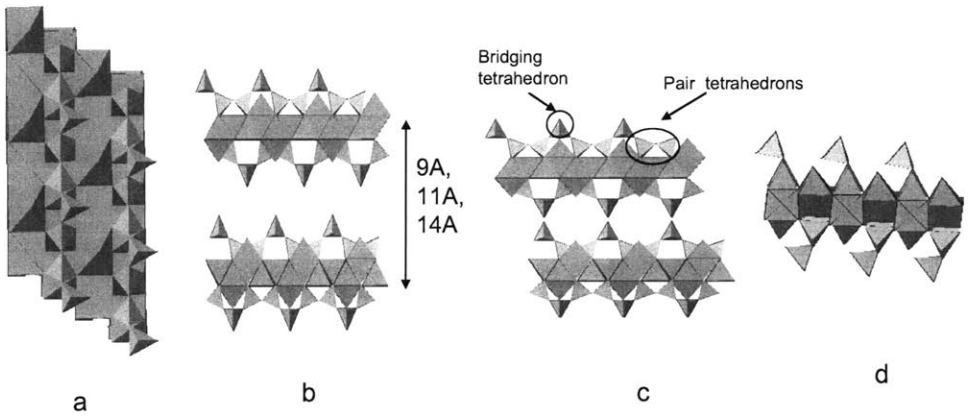

Figure 2-4: a) Top view of a typical tobermorite. b) a side view of a layered tobermorite with single silica chains. c) a side view of a layered tobermorite with double silica chains. d) [010] view showing the dangling bridging tetrahedra. Pink pyramids represent silicon tetrahedra and green ribbons indicate calcium layers.

tion, and NMR solid state spectroscopy [24],[80],[94],[100],[169][174]. Due to non hydroxylated oxygen atoms in the bridging silicon tetrahedra, tobermorite layers are negatively charged. But the overall electroneutrality of the cells is maintained through the existence of interlayer ions Ca^{+2}.

These studies show tobermorite 14 Å transforms into tobermorite 11 Å by heating up to 80°-100° C. Further heating up to 300° C for a few hours causes transformation to tobermorite 9 Å. Tobermorite 11 Å has two different structures: Hamid structure which is a Reitveld refinement that depicts tobermorite as independent layers [58] and Merlino structure which presents tobermorite as chemically bonded layers [103].

Merlino Structure

In Merlino type tobermorite (including 14 Å, 11 Å and 9 Å) there are two modular units: A calcium polyhedra with the smallest repeat unit length of 3.65 Å and a Wollastonite chain with typical length of 7.3 Å. Figure 2-4a shows a top view of the connection of silica chains to calcium ribbon in two equivalent ways shifted by 3.65 Å in b crystal direction. The silica chains are connected to calcium layers from both top and bottom. Figure 2-4b shows a side view of

tobermorite with two layers. The interlayer distance in general contain water molecules and Ca cations (or other cations) depending on the hydration degree and chemical environment.

If the bridging tetrahedron is dangling in the interlayer distance (Fig. 2-4b) or share an oxygen with the interlayer calcium ions, then this silica chain is called single silica chain. Otherwise head-to-head connection of bridging tetrahedra (such as in Fig. 2-4c) forms an iono-covalent Si-O-Si bond with the upper/lower layeres [119]. This direct interlayer links changes the 2D layered structure of tobermorite into a strong 3D network by making ring-type structures along the chains. This form of silica chains is called double silica chain. Figure 2-4d shows a [010] view of tobermorite and the flanking bridging tetrahedra. Merlino tobermorite 14 Å and 9 Å have single silica chains while Merlino tobermorite 11 Å is comprised of double silica chains. There are some specimens of tobermorite 11 Å that do not shrink to 9 Å upon heating and are called anomalous tobermorite to distinguish them from "Normal" tobermorite which shrink to 9 Å. A possible reason for such peculiar behavior has been recently hypothesized in [103]. A detailed study on natural and synthetic tobermorite minerals and procedures to produce them can be found in [14] and references therein.

Hamid Structure

This class of tobermorite only belongs to interlayer distance of 11 Å and has characteristics analogous to Merlino tobermorite 11 Å but with a main difference that it contains only single silica chains (i.e. independent layers). Figure 2-5a shows a layer of this tobermorite along with its side view (Fig. 2-5b). While this backbone layer is structurally unchanged, Hamid tobermorite can have three different Ca/Si ratios, namely 0.67, 0.83 and 1. This is feasible by adding calcium cations in the interlayer distance in the following way: for each addition of calcium cations two protons must be removed from the hydroxyl groups of the layers to ensure the cell neutrality.

2.4.2 Jennite

Jennite is a rare mineral analogous to C-S-H crystalline tobermorites that is believed to be closely related to the structure of cement at late stages of hydration process [153]. ^{29}Si NMR

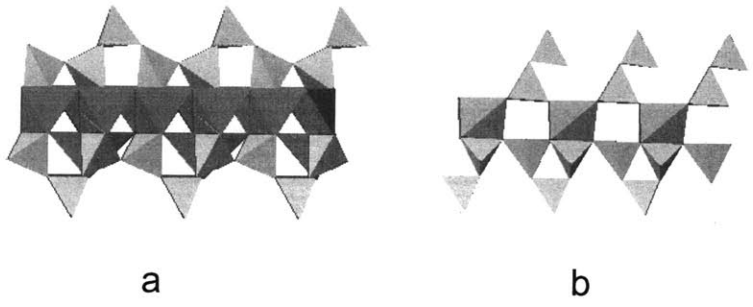

Figure 2-5: a) A layer of tobermorite 11 Å (Hamid structure) which has single silica chain. b) its [010] view. Pink pyramids represent silicon tetrahedra and green ribbons indicate calcium layers.

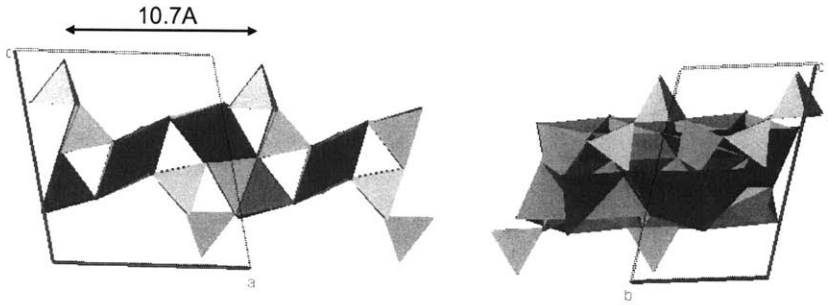

Figure 2-6: a) A layer of jennite shown with a unit cell. b) A [100] view of jennite. Pink pyramids represent silicon tetrahedra and green ribbons indicate calcium layers.

indicates that it has single silica chains [80] with Ca/Si=1.5. Its crystal structure is solved and refined in [16]. Similar to tobermorite, jennite losses water upon heating and transform into another phase called meta-jennite. Unlike the tobermorite family, the bridging tetrahedra of the silica chains in jennite are connected to the calcium-oxide layers as well. As in tobermorite, the negatively charged layers in jennite are counterbalanced by Ca^{+2} ions located in the interlayer space. Fig 2-6a shows a layer of jennite along with its unit cell. Note that the side distance between silica chains in jennite is around 10.7 Å which is much larger than that in all tobermorite family (about 7 Å). Figure 2-6b shows a side view of jennite in the *bc* plane.

2.4.3 C–S-H type I and II

C-S-H (I) is a result of ill-crystalline product during the synthetic of tobermorite 14 Å. Mainly, the lack of bridging silicon tetrahedra in tobermorite is what is known as C-S-H (I). Thus, the chains follow the (3n-1) rule and the Ca/Si increases spanning from 0.8 to 1.5 [84], [153]. The X-ray power diffraction patters indicate that the basal spacing in C-S-H (I) decreases with increasing Ca/Si.

Similarly, under certain thermodynamic conditions and water excess, a second ill-crystalline product may be formed that is called C-S-H (II). In this product with multiple imperfections the Ca/Si ratio can reach up to 2. X-ray diffractograms show lattice parameters similar to those found in jennite. Thus C-S-H (II) is as an disordered version of jennite and/or tobermorite with finite silicate chains following the 3n-1 rule.

2.5 C-S-H Gel Models

2.5.1 Models for the Atomic Structure

Imperfect version of crystalline minerals such as tobermorite, jennite or portlandite provide a appropriate framework to propose numerous models explaining the atomic structure of C-S-H. Two detailed review papers on this subject can be found in [132], [136]. In what follows, we briefly discuss the main features of these models.

Earlier models used portlandite structure in conjunction with monomeric silicate groups [57], [145]. Tobermorite models were suggested in 1952 after X-ray power diffraction studies on hydrated alite pastes [13]. This paper sets tobermorite family as a base for many models proposed afterwards. However, the main drawback of these models was its low Ca/Si, which was 0.83 while the average Ca/Si in real C-S-H was around 1.7 (Fig 2-7). Hence, some authors proposed a model based on a solid solution of tobermorite and portlandite [44], or tobermorite like layers sandwiched in between the portlandite sheets [76], or tobermorite models with more Ca^{+2} and OH^{-1} ions in between the layers [83].

Thus, all these models had a higher Ca/Si ratio but their silica chain was either all monomeric or infinite, neglecting the finite chain lengths of C-S-H gel. To resolve this issue, Taylor suggested to replace partial bridging SiO_2 units with interlayer Ca ions to achieve higher Ca/Si

ratios [154]. Hence, partial chain lengths were created by this approach. Later, other researchers extended this concept to two versions of C-S-H gel: one based on entirely dimeric silica chains and the other one based on polymeric silicate chains. Both versions had variable amount of ions in the interlayer distance to ensure the charge neutrality [149]. About three decades later, Taylor revised his first model to put forward the possibility of jennite like structures accounting for large Ca/Si ratios [152].

Perhaps the most general and comprehensive model belongs to Richardson and Groves [131], [132], [135], [134] who proposed a two-fold classification to clarify C-S-H chemistry. This classification references so-called tobermorite/jennite (T/J) models on one hand and tobermorite-calcium hydroxyl (T/CH) models on the other hand. The T/CH class considers models that are solid solutions of tobermorite layers sandwiching calcium hydroxide, hence providing a means to achieve a larger Ca/Si ratio than the one of tobermorite. The T/J class considers C-S-H as an assembly of tobermorite regions followed by jennite domains. While the T/CH class was found to be relevant for hydrated KOH-activated metakaolin Portland cement, more common water activated Portland cement pastes can be only partly described by the T/J or the T/CH approaches.

2.5.2 Models for the Nanostructure and Morphology

So far we have discussed the nature of the atomistic structure of the C-S-H gel as a combination of disordered tobermorite-jennite like crystals. But how these models grow and rearrange themselves to develop hardened C-S-H colloids is an important topic, which is still not well understood. Indeed, there are certain contradictions between the nature of crystalline (from tobermorite/jennite models) versus colloidal C-S-H gel at the nano level. The concept of colloidal nature in C-S-H gel was first introduced in 1909 [105]. Today this model is widely accepted as descriptive model for the C-S-H gel behavior at the nano level.

Power-and-Brownyard 1948 Model

This model is a benchmark in cement community to quantitatively describe the colloidal structure of C-S-H gel [122]. It provides an extremely simple model calibrated with water content and pore volume data. This model estimates an interlayer space of 1.8 nm and a constant

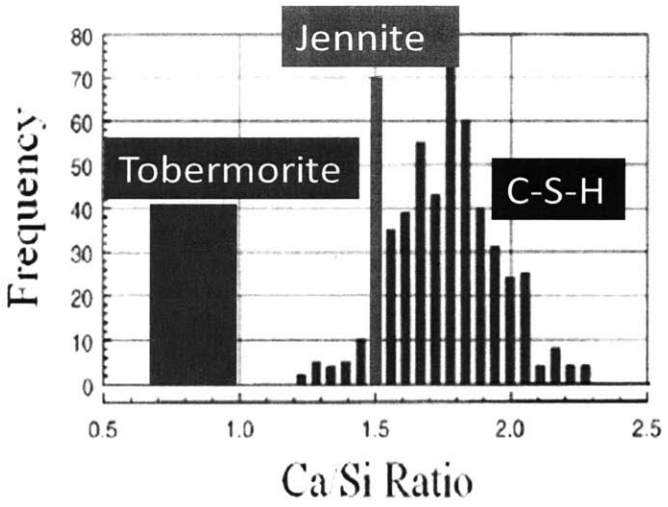

Figure 2-7: Ca/Si ratio frequency histogram in Portland cement pastes, measured by TEM microanalyses of C-S-H free of admixtures with other phases [135]. For comparison, the Ca/Si ratios for tobermorite minerals and jennite are also shown with wide and narrow rectangular boxes respectively.

porosity of 28% for the C-S-H phase. But now it is well-known that porosity changes during the hydration period.

Feldmann-Sereda Model

Feldman and Sereda proposed a morphological modification to the Power-Brownyard model to better explain the nanostructure of C-S-H gel structure [40]. This model depicts C-S-H particles as a group of a few tobermorite layers with interlaminar water in between them (Fig. 2-8). This model has the following features: i) The missing of water in between the layers causes the layers to get closer to each other and create local disorders, ii) free surfaces that are not in contact with other layers can have adsorbed water iii) the interlayer space varies from 0.5 to 2.5 nm. This model was rather qualitative than quantitative and was later modified by Daimon el al by incorporation of some internal pore structures with the pores in between the C-S-H particles suggested by Feldman-Sereda model [31].

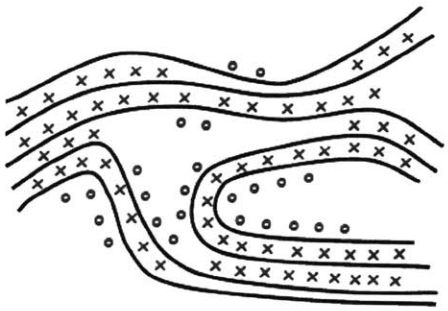

Figure 2-8: Feldman-Sereda model for the C-S-H gel nanostructure. The interlayer waters are shown by (**x**) while the physically adsorbed waters are represented by (**o**) [adapted from [95]].

Jennings Model

Perhaps the most successful model for quantitative consideration of morphology of C-S-H phases so far is due to Jennings and co-workers who resolved different inconsistent experimental data on the surface area, density and water contents [66], [155]. This model resolved contradictory results of the previous works on surface area measurements, i.e samples with the higher surface area exhibit lower gel porosity [66]. But one would expect the opposite if C-S-H had a single porosity. One way to resolve this was to consider several densities for the C-S-H gel. Thus new Specific Surface Area (SSA) measured by SANS [158] together with better interpretation of the N_2 sorption data, resulted in identifying the existence of two different C-S-H types, which differ only on porosity. However, a model with more than two C-S-H phases could equally justify the experimental data.

In this model, known as CM-I, the smallest building blocks were spheres with a characteristic radius of $\approx$1 nm and density $\approx$2.8 g/cm^3. These spheres tend to agglomerate to form larger structures so called "globules". The new feature of this model was that the globules could pack in two different ways, known as Low Density (LD) and High Density (HD), which respectively correspond to the *outer* and *inner* products suggested earlier. The parameters of this model (size, density, porosity) were fitted to an extensive set of experimental data on density, composition, surface measurements to obtain globules of approximately 2.5 nm in radius with an interglobule porosity of $\phi_G = 18\%$ and density $\approx$2.4 g/cm^3.(Fig. 2-9). The LD C-S-H and HD

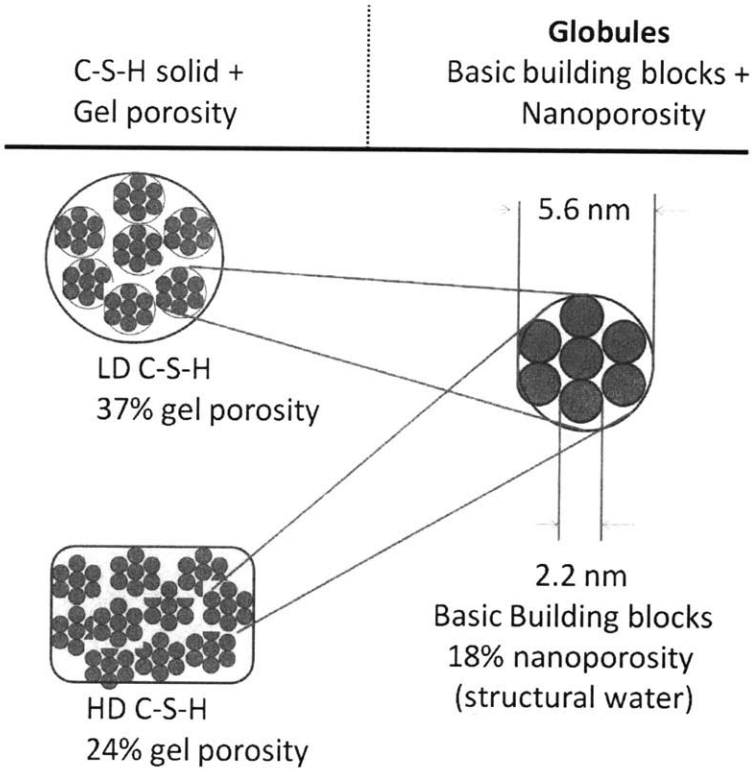

Figure 2-9: Jennings model of C-S-H, CM-I.

C-S-H were found due to the interglobular porosities of $\phi_{LD} = 37\%$ and $\phi_{HD} = 24\%$, with variable densities depending on the water content, $\rho_{LD} = 1.44 - 1.93$ g/cm^{3}and $\rho_{HD} = 1.75 - 2.13$ g/cm^3. This is, however, inconsistent with the SANS scattering data because there is a large particle size distribution with an overlap between them. Later Constantidines and Ulm [27] pointed out that the corresponding packing density (i.e. one minus porosity) of LD C-S-H and HD C-S-H is in fact very close to the limit packing densities of spheres, namely $\eta \approx 0.64$ for the random packing density of spheres [35],[64], which relates to LD C-S-H and $\eta \approx 0.74$ for the maximum packing of spheres [146], which relates to HD C-S-H and can be formed via two ways: the ordered-faced centered cubic (fcc) and hexagonal closed-packed random packing.

Based on the pore structures and surface configurations on LD and HD and the relation between the SSA measured by SANS with the degree of hydration, the authors suggested LD C-S-H gel as an appropriate model for the early stages of hydration, and HD C-S-H gel for late

stages of hydration (diffusion). Ulm and coworkers [25], [27], [162] performed extensive nanoindentation experiments on different cement paste samples, which showed a bimodal distribution of elastic properties, confirming the presence of LD C-S-H and HD C-S-H phases. Their results were based on extrapolation of elastic properties by correcting for the effect of interparticle porosity, via particle packing density, η, and determine the C-S-H particle indentation modulus, $m_s = E_s/\left(1-\nu_s^2\right)$, where E_s is the Young's elastic modulus, and ν_s is the Poisson's ratio. Recently, Van Damme and Ulm proposed the existence of a third (rare) phase as Ultra High Density C-S-H [162].

Refinement to the CM-I model was proposed by Jennings and co-workers, after obtaining a new set of data about C-S-H particles by SANS and SAXS [4],[72]. It was found that the density of the basic building blocks of C-S-H particles is $\approx$2.604 g/cm^3 with an average chemical formula of $(CaO)_{1.7}(SiO_2)(H_2O)_{1.8}$. In the new model, called CM-II, the globules were modified to include some features of Feldman-Sereda model (i.e tobermorite-jennite like layers) while the concept of LD C-S-H and HD C-S-H were still present due to the packing of globules. In this refined model, the water can be in several locations: interlaminar water, which fill the intraglobule space, or adsorbed water on the surface of globules or interglobules water located in between the globules (Fig 2-10).

2.6 Chapter Summary

The aim of this Chapter was to present the complexity and levels of hierarchy in cement hydrate with a traditional top-down zoom going from macro to nano scale. We showed that the core of the cement hydrate structure is a gelatious phase, so called, C-S-H, which is the principal source of strength and mechanical properties in all Portland cement concretes. While many crystal minerals such as tobermorite, jennite, portlandite or their natural or disordered combinations are postulated as models to explain the different structural pattern and properties of C-S-H, the structure itself is not fully resolved yet, in particular at the nano scale. Major inconsistencies lie in the Ca/Si ratio, the length of the C-S-H silica chains, the structure of the gel-porosity, and also in the intimate local order at the scale of the layers because XRD does indicate disordered glassy materials compared to tobermorite. Thus, satisfactory prediction of

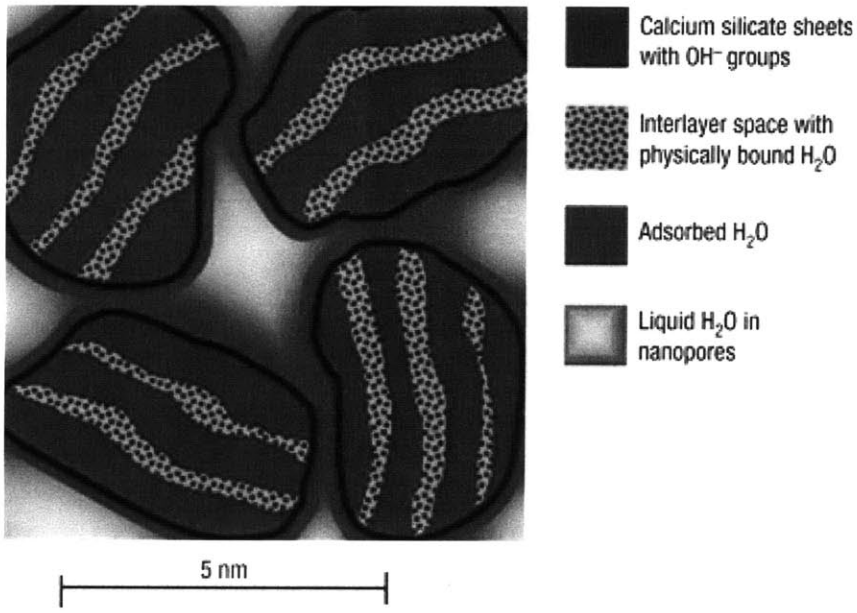

Figure 2-10: Refined Jennings model, CM-II, for the C-S-H gel nanostructure (from [4]).

fundamental physical properties such stiffness and strength at the atomistic level is far beyond the reach.

Several models attempted to shed light on the C-S-H gel morphology and density. Among others, the concept of various densities and globules stemmed from different porosities and SSA measurements were the most reliable approach in defining and linking the C-S-H morphologies to the experimental data. However, exploring the inside of the buildings blocks below the nano scale remain a formidable challenge, which will most likely have a tremendous impact on cement science. At this stage due to the insufficient atomistic resolution of experimental probes, or their prohibitive expenses, the implementation of computational materials science paradigms into the atomistic structure of C-S-H seems the only viable approach to address this challenge. In the next Chapter, we will introduce several atomistic modeling techniques, which will be incorporated in Part III and IV to develop a computational toolbox suitable for a comprehensive investigation of the C-S-H gel structure and properties.

Chapter 3

Overview of Computational Modeling Techniques

This Chapter is centered around the most common methods in computational materials science that are applicable to cement-based materials. We review the basic hypotheses, theories and equations of several methods such as first-principles calculations, Molecular Mechanics, Molecular Dynamics (MD), Monte-Carlo simulations, and coarse graining as a means to study dynamics and equilibrium properties of a system. Different levels of the theories were employed and each focuses on solving specific equations within their capabilities. In this Chapter, we also introduce two commonly used force fields for hydrated oxides, ClayFF and core-shell model. The force fields and methods presented in this Chapter will be extensively used in the next Parts where more simulation details for each problem will be given. In particular, first-principles calculations in Part III benchmarks the C-S-H crystal data. MD method in conjunction with Statistical Mechanics and Monte-Carlo simulation results in realistic molecular C-S-H models in Part IV.

3.1 Introduction to Atomistic Modeling Methods

Nowadays atomistic modeling of material has become an essential research tool to study various problems such as organic chemistry, drug design, DNA (un)folding and so forth. One of the first models applicable to the concept of atoms and molecules was the kinetic theory of gases

developed in the second half of the XIX century by Clausius, Maxwell and Boltzman. Other than a few simple systems such as ideal gases, this model was unable to calculate the properties of a real system [42]. In general, the Statistical Mechanics equations can be written but hardly solved analytically because of the complexity introduced in the interparticle interactions.

The emergence of computers made it possible to numerically solve the Statistical Mechanics equations. The first use of computers for simulations was carried out in Los Alamos in 1953 to study the interaction of liquids by Monte-Carlo (MC) method [104]. Three years later, Molecular Dynamics (MD) simulation of hard spheres was reported [2]. These simulations were based on classical Newtonian Mechanics to describe the atomic behavior. However, earlier in the past century, Planck, Einstein, Dirac, Pauli, Born, Schrödinger and others showed that the classical mechanics is not valid at the very small scales and established the framework of quantum mechanics. Following the previous works, Schrödinger in 1926 discovered a partial differential equation for the time evolution of the hydrogen atoms. The Schrödinger equation, named after him, is analogous to the Newton's second law for classical systems. This equation accurately describes the dynamics of the systems under the size of molecules and atoms and is based on wave functions that include all the information of a system.

3.2 First-Principles Method

First-principles or the Latin word *ab-initio* refers to a method that is entirely independent of any empirical input and is solely based on the electronic properties of a mater. The frontier between Classical and Quantum Mechanics is defined by the De Broglie Thermal Wave Length parameter

$$\Lambda = \frac{h}{\sqrt{2\pi m k_b T}} \tag{3.1}$$

In Eq. (3.1), h and k_b are the Planck and Boltzman constants, respectively and m and T are the mass and temperature of the particle. For a given temperature, when the De Broglie Thermal Wave Length is much less than the interparticle distance, the Classical Mechanics governs. Otherwise when Λ is on the order or larger than the interparticle distance, Quantum Mechanics will dominate. There are different flavors to include the relativistic effects and

electronic correlations but the common platform is as follows: A stationary electronic state $\Psi_i(\overrightarrow{r})$ is described by a wavefunction satisfying the time-independent Schrödinger equation

$$\widehat{H}\Psi_i(\overrightarrow{r}) = E\Psi_i(\overrightarrow{r}) \tag{3.2}$$

where $\widehat{H}$ is the Hamiltonian operator and E_i is the system energy at a state i. For a given system of N electrons and M nuclei, in the absence of external fields, the Hamiltonian can be written [85]:

$$\widehat{H} = \widehat{T}_e + \widehat{T}_n + \widehat{V}_{en} + \widehat{V}_{ee} + \widehat{V}_{nn} \tag{3.3}$$

where $\widehat{T}$ and $\widehat{V}$ stand for the kinetic and potential energy of the system and the subscript e , n refers to electrons and nuclei, respectively. Thus, $\widehat{T}_e$ shown the total energy of all electrons and $\widehat{V}_{en}$ total potential energy of the all interacting electrons with nuclei, and so on. These energy terms constitute the total energy of the system of electrons and nuclei and can be written as

$$\widehat{T}_e = -\frac{1}{2}\sum_{i=1}^{N}\nabla_i^2 \tag{3.4}$$

$$\widehat{T_n} = -\frac{1}{2}\sum_{A=1}^{M}\nabla_A^2 \tag{3.5}$$

$$\widehat{V}_{en} = -\sum_{i=1}^{N}\sum_{A=1}^{M}\frac{Z_A}{r_{iA}} \tag{3.6}$$

$$\widehat{V}_{ee} = \sum_{i=1}^{N}\sum_{j>i}^{N}\frac{1}{r_{ij}} \tag{3.7}$$

$$\widehat{V}_{nn} = \sum_{A=1}^{M}\sum_{B>A}^{M}\frac{Z_A Z_B}{r_{AB}} \tag{3.8}$$

In above equations, Z_A is the atomic number of the nucleus A, and r is the distance. The wavefunction $\Psi_i(\overrightarrow{r})$ is not an observable, hence it doesn't have a physical meaning, but its square indicate the probability distribution of finding the system at the determinate state i.

Except for a few simple systems, the analytical solution of the Schrödinger equation is

impossible [87]. However, the variational approach provides a convenient path to this end, and states that for any given trial wave function $\Psi_{trial}(\overrightarrow{r})$, E_{trial} will only be minimal, (i.e. ground state energy) if $\Psi_{trial}(\overrightarrow{r})$ is the ground state wave energy. Thus the basis of constructing a wave function is minimizing the system energy as much as possible to get closer to the ground state energy.

For molecules, the Schrödinger equation can be simplified by Born-Oppenheimer approximation [17], which is mainly based on the assumption that nuclei are much heavier than electrons and thus move much slower. According to this approximation, the wave function of a system can be separated into electronic (Φ_e) and nuclear (Φ_n) functions, hence Eq. (3.2) simplifies to

$$\widehat{H}\Phi_e(\overrightarrow{r})\,\Phi_n(\overrightarrow{r}) = E_{total}\Phi_e(\overrightarrow{r})\,\Phi_n(\overrightarrow{r}) \tag{3.9}$$

In Eq. (3.9), nuclei are first assumed to be frozen with respect to the motion of electrons, then the electronic arrangement are studies. In other words, the essence of Born-Oppenheimer approximation is that electrons can instantaneously adjust to the nuclei positions for any movement.

3.2.1 Density Functional Theory

In the previous Section, the central quantity was the wavefunction, and the information about the energy and electron density was derived from it. In Density Functional Theory (DFT), the central quantity is the electron probability density, $\rho(\overrightarrow{r})$, itself, as a function of the position $\overrightarrow{r}$. The energy, E, is a function of $\rho(\overrightarrow{r})$ and is written as $E[\rho]$. This simply means that there is a single energy, E, corresponding to the entire function $\rho(\overrightarrow{r})$. This notion provides an alternative to manipulation of wave functions. In fact, stemmed from the Thomas-Fermi model, Hohenberg-Kohn [61] put DFT on a firm theoretical footing by the two Hohenberg-Kohn theorems (H-K):

- The first H-K theorem demonstrates that the ground state properties of a many-electron system are uniquely determined by an electron density that depends on only 3 spatial coordinates. This theorem can be extended to the time-dependent domain to develop time-dependent density functional theory, which can be used to describe excited states.

- The second H-K theorem defines an energy functional for the system and proves that the correct ground state electron density minimizes this energy functional.

Although the H-K theorems prove that the energy functional exist, it does not determine its form. The exact form of the functional is still unknown and contemporary DFT methods constitute various approximations to it.

The exact ground state energy functional of an n-electron system reads

$$E[\rho] = E_{KE}[\rho] + E_{NE}[\rho] + E_{E_H}[\rho] + E_{XC}[\rho] \tag{3.10}$$

In Eq. (3.10), the first term is the kinetic energy of the electrons and its functional form is not known directly. However, by re-introducing the concept of wave function Kohn and Sham [78] were able to express the kinetic energy of electrons as

$$E_{KE}[\rho] = \frac{h^2}{2m_e} \sum_{1}^{n} \int \psi_i^* (\overrightarrow{r}) \nabla^2 \psi_i (\overrightarrow{r}) \, d\overrightarrow{r} \tag{3.11}$$

In above, the one-electron orbital, $\psi_i (\overrightarrow{r})$, are the Kohn-Sham molecular orbitals. They are related to, but different from, the ground state charge density, $\Psi_i (\overrightarrow{r})$, introduced in the previous Section. The $\psi_i (\overrightarrow{r})$ orbitals are the solutions to the Kohn-Sham Equations discussed below. The ground state charge density can be obtained from

$$\rho (\overrightarrow{r}) = \sum_{1}^{n} |\psi_i (\overrightarrow{r})|^2 \tag{3.12}$$

The second term in Eq. (3.10) is the electron-nuclear interactions:

$$E_{NE}[\rho] = -\sum_{i=1}^{n} \int \frac{Z_i e^2}{4\pi\varepsilon_0 \, |\overrightarrow{r} - \overrightarrow{r}_i|} \rho (\overrightarrow{r}) \, d\overrightarrow{r} \tag{3.13}$$

where the sum runs over all i nuclei; the $|\overrightarrow{r} - \overrightarrow{r}_i|$ is the separation of point $\overrightarrow{r}$ and nucleus i; ε_0 is the dielectric constant in vacuum and e is the charge of an electron.

The third term is the classical coulombic energy between the electron densities at point $\overrightarrow{r_a}$ and point $\overrightarrow{r_b}$:

$$E_{E_H}[\rho] = \frac{1}{2}\int \frac{\rho(\overrightarrow{r_a})\,\rho(\overrightarrow{r_b})\,e^2}{4\pi\varepsilon_0\,|\overrightarrow{r_a} - \overrightarrow{r}_b|} d\overrightarrow{r_a} d\overrightarrow{r_b} \tag{3.14}$$

This term is usually referred to as the "Hartree energy", because it correspond to the coulombic interactions between average electron densities.

The last term is Eq. (3.10), $E_{XC}[\rho]$, is the reason the form of the complete functional is not known. This term modifies the energy to account for the fact that the motion of each electron is influenced by the motions of all the other electrons. $E_{XC}[\rho]$ is also a function of the electron density and is called the Exchange-Correlation energy of the system.

It was mentioned above that the kinetic energy of the electrons is given in terms of the Kohn-Sham orbitals, $\psi_i(\overrightarrow{r})$, which are found by solving the Kohn-Sham equations:

$$\left(-\frac{h^2}{2m_e}\nabla^2 - \sum_{i=1}^{n}\frac{Z_i e^2}{4\pi\varepsilon_0\,|\overrightarrow{r} - \overrightarrow{r}_i|} + \int \frac{\rho(\overrightarrow{r_a})\,e^2}{4\pi\varepsilon_0\,|\overrightarrow{r_a} - \overrightarrow{r}_b|} d\overrightarrow{r_a} d\overrightarrow{r_b} + V_{XC}(\overrightarrow{r})\right)\psi_i(\overrightarrow{r}) = \varepsilon_i\psi_i(\overrightarrow{r}) \tag{3.15}$$

where the ε_i are the orbital energies and the exchange-correlation potential, V_{XC}, is simply

$$V_{XC}[\rho] = \frac{\delta E_{XC}[\rho]}{\delta\rho} \tag{3.16}$$

The Kohn-Sham equations are solved iteratively and self-consistently since the solution, $\rho(\overrightarrow{r})$, itself is a part of the Hamiltonian on the left hand side of Eq. (3.15). The process starts by making a guess at the charge densities, often by superimposing the atomic densities. Assuming a functional form is available for E_{XC}, the electron density can be used to solve Eqs. (3.15) to give an initial set of Kohn-Sham orbital $\psi_i(\overrightarrow{r})$. From these orbitals, an improved electron density can be found via Eq. (3.12), which can then be re-inserted into the Kohn-Sham equations. This iterative process can be continued until the electron density and E_{XC} have converged. Then, the total energy can be obtained from Eq. (3.10).

In principle, the process described so far is exact. However, the exact form of exchange-correlation functional, $E_{XC}[\rho]$, is unknown and must be approximated. The simplest approximation is the Local-Density Approximation (LDA), which is based upon exact exchange energy for a uniform electron gas, which can be obtained from the local values of the electron density

at that point, or from fits to the correlation energy for a uniform electron gas. However, for a molecule the electronic density is obviously not uniform. Hence, as the refinement of LDA, the General Gradient Approximation (GGA), uses functional forms that are dependent on both the local electron density and its gradient at that point.

There are different approaches to obtain the one electron states such as the use of Atomic Orbitals, Grid Sampling and Plane Waves (PW). In solid states physics, PW are common since the concept of the periodic boundary condition is indirectly implemented. PW are not only at nuclei but they are extended in all space to provide the solutions of the Schrödinger equation for a free electron particle [98]. In this method, each orbital wave function is expressed as a linear sum of 3D planes waves

$$\psi_i^k(\overrightarrow{r}) = \sum_g a_{i,k+g}.e^{i(k+g)\overrightarrow{r}} \tag{3.17}$$

where k, i, g are respectively the wave vector, the imaginary number and the reciprocal lattice vectors in a periodic cell. In theory, PW are a complete basis set. Thus as the number of planes waves increases, the basis set approaches the ground state energy. However, their computational cost can be higher when it comes to accurate results for the core orbitals localized around the nucleus.

3.3 Molecular Mechanics Method

Molecular mechanics can be used to study small molecules as well as large biological systems or material assemblies with many thousands to millions of atoms with low computational costs. There are two main assumptions in Molecular Mechanics:

- The configurational system energy can be calculated as a function of nuclei positions only with the electrons around them in an optimal distributions [85] through effective simple analytical functions called "Potential Functions" or "Force Fields".

- The Newtonian mechanics, which allows to study nuclei as classical particles where the presence of electrons are implicitly incorporated in the definition of particles. In this case, the temperature is assumed 0 K and equilibrium configuration can be obtained by

minimization of the system energy.

The potential energy of all systems in Molecular mechanics is calculated using force fields. If the force field parameters describe well the system, the accurate information on structure, thermodynamic properties and mechanical properties can be obtained. On the other hand, if the employed force field is not a good representative of the interatomic interactions, then all the subsequent results may be misleading although seemingly the system may function properly. Thus, unlike the first principles results, what is usually most taken as a reliable output from Molecular Mechanics is the general trend of the system versus a particular observation rather than the actual values of the output.

Furthermore, the set of interatomic functional forms, known as force field, developed to describe a system, are usually derived based on fitting to *ab-initio* or experimental results. The transferability of a force field to other environments is a crucial issue in Molecular Mechanics. In Chapter 6, we will discuss this issue in detail with two commonly used force fields in C-S-H systems.

3.3.1 Potential Functional Forms

The system energy in Molecular Mechanics is the sum of all interatomic interactions. The explicit functional forms between two atoms or a group of atoms are usually chosen based on physical insights to the nature of covalent or non-covalent bonding between atoms. The exact parameters of the functionals are fitted to *ab initio* or experimental results. In what follows, we briefly review the most common functional forms that are applicable in cement and cement-related systems. A larger set of general functional forms can be found in [45].

Coulombic Interaction This interaction is mainly essential in ionic solids, and its functional form for the energy is based on the Coulomb's law:

$$U_{ij}^{Colum} = \frac{q_i q_j}{4\pi\varepsilon_0 r_{ij}} \tag{3.18}$$

where q_i is the partial charge of atom i, ε_0 is the dielectric constant in vacuum and r_{ij} is the interatomic distance between atoms i and j. Eq (3.18) shows that the energy decays with the

inverse of distance, r_{ij}, hence Coulombic interactions are considered long range interactions. This may cause difficulties in systems with low symmetry when it comes to practical sum of all Coulombic terms due to he convergence issue. Because the number of ions increases proportional to the surface of a sphere, $4\pi r^2$, while the interatomic distance decrease according to $\frac{1}{r}$. Hence, the energy increases rather than decreases. There are different methods proposed to resolve this issue [42]. Among them Ewald's summation is the most widely used in computations [39] in which using the Laplace transformation, the Coulomb term is divided into two parts: one converges rapidly in the real space while the other one is in the reciprocal lattice space.

Dispersive Interaction

Dispersive interactions, also known as London's dispersive interactions or van der Waals interactions, are the second long range interactions [91] and are usually significant in systems where the Coulombic interactions are not large such as molecular crystals. Dispersive forces are not due to permanent dipole or induced permanent dipole interactions on the molecules as in ionic interactions, but are due to time-dependent quantum fluctuations of the electronic density. It may be imagined that an instantaneous picture of a molecule/solid would show various arrangements of nuclei and electrons having dipolar and higher multipolar moments [42]. For spherical atoms, these rapidly varying multipolar moments when averaged over a large number of configurations would give a resultant of zero. However, at any instant they would offer electrical interactions with another particle described by a series of terms increasing with the inverse of the 6th, 8th, 12th, ..nth power of the interatomic distance. However, dipolar moments are the leading contributors to dispersive interactions and usually the first term of the series is considered sufficient:

$$U_{ij}^{Dis} = -\frac{C}{r_{ij}^6} \tag{3.19}$$

where C is a parameter, which can be obtained from fitting.

Repulsive Interaction

At short interatomic distances, repulsive energies arise from overlapping electronic clouds. This interaction is perhaps easier to imagine compared to dipersive interactions. The most common functional form to explain such physical interatomic behavior is exponential functions or terms which are proportional to $\frac{1}{r^m}$ where m is typically larger than 10. Usually the dispersive and repulsive interactions are combined to give a single functional form. For example, the Buckingham functional form is written as

$$U_{ij}^{Buc} = Ae^{\left(-\frac{r_{ij}}{\rho}\right)} - \frac{C}{r_{ij}^6} \tag{3.20}$$

or Lennard-Jones (LJ) functional from reads

$$U_{ij}^{LJ} = \frac{C_m}{r_{ij}^m} - \frac{C_n}{r_{ij}^6} \tag{3.21}$$

where the A, ρ, C in Eq. (3.20) and C_m, C_n in Eq. (3.21) are parameters to be adjusted against *ab-initio* or experimental results. These potentials have a minimum at a certain interatomic distance. Away from this minimum point, the energy increases smoothly and rapidly at long and short distances. The extension of LJ potential for non-spherical particles is achieved by the Gay-Burn potential [51] that is much more complicated than simple LJ forms and contains angle dependence. In this case, the functional form takes into account the aspect ratio of the particles, 3D directional vector of each particle and several empirical parameters, which must be fitted via considering the particles in different distances and orientations.

Bonding Interaction

The covalent bonds between a pair of atoms or a group of atoms can be represented by a functional form known as the More Potential

$$U_{ij}^{Mor} = D\left[\left(1 - e^{-\alpha(r_{ij}-r_0)}\right)^2 - 1\right] \tag{3.22}$$

where r_0 is the equilibrium bond distance, D is the energy of the bond at r_0 and α is the curvature of the potential around the minium equilibrium distance. An alternative functional

form representing directional bonding is the harmonic potential, which penalizes the energy for any deviations from the optimum distance r_0 :

$$U_{ij}^{HB} = \frac{1}{2} K_B \left(r - r_0\right)^2 \tag{3.23}$$

where K_B is the stretching force constant. Since the bonding functional forms describe in an effective way all the different contributions to the chemical bond, usually the Coulombic interactions are subtracted within a bonded group.

In some cases, the hybridization of the covalent bonds results in specific shapes, such as tetrahedra bonds in carbon or silicon. For such cases, the bonding potential must consider the effect of more than two atoms. Similar to harmonic bonding terms, a three-body potential representing an angle energy is usually defined by

$$U_{ij}^{HA} = \frac{1}{2} K_A \left(\theta - \theta_0\right)^2 \tag{3.24}$$

where θ_0 is the optimum angle between the three atoms and K_A is the bending force constant.

In what follows, we specifically described two commonly used force fields for hydrated oxides. Rigorous comparison of the prediction capabilities of these force fields will be discussed in Chapter 6.

3.3.2 Potential Force Fields for Hydrated Oxides

ClayFF Potential

ClayFF is a force field suitable for molecular simulations of hydrated crystalline compounds and their interfaces with liquid phases [30]. It is based on an ionic-covalent description of metal-oxygen interactions associated with hydrated phases. To represent water, ClayFF considers the flexible simple point charge (SPC) water model [12]. In ClayFF, all atoms are represented as point charges and are allowed complete translational freedom. Metal-oxygen interactions are based on a simple 12-6 Lennard-Jones potential combined with Coulombic interactions.

The empirical parameters are optimized using known mineral structures. Partial atomic charges are obtained from cluster and periodic density functional theory, quantum chemical calculations of simple oxide, hydroxide, and oxyhydroxyle model compounds with well defined

structures. Oxygen and hydroxyl charges vary depending on their occurrence in water molecules, hydroxyl group and bridging environment. Harmonic terms are included to describe the bond stretch and bond angle (three-body) terms associated with water molecules and hydroxyls. The total energy is the sum of coulombic (electrostatic) interactions, short-range interactions (named as Van der Waals, VDW), and bonded (stretching/angular) interactions:

$$E_{tot} = E_{coul} + E_{LJ} + E_{stretch} + E_{angle} \tag{3.25}$$

For proximate intramolecular interactions, the coulombic and VDW interactions are excluded. The coulombic energy is represented as:

$$E_{coul} = \frac{e^2}{4\pi\varepsilon_0} \sum \frac{q_i q_j}{r_{ij}} \tag{3.26}$$

The VDW interactions are represented with the conventional 12-6 Lennard-Jones function that includes the short-range repulsion and the attractive dispersion energy:

$$E_{LJ} = \sum D_{ij} \left[\left(\frac{R_{ij}}{r_{ij}} \right)^{12} - 2 \left(\frac{R_{ij}}{r_{ij}} \right)^{6} \right] \tag{3.27}$$

In Eq. (3.27), D_{ij} are R_{ij} are parameters derived from the fitting of the Clay-FF model to a number of observed structural property data for oxides, hydroxides and oxy-hydroxides. The interaction parameters between the unlike atoms are calculated according to the arithmetic mean rule for the distance parameter, R_{ij}, and the geometric mean rule for the energy parameter D_{ij}:

$$R_{ij} = \frac{R_i + R_j}{2} \tag{3.28}$$

$$D_{ij} = \sqrt{D_i D_j} \tag{3.29}$$

Bond stretching energy is considered between O and H of either a hydroxyl or a water molecule and is described by a simple harmonic term as:

$$E_{stretch} = \sum K_1 \left(r_{ij} - r_{0ij} \right)^2 \tag{3.30}$$

Species	Partial Charge (e)	D (Kcal/mole)	R (Å)
Water Hydrogen (Hw)	0.41	-	-
Hydroxyl Hydrogen (Ho)	0.42	-	-
Water Oxygen (Ow)	-0.82	0.1554	3.5532
Hydroxyl Oxygen (Oh)	-0.95	0.1554	3.5532
Bridging Oxygen (O)	-1.05	0.1554	3.5532
Silicon (Si)	2.1	1.84E-6	3.7064
Calcium (Ca)	1.05	5.03E-6	6.2428

Table 3.1: ClayFF partial charges and nonbonded parameters .

where K_1 is twice the force stretching constant and r_{0ij} represents the equilibrium bond length, both values taken from the flexible version of the SPC water model [12]. To improve the description of the vibrational (librational) motion of hydroxyl groups, a bending (three-body) term is introduced in form of a harmonic relationship:

$$E_{angle} = \sum K_2 \left(\theta_{ijk} - \theta_{0ijk}\right)^2 \tag{3.31}$$

where K_2 is twice the force bending constant, θ_{ijk} is the bond angle for the hydrogen-oxygen-hydrogen, and θ_{0ijk} refers to the equilibrium bond angle between the three atoms. Table 3.1 and Appendix A show ClayFF partial charges and other non-bonded potential parameters for species relevant to C-S-H systems. Note that as shown in Table 3.1, the hydrogens in water molecules and hydroxyl groups in ClayFF do not have any Lennard-Jones parameters, indicating the effective character of the approach. Hence, they are considered not to exhibit VDW interactions with other species since they are assumed to have very small dipole polarizability. However, they have bond energies within a hydroxyl or water molecule. All the original parameters of the ClayFF potential are given in Appendix A.

Core-shell Potential

In contrast to the simple point charge force field, the core-shell model uses formal atomic charges and allows an extra degree of freedom between the core and shell of the anions. While the components of the total energy is essentially analogous to Eq. (3.25), their particular forms are different for short range energy (E_{LJ}) and bonded energy ($E_{stretch}$).

The core-shell model is based on Born model description [45] for ionic and iono-covalent

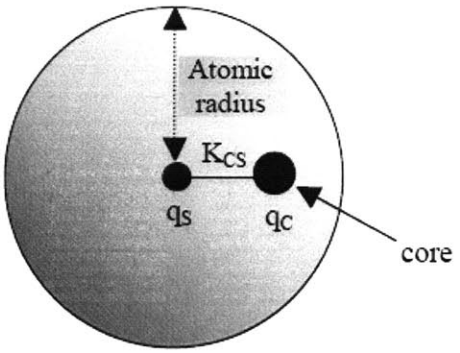

Figure 3-1: The core-shell model for an anion interact via a harmonic oscillator with a spring constant K_{CS}.

crystal structures. Point charges interact by means of electrostatic and short range semi-empirical potential functions. An essential ingredient for the transferability of the core-shell approach is the use of formal ionic charges for ionic species. As with ClayFF potential, the electrostatic (Coulombic) interactions are evaluated using the Ewald sum technique expressed by two convergent series in the real and reciprocal space [39]:

$$U_{coul}^{recip} = \frac{2\pi}{V} \sum_{G} \frac{\exp\left(\frac{-G^2}{4\eta}\right)}{G^2} \sum_{i} \sum_{j} q_i q_j \exp\left(-i\vec{G}.\vec{r}_{ij}\right) \tag{3.32}$$

$$U_{coul}^{\text{real}} = \frac{1}{2} \sum_{i} \sum_{j} \frac{q_i q_j}{r_{ij}} \operatorname{erf} c(\eta^{1/2} r_{ij}) \tag{3.33}$$

where *erfc* is the complementary error function, G is a reciprocal space vector ($G \neq 0$), q_i is the ionic charge of atom i. V is the volume of the unit cell and η a parameter that controls the division of work between real and reciprocal spaces. Note that i) the total electrostatic energy now refers to the ionic self-energy given by

$$U_{self} = -\sum_{j=1}^{N} q_i^2 (\frac{\eta}{\pi})^{1/2} \tag{3.34}$$

that is constant in canonical conditions (fixed number of ions, N); (ii) the choice of η controls the number of G vectors to be chosen for a given convergence accuracy; in this work it was set

Atomic species	Core charge (e)	Shell charge (e)	Coupling constant (eV Å^2)
Ca	2	-	
Si	4	-	
H	0.426	-	
Oh-0.8	0.86902	-2.29502	74.92
O-2	0.86902	-2.86902	74.92
Ow-0.8	1.25	-2.05	209.45
Hw	0.4	-	
Cw	2	-	

Table 3.2: coulombic interaction parameters within the core-shell model.

to 10^{-5} eV [47].

In modeling oxygen in silicate materials, electronic polarizability effects are taken into account by splitting the anion into two entities: a core and a massless shell, the (formal) ionic charge ($q_t = q_s + q_c$) being shared between these two species [45]. The core and the shell interact via an harmonic oscillator with a spring constant K_{CS} (see Fig. 3-1). The shell polarizability is then expressed by:

$$Y = \frac{q_s}{(K_{CS} + F_S)} \tag{3.35}$$

where F_S is a force acting on the shell and due to the local environment. During energy minimization process, the shell is allowed to relax relatively to its core, creating a local instantaneous dipole mimicking ion polarizability. Thus far, the explicit inclusion of polarization in the core-shell approach is the main difference with core-only potential based-model such as ClayFF. Table 3.2 shows the atomic charges for cores and shells and the coupling constant.

The short range interactions are described by a Buckingham potential which combine an exponential repulsive and an attractive dispersive term, Eq. (3.20). When using formal ionic charges in the case of iono-covalent systems such as silicates, a three body harmonic term similar to Eq. (3.31) is considered in order to mimic the correct angle O-Si-O distribution. The bonded O-H interactions in water and hydroxyl are simulated by Morse potential, Eq. (3.22).

All potential parameters used in this thesis are listed in Appendix A in which Cw is the interlayer calcium species, Ow and Hw are components of water, Oh corresponds to layer oxygen linked to a hydrogen. "Buck", "Lennard", and "Morse" stands for Bukingham, Lennard-Jones

and Morse potential functions as given above. "Three" denotes three-body interactions in the form of a harmonic bending term. "Inter/intra" marks the difference between inter and intra atomic potentials, i.e, when a pair of atoms is defined as chemically bonded, the electrostatic coulombic interaction is not calculated between them unless otherwise specified (this is the case for H_2O, see [34]). All these parameters in core-shell model are optimized to describe simple crystalline mineral oxides and their surface and water adsorption properties (see e.g. [22],[34],[171]).

3.4 Statistical Mechanics

There are two very different views of an equilibrium system namely "macroscopic" and "microscopic". The macroscopic state of a system is defined by a few everyday quantities such as temperature and pressure, whose magnitudes are measurable and steady in an equilibrium state. On the other hand, the microscopic state of a system relates to atomic or molecular state. It is defined, at a given moment, by the properties of the particles in the system (usually positions and velocities). Even at equilibrium, the microscopic state of a system is a constant flux, changing from instant to instant as the particles move and interact. The task of Statistical Mechanics is to relate the chaotic, dynamic, microscopic states of the system to the steady, everyday, macroscopic states.

The macroscopic state of a gas can be defined by three parameters: the temperature, the pressure and the volume. The microscopic state of a gas, comprised of N molecules, can, at a given time, be defined by $6N$ variable (three positions and three velocities for each molecule). It is clear that there is a huge loss of information in moving from the microscopic to the macroscopic description of a system. Hence, Statistical Mechanics is centered on relating the macroscopic properties to the averages of the microscopic properties.

3.4.1 Ensemble Averages and The Ergodic Hypothesis

Assume a sample of a gas at pressure P_{abs}. As the molecules in the gas bombard the walls of the container, the pressure, at a given instant, can be calculated from sum of the molecular forces exerted on the wall divided by the area of the wall container. The molecules strike the wall

with random motions, so the pressure, p, fluctuates with time. If the instantaneous pressure is averaged over a sufficiently long time, τ, then the average value must be both independent of the starting time and be equal to the observed pressure:

$$\frac{1}{\tau}\int_{t=n\tau}^{t=(n+1)\tau} p(t)dt = P_{abs} \tag{3.36}$$

where n is any integer number. More generally, if we define some observable property F_{abs}, then the macroscopic value is expected to be the long-time average of the instantaneous microscopic value, $F(t)$. Statistical Mechanics, reposes this observation in terms, not of a time average, but of an ensemble average.

An ensemble is a large imaginary collection of systems that have different instantaneous values of some quantity, F, but share the same long-time average value of $\overline{F}$. Thus the system in an ensemble is microscopically diverse, but macroscopically identical. The ensemble average of a quantity, F, is defined as

$$< F >= \frac{1}{\mathbb{N}}\sum_{j=1}^{\mathbb{N}} F_j \tag{3.37}$$

where $\mathbb{N}$ is the number of systems in the ensemble and F_j is the value of the property in system j. There are two central postulates in statistical mechanics:

- As the number of states in a system tends to infinity, the ensemble average of a quantity becomes equal to the long time average of that quantity

$$\frac{1}{\mathbb{N}}\sum_{j=1}^{\mathbb{N}} F_j(t) = \frac{1}{\tau}\int_{t=0}^{t=\tau} F(t)dt \tag{3.38}$$

where $\mathbb{N} \rightarrow \infty$ and $\tau \rightarrow \infty$

- All possible microscopic states are equally probable.

Thus, if the two postulates are combined, they imply that any isolated system, over a long time, spends equal amounts of time in all the available microscopic states. This is known as ergodic hypothesis.

3.4.2 The Canonical Ensemble

In the canonical ensembles, the volume, V, the number of molecules, N, and the temperature, T, are fixed in each system. The walls surrounding each system are impermeable to molecules but are perfectly thermally conducting, and the system is surrounded by a fictitious infinite heat reservoir at temperature T.

To build the model of the ensemble, we take a large number, $\mathbb{N}$, of individual systems, and couple them together such that the heat can flow throughout. The ensemble is then coupled to an infinite heat bath at temperature T, which will be the temperature of the ensemble at equilibrium too. The constraints on the ensemble are the total energy, E_t and number of systems, $\mathbb{N}$, in the ensemble:

$$\sum_1 n_i = \mathbb{N} \tag{3.39}$$

$$\sum_1 n_i E_i = E_t \tag{3.40}$$

In Eqs. (3.39-3.40), n_i refers to the number of individual systems with an identical energy E_i. There are many different distributions consistent with these constraints, and each appear with a probability P^{dis} defined by

$$P_i^{dis} = \frac{n_i}{\mathbb{N}} \tag{3.41}$$

On the other hand, the number of possible ensemble states, Ω^{dis}, consistent with a given energy distribution n_1, n_2, n_3, ... is given by a combinatorial formula

$$\Omega^{dis} = \frac{(n_1 + n_2 + n_3 + ...)!}{n_1! n_2! n_3! ...} = \frac{\mathbb{N}!}{\Pi n_i!} \tag{3.42}$$

Thus, in principle, a formula for a probability of a system in the canonical ensemble having an energy E_i reads

$$P^i = \frac{\sum_{dis} \Omega^{dis} n_i^{dis}}{\mathbb{N} \sum_{dis} \Omega} \tag{3.43}$$

It is clear that the above formula requires a sum over a potentially infinite number of possible energy distributions that are consistent with the constraint. However, this problem can be solved by allowing $\mathbb{N}$ to tend to infinity. It can be shown that at very small values of $\mathbb{N}$, one energy distribution is considerably more probable than the rest. As $\mathbb{N}$ rises, the probability of the most prevalent distribution rapidly grows, until, as $\mathbb{N}$ tends to infinity, the probability of the most likely energy distribution, $P_{\max}^{dis}$, tends to one. This means that for a system of macroscopic proportions, there is negligible error in summing Eq. (3.43) only over the single most probable distribution, and so:

$$P^i = \frac{\Omega_{\max}^{dis} n_i^{\max}}{\mathbb{N} \Omega_{\max}^{dis}} = \frac{n_i^{\max}}{\mathbb{N}} \tag{3.44}$$

where $n_i^{\max}$ is the number of systems with energy E_i in the most probable energy distribution of the ensemble. This concept is the essence of the Central Theorem in Statistical Mechanics. The method of undetermined multipliers gives the most probable distribution as

$$n_i^{\max} = \mathbb{N} \exp(-\alpha) \exp(-\beta E_i) \tag{3.45}$$

where α and β are the undetermined multipliers. Substituting Eq. (3.45) into the constraints on the total number of systems in the ensemble, Eq. (3.39), and the total energy, Eq. (3.40), gives

$$\exp(\alpha) = \sum \exp(-\beta E_i) \tag{3.46}$$

$$< E >= \frac{\sum_i E_i \exp(-\beta E_i)}{\sum_i \exp(-\beta E_i)} \tag{3.47}$$

where the $< E >$ is the ensemble average energy. Note that we no longer need the number

of systems in the ensemble, $\mathbb{N}$, as it cancels out. In fact, it can be shown that the ensemble average of any quantity, F, that depends on the state of the system can be found from

$$< F >= \frac{\sum_i F_i \exp(-E_i(N,V)/k_bT)}{Q(N,V,T)} \tag{3.48}$$

where $Q(N,V,T)$ is the canonical ensemble partition function:

$$Q(N,V,T) = \sum_i \exp(-E_i(N,V)/k_bT) \tag{3.49}$$

3.4.3 The Grand-Canonical Ensemble

The canonical ensembles discussed so far is based on constant total number of particles, N. However, is some systems, one may need to know the average number of particles as a function of external conditions. For instance, in adsorption studies one is interested to know the amount of adsorbed materials as function of the pressure or temperature of the reservoir with which the system is in contact with. A careful choice of an ensemble can greatly reduce the computational efforts. In this example, for adsorption studies, a natural ensemble to use in the Grand Canonical Ensemble (μVT), in which the temperature, volume and the chemical potential, μ, are fixed. The criteria for equilibrium is that the chemical potential and temperature of the gas inside and outside the adsorbent must be equal, whereas the number of particles can fluctuate during the simulations [42].

Analogous to the canonical ensemble, there maybe many possible distributions satisfying the following constraints in a μVT ensemble:

$$\sum_1 n_i = \mathbb{N} \tag{3.50}$$

$$\sum_1 n_i E_i = E_t \tag{3.51}$$

$$\sum_1 n_i N_i = N_t \tag{3.52}$$

where the N_t is the total number of particles. Once more, the most probable distribution swamps all the rest as $\mathbb{N}$ tends to infinity. The most probable distribution is given by

$$n_i^{\max} = \mathbb{N} \exp(-\alpha) \exp(-\beta E_i) \exp(-\gamma N_i) \tag{3.53}$$

where α, β and γ are undetermined multipliers. Again α is eliminated and it can be shown that the probability of a system in the grand canonical ensemble containing N_i particles and having an energy E_i is:

$$P_i(\mu, V, T) = \frac{\exp(-E_i/k_bT + N_i\mu/k_bT)}{\Xi(\mu, V, T)} \tag{3.54}$$

where $\Xi(\mu, V, T)$ is the grand canonical ensemble partition function:

$$\Xi(\mu, V, T)) = \sum_i \exp(-E_i/k_bT + N_i\mu/k_bT) \tag{3.55}$$

For a more details and discussion on different ensembles and their physical importance, see [3],[42],.

3.5 The Monte Carlo Method

Monte Carlo (MC) methods are a class of computational algorithms that rely on repeated random sampling to compute a system property. MC simulation methods are especially useful in studying systems with a large number of coupled degrees of freedom, such as fluids, disordered materials, strongly coupled solids, and cellular structures. More broadly, MC methods are useful for modeling phenomena with significant uncertainty in inputs, such as risk analysis. A classic use of MC method is in mathematics for the evaluation of definite integrals, particularly multidimensional integrals with complicated boundary conditions.

Within the context of materials simulations, MC method calculates system properties at the equilibrium configuration whereas MD can be employed for both the equilibrium configuration and the dynamical time evolution of the system to get to the equilibrium configuration. Hence, if only properties at equilibrium are sought, then MC might be more efficient. Additionally, compared to MD simulations, MC methods are less prone to be stuck behind a energy barrier.

3.5.1 Sampling Schemes

We have seen that the ensemble average, $< F >$, of a quantity is given by:

$$< F >= \sum_i P_i F_i \tag{3.56}$$

One approach to solving this equation would be to generate random molecular configurations of the system, then calculate the probabilities, and finally $< F >$. Such a technique is often known as "naive sampling" and although correct, it does not give good results as most of the states have low probability. A better sampling scheme would be one in which we could generate the molecular configurations based on their probability. In other words, the probability of generating state i is actually given by P_i. This approach is called" importance sampling" since each configuration is sampled according to its importance.

3.5.2 The Monte Carlo Method

The means of achieving the importance sampling is to set up an irreducible Markov chain of states of the system. The quantity of interest is then averaged over the states in the chain, rather than all possible states. A Markov chain is sequence of states in which each new state, N, depends only on the current state (M), and belongs to a finite number of possible states. A Markov chain is characterized by a fixed transition probability for any pair of states, π^{MN}, which is the probability of the next state in the chain being N, if the correct states is M. By defining this quantity for all the pair of states, we build a B x B matrix called the transition probability matrix, π. Since the probability of staying in the same state, or moving to another state, must adds up to one, the rows of the transition probability matrix must also adds up to one:

$$\sum_N^B \pi^{MN} = 1 \tag{3.57}$$

Let us denote the probability of state M occurring in the Markov chain, as ρ^M defined for example in a canonical ensemble. Finding such a probability for all B states leads to a vector of probabilities, ρ. The value of this vector will depend on the values of the π. We wish to find

a transition probability matrix such that

$$\rho^M = P^M(N,V,T) = \frac{\exp(-E_M/k_bT)}{Q(N,V,T)} \tag{3.58}$$

where E_M is the energy of state M. Suppose from an initial state M, we generate a new possible state N. We can then use the appropriate row of the transition probability matrix to decide whether we move to our new trial state or not. If we repeat the process, we then generate a Markov chain of states. Now as we move along the chain, we collect the average of the quantity, F, that we were interested in. It can be shown that the average $\overline{F}$, taken over each of the τ states in the chain, converges to the average taken over the limiting distribution of the chain provided two criteria are met [42]. Firstly, for each state, there is a finite chance of getting to any other state in a finite number of steps. Secondly, the probability of seeing a state, N, is the chain must be equal to the sum of the probability of moving from every other state, M, weighted by the probability of state M :

$$\sum_M \rho^M \pi^{MN} = \rho^N \tag{3.59}$$

Metropolis *et al.* was able to find a transition probability matrix that characterizes a Markov chain with the ensemble probability of states as it limiting distribution [104]. Setting up such a chain to calculate $\overline{F}$, will result in the ensemble average.

The π matrix elements derived by Metropolis *et al.* are given by three equations:

$$\pi^{MN} = \alpha^{MN}; \rho_N \geq \rho_M; M \neq N \tag{3.60}$$

$$\pi^{MN} = \alpha^{MN}\frac{\rho_N}{\rho_M}; \rho_N < \rho_M; M \neq N \tag{3.61}$$

$$\pi^{MN} = 1 - \sum_{N \neq M} \pi^{MN}; M = N \tag{3.62}$$

The transition matrix, with elements α^{MN}, is often termed the underlying matrix of the Markov chain. For the Metropolis transition probability to satisfy Eq. (3.59), the matrix α

must be symmetric. This means that the way we generate trial states should be such that the probability of generating a trial $M \rightarrow N$ is the same as $N \rightarrow M$.

The first equation tells us if the trial state is more probable than (or as probable as) the old one ($\rho_N \geq \rho_M$), we should make the transition with a probability of α^{MN}. Since this was the probability of generating this particular trial anyhow, we should accept the transition.

The second equation tells us if the new trial state is less likely than the old one ($\rho_N < \rho_M$), we should make the transition with a probability of ($\alpha^{MN}\frac{\rho_N}{\rho_M}$). Since the probability of generating the state in the first place was α^{MN}, there should be a ($\frac{\rho_N}{\rho_M}$) chance to make the transition. Finally, the third equation indicates that the old state of the system should be taken as the new state whenever the transition is not made. The Metropolis algorithm outlined above are general and applicable to any ensemble. In what follows, we illustrate how this efficient algorithm can be implemented in different ensembles

3.5.3 Canonical Ensemble Monte Carlo

In view of the transition probability matrix, for a canonical ensemble the ($\frac{\rho_N}{\rho_M}$) can be written:

$$\rho^N/\rho^M = \frac{\frac{\exp(-E_N/k_bT)}{Q(N,V,T)}}{\frac{\exp(-E_M/k_bT)}{Q(N,V,T)}} = \exp(-(E_N - E_M)/k_bT) \tag{3.63}$$

Note that since the partition function cancels out, this makes the Monte Carlo method very tractable. In order to ensure we accept a transition with the above probability, the following acceptance/rejection criteria is helpful [42],[3]

$$P_{acc} = \min\left[1, \exp\left(-\frac{(E_N - E_M)}{k_bT}\right)\right] \tag{3.64}$$

Thus if the energy of the new system is less than the old system ($E_N \leq E_M$), then $\exp\left(-\frac{(E_N-E_M)}{k_bT}\right)$ is always greater than one, therefore we accept the transition. Physically this makes sense since the new state is energetically more stable. Otherwise, if $E_N > E_M$, we accept the transition by the probability of $\exp\left(-\frac{(E_N-E_M)}{k_bT}\right)$ which is less than one. To do so, we throw a random number between 0 and 1. If the random number is less than or equal to $\exp\left(-\frac{(E_N-E_M)}{k_bT}\right)$, we accept the transition, otherwise we reject it. Note that in this way, even the new trial states with larger energies are likely to be sampled; hence enabling the MC

method to overcome energy barriers once in a while.

3.5.4 Grand Canonical Monte Carlo (GCMC)

To generate a Markov chain in the grand canonical ensemble, two new moves should be added that generate trial states with differing number of molecules. Thus, at every step in the chain, we decide at random whether to move a molecule, create a new molecule or destroy an existing molecule. In order to satisfy the symmetry in the underlying transition matrix, it is required that the probability of creating a molecules is the same as the probability of destroying it immediately. For a Grand Canonical ensemble, the acceptance/rejection probability in Metropolis algorithm is much more complex than that Eq. (3.64). It can be shown that for creation of a new molecule Eq. (3.64) becomes (see [42])

$$P_{acc} = \min\left[1, \frac{V}{\Lambda(N+1)} \exp\left(-\frac{(\mu - E_N(N+1) + E_M(N))}{k_b T}\right)\right] \tag{3.65}$$

where μ is the target (reservoir) chemical potential and N is the number of molecules while V is the system volume. Similarly, the acceptance condition for "deletion" of a molecule in μVT ensembles reads (see [42])

$$P_{acc} = \min\left[1, \frac{\Lambda^3 N}{V} \exp\left(-\frac{(\mu + U_{new}(N+1) - U_{old}(N)}{k_b T}\right)\right] \tag{3.66}$$

3.6 Molecular Dynamics Methods

Molecular dynamics (MD) is a form of computation that allows following interacting atoms and molecules in time. MD gives the motion of the particles based on the Newton's 2nd law at finite temperatures. Then, the properties are defined according to the Statistical Mechanics averages. MD has also been termed "statistical mechanics by numbers" and "Laplace's vision of Newtonian mechanics" of predicting the future by animating nature's forces [143]. MD, although constrained by numerical strategies, lets scientists peer into the motion of individual atoms in a way which is not possible in laboratory experiments. This method elucidates detailed time and space resolution into representative behaviors in phase space.

For a given system, any state can be entirely described by the positions, $\mathbf{q}$, and momentum,

$\mathbf{p}$, of all the particles within the system.

$$\mathbf{q} = (\overrightarrow{q}_1, \overrightarrow{q}_2, ..., \overrightarrow{q}_n) \tag{3.67}$$

$$\mathbf{p} = (\overrightarrow{p}_1, \overrightarrow{p}_2, ..., \overrightarrow{p}_n) \tag{3.68}$$

The two set of vectors, $\mathbf{q}$ and $\mathbf{p}$, represent each single point in the phase space whose evolution trajectory can be tracked. Most of the system thermodynamic properties in MD can be averaged over different ensembles using $\mathbf{q}$ and $\mathbf{p}$. For instance, for a system property, say A, at equilibrium, the ensemble average reads

$$< \mathbf{A} > = \iint A(\mathbf{q}, \mathbf{p}) P(\mathbf{q}, \mathbf{p}) d\mathbf{p} d\mathbf{q} \tag{3.69}$$

In Eq.(3.69), $P(\mathbf{q}, \mathbf{p})$ is the probability of the system to be at the phase space point $(\mathbf{q}, \mathbf{p})$, and $A(\mathbf{q}, \mathbf{p})$ is the system property value at that point.

In MD, all the system properties can be computed from $\mathbf{q}$ and $\mathbf{p}$ and classical thermodynamic relations. For example, the temperature can be calculated via equipartition principle

$$\frac{3}{2} k_B T = \frac{1}{2} < m v_i^2 > \tag{3.70}$$

To track the time evolution of the system in MD, one only needs to track the evolution of the $\mathbf{q}$ and $\mathbf{p}$. The time evolution of the particles in MD is based on the classical Newton's motion equation :

$$F_i = m \frac{\partial^2 q_i}{\partial t^2} \tag{3.71}$$

Here, the De Broglie wave length parameter must be on the order or larger than the inter-particle distances; hence justifying the choice of classical mechanics. In MD, forces are obtained from the derivative of the interatomic energies, which are usually described by force field potentials. One can envision implementing quantum calculations in MD simulations. One common such method is the *Car-Parrinello* method [18], which is the combination of MD and DFT calculations where forces are calculated from DFT rather than Molecular Mechanics. Hence,

electronic degrees of freedom are considered as fictitious dynamic variables to solve coupled equations for both nuclei and electrons.

For large systems, in the favor of computational costs, hybrid quantum mechanics MD are used to treat part of the system with *ab-initio* MD and the rest with classical MD. Long MD simulations are mathematically unstable, generating cumulative errors in numerical integration that can be minimized with proper selection of algorithms and parameters. This issue is discussed next.

3.6.1 Integrating the Equation of Motion

To numerically solve the system of partial differential equations in Eq. (3.71), many algorithms have been proposed [42]. Perhaps the most common algorithm is due to Verlet [165] who proposed a simple, yet efficient method to integrate Eq. (3.71). In Verlet algorithm, the initial velocities are usually adjusted to a desired kinetic energy to conserve the zero value of the momentum. Next, both the backward $(t - \Delta t)$ and forward $(t + \Delta t)$ Taylor expansion of the particles coordinates are written around the time step, Δt, up to the fourth term. Summing both backward and forward Taylor expansions gives

$$q(t + \Delta t) \approx 2q(t) - q(t - \Delta t) + \frac{F(t)}{m}\Delta t^2 \pm O\left(\Delta t^4\right) \tag{3.72}$$

where F, m and t are the forces acting on the particle, mass of the particle and the current time, respectively. In Verlet algorithm, to calculate the next positions, only the past and current positions are needed and not the velocities. However, analogous to positions, velocities can be obtained from the rest of the Taylor expansion for both backward and forward directions:

$$v(t) \approx \frac{q(t + \Delta) - q(t - \Delta t)}{2\Delta t} \pm O\left(\Delta t^2\right) \tag{3.73}$$

From Eqs (3.72) and (3.73), it appears that the numerical error in positions and velocities scales with Δt^4 and Δt^2 respectively.

Alternative algorithms to Verlet include Euler, the Leap-Frog, the velocity Verlet algorithms, or Predictor-Correction algorithms, which use higher order terms in Taylor expansion. More details on all these schemes can be found in [42] and the references therein.

3.7 Coarse-Graining Method

At the other end of the multi-scale methods are coarse-grained and lattice models. In coarse graining method, instead of explicitly representing every atom of the system, one uses "pseudo-atoms" or "united atoms" to represent groups of atoms. For instance, "united-atoms" employed in many simulations represent a collection of atoms such as methyl and methylene groups as a single particle, or large protein systems are commonly simulated using a "bead" model that assigns two to four particles per amino acid. This is particularly helpful for very large systems because MD simulations on these systems may require such large computer resources that they cannot easily be studied by traditional all-atom methods.

Similarly, simulations of processes on long time scales (beyond about 1 microsecond) are computationally quite expensive. In these cases, coarse-grained models or reduced representations provide a viable way to tack the problem via the mean field theory to provide an effective averaged interactions. Examples for coarse graining (CG) methods are discontinuous molecular dynamics [147] and Go-models [117].

The fitting of the parameters of the coarse-grained models must be done empirically, by either matching the behavior of the model to appropriate experimental data or to all-atom simulations. Ideally, through these parameters both enthalpic and entropic effects should be accounted for in free energy. However, when coarse-graining is performed at higher levels, the accuracy of the dynamic description of the system may be less reliable. Several coarse-grained models with different potential functional form have been used successfully to study a wide range of questions in computational material science, particularly in structural biology.

3.8 Chapter Summary

Introducing several atomistic modeling schemes applicable to the amorphous C-S-H systems was the aim of this Chapter. We reviewed basic hypotheses, fundamentals and equations of a variety of methods that are each customized for different length- and time-scales. In general, as the system size under study becomes larger, the accuracy decreases while the length- and time-scales both increases. Thus, there is a trade-off on what method to choose although for very large systems, the *ab-initio* methods is currently prohibitive.

MC methods that are carefully adjusted for the system ensemble are an efficient approach to examine the properties of a system near equilibrium. For detailed investigation of dynamical trajectory of a system before and at equilibrium, MD methods provide useful information, although the limited time scale of the MD is still a major drawback in rendering realistic physical observations On the other hand, in favor of time and length scales, coarse-grained models are useful to condense all the atomistic information of a group of atoms into a single particle information.

Seamlessly linking different scales to pass information from one to another is a difficult task. In both force field potentials and coarse-grained models, the challenge remains how to accurately and reliably parametrize the system functional forms from *ab-inito* or experimental data. In the next Part, we will use DFT method to study several C-S-H crystals, and use those results to parametrize a force field potential in Part IV.

Part III

Benchmarking C-S-H Crystals

Chapter 4

First-Principles Study on Structural and Mechanical Properties of C-S-H Crystals

With increasing interests in mineral analogs of C-S-H at the nanoscale, their mechanical properties are undoubtedly a crucial part of the evaluation and suitability of the interatomic potential model. This Part benchmarks and evaluates the structural, mechanical and acoustic properties of several C-S-H crystals that were discussed in Part II. Chapter 4 presents original first-principles calculations of the structural and mechanical properties of tobermorite family and jennite minerals. Chapter 5 is devoted to analyzing the fundamental sound waves and directional velocities of these minerals.

In recent years, with the emergence of improved computational powers, the first-principles calculations of the mechanical properties of crystalline minerals are now considered as alternative routes with respect to experiments [170]. In this Chapter, we comprehensively study the structure, elasticity and strength properties of several C-S-H crystals based on the DFT method. This Chapter is divided into three main Sections: Computational Methods, Results for Elastic Regime, and Results for Inelastic Regime. The results of this Chapter will be used in Part IV for a force field potential parametrization to be used in MD simulation of the C-S-H models.

4.1 Computational Methods

Except otherwise stated, all calculations reported in this Chapter are performed by Density Functional Theory (DFT) [61, 78] using GGA exchange correlation functionals. For energy and stress calculations, we used ultrasoft pseudopotentials [164] with a plane wave basis set and a cutoff energy of 420 eV for the wavefunctions and 5035 eV for the charge density, as implemented in the PWSCF package of Quantum Espresso distribution [11].

Considering first-principles calculations, it is important to ensure that the convergence in k-point sampling and plane wave energy cutoffs are satisfactory. However, the computational costs grow exponentially when the system size becomes large, and thus there is a trade-off in the desired accuracy and the available resources to achieve it. In our study, because the system sizes were relatively large ($\approx$70 to $\approx$100 atoms per unit cell) we used gamma-point-sampling of the Brillouin zone.

Before calculating the mechanical properties, we perform 0 K energy minimizations as implemented in PWSCF to fully relax the crystals. The importance of obtaining the equilibrium state is first, to avoid any possible meta-stable state and second to make sure that the current state is not far from the regions where linear elasticity holds. The latter is in particular the key in calculating the elastic constants. To achieve equilibrium ground state the following two criteria are met concurrently: each of the stress components is below 0.5 kbar; each of the X, Y and Z component of the force on any single atom is below 0.01 eV/ Å.

Among mechanical behaviors, calculation of elastic properties is the first and most fundamental concern as all the other mechanical behaviors can be derived or related to elastic constants. Most ambiguity in material's behaviors such as understanding interatomic interactions, phase transition, mechanical stability, internal structure and fracture energy can be obtained or related to elastic properties.

Once all crystalline minerals have attained relaxed states, we apply strains to the cell coordinates to calculate elastic constants. We use stress-strain approach to calculate the elastic constants [113], which allows one to obtain second-, third-, and fourth-order elastic constants. In this method, for each strain, by calculating the stress tensor, one can construct a linear system relating stresses to strains. Then by using an orthogonal matrix factorization and the best least square fit, elastic constants are found. Further details of this technique and its application

to a wide range of ceramics can be found in [172] and references cited therein. The generalized Hooke's law in linear elasticity is given by

$$\begin{bmatrix} \sigma_1 \\ \sigma_2 \\ \sigma_3 \\ \sigma_4 \\ \sigma_5 \\ \sigma_6 \end{bmatrix} = \begin{bmatrix} C_{11} & C_{12} & C_{13} & C_{14} & C_{15} & C_{16} \\ & C_{22} & C_{23} & C_{24} & C_{25} & C_{26} \\ & & C_{33} & C_{34} & C_{35} & C_{36} \\ & & & C_{44} & C_{45} & C_{46} \\ & & & & C_{55} & C_{56} \\ & & & & & C_{66} \end{bmatrix} \begin{bmatrix} e_1 \\ e_2 \\ e_3 \\ e_4 \\ e_5 \\ e_6 \end{bmatrix} \tag{4.1}$$

Since the crystalline minerals under investigation are either monoclinic or triclinic, we apply all 6 strains. By applying any nonzero strain in Eq. (4.1) and calculating stresses, one can determine a column of elastic constants. Thus by repeating this procedure for all strains we cover the whole elastic tensor. In this method, off-diagonal components appear twice in the calculations and to have a better estimate, we take the average of the two equivalent off-diagonal terms.

As elastic constants are defined in an orthogonal coordinate system, we relate cell parameters to Cartesian system XYZ (subindex 1 in Eq. (4.1) refers to X axis; 2 to Y and 3 to Z) in the following way: the first cell parameter, a, is parallel to X axis; second cell parameter, b is in the XY plane and finally the third cell parameter, c, is a vector in XYZ space. The variables e_4, e_5 and e_6 are the shear strains between YZ, XZ and XY planes respectively. We apply both positive (stretch) and negative (compression) strains. Thus in total we perform 12 simulations for each crystal. Next, by using least square method, we minimize

$$|(\sigma_i - \sigma_i^r) - C_{ij}\,(e_i - e_i^r)| \tag{4.2}$$

where σ_i^r and e_i^r are residual stress and residual strain respectively, and $(e_i - e_i^r)$ is the applied strain. In this way, the uncertainty in C_{ij} values will be minimized with enhanced overall accuracy. Choosing the correct magnitude for the applied strain is critical. Sufficiently small strains are needed to ensure that elastic constants are within the linear theory of elasticity, but this will require higher precision accuracy in calculating the total energy and forces on each atom. This is computationally very expensive, and therefore there is a trade-off between the

Partial charges	Si_{intra}	Ca_{intra}	Ca_{inter}	O_{intra}	O_W	H_W
interlayer distance 11 Å	+2.24	+1.66	+1.72	-1.2	-0.88	+0.44
interlayer distance 14 Å	+2.24	+1.66	+1.72	-1.2	-0.8	+0.4

Table 4.1: Partial charges for tobermorite (hamid structure) Ca/Si=0.83 at the interlayer distance of 11 Å and 14 Å . The subindices " inter", "intra" and "W" refer to interlayer, intralayer and water respectively.

desired level of accuracy and computational time. In practice it has been shown that 1% strain is sufficiently accurate for calculating elastic constants [172, 88]. Thus we use ± 0.01 for all strains and let the system relax after each strain because electronic vibrations are coupled to ionic motions. Once we obtain the elastic constant tensor we invert it to obtain the compliance tensor by $S_{ij} = C_{ij}^{-1}$, where the first three diagonal terms of the compliance tensor, S_{11}, S_{22}, S_{33}, represent the inverse of the Young's modulus in the corresponding X, Y and Z directions, respectively.

In order to calculate the partial atomic charges (Table 4.1), we performed variational static calculations at the Hartree-Fock (HF) approximation (without a posteriori account for electron correlation effects) using the CRYSTAL code developed for solid state applications [178]. Multielectron wave functions are described by linear combination of crystalline orbitals expanded in terms of Gaussian-type basis sets. Considering the system size, we have chosen the 6-31G* split valence basis set for O [28] and the standard 6-21 G for H. Ca and Si species are described by Barthelat and Durand pseudo potentials respectively as implemented in [178]. Convergence parameters were set for a high level of accuracy (ITOL1 = ITOL2 = ITOL3 = 5, ITOL4 = 6, ITOL5 = 11). Atomic partial charges were determined following the Mulliken partitioning scheme. This provides an easy way to characterize the type of bonding schemes (covalent, iono-covalent, coulombic) that are in action.

DFT at its current state of development does not yield accurate van der Waals dispersion forces [77, 140]. In C-S-H models, the interlayer interactions are dominated by coulombic forces rather than van der Waals dispersion forces [119]. Thus the predicted interlayer interactions for C-S-H models should not be affected by this issue. In this work, we used Jmol [75] to create 3D visualizations of the crystal structures. In what follows,we present the computational results in two separate Sections: Elastic and Inelastic regimes.

	Cell parameter	a (Å)	b (Å)	c (Å)	α (deg)	β (deg)	γ (deg)
tobermorite 14 Å	Experiment	6.735	7.425	27.987	90	90	123.25
$Ca_5Si_6O_{16}(OH)_2.7H_2O$	*ab initio*	6.87	7.43	28.49	89.96	90.05	123.47
Ca/Si=0.83	Error (%)	2.00	0.13	1.80	0.006	0.004	1.31
tobermorite 11 Å (Merlino)	Experiment	6.735	7.385	22.487	90	90	123.25
$Ca_4Si_6O_{15}(OH)_2.5H_2O$	*ab initio*	6.80	7.51	22.572	89.83	89.05	123.43
Ca/Si=0.67	Error(%)	1.00	1.70	0.38	0.18	1.00	0.15
tobermorite 9 Å	Experiment	11.156	7.303	9.566	101.08	92.83	89.98
$Ca_5Si_6O_{16}(OH)_2$	*ab initio*	11.211	7.389	9.710	102.65	92.54	89.75
Ca/Si=0.83	Error (%)	0.49	1.17	1.5	1.55	0.28	0.25
tobermorite 11 Å (Hamid)	Experiment	6.69	7.39	22.779	90	90	123.49
$Ca_6Si_6O_{18}.2H_2O$	*ab initio*	6.60	7.40	23.13	90.00	90.00	123.62
Ca/Si=1	Error(%)	1.4	0.08	1.5	0	0	0.11
tobermorite 11 Å (Hamid)	Experiment	6.69	7.39	22.779	90	90	123.49
$Ca_5Si_6O_{16}(OH)_2.2H_2O$	*ab inito*	6.708	7.373	22.54	90	90	123.71
Ca/Si=0.83	Error (%)	0.27	0.22	1.00	0	0	0.18
tobermorite 11 Å (Hamid)	Experiment	6.69	7.39	22.779	90	90	123.49
$Ca_4Si_6O_{14}(OH)_4.2H_2O$	*ab inito*	6.898	7.371	22.153	90	90	124.64
Ca/Si=0.67	Error (%)	3.10	0.24	2.74	0	0	0.9
jennite	Experiment	10.575	7.265	10.931	101.3	96.98	109.65
$Ca_9Si_6O_{18}(OH)_6.8H_2O$	*ab inito*	10.702	7.342	10.891	102.11	95	109.82
Ca/Si=1.5	Error (%)	1.2	1.06	0.36	0.8	2.0	0.16

Table 4.2: First-principles calculation of cell parameters for the tobermorite family and jennite.

4.2 Results for Elastic Regime

4.2.1 Cell Parameters and Elastic Constants

In this Section, we focus on structural data at equilibium and mechanical properties within the elastic regime. Table 4.2 shows the cell parameters for the studied C-S-H models (6 tobermorite polymorphs and a jennite polymorphs) obtained by first-principles calculations. Compared to experiments, the average error of these results is typically smaller than 1%, and the maximum error is approximately 3% for tobermorite 11 Å (Hamid) Ca/Si=0.67. This error may stem partly from 0 K temperature conditions used in first-principles calculations versus room temperature in experiments, and may also be due to the fact that the final stress components during the course of relaxation are not exactly zero. Thus it is expected that there could be small residual stresses that disturb the equilibrium lattice parameters.

	Tobermorite (Merlino)			Tobermorite (Hamid, 11 Å)			Jennite
Elastic constant (GPa)	14 Å	11 Å	9 Å	Ca/Si=1	Ca/Si=0.83	Ca/Si=0.67	Ca/Si=1.5
C_{11}	77.60	116.95	169.15	148.25	131.95	102.65	100.1
C_{12}	35.90	45.83	54.48	63.25	48.30	41.68	26.85
C_{13}	20.18	27.88	37.45	26.75	23.15	27.70	32.03
C_{14}	0	0	-1.05	0	0	0	1.30
C_{15}	0	0	-8.90	0	0	0	1.45
C_{16}	3.08	0.3	2.7	6.63	-6.55	1.25	3.30
C_{22}	104.5	126.10	169.95	138.35	128.30	125.05	45.70
C_{23}	26.3	46.20	36.15	32.55	30.63	18.83	4.40
C_{24}	0	0	3.55	0	0	0	7.35
C_{25}	0	0	-11.75	0	0	0	-6.20
C_{26}	-1.75	-14.93	-1.08	1.85	-10.98	-4.10	-3.18
C_{33}	32.05	126.35	92.70	68.40	83.85	83.80	59.15
C_{34}	0	0	2.60	0	0	0	-1.30
C_{35}	0	0	-3.45	0	0	0	1.40
C_{36}	3.03	-9.35	0.60	-1.73	-8.58	-3.38	0.07
C_{44}	24.5	30.20	40.60	32.75	26.00	22.90	21.95
C_{45}	-9.43	-11.10	0.43	-1.93	-8.35	-11.93	-1.73
C_{46}	0	0	-5.48	0	0	0	-1.6
C_{55}	14.65	20.75	17.85	25.65	21.75	23.25	21.00
C_{56}	0	0	-1.85	0	0	0	2.73
C_{66}	38.10	44.35	45.65	53.30	49.35	50.20	26.55

Table 4.3: First-principles calculation of elastic constants for the tobermorite family and jennite.

Table 4.3 summarizes the elastic constants obtained from first-principles calculations. Tobermorite 9 Å and jennite (triclinic crystals) have 21 independent second order elastic constants. The remaining crystals which are monoclinic have only 13 independent elastic constants [116]. For monoclinic crystals, we assumed that the unique axis is in the direction of the c cell parameter.

For tobermorite 9 Å, we were able to compare the results with higher k-points sampling (4 k-points with a mesh of $2\times2\times1$) using Monkhorst-Pack scheme [107]. In this case, the maximum errors on lattice parameters and elastic constants were less than 0.3% and 2 GPa, respectively. The use of GGA exchange correlation potentials lead to larger exchange correlation energy and therefore favor longer bonds. This results in lattice parameters that are overall larger than experiments, and corresponding elastic constants that are slightly underestimated. On the other hand, the use of LDA exchange-correlation functions results in overbinding the system.

As an example, we relaxed the cell parameters and atomic positions of tobermorite with LDA norm conserving pseudopotentials with cutoff energy of 840 eV for the wavefunctions (twice as large as that of in the GGA exchange-correlation function) and 3360 eV for the charge density cutoff. With these large cutoffs, LDA calculations are computationally quite expensive for the tobermorite systems. However, we were able to obtain the following cell parameters for tobermorite 11 Å (Hamid) with Ca/Si=0.83: a = 6.85 Å (2.4%), b = 7.22 Å (-2.2%), c = 19.49 Å (-14.4%), α = 90.016 deg (0.02%), β = 90.016 deg (0.02%) and γ = 123.07 deg (-0.33%). The values in the parentheses indicate the error percentages as compared to the experimental values. In view of cell parameters, it turns out that the LDA predictions are less accurate than GGA predictions (see Table 4.2). In particular, for the interlayer direction, the c parameters is shrunk by more than 14% (far beyond the elastic regime) compared to the experiment. Thus, despite the heavier calculations, the LDA exchange-correlation functions are not performing well for predicting the long range interlayer interactions for the complex tobermorite layers. This issue is less pronounced for intralayer interactions, but still the errors are larger than those calculated by GGA. Analogously, one can verify that this overbinding by LDA exchange-correlation functions, results in very large (and incorrect) elastic constants for tobermorite. Indeed, with 14% shrinkage in the interlayer space, the tobermorite is beyond the fracture point and since all the cell parameters are coupled together, calculating the elastic constants with this interlayer distance becomes pointless. Increasing the energy cutoffs in LDA would decrease the errors to some extent, however, the computational costs become prohibitively expensive.

4.2.2 Hinge Deformation Mechanism in Tobermorite 9 Å and 11 Å

In this section, via classical rotation of the compliance tensors [116] we focus on the Young's modulus along any arbitrary direction. This enables us to identify the critical directions of a crystal where the softest or stiffest Young's moduli are located. While we performed this analysis for all crystals, here we only report the findings for tobermorite 11 Å.

Because tobermorite minerals have layered structures, it is expected intuitively that the softest direction is perpendicular to the layers and hence parallel to the interlayer direction. This is the case for tobermorite 14 Å with the interlayer stiffness C_{33} = 32 GPa which is about

18% of the average intralayer stiffness. However, when the interlayer distance is decreased to 11 Å or less, in contrast to this conjecture, we find that the interlayer direction is not always the softest direction. For tobermorite 11 Å, there are two possible structural forms:

Hamid Structure:

In Hamid structures, it is hypothesized that the layers are not connected through covalent bounds, instead the layers interact via long range coulombic forces [118]. To validate this hypothesis, we calculate the atomic charges at different interlayer distances. Table 4.1 shows that the average partial charges for tobermorite Ca/Si=0.83 at the interlayer distance of 11 Å and 14 Å remain unchanged (except for a small redistribution of partial charges in water molecules due to the different adsorption sites). Thus pulling the layers apart does not involve any covalent bond breakage. Otherwise, the partial atomic charges should have been changed upon stretching and bond breakage. Hence, there exists no covalent bonds in between the layers; instead long range coulombic forces form the interlayer interactions. As an example, Fig. 4-1(a) shows a unit cell of tobermorite 11 Å (Hamid) with Ca/Si=0.83. In Fig. 4-1(b) the sphere with the unit radius represents directional Young's modulus for this structure. In view of 4-1(b), it turns out that the interlayer directions is not the softest direction and there are two inclined soft regions (blue areas on the sphere).

Considering table 4.3, in tobermorite 11 Å (Hamid) with Ca/Si=0.83, the coulombic interlayer interactions - which results in $C_{33} \approx 83$ GPa - are now comparable to the iono-covalent intralayer interactions ($C_{11}, C_{22} \approx 130$ GPa). However, this requirement does not necessarily make two inclined soft regions in layered structures. Fig. 4-2 shows the top views for different isomorphs of tobermorites 11 Å (Hamid type) with Ca/Si=0.67, Ca/Si=0.83 and Ca/Si=1. These three isomorphs of Hamid structures are formed by adding (removing) an interlayer Ca and removing (adding) two protons. It is interesting to note that by increasing Ca/Si ratio, the two inclined soft regions (blue regions) shift towards the interlayer direction. Therefore at Ca/Si=1, the interlayer direction becomes the softest direction.

In order to investigate this later effect further, we quantify the total coulombic energy in the interlayer direction for each isomorph. To do so, we identically increase the interlayer distance for each Ca/Si ratio and relax the structure using DFT method. This allows us to monitor the

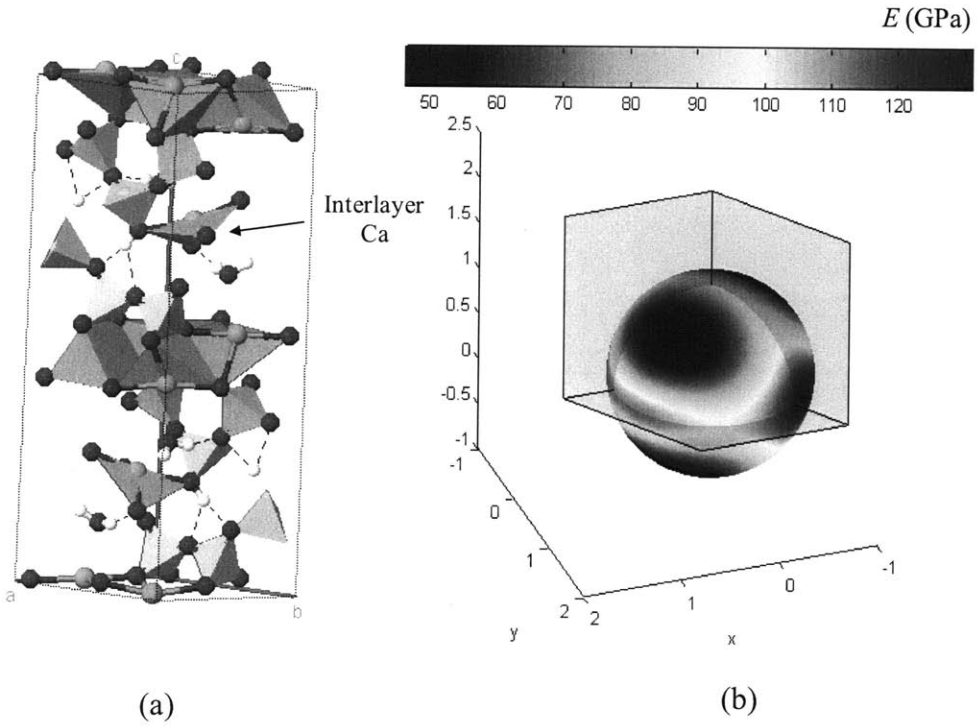

Figure 4-1: Tobermorite 11 (Hamid) Ca/Si=0.83. (a) Fully relaxed unit cell. Pink pyramids are silicon tetrahedra; green ribbons are calcium polyhedra; red circles are oxygen atoms and white circles are hydrogen atoms. (b) Young's modulus in any arbitrary direction. Any point on the sphere with the unit radius represents the tip of a unit vector which is drawn from the center of the sphere (intersection of the three crystal planes). The surface of the sphere covers all possible 3D arbitrary unit vectors.

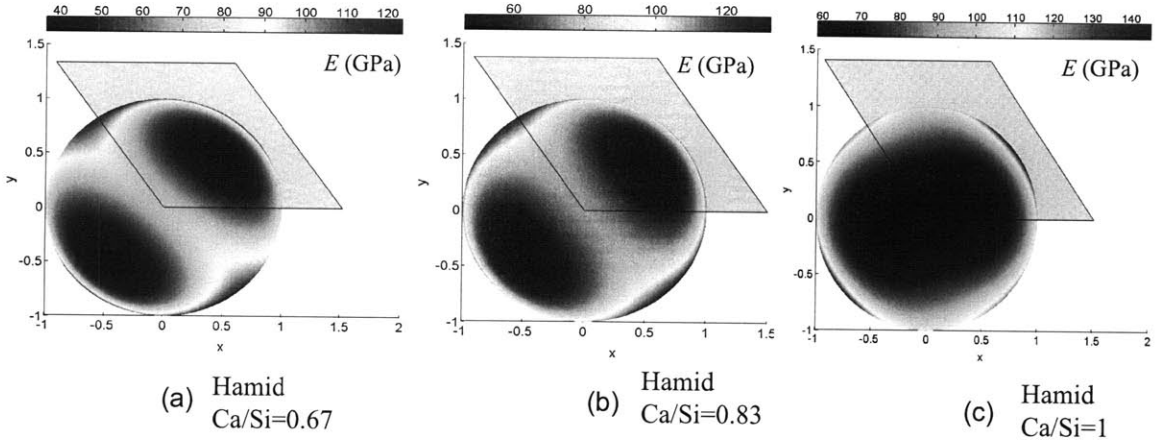

Figure 4-2: Top views for Tobermorite 11 (Hamid). (a) tobermorite 11 (Hamid) Ca/Si=0.67. (b) tobermorite 11 (Hamid) Ca/Si=0.83. (c) tobermorite 11 (Hamid) Ca/Si=1. Any point on the spheres with the unit radius represents the tip of a unit vector which is drawn from the center of the spheres (intersection of the three crystal planes). In this figures, two of the crystal planes are perpendicular and are not seen. The surface of the spheres cover all possible 3D arbitrary unit vectors.

change in total coulombic energy for each case. For a 0.3 Å interlayer displacement, the change in Ewald corrected coulombic energy for Ca/Si=0.67, Ca/Si=0.83 and Ca/Si=1 is respectively 1.08 $\frac{\text{eV}}{\text{Å}^3}$, 0.78 $\frac{\text{eV}}{\text{Å}^3}$ and 0.46 $\frac{\text{eV}}{\text{Å}^3}$ per unit cell for a constant interlayer spacing of 11.076 Å. This indicates that adding extra Ca ions (increasing Ca/Si ratio) in the interlayer distance reduces the contribution of coulombic interlayer interactions and hence shields the long range interlayer bonds. This eventually leads to shifting the two inclined soft regions to a single straight interlayer direction (Fig. 4-2).

Merlino Structure:

Figure 4-3(a) shows a side view of the tobermorite 11 Å (Merlino) unit cell. The arrows indicate the direction of the softest Young's modulus. Fig. 4-3(b) gives a top view of the same unit cell indicating two equivalent soft regions (blue color). In this case, the interlayer direction is considerably strengthened by covalent Si-O-Si interlayer bounds, which is due to the presence of double silica chains (head-to-head connection of bridging tetrahedra). From a structural point of view, it thus appears as if the unit cell is easier to pull (or push) along the blue regions.

Therefore, the shared oxygen atom of the double silica chain acts as a hinge, and the entire set of upper and lower atoms can pivot around this point. This is illustrated in Fig. 4-3(a) by a blue and black arrows.

Similar to tobermorite 11 Å (Merlino), there are covalent interlayer bonds in tobermorite 9 Å which lead to the hinge mechanism. Physically the hinge mechanism implies that atomic reorientations are preferred over straight bond stretches to achieve the minimum energy. Because of the covalent interlayer bonds, the strengthening of the interlayer interactions in Merlino structure is less surprising than those in Hamid structures, and perhaps in consistent with the common perception.

There are, in deed, hinge deformation mechanisms in tobermorite (Hamid) with Ca/Si=0.67 and Ca/Si=0.83 (but not for Ca/Si=1). However, unlike tobermorite 11 Å (Merlino), since there are no interlayer covalent bonds in Hamid structures, no particular atom acts as a hinge point. Instead a chemical site in the interlayer space becomes the center for such mechanism.

4.2.3 Averaged Elastic Properties

To compare with measurements of elastic properties of C-S-H gels, it is useful to characterize the single-crystal level elastic properties. We use the Reuss-Voigt-Hill approximation [60, 130, 167] to calculate the bulk modulus, K, shear modulus, G and average Young's modulus, E. One can also relate K and G to the plane-stress modulus M, which is accessible for example by indentation techniques based on the Hertz theory contact solution [48, 148]. In the isotropic case, M relates to the bulk and shear modulus (K, G) of the indented half-space by:

$$M = 4G\frac{3K+G}{3K+4G} \tag{4.3}$$

Table 4.4 provides the values of the average elastic properties for tobermorite and jennite and Fig. 4-4 shows the average properties as a function of the density. Accurate nanoindentation experiments performed on C-S-H, indicates $M \approx 63$ GPa for solid C-S-H phases (Table 3 in reference [27], table II in [160]). They somewhat relate to M values for tobermorite 14 Å and jennite ($M \approx 56$ GPa). This confirms earlier hypotheses [21, 152] that tobermorite 14 Å and jennite are among the best C-S-H analogs (but not with the correct density).

It is interesting to note that tobermorite 14 Å and jennite have almost the same values

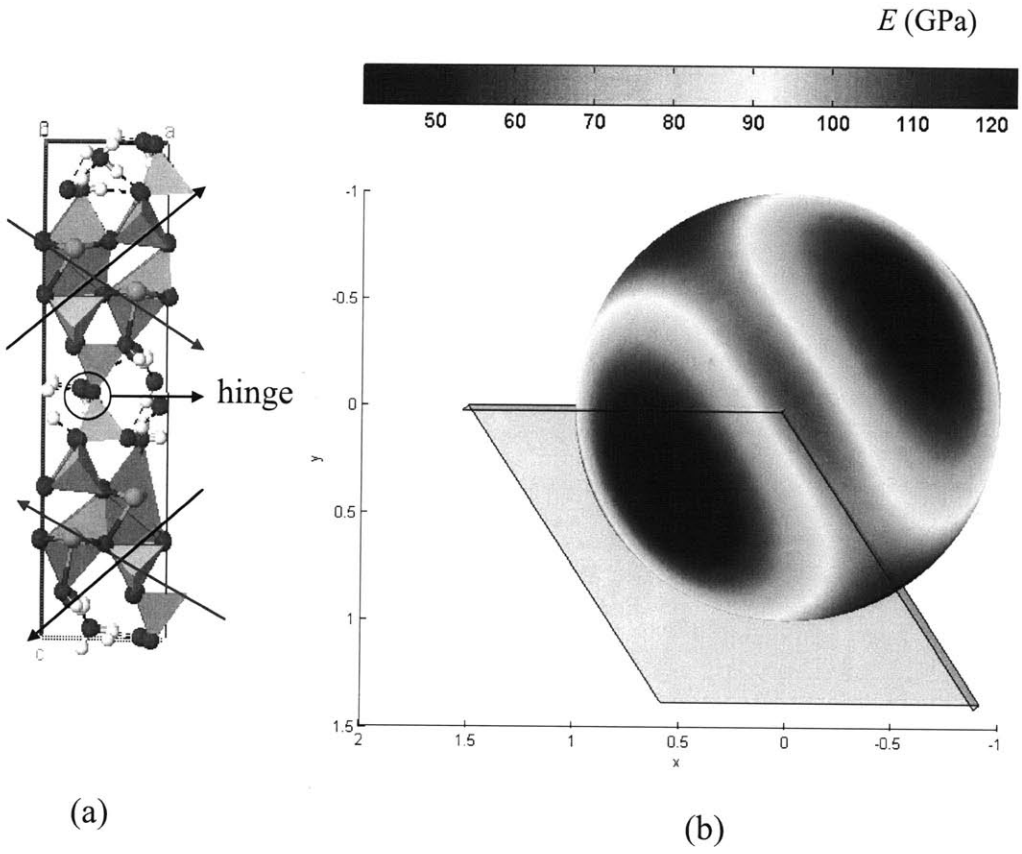

Figure 4-3: Tobermorite 11 (Merlino): (a) Side view of : Blue (or black) coupled arrows indicate the deformation mechanism along the softest Young's modulus. (b) A top view of directional Young's modulus representing two equivalent inclined soft regions. The embedded lines on the sphere represent the crystal directions in (a) and are not drawn to scale. Any point on the sphere with the unit radius represents the tip of a unit vector which is drawn from the center of the sphere (intersection of the three crystal planes). In this figure, two of the crystal planes are perpendicular and are not seen. The surface of the sphere covers all possible 3D arbitrary unit vectors.

	Tobermorite (Merlino)			Tobermorite (Hamid, 11 Å)			Jennite
	14 Å	11 Å	9 Å	Ca/Si=1	Ca/Si=0.83	Ca/Si=0.67	Ca/Si=1.5
K (GPa)	35.91	66.65	71.42	60.84	58	52.68	31.83
G (GPa)	20.61	32.03	37.18	35.97	32.56	29.81	21.96
M (GPa)	55.64	90.59	103.03	96.31	88.44	80.77	56.26
E (GPa)	51.90	82.82	95.06	90.14	82.29	75.23	53.55

Table 4.4: Reuss-Voigt-Hill average of the elastic constants for the tobermorite family and jennite obtained from first-principles calculation.

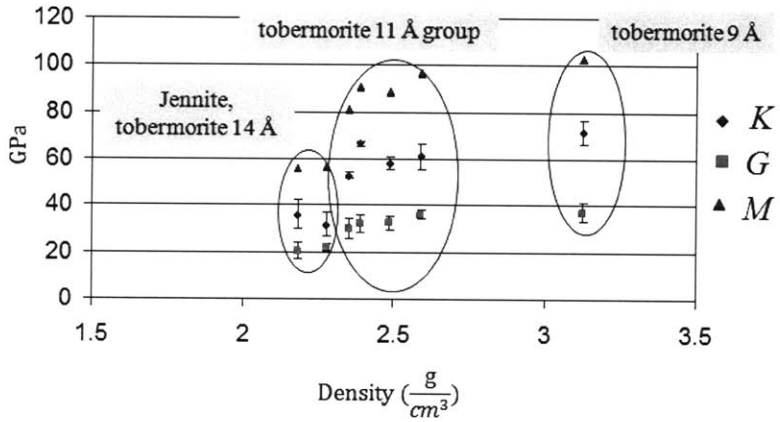

Figure 4-4: DFT calculations for bulk modulus, K, shear moduli, G and indentation modulus M versus density for the studied minerals. The bar indicate Reuss and Voigt approximations for K and G.

for all average elastic properties. This is of some importance, since it has been noted that the C-S-H gel at an early stage resembles tobermorite 14 Å, while it resembles jennite after a period of months or years [21, 152].

Having the atomic coordinates for each deformation, we can compute the average directional bond strain in Ca-O, Si-O and O-H in each of X, Y and Z directions. Figure 4-5 shows that average directional bond strains have following common characteristics:

First, in all crystals under constant strain of 1%, Ca-O bond strains are greater than Si-O bond strains, indicating that Si-O bonds are much stronger than Ca-O bonds. Note that while the total applied strain is 1%, each individual bond strain can in general be larger than 1%. Second, for tobermorite 14 Å and jennite, O-H strains are always greater than corresponding strains in other minerals under study. This indicates a structural role of O-H bonds in

these two C-S-H analogs which have large amount of water molecules in the interlayer distance. The large values of the O-H strains in jennite and tobermorite 14 Å indicate that the water molecules act as a weak bridge in the interlayer bond connecting adjacent layers, that is $Si(OH)-H_2O-$ Si(OH). These water molecules are part of the crystal-chemistry of the mineral and are not bulk water; that is, they are attached to the layers and can not freely move in the interlayer space. This is analogous to the studies of state of water in Portland cement pastes [157].

4.2.4 Effect of Ca/Si ratio on Elasticity

Although we showed an excellent agreement between experimental indentation modulus, M, performed on C-S-H with those obtained from DFT calculations on tobermorite 14 Å and jennite, there are major differences in chemical compositions between the two. C-S-H has an average $Ca/Si \simeq 1.7$ whereas for jennite $Ca/Si = 1.5$ and for tobermorite 14 Å this ratio is $Ca/Si = 0.83$. Here, we investigate systematically the effect of Ca/Si ratio on C-S-H crystals. Later in Chapter 8, we complement this study over a wide range of Ca/Si ratios on a variety of combinatorial C-S-H systems. In what follows, we use Hamid tobermorite, which is synthetically established to exist with three different Ca/Si without a major change in its layered structural form [58].

While the cell shape is overall unchanged, addition of each Ca ion in the interlayer distance of tobermorite removes two hydrogen atoms of two hydroxyl groups to make the cell neutral [58]. This has an advantage that these ratios are experimentally validated [58] and since the overall layered structure does not change, one can carefully monitor the direct effect of the additional interlayer Ca ions. Figure 4-6 shows that by increasing Ca/Si ratio from 0.66 to 1, all averaged elastic properties increase linearly (except Poisson's ratio which remains constant $\simeq 0.26$). This is due to the additional in-plane bonding that the the extra Ca ions make with $Si-O$ groups.

Similar to tobermorite 11 Å, tobermorite 14 Å and jennite have single silica chains with flanking bridging tetrahedra in the interlayer distance. Thus, increasing Ca/Si ratio in tobermorite 14 Å and jennite, most likely forms similar bonds and increases linearly the averaged elastic properties. In the case of tobermorite 14 Å, these elastic properties at $Ca/Si \simeq 1.7$

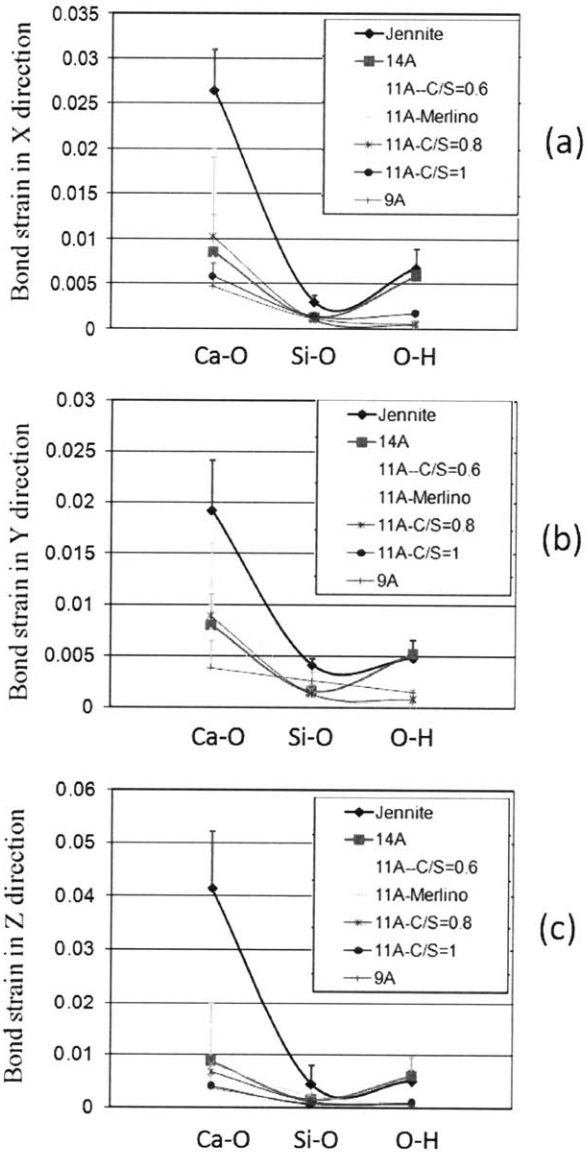

Figure 4-5: Average bond strains in Ca-O, Si-O and O-H for different C-S-H crystals. Applied strain on all crystals is 0.01: (a) average bond strains in X direction; (b) average bond strains in Y direction; (c) average bond strains in Z direction. In all figures the bar symbols indicate the positive error.

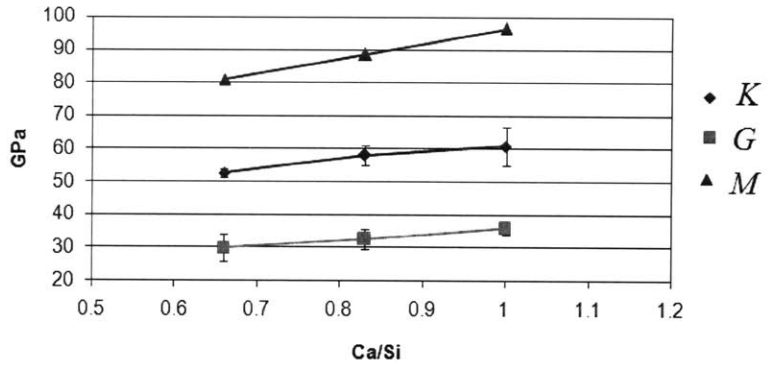

Figure 4-6: Effect of Ca/ Si ratio on K, G, and M for tobermorite (hamid type). The bar error on K and G indicates the lower (Reuss) and upper (Voigt) bound approximations.

clearly surpass the experimental values of nanoindentation test on C-S-H, however, these crystalline minerals (including tobermorite 14 Å) have silica chains of an infinite length whereas experiments and ^{29}Si (magic angle spinning) MAS NMR studies [24] show that silica chains in C-S-H have discrete lengths of $m = 3n - 1$ where n is an integer number. Therefore a finite (broken) silica chain with less stiffness - compared to an infinite chains - must compensate for match in elastic properties with nanoindentation on C-S-H.

4.2.5 Effect of Wat/Ca ratio on Elasticity

Another interesting aspect of the C-S-H minerals is their water molecules and their effect on mechanical properties. Fig. 4-7 shows the general decreasing trend of the averaged elastic properties of C-S-H crystals versus the ratio of number of water molecules over Ca ions, Wat/Ca. This is because water molecules shield the coulombic interactions and therefore the layers can't feel the presence of the neighboring layers. In this figure, tobermorite 9 Å has zero water molecules, and is the stiffest. Next are the three Hamid tobermorites. Note the single data points correspond to tobermorite 11 Å (Merlino type) which has a double silica chains. These double silicate chains relate to bridging silicon tetrahedra in which the Si atoms have three neighboring Si atoms: two intralayer Si atoms and one from the lower or upper layers. This Si arrangement indicates the presence of Q_3 in terms of ^{29}Si NMR analysis, and are known to form strong 3D bonds, which in this case link the two adjacent layers by making iono-covalent Si-O-Si

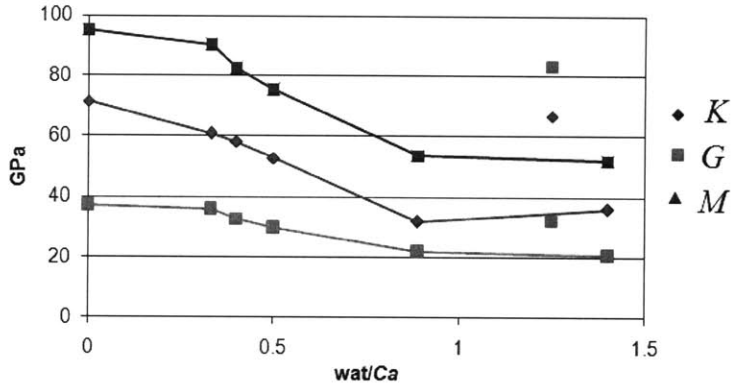

Figure 4-7: DFT results on the effect of wat/Ca on elastic properties. The single points correspond to tobermorite 11 A (Merlino) with double silica chains which behaves differently compared to other minerals with single silica chains (i.e. C-S-H analogous minerals)

bonds in the interlayer direction. As a result, these 3D bonds form a closed network or rings of Si-O-Si bonds, which can engulf large number of water molecules without affecting elastic properties. Among all studied minerals in the present work, tobermorite 11 Å Merlino is the only one with double silica chain and thus it may not be surprising that it behaves differently compared to other minerals.

4.2.6 Correlation Between Young Modulus and Silica Chain Density

Table 4.5 and Fig 4-8 shows the correlation between the surface density of infinite silica chains in all studied minerals with Young's modulus parallel to the axis of silica chains. This correlation ramps up linearly up to a certain value and then it becomes saturated as it approach the closest packing density of silica chains. Note also that increasing the Ca/ Si ratio in Hamid tobermorite structure increases the Young's modulus linearly. However, it seems that among all studied parameters in this work, the density of silica chains has paramount effect in determining in-plane Young's modulus of C-S-H crystals. Thus given the density of silica chains in other similar C-S-H minerals (such as hillebrandite $Ca_6\,Si_3\,O_{10}\,(OH)_4$, Ca/ Si = 2, foshagite, $Ca_8\,Si_6\,O_{16}\,(OH)_2$, Ca/ Si = 1.3, nekoite, $Ca_3\,Si_6\,O_{15}.7H_2O$, Ca/ Si = 0.5 and so on), the linear equation on Fig 4-8 can be used to predict the Young's modulus parallel to their silica axis.

Fig 4-9, 4-10 and 4-11 show the variation of Young's modulus for all studied minerals in

Mineral	# of silica chains	*ac area* (nm^2)	chain density ($1/nm^2$)	E (GPa)
tobermorite 14A	4	1.958	2.043	90
tobermorite 11A	4	1.527	2.620	126
tobermorite 9A	4	1.065	3.757	146
T-Hamid Ca/ Si = 1	4	1.537	2.602	123
T-Hamid Ca/ Si = 0.83	4	1.510	2.649	135
T-Hamid Ca/ Si = 0.67	4	1.529	2.617	126
Jennite	2	1.161	1.723	45

Table 4.5: Correlation between density of silica chains (number of silica chains per unit area) with Young's modulus parallel to the direction of silica chain.

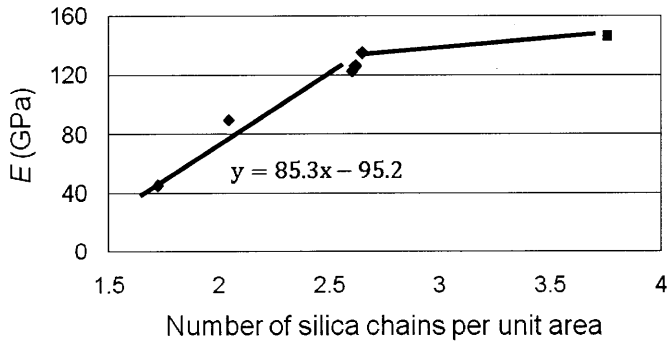

Figure 4-8: Correlation between density of infinite silica chains (i.e. x parameter on the plot) and Young's modulus parallel to the axis of the chains (y parameter).

all directions in the XZ, YZ and XY planes. Several observations can be obtained from these plots: i) tobermorite 14 Å and jennite are the softest members of the studied minerals, ii) as discussed earlier, the interlayer direction in some crystals is not the softest direction (note the variation of the color in Z direction), and iii) the in-plane (XY plane) stiffness is typically highest among the three planes because all silica chains are in this plane.

4.3 Results for Inelastic Regime

In this Section, by applying incremental strains to the C-S-H crystals, we investigate their deformation mechanisms and mechanical properties far beyond the elastic regime. In particular, we apply incremental strains parallel to the softest direction, **n**, in each crystal. As discussed in the previous Section, the critical softest direction in tobermorite 14 Å and tobermorite 11 Å (Hamid with Ca/Si=1), is along the interlayer direction (i.e. $n_x = 0$, $n_y = 0$, $n_z = 1$), while it lies in an inclined plane for other crystals. At each strain, we let the system relax via DFT calculations with identical convergence parameters as described in 4.1. This relaxation is important because electronic vibrations are coupled to ionic motions. Next we calculate the normal stress on the plane whose unit vector is parallel to **n**. To do so, we first calculate traction stress vector: here let's remind for any given stress tensor, σ_{ij}, the traction vector, $T_i = \sigma_{ij} n_i$, represents the components of the stress tensor on any arbitrary plane whose normal is **n**. Thus the normal stress on the plane is obtained by $T_n = T_i.n_i$.

4.3.1 Cohesive and Repulsive Stresses in C-S-H Crystals

We employ both positive (stretch) and negative (compression) strains and calculate normal stress T_n which corresponds to cohesive (when stretched) or repulsive (when compressed) stresses (Figs. 4-12 to 4-18). From these plots, one can find the maximum cohesive stress, σ_C, and maximum repulsive stress, σ_R that a crystal can withstand prior to failure. Table 4.6 shows that in all studied C-S-H crystals the maximum cohesive stress is always less than the maximum repulsive stress. The reason lies in efficient atomic arrangement in compression that leads to maximum atomic packing density within the crystals.

Among all crystals, tobermorite 11 Å of Merlino has the largest σ_C and σ_R because head-

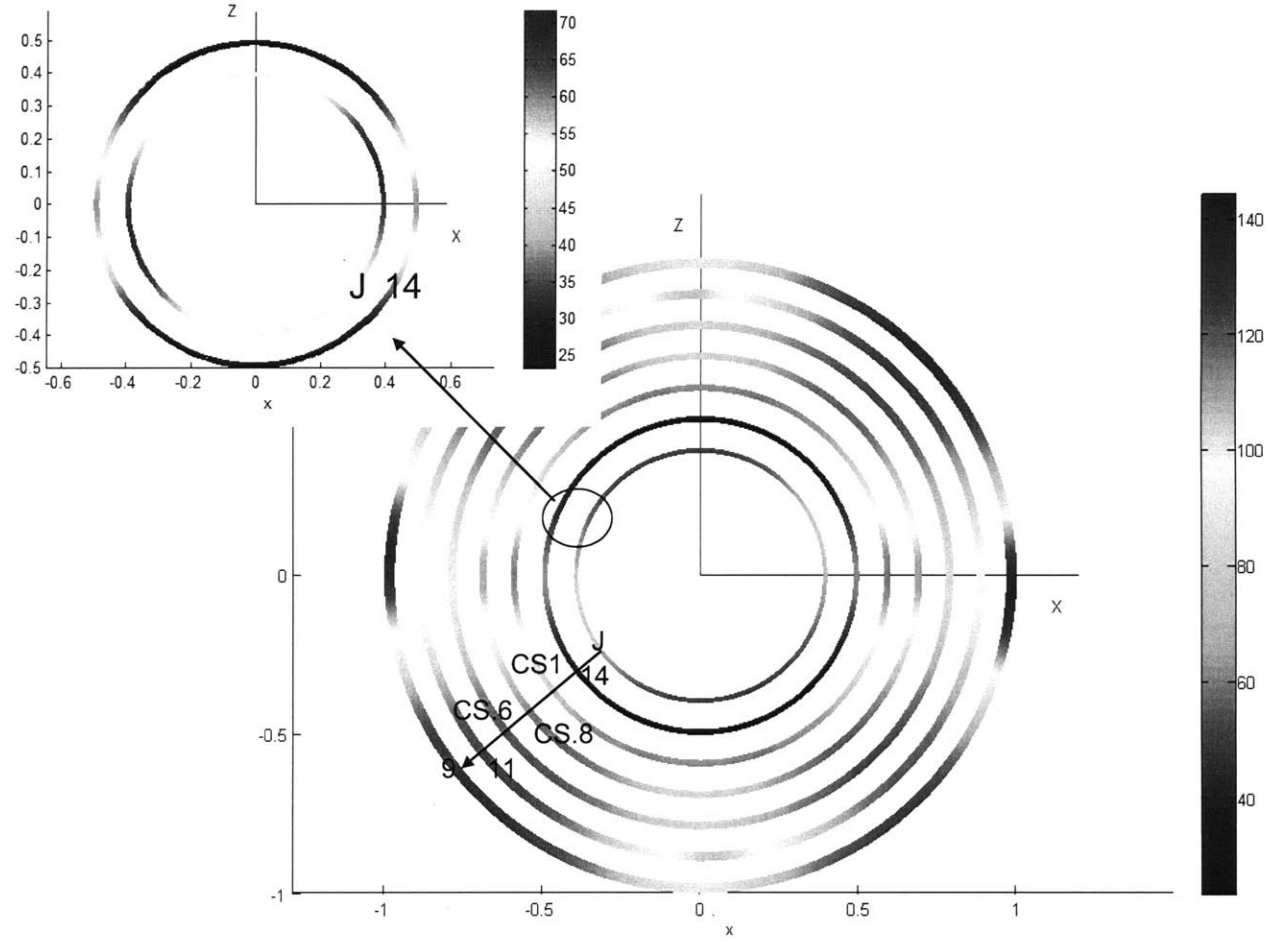

Figure 4-9: Values of Young's modulus in XZ plane for tobermorite family and jennite. J symbol stands for jennite, 14 for tobermorite 14 Å, CS1 for tobermorite 11 A (Hamid) with Ca/ Si = 1,CS.8 for tobermorite 11 Å (Hamid) with Ca/ Si = 0.83, CS.6 for tobermorite 11 Å (Hamid) with Ca/Si= 0.67 and finally 9 indicates tobermorite 9 Å. Inset shows tobermorite 14 Å and jennite.

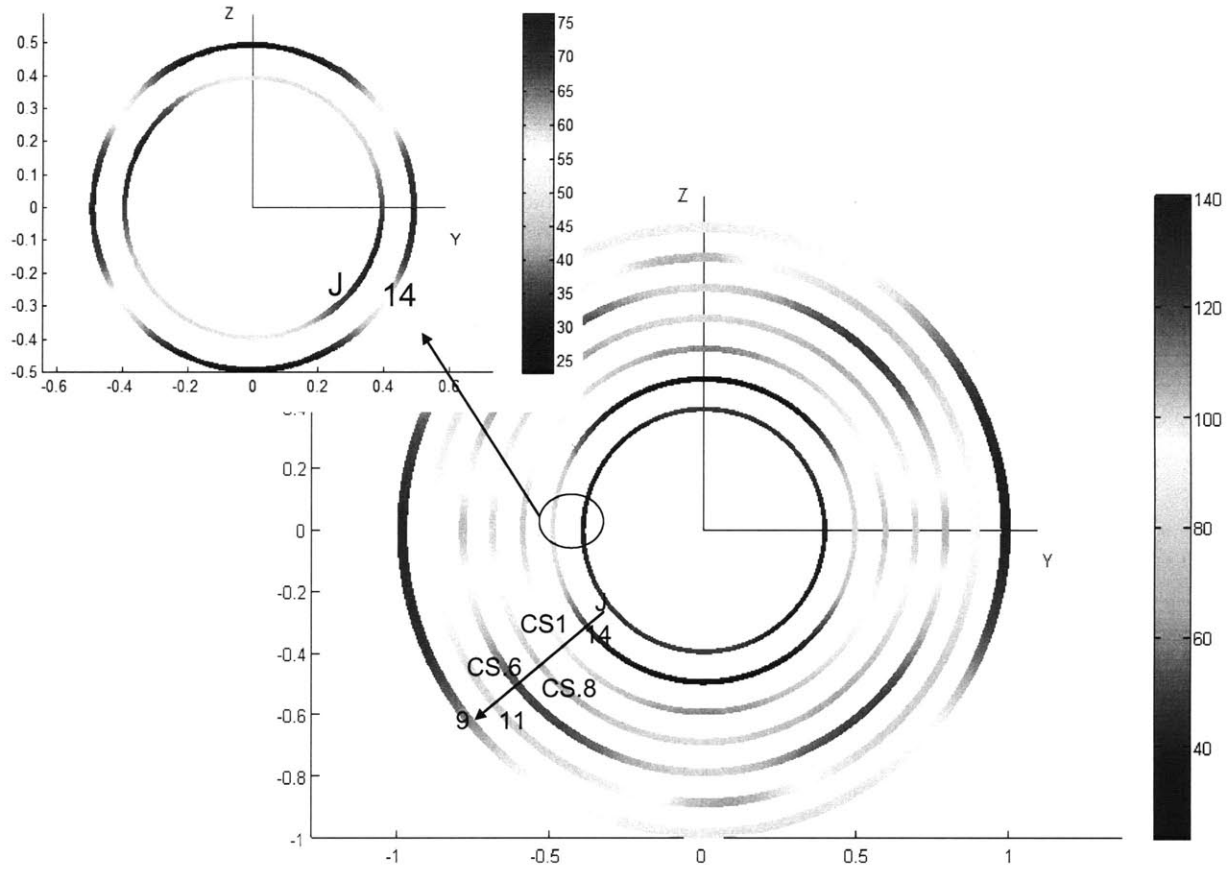

Figure 4-10: Values of Young's modulus in YZ plane for tobermorite family and jennite. J symbol stands for jennite, 14 for tobermorite 14 Å, CS1 for tobermorite 11 A (Hamid) with Ca/ Si = 1,CS.8 for tobermorite 11 Å (Hamid) with Ca/ Si = 0.83, CS.6 for tobermorite 11 Å (Hamid) with Ca/Si= 0.67 and finally 9 indicates tobermorite 9 Å. Inset shows tobermorite 14 Å and jennite.

C-S-H mineral	σ_C (GPa)	σ_R (GPa)
tobermorite 14 Å	3	-18.1
tobermorite 11 Å	8.7	-47.8
tobermorite 9 Å	4.8	-32.6
Tobermorite-Hamid Ca/Si= 1	6.1	-16.6
Tobermorite-Hamid Ca/Si= 0.83	4.3	-16
Tobermorite-Hamid Ca/Si= 0.67	3	-20.6
jennite	4.2	-

Table 4.6: Maximum cohesive and repulsive stresses for two closely related C-S-H crystalline minerals: tobermorite family and jennite.

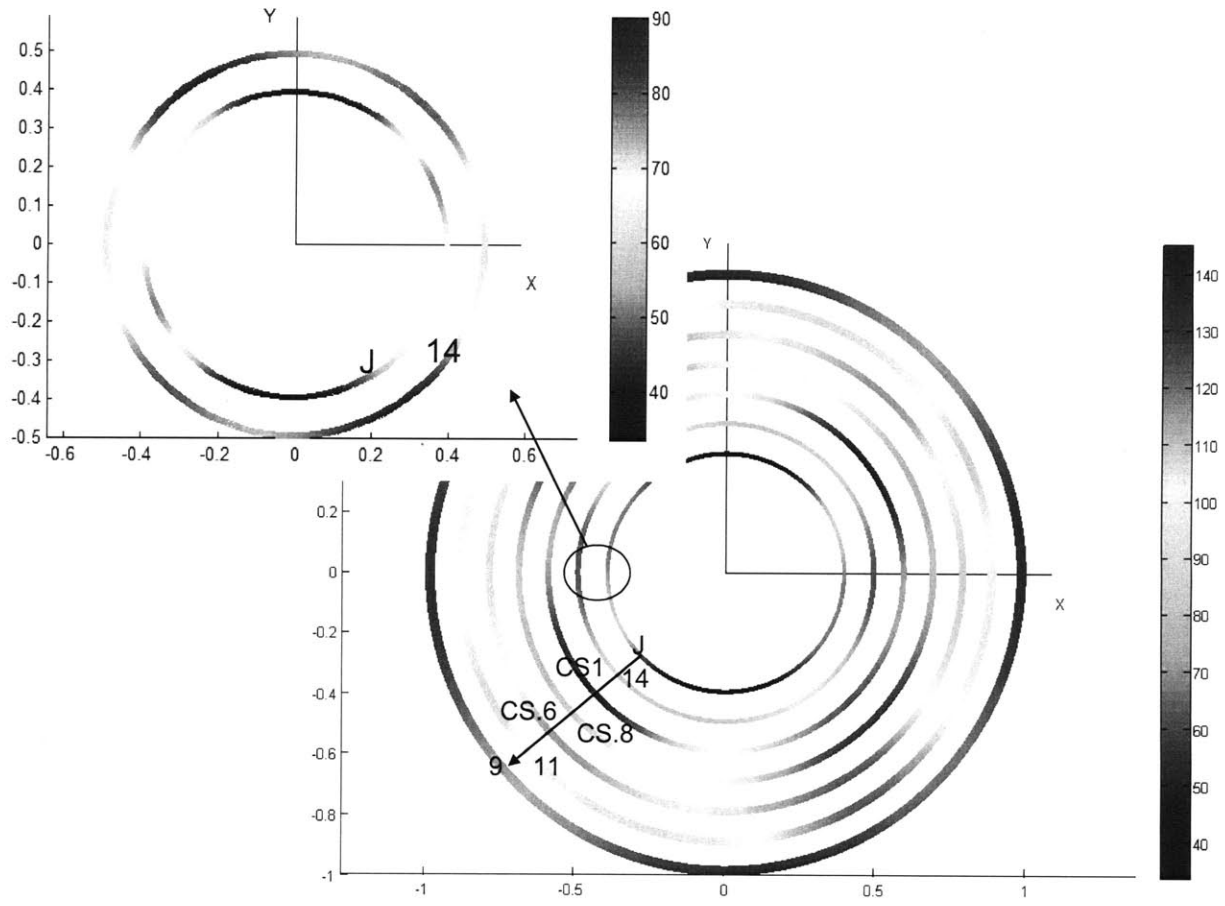

Figure 4-11: Values of Young's modulus in XY plane for tobermorite family and jennite.J symbol stands for jennite, 14 for tobermorite 14 Å, CS1 for tobermorite 11 A (Hamid) with Ca/ Si = 1,CS.8 for tobermorite 11 Å (Hamid) with Ca/ Si = 0.83, CS.6 for tobermorite 11 Å (Hamid) with Ca/Si= 0.67 and finally 9 indicates tobermorite 9 Å. Inset shows tobermorite 14 Å and jennite.

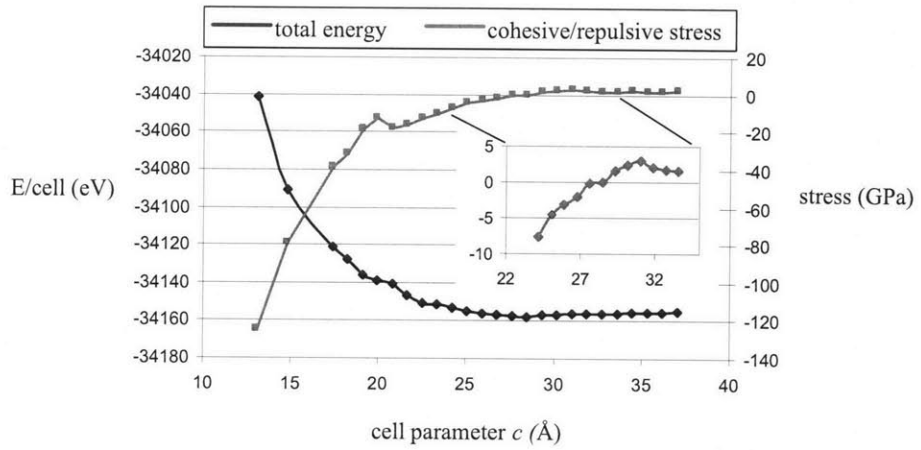

Figure 4-12: Total energy and cohesive/repulsive stresses for tobermorite 14 Å .

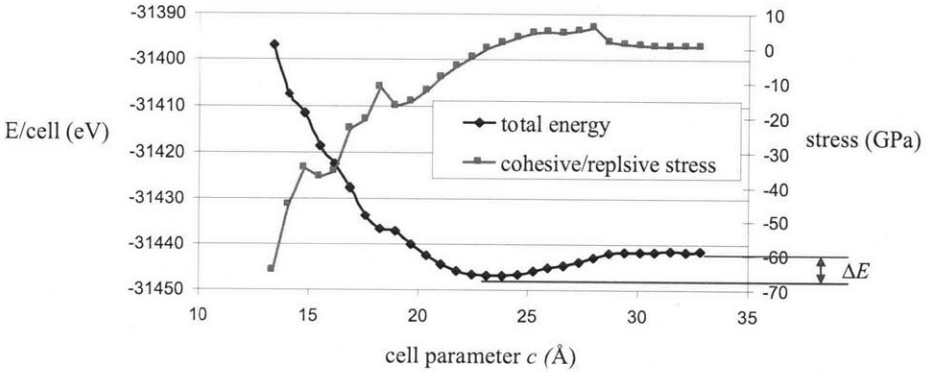

Figure 4-13: Total energy and cohesive/repulsive stresses for tobermorite 11 Å (Hamid, Ca/Si=1). ΔE is the energy required to create free surfaces.

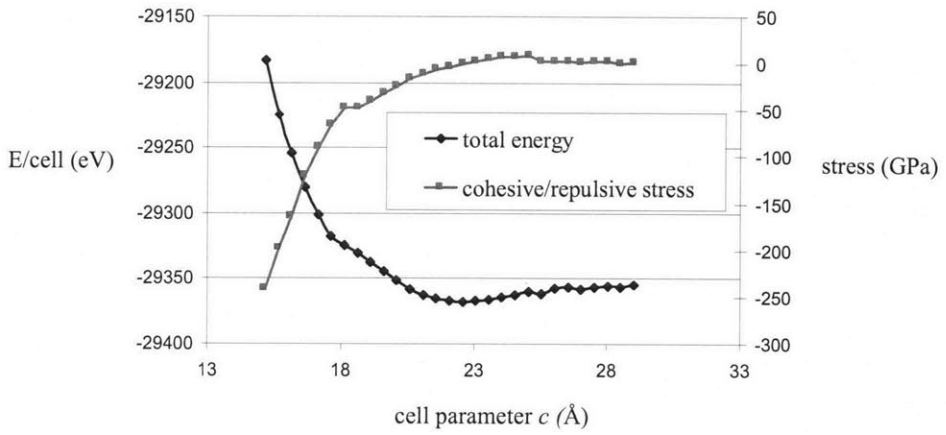

Figure 4-14: Total energy and cohesive/repulsive stresses for tobermorite 11 Å (Merlino).

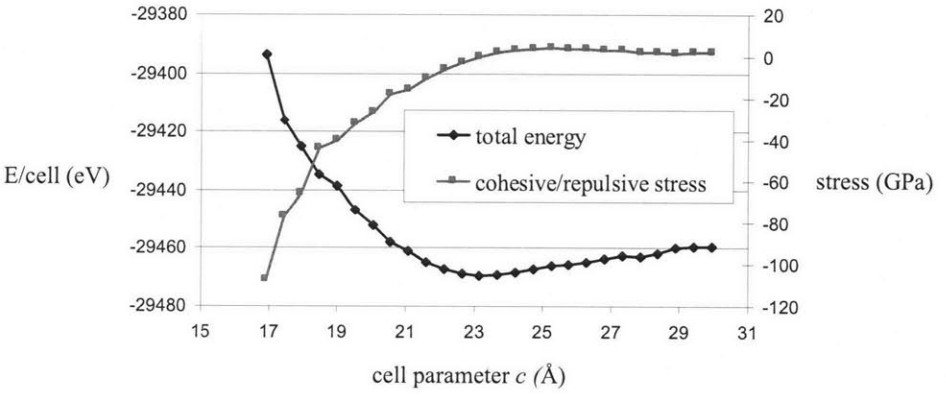

Figure 4-15: Total energy and cohesive/repulsive stresses for tobermorite 11 Å (Hamid, Ca/Si=0.83).

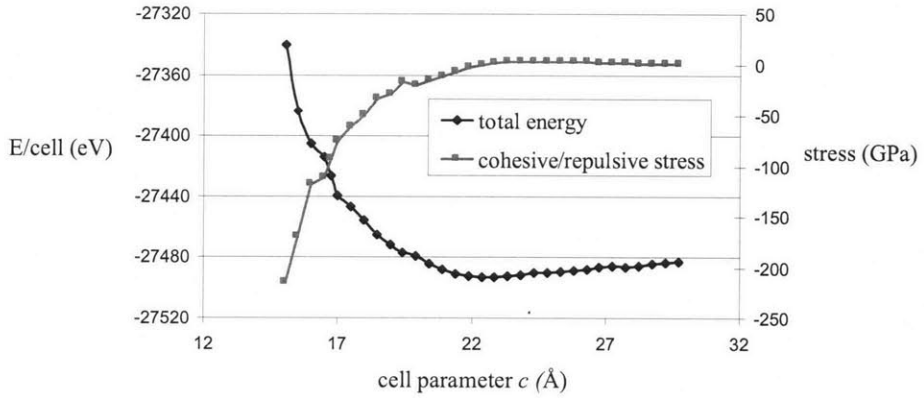

Figure 4-16: Total energy and cohesive/repulsive stresses for tobermorite 11 Å (Hamid, Ca/Si=0.67).

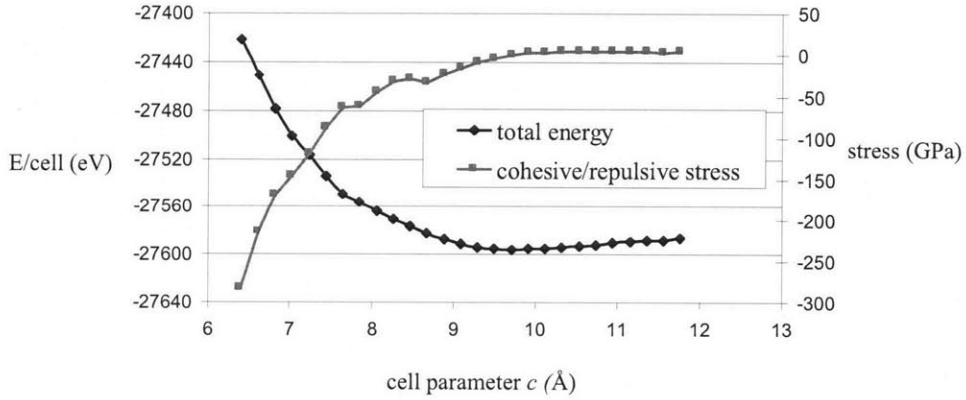

Figure 4-17: Total energy and cohesive/repulsive stresses for tobermorite 9 Å

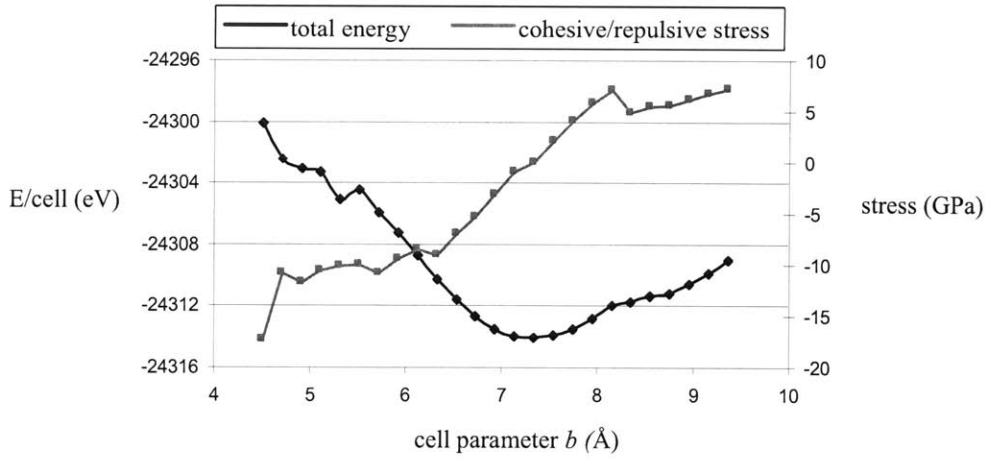

Figure 4-18: Total energy and cohesive/repulsive stresses for jennite.

to-head connections of the silica chains (double silica chains) make a strong Si-O-Si bonds. Tobermorite 14 Å and tobermorite 11 Å (Hamid, Ca/Si=0.67) have the minimum $\sigma_C = 3$ GPa. In tobermorite 14 Å, the interlayer distance is larger than those in other crystals. Thus there are no strong bonds in the interlayer direction. Considering Hamid tobermorite, increasing Ca/Si ratio from 0.67 to 1, increases the maximum cohesive stress. Because the additional Ca ions make iono-covalent Ca-O-Si bonds [119] in the interlayer distance and improves the cohesion.

4.3.2 Uncommon Failure Mechanism in Layered Materials

By elongating the crystals along their softest directions, there will be a point after which the total energy doesn't change upon stretching. This point indicates the rupture within the crystal where the lamella are separated. As these C-S-H crystals have a layered structure, atomic debonding and rupture must happen within the interlayer distance and create two surfaces in there. This is the case for tobermorite 14 Å. However, when the interlayer space decreases to 11 Å, surprisingly rupture happens in the intralayer space where the backbone of the structures are located (Figs. 4-19 and 4-20). This is particularly the case for tobermorite 11 Å (Hamid, Ca/Si=1 and Ca/Si=0.83) and tobermorite 11 Å (Merlino).

This surprising new failure mechanism can be explained in the following way: for Hamid

tobermorite 11 Å (Fig. 4-19), the coulombic interlayer interactions are stronger that intralayer iono-covalent Ca-O-Si bonds. For the case of Merlino tobermorite 11 Å, there is less surprise because the interlayer link formed by the head-to-head connection of silica chains (Si-O-Si bond) significantly enhances the interlayer coulombic interactions. This result in much stronger interlayer bonds than any intralayer counterpart within the crystal, hence rupture occurring in the intralayer space (Fig. 4-20).

In general, the existence of charge layers in these lamella and ionic concentration fluctuation in the interlayer distance relates to these surprising failure mechanisms. More detailed study and discussion of these parameters on C-S-H gel can be found in [119] and the references therein. Together with the results of elastic properties in the previous section, it turns out that when the interlayer distance is such that coulombic interlayer interactions become comparable to the iono-covalent intralayer interactions, or there is 3D bonding network due to the presence of Q_3 ^{29}Si NMR, new mechanical phenomena happen that are quite out of expectations for layered materials.

4.3.3 Surface Energies for C-S-H Crystals

Further elongation beyond the rupture point creates free surfaces. The difference between global minimum energy at equilibrium and final energy when free surfaces are created, ΔE, is the required energy to make such free surfaces. As an example, Fig. 4-13 shows ΔE for tobermorite 11 Å. Thus one can find the surface energies as

$$\sigma_s = \frac{\Delta E}{2A_{ab}} \tag{4.4}$$

where A_{ab} is the area of ab plane. The factor 2 is needed because there are two free surfaces created. Table 4.7 shows surface energies, for four tobermorite polymorphs. In other crystals, since the softest directions lay in an inclined axis, the rupture did not create free surfaces but a somewhat distorted atomic arrangement.

Surface energies indicate that tobermorite 14 Å and 11 Å require minimum and maximum energies respectively to separate their lamella and create free surfaces. Although surface energies can be best approximated by creating supercells, these crystals are relatively large (~70 to ~100 atoms) and the free surfaces do not interact much with each other. Furthermore, DFT

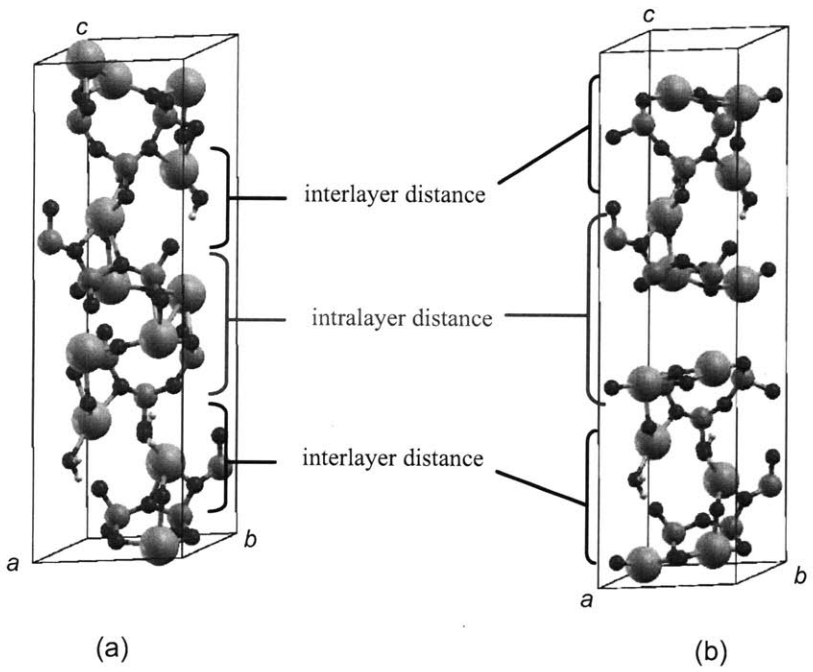

Figure 4-19: Tobermorite (hamid, Ca/Si=1) (a) a unit cell at equilibrium. Blue spheres represent Ca, green spheres represent Si, red sphere represent O and yellow spheres represent H atoms. (b) a unit cell when rupture occurs inside the backbone of the crystal (the intralayer space). The 3D structures are created by using Xcrysden [79].

calculations of total energies for a C-S-H supercells similar to what we conducted here for a unit cell is extremely difficult with current computational powers.

4.4 Chapter Summary

In this Chapter, using first-principles calculations we found lattice parameters, elastic constants and cohesive and repulsive stresses for two classes of complex layered hydrated oxides, tobermorite family and jennite. Carefully post-analyzing the data reveals new deformation and fracture mechanisms that are quite uncommon for layered materials. For tobermorite 14 Å, the large interlayer distance makes the coulombic interlayer interactions relatively insignificant compared to the iono-covalent intralayer interactions. In addition, the existence of water molecules as well as Ca ions in the interlayer space shield the coulombic interlayer interactions.

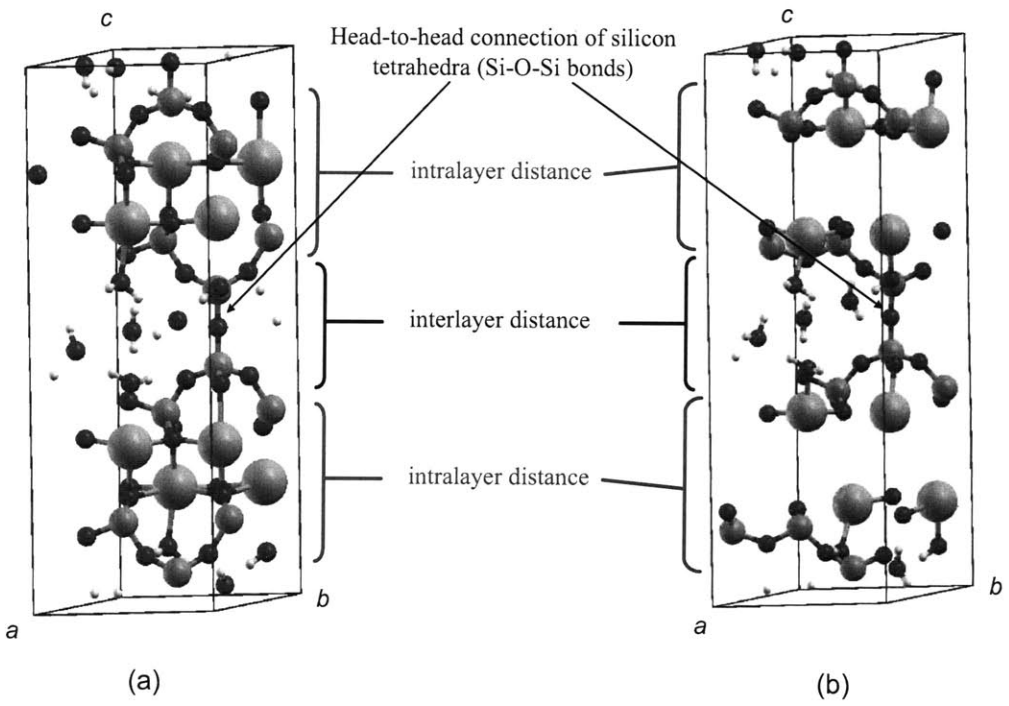

Figure 4-20: Tobermorite (Merlino) (a) a unit cell at equilibrium. Blue spheres represent Ca, green spheres represent Si, red sphere represent O and yellow spheres represent H atoms. (b) a unit cell when rupture occurs inside the backbone of the crystal (the intralayer space).

C-S-H mineral	Surface energy ($eV/Å^2$)
tobermorite 14 Å	0.03
tobermorite 11 Å	0.104
Tobermorite-Hamid Ca/Si= 1	0.064
Tobermorite-Hamid Ca/Si= 0.83	0.08
jennite	0.032

Table 4.7: Surface energy for tobermorites

Thus as expected, the interlayer direction is the softest direction and rupture happens in the interlayer space.

By decreasing the interlayer distance to 11 Å, the long range coulombic interlayer interactions become comparable to the iono-covalent intralayer interactions. This was earlier suggested through using an empirical force field [119], and in our work is accurately inferred through two separate analyses:

1. Comparison of the interlayer and intralayer elastic constants:

   This analysis showed that when the interlayer and intralayer elastic constant become comparable, the softest direction in layered materials is not the interlayer direction anymore. In this case, the softest directions are two inclined regions that form a hinge mechanism. By quantifying total coulombic energy in the interlayer direction for different isomorphs of tobermorite 11 Å (Hamid types), we showed adding Ca in the interlayer space shields the coulombic interlayer interactions, hence shifting the two inclined soft regions towards a single straight interlayer direction.

   Thus, in contract to the common perception that layered materials are soft in layer direction, we found that this is not the case. However, this is not the only requirement and the existence of interlayer ions and water molecules may shield the coulombic interlayer interactions. In the case of tobermorite 11 Å (Merlino type) and tobermorite 9 Å, the covalent interlayer bonds considerably strengthen the interlayer direction which lead to hinge (gliding) mechanism.

2. Rupture mechanism

Upon stretching the crystals until rupture along their softest directions, quite surprisingly for tobermorite 11 Å (Hamid, Ca/Si=1 and Ca/Si=0.83) and tobermorite 11 Å (Merlino) the atomic debondings occur in the intralayer space (and not the interlayer space). These debondings lead to complete failure in the intralayer space by creating two free surfaces in the backbone of the crystals. This new failure mechanism indicates that the interlayer coulombic interactions in Hamid and Merlino structures are much stronger than the intralayer bonds. In the case of Merlino structure, the coulombic interlayer interactions are further enhanced by the interlayer links (iono-covalent Si-O-Si bonds).

Finally, the characterization of the structural and mechanical properties of tobermorite family and jennite led to the following five observations: i) Si-O bonds are much stronger than Ca-O bonds, ii) H_2O molecules in tobermorite 14 Å and jennite - compared to other studied minerals - have a structural role and are part of a $Si(OH)-H_2O-$ Si(OH) bridge in the interlayer distance, iii) increasing the Ca/Si ratio within an unchanged backbone of the tobermorite Hamid, increases the elastic properties, iv) increasing the Wat/Ca ratio decreases the average elastic properties for all tobermorite (except 11 Å Merlino) family, and v) increasing the silica chain density per unit area increases the Young modulus parallel to the silica chain direction.

We now have a wealth of reliable data on the structure, elastic, and strength properties and deformation mechanisms of a variety of C-S-H crystalline family, which serve as a DFT benchmark on these complex minerals. We use the results of this Chapter to analyze the fundamentals sound waves in the next Chapter, and develop a new force field potentials in Part IV.

Chapter 5

Acoustic Properties of C-S-H Crystals

A full elastic tensor enables a complete analysis of the fundamentals sound waves for an anisotropic material. In this Chapter, we first focus on directional sound velocities to derive a novel statistical averaging scheme for the bulk modulus, K, and shear modulus, G, for an anisotropic material. We show our averaging scheme is superior than the classical approximation methods such as Voigt-Reuss-Hill approximation and Molinary approximation. Second, by using our DFT results in Chapter 4, we calculate the three fundamental wavespeeds and the associated polarization vectors at any arbitrary location for tobermorite family and jennite.

5.1 Acoustic Properties of C-S-H Crystals at 0 K

5.1.1 Averaging Methods for Elastic Properties

In mechanics and physics, bulk modulus, K and shear modulus, G, of isotropic materials are of tremendous use. There are numerous experiments and theoretical derivations based on these two parameters. For anisotropic materials, since there are more than two elastic constants, one has to condense the full elasticity tensor components into quasi-isotropic properties in order to utilize the available experimental data and better conceptualize the complex behavior of anisotropic materials. Averaging the elastic constants in an old, well-known problem in

mechanics. Here, we very briefly review two classic averaging schemes that are most commonly used for anisotropic materials:

Voigt-Reuss-Hill Approximation

This approach is the most common approach based on the Voigt [167] and Reuss [130] routes that define an upper and lower bound for bulk modulus, K, and shear modulus, G. This approach employs hydrostatic stress and strains in conjunction with stored energy to estimate the bounds. The arithmetic mean of Voigt and Reuss bounds is known as the Voigt-Reuss-Hill (VRH) approximation [60], which is classically used in mineralogy to estimate the elastic constants corresponding to a random polycrystal.

As shown by Povolo and Bolmaro [121], both Voigt and Reuss models are built using the invariance of the trace of the 9 x 9 matrix representing the stiffness and compliance tensors, respectively. This leads to the observation (made by Hill [60]) that the Voigt and Reuss averages only use 9 of the 21 independent elastic constants. Denoting by $I_1 = C_{iijj}$ and $I_1^* = C_{ijij}$ the traces (or linear invariants) of tensors C_{iikl} and C_{ijjl}, respectively, the Voigt average is obtained from a comparison of those traces with their corresponding isotropic expressions, leading to:

$$K_{Viogt} = \frac{I_1}{9} = \frac{1}{9}\left(C_{11} + C_{22} + C_{33} + 2\left(C_{12} + C_{13} + C_{23}\right)\right) \tag{5.1}$$

$$G_{Viogt} = \frac{\left(3I_1^* - I_{1)}\right)}{30} = \frac{1}{15}\left(C_{11} + C_{22} + C_{33} + 3\left(C_{44} + C_{55} + C_{66}\right) - C_{12} - C_{13} - C_{23}\right) \tag{5.2}$$

where C_{ij} denotes the Voigt notation of the elastic constants. Applying a similar procedure to the compliance tensor $S_{ijkl} = C_{ijkl}^{-1}$, the Reuss average is obtained:

$$K_{\mathrm{Re}uss} = \frac{1}{J_1} = \left(S_{11} + S_{22} + S_{33} + 2\left(S_{12} + S_{13} + S_{23}\right)\right)^{-1} \tag{5.3}$$

$$G_{\mathrm{Re}uss} = \frac{15}{\left(6J_1^* - 2J_1\right)} = \frac{15}{4\left(S_{11} + S_{22} + S_{33} - S_{12} - S_{13} - S_{23}\right) + 3\left(S_{44} + S_{55} + S_{66}\right)} \tag{5.4}$$

where $J_1 = S_{iijj}$ and $J_1^* = S_{ijij}$ are the corresponding traces of the compliance tensors S_{iikl} and S_{ijjl}, respectively.

There are two common objections to both Voigt and Reuss averages (and hence to Hill average): first because it is based on linear invariants of the elasticity tensors, it involves only 9 out of the 21 elastic constants. This may be relevant for simple geometries such as cubic or hexagonal where most of the elastic constants not considered in the VRH averaging scheme are zero; it may, however, be of importance for symmetries such as trigonal, monoclinic (e.g. tobermorite 11 Å and 14 Å) and triclinic (tobermorite 9 Å). Second, Voigt and Reuss derivations consider orthogonal symmetries and hence are only invariant under orthogonal transformations. That means that if one considers a crystal whose coordinates is tilted other than right angles, the VRH results is different values. In other words, the VRH is not completely frame-indifferent (or so called objective in Continuum Mechanics terminology), hence the physical properties depend on the location of the observer.

Molinary Approximation

Molinary approximation is another common approximation for elastic constants that is mostly used for polycrystals [82]. This approach is based on probability distributions and statistical moments which lead to

$$K = \frac{C^2}{C_{11} + 2C_{33} + C_{12} - 4C_{13}} \tag{5.5}$$

$$G = \frac{3C^2}{2\left(2C_{11} + C_{33} + 2C_{12} + 4C_{13}\right)} \tag{5.6}$$

with

$$C^2 = C_{33}\left(C_{11} + C_{12}\right) - 2C_{13}^2 \tag{5.7}$$

While Molinary's approach may resolve the second shortcoming of VRH, it fails to consider the full anisotropy effect. Hence, both approaches consider identical elastic constants, and their sole difference is in the combination of them.

New Statistical Averaging Method for Elastic Constants: Sound Wave Approach

Recognizing the VRH and Molinary's limitations, Povolo and Bolmaro [121] proposed the consideration of higher order invariants of the elasticity tensors to estimate average elastic constants. While this approach is complex and lacks physical insights, here we derive a simple, yet efficient averaging scheme based on acoustic tensor analysis in which all the 21 elastic constants as well as all random orientations contribute to the average quasi-isotropic elastic properties. To this end, we briefly recall that the principle acoustic wave velocities in an anisotropic medium are obtained from the eigenvalue-eigenvector problem (see e.g. [29]):

$$\mathbf{A}.\mathbf{v} = c^2\mathbf{v} \tag{5.8}$$

where c is the wavespeed, $\mathbf{v}$ is the particle-motion direction and $\mathbf{A}$ is the acoustic tensor defined by

$$\mathbf{A} = \frac{1}{\rho}\mathbf{n}.\mathbf{C}.\mathbf{n};\ A_{jk} = \frac{1}{\rho}n_i C_{ijkl} n_l \tag{5.9}$$

In above, ρ is the density, $\mathbf{C}$ is the fourth order elastic tensor and $\mathbf{n}$ is the unit normal of the incident wave propagation. Equation (5.8) is a eigenvalue-eigenvector problem known as Christoffel equation [93]. It specifies the propagation velocity and particle-motion direction (polarization vector) for each plane wave component in space.

Wavespeeds in Eq. (5.8) are the roots of characteristic equation $\det(\mathbf{A} - c^2\mathbf{1}) = 0$ where $\mathbf{1}$ is the second order unit tensor. The symmetry of the acoustic tensor, $\mathbf{A}$, ensures that the underlying eigensystem is well-behaved. Thus we can find three distinctive velocities $c_3 \leq c_2 \leq c_1$ associated with three orthogonal directions of particle motions: c_1 represents (quasi) longitudinal sound waves, while c_2 and c_3 represent respectively the higher and the lower transverse sound waves.

By taking the volume average of the three sound waves over all directions, one can obtain:

$$\overline{c_J} = \frac{1}{4\pi}\int_{\phi=0}^{2\pi}\int_{\theta=0}^{\pi} c_J\left(n_i\right)\sin\theta d\theta d\phi \tag{5.10}$$

These mean velocities represent statistical averages of the longitudinal ($V_L = \overline{c}_1$) and shear

velocities, $\overline{c}_2$ and $\overline{c}_3$. Taking the mean for the two shear velocities, i.e.

$$V_S = \frac{\overline{c}_2 + \overline{c}_3}{2} \tag{5.11}$$

and making use of the classical relations between velocities and isotropic properties, we determine the statistical average of the bulk and shear modulus from:

$$K^{Vel} = \rho \left(V_L^2 - \frac{4}{3} V_S \right) \tag{5.12}$$

$$G^{Vel} = \rho V_S^2 \tag{5.13}$$

For an anisotropic material, our new statistical averaging scheme ensures that not only all 21 elastic constants are taken into account but all random directions contribute to the average bulk and shear moduli. With such an approach, one can thus evaluate the contribution of those elastic constants not considered in the VRH and Molinary schemes. By way of illustration, in the next section we show the three fundamental sound velocities for C-S-H crystals along any arbitrary direction in space. This will greatly simplify the 3D conceptualization of soft and stiff areas in complex anisotropic materials, hence making our averaging scheme more meaningful. Later in Chapter 6, we present a detailed numerical example of application of our new averaging method. The numerical code for the new averaging scheme and 3D visualizations are given in Appendix B.

5.1.2 Directional Wave Speeds

We use the elastic constants of C-S-H crystals obtained in Chapter 4 along with Eqs. (5.8) and (5.9) to calculate the three fundamental plane waves in each arbitrary direction in space. Figures 5-1 to 5-7 shows the three fundamental sound speeds for each crystal. The sphere with unit radius indicates arbitrary directions in space. Several observations can be made from Figs. 5-1 to 5-7, but the following features deserve most attention:

(a) As these crystals are either monoclinic or triclinic [14],[16],[58],[103], the elastic tensor is anisotropic. Thus, none of these fundamental waves are purely longitudinal or

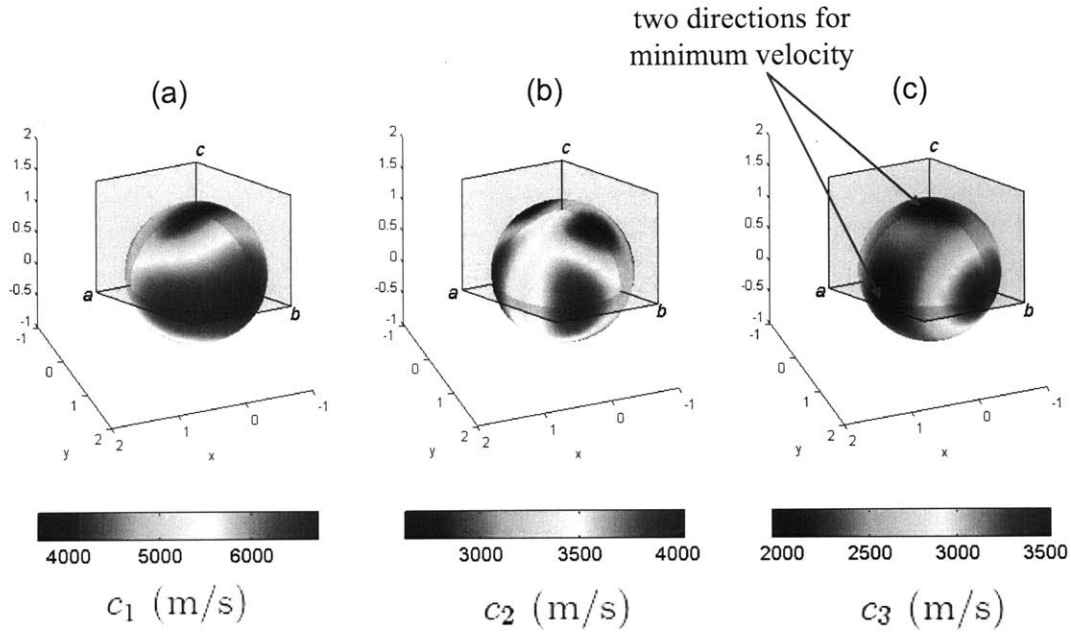

Figure 5-1: Directional sound speeds in tobermorite 14 Å. (a) maximum sound speed c_1. (b) medium sound speed c_2. (c) minimum sound speed c_3.

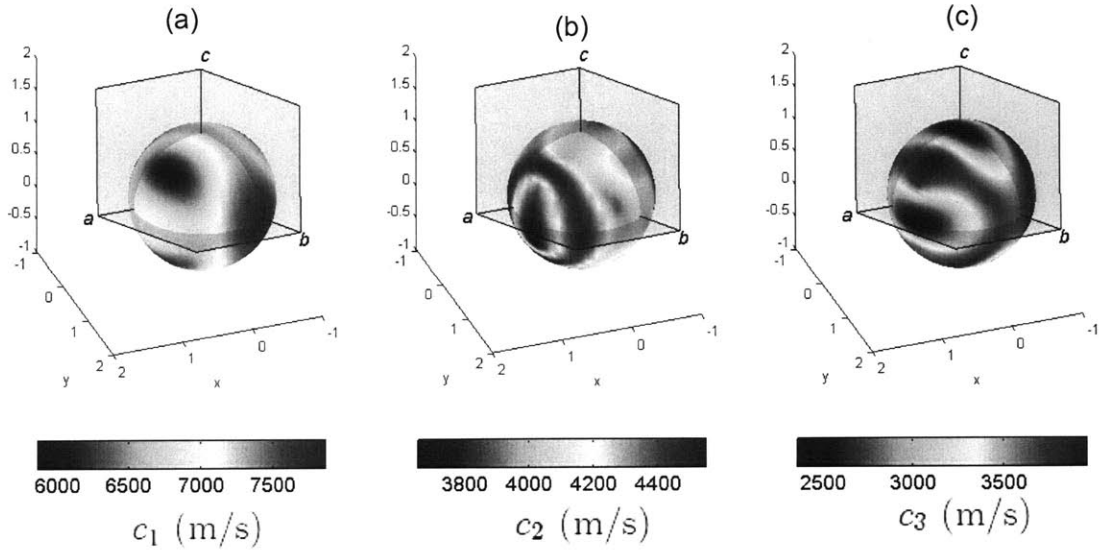

Figure 5-2: Directional sound speeds in tobermorite 11 Å. (a) maximum sound speed c_1. (b) medium sound speed c_2. (c) minimum sound speed c_3.

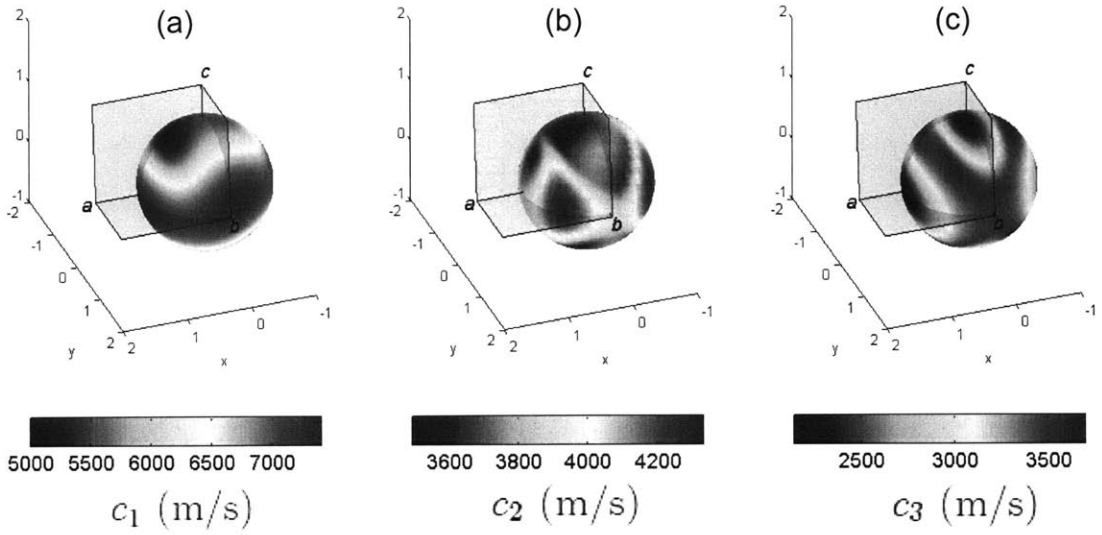

Figure 5-3: Directional sound speeds in tobermorite 9 Å. (a) maximum sound speed c_1. (b) medium sound speed c_2. (c) minimum sound speed c_3.

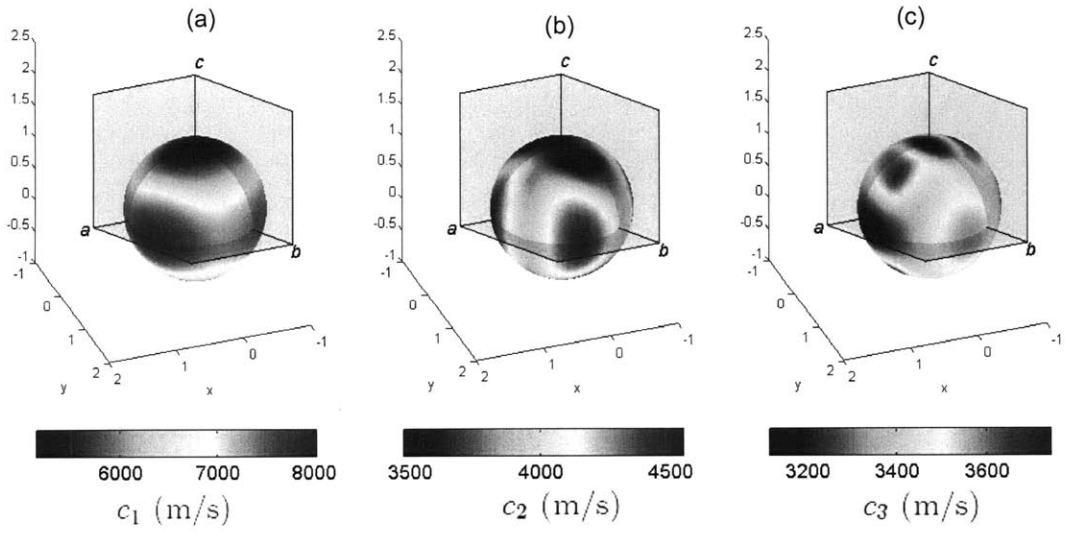

Figure 5-4: Directional sound speeds in tobermorite 11 Å (Hamid Ca/Si=1). (a) maximum sound speed c_1. (b) medium sound speed c_2. (c) minimum sound speed c_3.

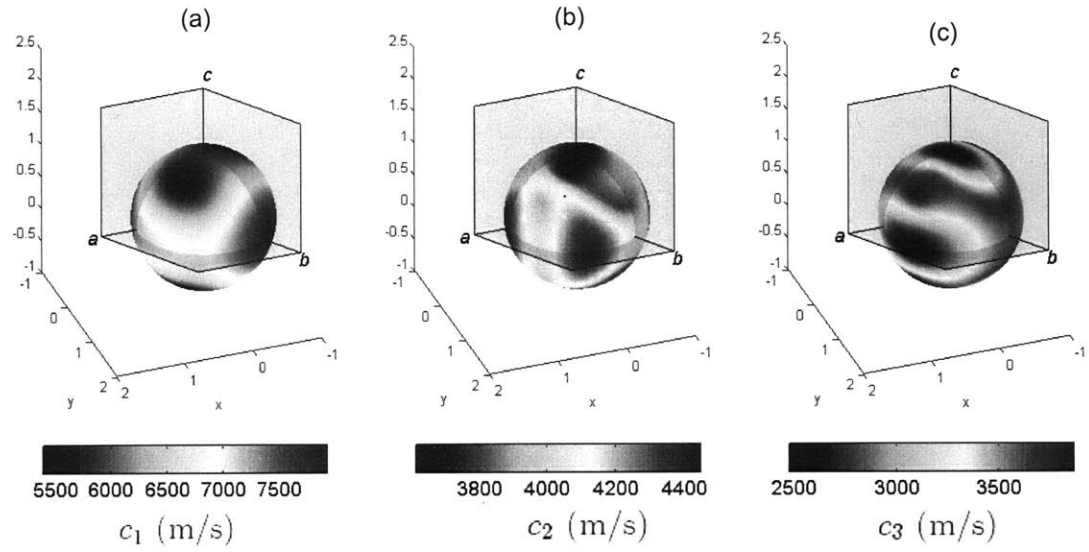

Figure 5-5: Directional sound speeds in tobermorite 11 Å (Hamid, Ca/Si=0.83). (a) maximum sound speed c_1. (b) medium sound speed c_2. (c) minimum sound speed c_3.

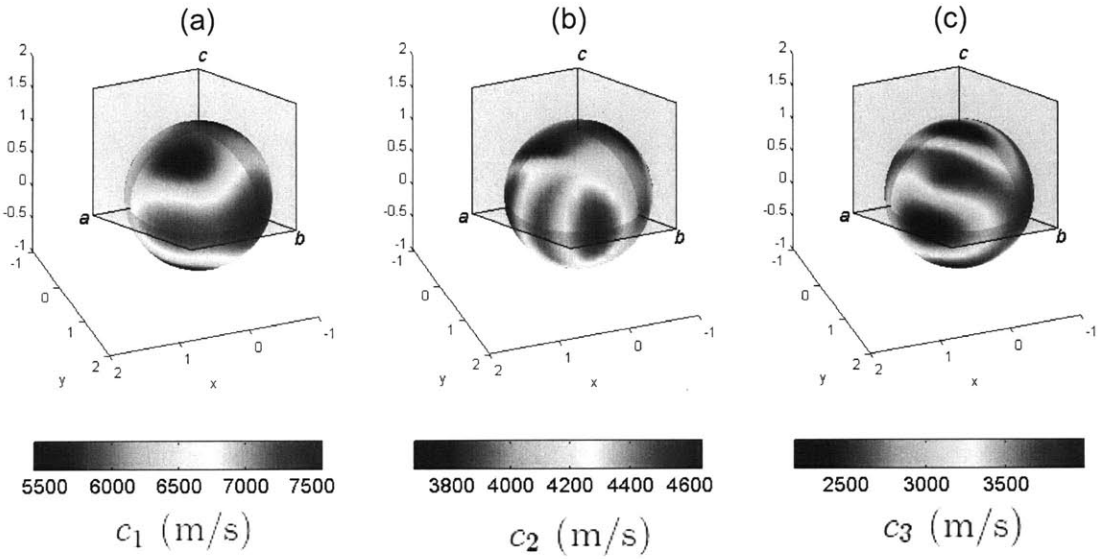

1.

Figure 5-6: Directional sound speeds in tobermorite 11 Å (Hamid, Ca/Si=0.67). (a) maximum sound speed c_1. (b) medium sound speed c_2. (c) minimum sound speed c_3.

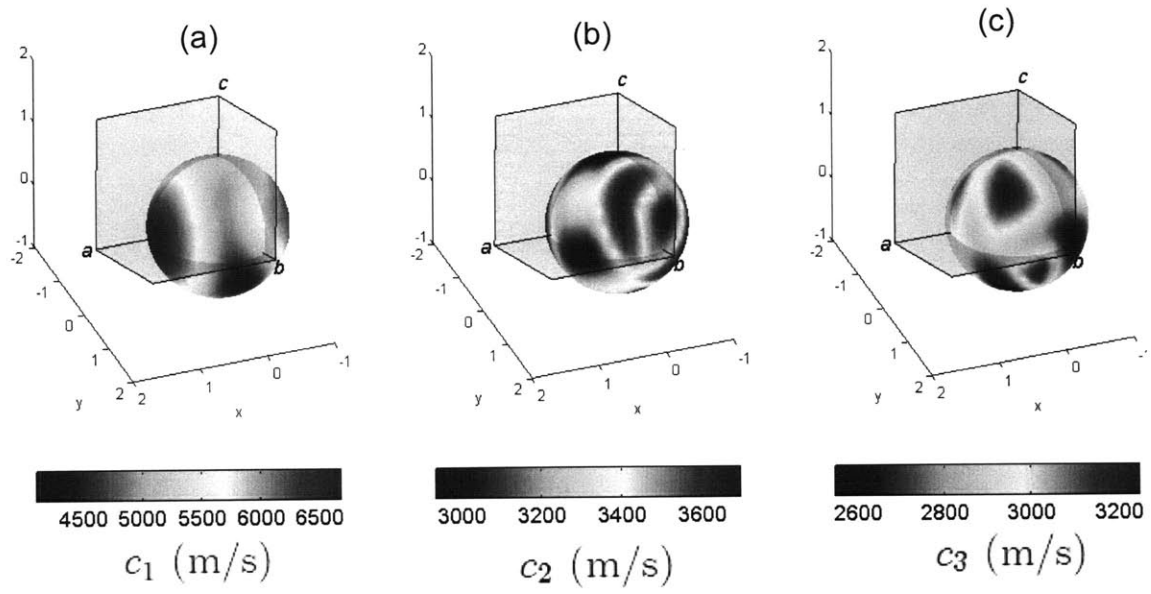

Figure 5-7: Directional sound speeds in jennite. (a) maximum sound speed c_1. (b) medium sound speed c_2. (c) minimum sound speed c_3.

purely transverse.

(b) The direction of maximum velocity in all crystals is almost coincided with the direction of Young's modulus (and not the stiffness C_{ii}) calculated in Chapter 4. This has been shown for tobermorite 14 Å as an example in Fig. 5-8.

(c) In tobermorite family, the lowest values of shear velocities are along both the in-plane and the interlayer directions.

(d) The maximum directional velocity is around 8000 m/s along the in-plane direction of tobermorite 11 Å (Hamid type, with Ca/Si=1) while the average maximum velocity (average over all directions on the unit sphere) is highest in tobermorite 11 Å (Merlino type). This is because of the overall enhanced elastic properties in 3D due to the existence of interlayer links (Q_3 ^{29}Si NMR).

(e) In all crystals, the magnitude of the medium and minimum velocities are relatively close as they are both somewhat transverse velocities (not purely).

(f) The minimum directional velocity is around 2000 m/s parallel to the interlayer direc-

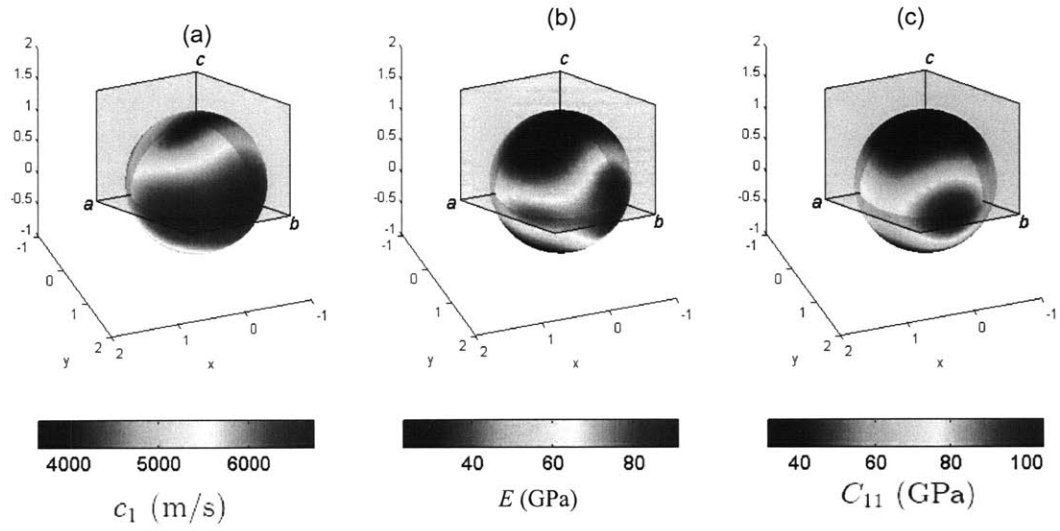

Figure 5-8: Tobermorite 14 Å. (a) Directional longitudinal sound speed . (b) Directional Young modulus. (c) Directional stiffness. The results for parts (b) and (c) are taken from Chapter 4.

tion in tobermorite 14 Å. The average minimum velocity is also lowest in tobermorite 14 Å. Figure 5-9 shows the average three velocities in each of the crystals as a function of density. For all three velocities, tobermorite 14 Å and jennite have the lowest average velocity between all crystals. In the case of c_3, jennite and tobermorite 9 Å have a very close average minimum velocity. In addition, although tobermorite 9 Å is the stiffest crystal among these minerals (see Chapter 4), the sound velocity is not maximum due to the interference of density.

5.1.3 Polarization Vectors

For any of the directional velocities of C-S-H crystals calculated in the previous section, one can find three orthogonal eigenvectors. The real value wavespeeds and orthogonality of particle-motion directions (polarization vectors) relate to the crystal's stability. The real value wavespeeds assures that the fluctuations of energy are spontaneously redistributed in the crystals through the travelling waves. Otherwise, the energy fluctuations can locally accumulate which tends

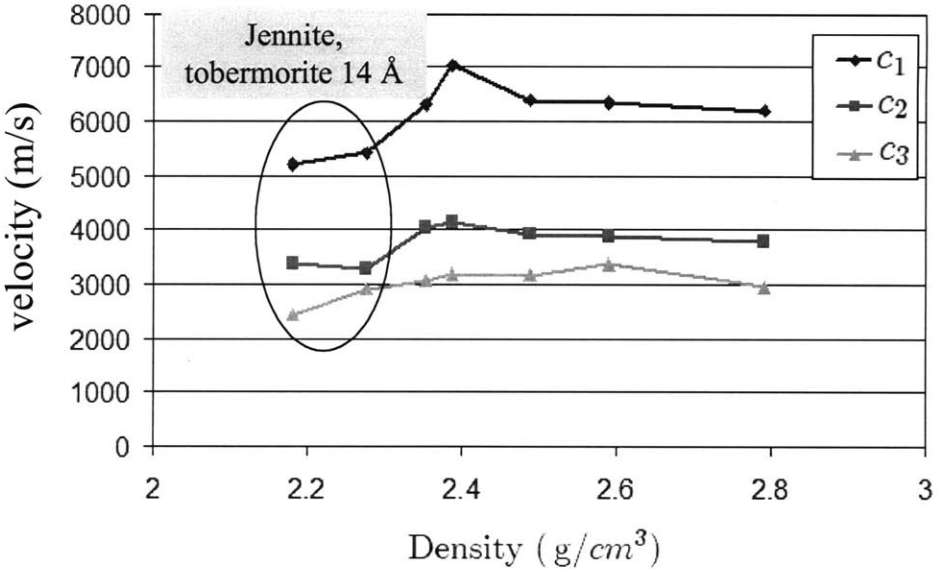

Figure 5-9: Average maximum, medium and minimm velocities for tobermorite family and jennite.

to shift the crystal from its natural equilibrium. On the other hand, orthogonality of particle-motion directions ensures that no resonance can occur between two travelling waves. Because orthogonality requires no energy exchange between orthogonal directions. More detailed discussion on stability of traveling waves and polarization vectors can be found in [29].

In this work, we studied the polarization vectors associated with the maximum velocity for all C-S-H crystal in table 4.6. In this case, it turns out that due to the stability of the crystal structures, the polarization vectors are not always parallel to the directional velocities (as is the case in isotropic materials). Indeed, they tend to bend over closest areas where the Young's modulus is higher. Figure 5-10 schematically shows how this effect takes place. For points A or C, the directions of maximum velocity and polarization are identical while these directions are different for point B. The polarization vector for point B, leans towards the in-plane direction. To clarify, we show this effect for three types of C-S-H crystals (Figs. 5-11, 5-12 and 5-13). For simplicity, we only show one eighth of the spheres where all components of the polarization vectors are positive.

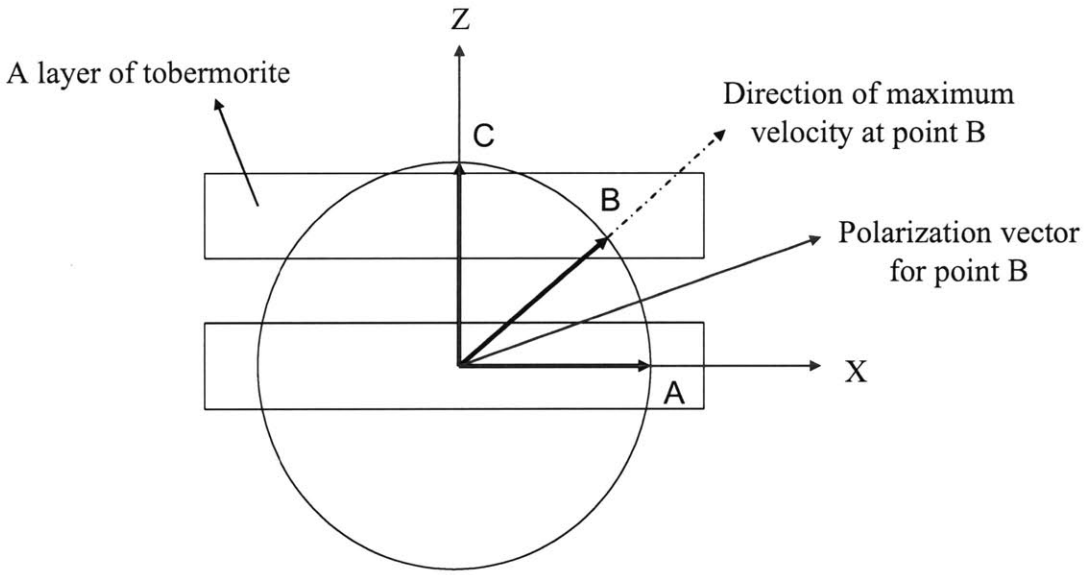

Figure 5-10: Schematic diagram representing the directional velocities (black lines) and their corresponding polarization vectors (red lines).

For tobermorite 11 Å (Hamid, Ca/Si=1), Fig. 5-11(a) shows the direction of maximum velocity while Fig. 5-11(b) indicates the polarization direction. Identical colors between Fig. 5-11(a) and Fig. 5-11(b) refer to velocities and their corresponding polarization vectors. Similar to the schematic illustration in Fig. 5-10, Fig. 5-11(b) shows how the direction of all polarization vectors (points such as B) are shifted down. Figure 5-12 shows same phenomenon for tobermorite 11 Å (Merlino) where unlike the previous case, the softest direction is not the interlayer direction, but an inclined axis (blue regions in Fig. 5-12(a)). In this case, as Fig. 5-12(b) shows the polarization vectors for all the points in the middle (where the Young's modulus is the lowest) are shifted towards the sides and the area of the blue region expands.

For jennite, as its crystal structure is different, the direction of the polarization vectors are different but still the same detour happens in polarization directions due to the crystal stability condition, that is leaning towards the areas with larger Young modulus (Fig. 5-13).

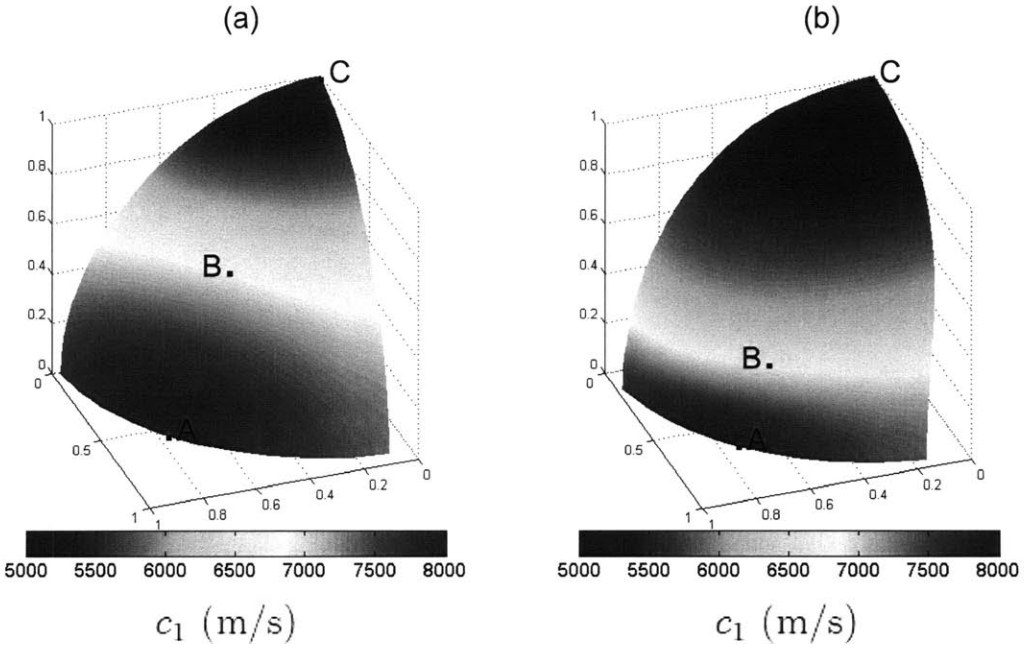

Figure 5-11: Tobermorite 11 Å (Hamid, Ca/Si=1). (a) maximum directional velocity, (b) polarization vectors for the maximum velocities in (a). Downward shifting of the wrinkles represent the change of polarization vectors toward areas with higher Young's modulus.

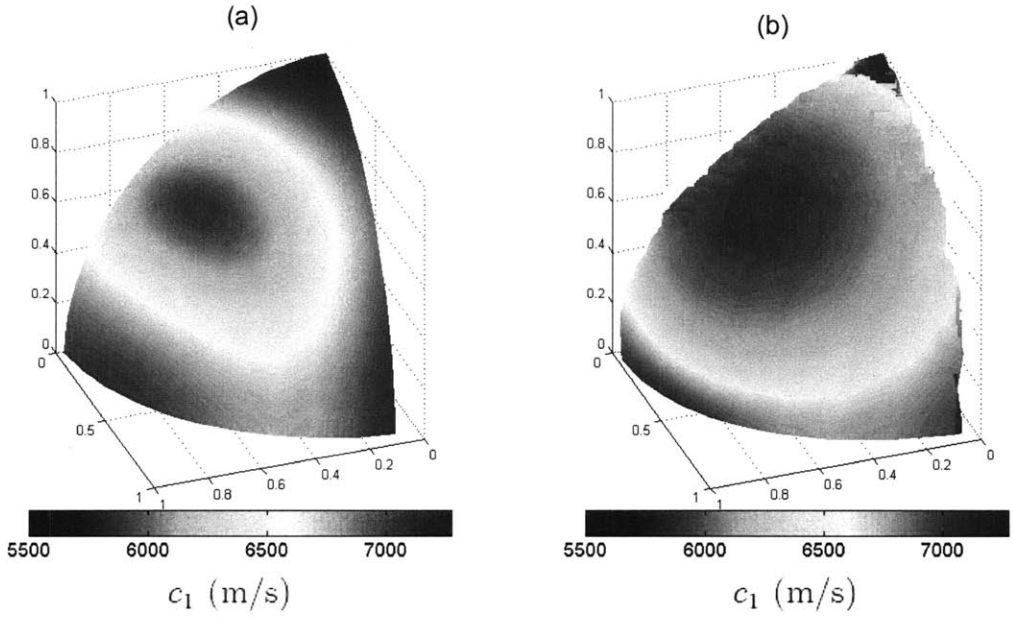

Figure 5-12: Tobermorite 14 Å. (a) maximum directional velocity. (b) polarization vectors for the maximum velocities in (a). Deviation of wrinkles from the center area represent the change in polariation vectors from soft center regions towards stiff side-areas with higher Young's modulus.

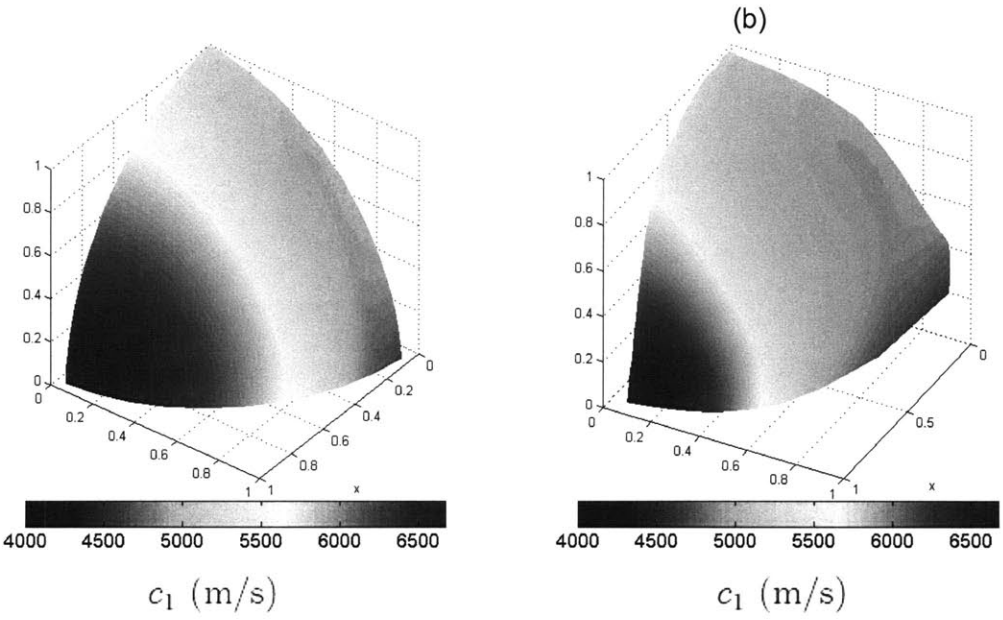

Figure 5-13: Jennite. (a) maximum directional velocity. (b) polarization vectors for the maximum velocities in (a). Concentration of wrinkles towards stiff areas represents the change in the direction of polariation vectors.

5.2 Chapter Summary

In this Chapter, based on acoustic tensor analysis, we developed a simple, yet efficient averaging scheme for quasi-isotropic elastic properties. Our statistical approach overcome the shortcomings of classical averaging schemes such as Voigt-Reuss-Hill and Molinary approximation in that i) it considers all 21 independent elastic constants of an anisotropic material, ii) is invariant under any arbitrary rotation in space, and iii) it conveniently provides a physical insight to conceptualize the complex contributions of softest and stiffest directions of an anisotropic material into quasi-isotropic elastic properties, K, and G. This novel statistical approach is independent of any length-scale and can be applied to any anisotropic materials spanning from tiny atomistic crystals to giant structural components.

Next, we presented the three fundamental wave velocities along any arbitrary direction for tobermorite family and jennite. It turns out that the locations of maximum wave velocity follow the footprints of the directional Young's modulus. We showed polarization vectors associated with the maximum wave velocity tend to be leaned towards areas with higher Young moduli. This is due to the crystal stability to ensure the integrity of particle motions are maintained.

In Part III, all our focus was on characterization of C-S-H crystals based on DFT calculations. In the next Part, we turn our attention to Atomistic Simulations methods (MD and MC) as a means to handle larger C-S-H systems, which enable addressing more realistic C-S-H phases.

Part IV

Investigation of C-S-H Phases via Atomistic Simulations

Chapter 6

Empirical Force Fields for C-S-H Gel: Development of CSH-FF

Part III of this thesis was centred around first-principles calculations on C-S-H crystalline models and their structural and mechanical features. However, C-S-H crystals are not a strict analog for an amorphous real C-S-H phase. This Part employed the Atomistic Simulation methods (MD and MC) to tackle larger systems and is composed of three Chapters: The first Chapter uses the DFT results in Part III to develop a new force field, CSH-FF, customized for the C-S-H family. Second Chapter focuses on developing a consistent molecular model based on the most frequently measured local value of Ca/Si. Finally, in the third Chapter CSH-FF is used in conjunction with statistical mechanics to decode a wide variety of C-S-H molecular phases across different Ca/Si ratios

In this Chapter, we focus on comparing two common empirical force fields, the simple point charge ClayFF potential developed for clay minerals and the core-shell potential that are both widely used in simulating hydrated oxides such as tobermorite. We start by investigating the predictive capabilities of these force fields against our benchmark DFT results in Part III. We show that transferability of force fields to analogous hydrated oxides without rigorous investigations may result in misleading predictions in properties. To overcome the deficiencies of common force field potentials, we use both structural and elasticity data to develop a new force field potential, CSH-FF, for hydrated calcio-silicates as an improved version of ClayFF.

6.1 Introduction

The use of empirical force fields is now a standard approach in predicting the properties of hydrated oxides which are omnipresent in both natural and engineering applications. The use of empirical force fields is a common approach in Computational Materials Science or Mineralogy. Recently, several attempts have been made to apply this approach to hydrated oxides [9],[22],[30],[36],[141],[171] including Calcium-Silicate-Hydrate (C-S-H) [97]. Yet progress on the "atomistic concrete front" has been slow due to uncertainty in the degree of transferability of empirical force fields used to simulate complex hydrated oxides, such as C-S-H, whose characteristic grain size is beyond the reach of state-of-the-art first principles calculations such as DFT.

One way to resolve this issue is to benchmark empirical potentials against first principles calculation results for a selected number of hydrated oxides with relevant chemistry, for which the atomic structure is well known. In Chapter 4, we presented such first principles results for tobermorite family and jennite. By comparing results from first principles simulations, we aim in the present Chapter at evaluating the degree of transferability of empirical potentials for such complex hydrated oxides. In particular, we focus on two different families of empirical force fields commonly in use for calcio-silicate minerals: simple point charge models represented by the ClayFF potential [30] and the core-shell model [45],[46],[47].

In the core-shell model, anion charges are divided between an atomic core (with a positive charge) and a shell (with a negative charge) such that the sum of these charges is equal to the formal atomic charge (or to a given partial charge as for oxygen in water for instance). The comparison with the first principles results is made for both structural data and elastic properties for two tobermorite polymorphs distinguished by their basal spacing and hence water content: tobermorite 14 Å and tobermorite 11 Å Hamid with Ca/Si=1. No further fitting to tobermorite properties was attempted for core-shell model in this thesis. Thus, the results presented here are predictions for the used potential models and related parameters.

Note that in core-shell model 50 % of the coulombic intra-molecular energy within the water molecule is subtracted. This 50% reduction is the feature of the de Leeuw-Parker water potential [34] and may not lead to very satisfactory predictions of bulk liquid water density at room temperature. However, in the case of the hydrated calcio-silicate compounds, this is not

an issue as interlayer water molecules do not form a confined dense phase such as those in clay minerals; water molecules in tobermorite minerals or in C-S-H are usually called "structural water molecules". All the parameters of the core-shell potential are given in Appendix A.

6.2 Comparison of Empirical Potentials with DFT

With a focus on transferability of empirical potentials, there are structural data at room temperature from experiments on tobermorite crystals, however, there are no experimental data on higher order properties such as elastic constants. Hence, because of lack of experimental data, wherever needed, we employ first-principles results as reference data to compare higher order properties of tobermorite crystals. Thus, this section compares first principles results with predictions obtained with two commonly used empirical force field potentials for the C-S-H minerals, namely ClayFF and core-shell model. For comparison, we consider the benchmark results obtained from first-principles Density Functional theory using GGA exchange correlation functional (GGA-DFT) as reported in Chapter 4. Comparison is made for both structural and elasticity data of tobermorite 14 Å and 11 Å minerals. For this purpose, we implemented both the ClayFF potentials and the core-shell potentials in the GULP code [47].

6.2.1 Structural Data

We minimize the total energy of tobermorite 14 Å and 11 Å at 0 K allowing all degrees of freedom to relax including cell parameters, angles and all atomic positions. The unit cell of tobermorite 14 Å has 14 water molecules while 11 Å tobermorite has 4 water molecules. The experimental unit cell dimensions for both of these minerals are given in Tables 6.1 and 6.2.

From these tables, it can be inferred that DFT minimization for tobermorite 14 Å and 11 Å tobermorite structures at 0 K quite accurately refine experimental XRD data. Interestingly enough, both inter-atomic potentials predict lattice parameters with an acceptable accuracy compared to experiments or DFT results. The reason for which the ClayFF-relaxed systems are somewhat of lower symmetry compared to that obtained with the core-shell approach is not obvious. ClayFF is a simple charge potential model with no anionic polarization by contrast to the core-shell model. Hence, one may conclude that allowing anion polarization allows

	a (Å)	b (Å)	c (Å)	α (deg)	β (deg)	γ (deg)
Exp.	6.69	7.39	27.99	90	90	123.25
DFT	6.87	7.43	28.49	89.96	90.05	123.47
Core-shell	6.94	7.35	28.35	90	90	123.07
ClayFF	6.87	7.37	28.55	89.25	90.95	122.69
CSH-FF	6.7	7.41	28.7	90.01	89.81	123.77

Table 6.1: Tobermorite 14 Å (Ca/Si = 0.83, 14 H2O/unit cell). Comparison between experiment, 0K DFT, core-shell, ClayFF and CSH-FF empirical force fields. Note that CSH-FF is a re-parametrized and simplified version of Clay-FF, see text.

	a (Å)	b (Å)	c (Å)	α (deg)	β (deg)	γ (deg)
Exp.	6.73	7.42	22.78	90	90	123.49
DFT	6.6	7.4	23.13	90	90	123.62
Core-shell	6.65	7.3	24.45	90.28	89.93	123.75
ClayFF	6.77	7.33	24.51	91.13	89.98	123.05
CSH-FF	6.6	7.39	24.37	90	90	123.88

Table 6.2: Tobermorite 11 Å (Ca/Si = 1, 4 H2O/unit cell). Comparison between experiment, 0K DFT, core-shell, ClayFF and CSH-FF empirical force fields. Note that CSH-FF is a re-parametrized and simplified version of Clay-FF, see text.

maintaining larger system symmetry. In addition, it is interesting to see that thermal expansion/contraction effects at room temperature (as in experiment) are small since both DFT and experimental data agree within a few percents; that is to say kT represents a small fraction of all different iono-covalent bond energies found in these systems.

In order to analyze the internal atomic structure, we plot the histograms of major iono-covalent bonds and angles (Fig. 6-1). As expected DFT predictions for bond and angle distribution spectrum are in general in good agreement with those from experiments [15],[58]. For Ca-O bond distances in tobermorite 14 Å and 11 Å, both force field potentials predict approximately the same mean and relatively comparable distribution spectrum compared to experiment or those from DFT results. For Si-O bonds in tobermorite 14 Å, both force fields estimate a mean bond distance which is comparable to experiment while it is about 3% larger than that predicted by DFT method which predicts a narrower distribution. In the case of tobermorite 11 Å, this difference almost vanishes for the core-shell potential, while ClayFF tends to underestimate the mean bond distance.

Analyzing DFT results, one can see that the Si-O-Si angle (Fig. 6-2) linking two tetrahedra is on the order of 135 ° to 145 ° while this angle is between 137.5 ° to 138.5 ° from experiments, thus showing a spike in Fig. 6-1(c). For comparison, this angle in quartz is 144 ° [62]. This indicates that silica chains in tobermorite polymorphs are more packed than quartz and this will likely affect the partial charge distribution and mechanical properties of SiO_2 chains in tobermorite. In both tobermorite 14 Å and 11 Å, core-shell potential predicts mean Si-O-Si angles that are close to experiments and DFT results. In summary, considering first-order (i.e. structural) information both semi- empirical potentials give relatively satisfactory results. Core-shell estimations seem to be more in agreement with the DFT results, while ClayFF results give wider bond distance and angle distributions.

6.2.2 Elastic Constants

Once the tobermorite structure is in a fully relaxed stable state, we turn to higher order properties and determine the elastic constants. Since tobermorite 14 Å and 11 Å are triclinic crystals, in theory there are 13 independent elastic constants. There are no experimental values for these independent elastic constants. We thus consider our DFT results as reference data. In Tables 6.3 and 6.4, we report values for the full elastic tensors for tobermorite 11 Å and 14 Å polymorphs using the DFT method and the two force field potentials (we also report results obtained with a newly fitted force field potential, CSH-FF, which will be discussed in detail in the last section).

6.2.3 Elastic Tensor Metrics

In order to quantitatively compare these fourth-order elastic tensors, one-to-one comparison of the components and corresponding statistical analysis are not of much help. One way of measuring the closeness of these square matrices with the DFT-results as a reference is to utilize an Euclidean distance to define a metric on the tensor space, i.e.

$$d_E(C_{DFT}, C_{FF}) = \|C_{DFT} - C_{FF}\|_E \tag{6.1}$$

where the associated norm is defined by:

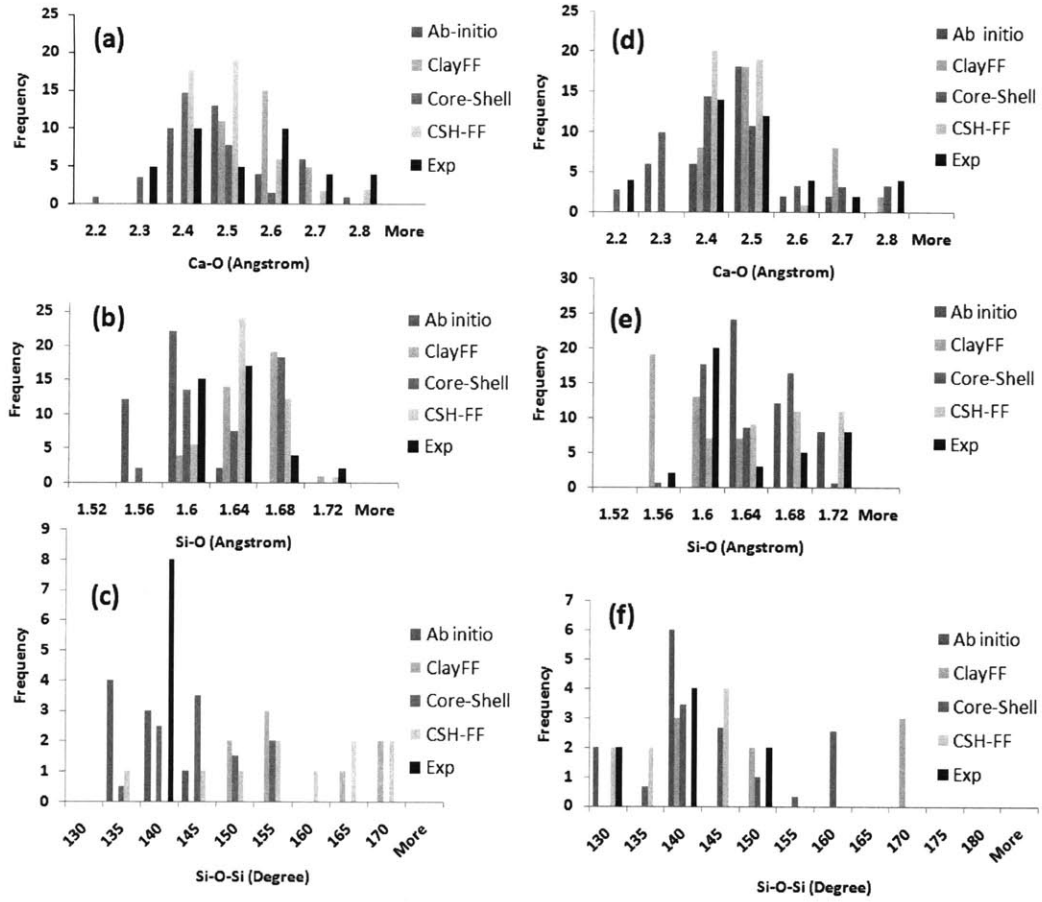

Figure 6-1: (a) to (c) Histograms of the bond distance Ca-O, Si-O and bound angle Si-O-Si for tobermorite 14 Å. (d) to (f) Histograms of the bond distance Ca-O, Si-O and bound angle Si-O-Si for tobermorite 11 Å. Note that CSH-FF is a corrected and simplified version of Clay-FF that is described later in this Chapter.

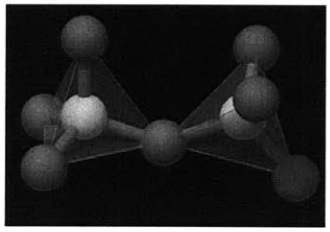

Figure 6-2: The angle Si-O-Si between two tetrahedral in tobemorite. White and red spheres represent silicon and oxygen atoms respectively.

	DFT	ClayFF	core-shell	CSH-FF
C_{11}/GPa	148.25	112.98	167.5	151.34
C_{12}/GPa	63.25	29.17	47.78	54.27
C_{13}/GPa	26.75	22.11	41.13	25.18
C_{16}/GPa	6.63	-16.24	6.78	1.05
C_{22}/GPa	138.35	99.24	142.8	123.16
C_{23}/GPa	32.55	9.36	35.18	20.9
C_{26}/GPa	1.85	-9.12	3.05	-3.16
C_{33}/GPa	68.4	28.45	67.87	61.33
C_{36}/GPa	-1.73	-1.2	7.64	-1.99
C_{44}/GPa	32.75	18.53	18.37	37.33
C_{45}/GPa	-1.93	-0.45	3.32	-0.15
C_{55}/GPa	25.65	17.53	32.49	27.36
C_{66}/GPa	53.3	40.65	46.44	54.86

Table 6.3: Comparison of elastic constants for tobermorite 11 Å obtained with DFT, and the two empirical potentials, ClayFF and core-shell. The CSH-FF predictions refer to the corrected simgle charge model. The DFT data of tobermorite 11 Å has been used for fitting the potential parameters of the CSH-FF potential that is an improved version of Clay-FF (see text).

	DFT	ClayFF	core-shell	CSH-FF
C_{11}/GPa	77.6	62.8	96.74	101.42
C_{12}/GPa	35.9	30.88	42.07	35.12
C_{13}/GPa	20.18	19.76	20.43	17.15
C_{16}/GPa	3.08	-7.72	-3.17	-7.602
C_{22}/GPa	104.5	80.81	102.82	88.04
C_{23}/GPa	26.3	18.38	25.16	25.12
C_{26}/GPa	-1.75	-12.62	-7.6	3.36
C_{33}/GPa	32.05	55.33	59.03	57.05
C_{36}/GPa	3.03	-6.24	-5.25	-4.08
C_{44}/GPa	24.5	17.9	25.46	13.76
C_{45}/GPa	-9.43	-11.1	-6.62	-5.91
C_{55}/GPa	14.65	20.75	7.74	11.13
C_{66}/GPa	38.1	44.35	42.45	34.09

Table 6.4: Comparison of elastic constants for tobermorite 14 Å obtained with DFT, and the two empirical potentials, ClayFF and core-shell. The CSH-FF predictions refer to the corrected simgle charge model. The DFT data of tobermorite 11 Å has been used for fitting the potential parameters of the CSH-FF potential that is an improved version of Clay-FF (see text).

Metric Type	Tensor	ClayFF	core-shell	CSH-FF
$d_E(C_{DFT}, C_{FF})/\left\|C_{DFT}\right\|_E$	Stiffness	0.39	0.17	0.11
$d_E(S_{DFT}, S_{FF})/\left\|S_{DFT}\right\|_E$	Compliance	0.71	0.51	0.106
$d_R(P_1, P_2)$	Stiffness and Compliance	1.04	0.84	0.29

Table 6.5: Comparison of the relative Euclidean and Riemannian metrics for elastic tensors for tobermorite 11 Å. The CSH-FF predictions refer to the corrected Clay-FF model. A perfect agreement with the targeted DFT results would result in a zero value of the relative metric.

Metric Type	Tensor	ClayFF	core-shell	CSH-FF
$d_E(C_{DFT}, C_{FF})/\left\|C_{DFT}\right\|_E$	Stiffness	0.29	0.24	0.28
$d_E(S_{DFT}, S_{FF})/\left\|S_{DFT}\right\|_E$	Compliance	0.37	0.64	0.50
$d_R(P_1, P_2)$	Stiffness and Compliance	1.06	1.12	1.20

Table 6.6: Comparison of the relative Euclidean and Riemannian metrics for elastic tensors for tobermorite 14 Å. The CSH-FF predictions refer to the corrected Clay-FF model. A perfect agreement with the targeted DFT results would result in a zero value of the relative metric.

$$\|A\|_E = \left(tr\left[A^T A\right]\right)^{0.5} \tag{6.2}$$

Because of its simplicity, the Euclidean metric may be a preferable metric. However, it is not a rigorous metric for positive definite matrices and lacks certain properties [8]. For instance, it is not invariant under inversion. The inverse of the elastic tensor is the compliance tensor, $S = C^{-1}$, which renders important information about the average elastic properties. A more robust metric for symmetric positive-definite matrices is the Riemannian metric which is independent of the coordinate system; it preserves material symmetry and it is invariant under inversion [108]. For two symmetric positive-definite matrices P_1 and P_2, the Riemannian metric is:

$$d_R(P_1, P_2) = \left\|\log\left(P_2^{1/2} P_1^{-1} P_2^{1/2}\right)\right\|_R = \left(\sum_{i=1}^{n} \ln^2 \lambda_i\right)^{0.5} \tag{6.3}$$

where λ_i are the eigenvalues of the $P_1^{-1} P_2$ matrix.

Tables 6.5 and 6.6 show the relative Euclidean and Riemannian metrics for the elastic tensors reported in tables 6.3 and 6.4 respectively. A perfect agreement with the targeted DFT results would result in a zero value of the relative metric. For both tobermorite 11 Å and 14 Å, the relative Euclidean metric for stiffness tensors predicted by the core-shell force

field potential is smaller than that predicted by ClayFF. For the compliance tensors, the same trend is observed for tobermorite 11 Å. In return, in the case of tobermorite 14 Å, the relative Euclidean distance is larger for core-shell than for ClayFF. In the case of tobermorite 11 Å, the Riemannian metric for core-shell potential is considerably smaller than that for ClayFF (about 66%). For tobermorite 14 Å , the Riemannian distances for ClayFF and core-shell are about the same (core-shell metric is only 6% larger than ClayFF metric).

It seems since ClayFF is originally developed for hydrated crystalline compounds and their interfaces with liquid phases, its prediction power is better for water-rich compounds such as tobermorite 14 Å as opposed to tobermorite 11 Å. Additionally, the slight increases in core-shell metrics in tobermorite 14 Å may suggest that the water model used in core-shell model may not be well suited for expanded phases such as tobermorite 14 Å with more water molecules. However, overall considering the magnitudes of metrics for both tobermorites 11 Å and 14 Å, it turns out that core-shell predictions are closer to DFT results.

6.2.4 Averaged Elastic Properties

Another way for comparing the elastic tensors is by condensing the elasticity tensor components into quasi-isotropic bulk modulus, K, and shear modulus, G. Here, in view of our analytical derivations and discussion in Chapter 5, we compare the average elastic properties via two approaches: i) Voigt-Reuss-Hill Approach (VRH), and ii) Sound Wave Approach, which we developed in Chapter 5 and was shown to be superior than VRH for highly anisotropic materials such as tobermorite crystals (see Section 5.1.1 for the exact analytical relations of each averaging scheme).

Tables 6.7 and 6.8 display the values for the bulk and shear modulus calculated based on VRH and Velocity approach for tobermorites 11 Å and 14 Å respectively. Given the small values of the elasticity constants not considered in the VRH averages (namely, C_{16}, C_{26}, C_{36} and C_{45} in Tables 6.3 and 6.4), K and G do not differ by more than about 8% by using the different averaging methods. In another comparison which is physically more perceivable, Fig. 6-3 shows the principle sound velocities along any arbitrary direction for tobermorite 11 Å. From this figure it appears that, the core-shell model predictions for the longitudinal velocity, c_1, better matches with that calculated by DFT (note the color map for c_1 in Fig. 6-3a and

	DFT	ClayFF	core-shell	CSH-FF
K^{Voigt}/GPa	66.7	40.2	69.6	59.6
G^{Voigt}/GPa	37.8	27.3	36.4	39.6
K^{Ruess}/GPa	55	24.8	57.1	47.7
G^{Ruess}/GPa	34.1	20.8	30.1	35.8
K^{VRH}/GPa	60.8	32.5	63.3	53.6
G^{VRH}/GPa	36	24.1	33.2	37.7
K^{Vel}/GPa	58.9	35.5	63.2	51.5
G^{Vel}/GPa	34.5	22	31.5	36

Table 6.7: Average elastic properties of tobermorite 11 Å based on VRH approximation and Sound Wave Velocity Approach.

	DFT	ClayFF	core-shell	CSH-FF
K^{Voigt}/GPa	42.1	37.4	48.2	44.6
G^{Voigt}/GPa	24.2	21.2	26.5	23.1
K^{Ruess}/GPa	29.7	33.8	42.6	40.2
G^{Ruess}/GPa	17	15.7	15.8	15.3
K^{VRH}/GPa	35.9	35.6	45.4	42.4
G^{VRH}/GPa	20.6	18.5	21.1	19.2
K^{Vel}/GPa	38	38.6	47.6	44.5
G^{Vel}/GPa	20.1	18.5	22.1	19.2

Table 6.8: Average elastic properties of tobermorite 14 Å based on VRH approximation and Sound Wave Velocity Approach.

Fig. 6-3c).

With different estimates now in hand, it is possible to benchmark the polycrystal elastic properties predicted by ClayFF and core-shell against DFT results. The results displayed in Tables 6.7 and 6.8 reflect, in terms of polycrystal properties, the conclusions from the tensor metrics analysis: in the case of tobermorite 11 Å, the core-shell results are in very close agreement with the DFT results; while ClayFF significantly underestimates, by 40%, both the bulk modulus and the shear modulus. In turn, in the case of the tobermorite 14 Å, both empirical approaches provide reasonable results for the shear modulus; the core-shell approach overestimates by roughly 25% the DFT bulk modulus. It thus appears, from both the tensor metrics analysis and the polycrystal properties for both tobermorite 14 Å and 11 Å, that the core-shell model predicts second-order approximations (i.e. elastic constants) reasonably well, while the ClayFF approach has some shortcomings when it comes to hydrated oxides with small water content such as for tobermorite 11 Å. Consistent with this observation is the fact that the ClayFF model predicts elastic properties of quartz that are about 50% lower than experiments.

The core-shell model utilizes (unphysical) formal charges for all in-solid species even though the bonding in tobermorite layers is iono-covalent in nature. This approach may be more justifiable to guarantee the transferability of a force field as formal charges are unchanged regardless of the (hydrated) oxide. Overall, in both semi-empirical potentials the error in predicting bulk modulus is larger than the error for shear moduli.

6.3 An Improved Potential Customized for C-S-H Phases

Despite the core-shell model's higher degree of transferability, an improvement for the core-only model for hydrated calcio-silicates is highly desirable since core-only models are less computationally expensive and thus more efficient for larger systems. Such a development is presented below. Obviously, such a new core potential for hydrated calcio-silicates may not be transferable to other oxides with different element types. ClayFF's shortcomings in predicting elastic properties of low-hydrated oxides do not come as a surprise: ClayFF was designed for predicting structural data (which it does reasonably well) rather than elastic properties. Thus an improvement of ClayFF would require improving the second-order predictive capabilities.

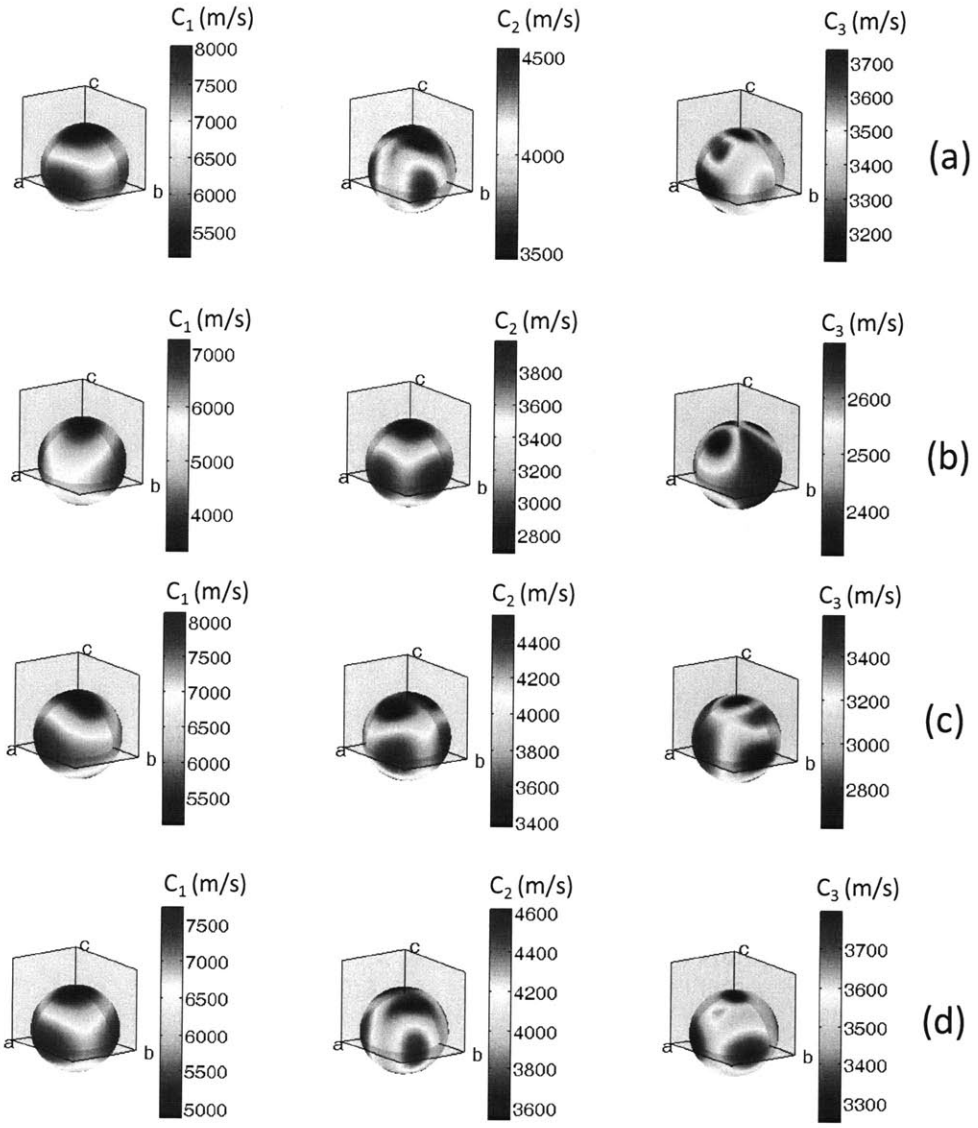

Figure 6-3: Comparison of the principle sound velocities for tobermorite 11Å in any arbitrary direction. Any point on the sphere with the unit radius represents the tip of a unit vector which is drawn from the center of the sphere (intersection of the three crystal planes). The surface of the sphere covers all possible 3D arbitrary unit vectors. a) DFT-results b) ClayFF c) core-shell d) CSH-FF. The CSH-FF predictions refer to the corrected Clay-FF simple charge model.

6.3.1 Developing CSH-FF Potential

An inspiration for such an improvement comes from SiO_2 core-only potentials that give a good account of many properties of quartz including structural and elasticity properties [161]. These potentials are based on the same set of equations as ClayFF but use different parameters. In view of this approach, we first note that some of the partial charges used in the ClayFF model, although obtained from quantum calculations, are significantly different than those we derived from our DFT calculations in Chapter 4.

It is well known that there are different schemes to calculate partial charges, the Mulliken scheme being the most popular. Thus first-principles derived atomic or ionic charges can be used as a guideline to understand chemical and bonding processes; but they can also be considered as fitting parameters in force field potential determination; *ab initio* data providing a good starting point for any potential parameter fitting procedure. In the CRYSTAL98 *ab initio* calculations in Chapter 4, we found: q_{Si}=+2.25 ē, $q_{Obridge}$=-1.22 ē, q_O=-1.36 ē, q_{Ca}=1.66 ē and q_{Cw}=1.70 ē in the case of tobermorite 11 Å with Ca/Si=1 and 4 H_2O molecules per unit cell (Cw refers to interlayer calcium). By comparing with the ClayFF parameter data set in [30], one can see noticeable differences, which indicates that the overall Coulombic energy is likely to be very different. Interestingly, water species partial charges were the same as those in ClayFF, and are thus compatible with the flexible SPC water model. As a consequence, we did not attempt to change intra molecular potential parameters.

As a further simplification with respect to ClayFF, we did not consider short-range (Lennard-Jones) interactions between cations in the spirit of the core-shell approach, and assume that the cation-cation Coulombic repulsion is sufficient, leading to a simpler description as compared to ClayFF. We thus start our fitting parameter process by considering the ClayFF set of short-range parameters and let all charges adjust (except those of water species) by using the potential fitting procedure within the GULP code [47]. Note that we made a distinction between interlayer calcium, Cw, and intralayer calcium, Ca, based on quantum-derived charges.

As we aim the new force field to show good performances not only at the structural level but for elasticity as well, we used as a set of fitting data from our DFT calculations including the cell parameters, the bulk and shear moduli and the entire elastic tensor of tobermorite 11 Å; thus in total 29 input data. In a second stage, we let all short range (Lennard-Jones)

Species	charge ($\bar{e}$)
Water hydrogen (Hw)	0.41
Water oxygen (Ow)	-0.82
Oxygen (formally carrying a H atom) (Oh)	-1
Bridging oxygen (O)	-1.14
Silicon (Si)	1.72
Calcium (Ca)	1.43
Interlayer Calcium (Cw)	1.7
Hydrogen (H)	0.29

Table 6.9: Partial charges for the CSH-FF force field.

		D_{ij} (eV)	R_{ij} (Å)
Ca	O	3.77E-05	4.898
Ca	Oh	3.06E-05	6.125
Cw	O	6.33E-05	4.898
Cw	Oh	4.51E-05	4.9866
Si	O	2.43E-05	3.6716
Si	Oh	2.58E-05	3.6627
O	O	5.39E-02	3.0687
Oh	Oh	2.68E-03	3.8652
O	Oh	1.98E-03	4.0654
Si	Ow	2.30E-05	3.6298
Ca	Ow	3.80E-05	4.898
Cw	Ow	2.62E-05	5.0168
O	Ow	2.28E-04	4.7557
Oh	Ow	3.78E-02	3.2513

Table 6.10: Non-bonded parameters for different interaction in CSH-FF. D and R are empirical Lennard-Jones parameters as symbolized in original ClayFF model.

parameters (except the Cw-O, Ow-Ca and Ow-Si parameters fixed to ClayFF initial values as they are found to have no significant energy contribution) freely adjusting toward DFT data. At this point, we have 29 parameters to adjust (Lennards-Jones parameters + charges) for 29 input data with equal convergence weight set to 0.01. As a final and third step, as approaching a converged mathematical solution (i.e. minimizing the sum of the squared differences with DFT inputs), we ran a fit-relaxation calculation in order to optimize the final structure as well as the set of fitting parameters.

The set of fitted potential parameters for this new C-S-H force field that we name CSH-FF, are given in Tables 6.9 and 6.10.

	a (Å)	b (Å)	c (Å)	α (deg)	β (deg)	γ (deg)
core-shell	13.31	29.52	23.69	92.01	88.52	123.58
CSH-FF	13.06	29.02	23.08	91.69	87.86	122.68

Table 6.11: Structural data of cCSH, comparison of CSH-FF and core-shell performances.

We note that newly fitted partial charges in CSH-FF are significantly different from both DFT and ClayFF charges except for water (unchanged during fitting). Therefore, they should be considered as effective potential fitting parameters with no real physical meaning which is only relatively well captured by DFT approaches. This also acknowledges the fact that Lennard-Jones potentials are effective and a rather crude approximation of the repulsive and dispersion interactions as one can see from the more rigorous quantum perturbation theory based multipole expansion for the latter [120]. The quality of the fitting can be seen for tobermorite 11 Å, in both structural data (see Table 6.2 and Fig 6-1d to Fig 6-1f), elasticity data (see Tables 6.3, 6.5 and 6.7) and sound wave velocity (see Fig. 6-3). Note that for hydroxyl groups (OH) present in tobermorite 14 Å, CSH-FF uses the same parameters as derived in ClayFF. In this case, to ensure the charge neutrality of the cell, the small extra positive charge will be divided between all the cation atoms.

6.3.2 Validation of CSH-FF

The validation of CSH-FF is achieved for tobermorite 14 Å, which has not been used for fitting, showing a good agreement in both structural data (see Table 6.1 and Fig 6-1a to Fig 6-1c) and elasticity data (Tables 6.4, 6.6 and 6.8), displaying in some cases superior performance than the core-shell model for a significantly smaller computational effort.

Finally as a full scale demonstration of the ability of our re-parameterized version of ClayFF, in predicting, not only structural but also elastic properties, we used CSH-FF in an energy minimization of the atomic-scale consistent model of cement hydrate (cC-S-H). This model with a chemical composition of $(CaO)_{1.65}(SiO_2)(H_2O)_{1.75}$ is able to properly predicts essential structural features and fundamental physical properties of real cement hydrates (see Chapter 7).

In fact, this model shows cement hydrate as being a porous glassy calcio-silicate at short–

	K^{VRH} (GPa)	G^{VRH} (GPa)	M (GPa)	ν
core-shell	49.53	22.69	64.92	0.3
CSH-FF	50.5	21.69	63.06	0.31
Experiment	49.3	22.7	65	~0.3

Table 6.12: Average elastic properties of cCSH, comparison of CSH-FF and core-shell performances with experiments on real cement hydrate samples [27].

range with some reminiscence of tobermorite layer-to-layer longer range correlations. By comparison with tobermorite polymorphs, cement hydrate has a rather different chemistry with significantly larger calcium (and water) content. This large Ca/Si ratio in cC-S-H is achieved by having silica chains of finite lengths (unlike tobermorite which has infinite chains). In other words, the cC-S-H model of cement hydrates is a stringent test of our CSH-FF potential as it contains many defects and also larger water content compared to tobermorite polymorphs.

Note that electroneutrality of the cC-S-H model, although very defective, is maintained. Tables 6.11, 6.12 and 6.13 present a comparison of structural and elastic data of cC-S-H unit cell obtained using both core-shell and CSH-FF potential models. It can be seen that CSH-FF predicts fairly accurate both structural and elastic properties of a complex material such as cement hydrate. In particular, indentation modulus, M=63.06 GPa, which relates to bulk and shear moduli agrees well with that extrapolated from nanoindentation experiments on real cement hydrates [27]. Note that the experimental bulk and shear moduli are back-calculated from elasticity relations considering $\nu = 0.3$ and $M = 65$ GPa.

This is very encouraging given the relative simplicity and higher efficiency of CSH-FF as a core-only force field. For instance, assuming equal CPU resources, in the case of cC-S-H, the CSH-FF considers only N=672 core species while the core-shell model needs additional 317 shells for negative ions for a total of 989 species. Hence, CSH-FF results in 3.4 times more efficiency than a core-shell model in terms of computational time for energy minimization, which scales with N^3. Similarly, MD simulations with CSH-FF are at least 2 times faster than those with a core-shell model. Additionally, since CSH-FF does not have the complexity of a core-shell structure (i.e. massless shells in anions), the MD times steps can be around an order of magnitude larger than that used in typical MD simulations with core-shell models. Finally, for the sake of comparison, we compare the CSH-FF computational speed with DFT. As expected

	core-shell	CSH-FF
C_{11}/GPa	93.4939	86.187
C_{12}/GPa	45.3728	34.2917
C_{13}/GPa	26.0704	35.6453
C_{16}/GPa	3.4574	1.2588
C_{22}/GPa	94.8693	85.4978
C_{23}/GPa	30.0581	32.3433
C_{26}/GPa	-3.007	3.22652
C_{33}/GPa	68.4554	80.4045
C_{36}/GPa	-0.5734	1.9247
C_{44}/GPa	19.2291	18.2580 -
C_{45}/GPa	0.3323	0.674
C_{55}/GPa	16.1189	17.7185
C_{66}/GPa	31.2336	24.3994

Table 6.13: Elastic constants for cCSH, comparison of CSH-FF and core-shell performances.

DFT calculations take orders of magnitude more time than empirical force fields. For a full cell relaxation (including internal atomic positions and six cell parameters) for tobermorite 14 Å with 104 atoms, DFT took almost 4 days with 4 parallel CPUs, whereas this relaxation with empirical force fields takes maximum a few hours with a single CPU.

Since our benchmark comparison data was our previous DFT results, it is worthwhile to mention that DFT at its current state may not predict accurate van der Waals dispersive forces. However, in crystalline C-S-H minerals such as tobermorite the interlayer interactions between charged layers are dominated by coulombic interactions rather than van der Waals dispersive forces [119]. Moreover, real cement hydrate models such as cC-S-H have a 3D defected structure where the 2D layered structure is much less pronounced than crystalline C-S-H minerals. Hence, the dispersive interactions in real cement hydrates are much less critical than other neutral layered materials such as $Mg(OH)_2$, $Ca(OH)_2$ and kaolinite as discussed in [159]. Hence, the dispersive forces do not play a significant role for interlayer interaction in both C-S-H models such as tobermorite and the realistic cement hydrate systems such as cC-S-H which are our final target for CSH-FF potential transferability.

6.4 Chapter Summary

In this Chapter, we rigorously evaluated the performances of empirical force fields in the context of structural and mechanical properties of complex hydrated oxides such as tobermorite 14 Å and 11 Å polymorphs. By benchmarking two different classical approaches against reference DFT data, one based on a simple point charge model, ClayFF, and the second based on the core-shell potential model, we found that the structural prediction of both force fields seem to be in close agreement with DFT results. However, a comprehensive investigation of the degree of transferability of such force fields requires the consideration of higher order properties such as elastic constants, which relate to second order derivatives of energy. By comparing the elastic tensors as obtained from the DFT quantum route with the predictions of ClayFF and core-shell models (in terms of Euclidean and Riemannian metrics, Voigt-Reuss-Hill scheme, and a new averaging scheme based on sound wave velocity calculations), we found that the core-shell model well predicts elastic properties while ClayFF underestimates them. This suggests that a core-shell model has a greater degree of transferability than ClayFF.

On the other hand, we demonstrated that the shortcomings of the simple point charge model can be overcome by deriving a new set of potential parameters from an original fitting procedure that includes concurrently structural and elastic data. A core-only force field for hydrated calcio–silicate materials is proposed in this Chapter. For tobermorite polymorphs, this re-parameterized version of ClayFF, named CSH-FF, performs well when compared to the core-shell approach in terms of both structural and elastic property predictions. CSH-FF is also significantly less computational intensive than the core-shell model.

As a full-scale test of CSH-FF within the framework of calcio-silicate solids, we compared CSH-FF and core-shell predictions on the consistent atomistic model of cement hydrate, cC-S-H, that is structurally and chemically quite different than the tobermorite polymorph originally used in the fitting process. We found that CSH-FF provides satisfactory predictions for structural data. Average elastic constants predicted by CSH-FF for cement hydrates agree with those obtained from nanoindentation experiments on C-S-H. However, rigorous analyses of this prediction for individual elastic constants requires experimental values to become available. Nevertheless, this new tool provides a means to start performing large scale simulations of cement hydrates bridging the gap between nano and micron-scale approaches [138]. In the next

Chapter, we will discuss the cCSH development using core-shell model. In Chapter 8, CSH-FF will be extensively used to establish the link between composition, density and morphology of hundreds of C-S-H phases existing in real cement pastes.

Chapter 7

A Consistent Molecular Structure of C-S-H

In this Chapter, we propose a consistent molecular model of C-S-H based on an atomistic simulation approach that considers only the experimental NMR precursors as the overriding constraint. The overall goal of this Chapter is to show how the molecular components of C-S-H such as CaO, SiO_2, and H_2O interact with each other to form a defected silica chain morphology that links to realistic values for density and chemical composition of an averaged C-S-H phase. We show how core-shell model is utilized to build the consistent model of C-S-H. Validated by experiments, this model predicts several essential structural features and fundamental physical properties such as mechanical stiffness and strength of real cement paste systems

7.1 Introduction

With the recent determination of the calcium/silicon (Ca/Si =1.7) ratio and the density of the C-S-H particle (2.6 g/cm^3) by small-angle neutron scattering measurements [4], there is new urgency to the challenge of explaining these essential properties. Although our DFT results in Chapter 4 implied tobermorite 14 Å and jennite as the best C-S-H crystalline analogs among all C-S-H minerals, from the standpoint of constructing a molecular model of C-S-H, these C-S-H analogs do not possess strict structural and morphological resemblance to those in realistic C-S-H. For instance, Ca/Si and density values clearly cannot be obtained from either tobermorite

(Ca/Si = 0.83, 2.18 g/cm^3) or jennite (Ca/Si = 1.5 and 2.27 g/cm^3).

In this Chapter, we adopt the perspective that the chemical composition of C-S-H is the most essential property in formulating a realistic molecular description. We show that once the Ca/Si ratio is described correctly, a number of characteristic structural features and physical properties follow naturally in atomistic simulations. We view the present model and its subsequent refinements as enabling a new bottom-up perspective on the broad science of cementitious materials and the innovative engineering of concrete. Manipulation of such a testable model should ultimately allow the establishment of the critical links between nanoscale microstructure and macroscale behavior (see Chapter 9).

7.2 Computational Details

All energy minimizations, Grand Canonical Monte-Carlo and NPT-MD were carried out with the GULP code [47]. The advantage of such an approach compared to *ab-initio* quantum mechanical methods is that for large systems with low symmetry, one can compute not only structural data but also thermodynamic and elastic properties. The core-shell force field potential [45],[46],[47] was adopted for interatomic interactions, which is based on Born model description [45] for ionic and iono-covalent crystal structures. A detailed discussion of the strengths and weaknesses of the core-shell predictions for C-S-H systems is presented in Chapter 6.

Energy minimization for finding an equilibrium structure consists in tracking stationary points that correspond to a minimum energy gradient with positive energy curvature (i.e. finding a set of atomic positions that minimizes system energy and give a Hessian operator with positive eigenvalues only). A phonon spectrum calculation at the center of the Brillouin zone is then used as a final validation from which one gets the list of lattice vibration frequencies that should be all positive except the first three that should be zero (unit cell translational invariance). Such minimization procedure gives a zero temperature solution.

All degree of freedom were considered including atomic positions, unit cell dimensions and angles. The same approach but at fixed negative hydrostatic stress was used to perform cell relaxation to calculate rupture properties: for each incremental value of stress, all cell parameters were recorded until one of them was diverged, indicating rupture. The maximum stress at

which cell volume diverges is considered as cohesive stress.

7.2.1 The Grand Canonical Monte-Carlo Technique for Water Adsorption:

In developing a realistic C-S-H model, we first produced an anhydrous version of the C-S-H substrate and subsequently calculated the maximum amount of water that can be accommodated in its pore voids. For this purpose, we used the Grand Canonical Monte-Carlo simulation technique that is a well-suited method to study adsorption/desorption processes. The Grand Canonical Monte Carlo simulations (GCMC) involves the determination of the properties of a system at a constant volume V (the pore with the adsorbed phase) in equilibrium with an infinite fictitious reservoir of particles imposing its chemical potential μ and its temperature T [43],[112]. For different values of μ, the absolute adsorption isotherm can be determined as an ensemble average of the adsorbed atom numbers in the system versus the relative pressure of the gas reservoir P (the latter can be obtained from the chemical potential according to the equation of state for the bulk gas).

The adsorption and desorption processes can be respectively simulated by increasing or decreasing the chemical potential of the reservoir; the final configuration of a simulation is the initial state for the next point. Similar to energy minimization procedures, periodic boundary conditions was used in all directions of space. An equal number attempt for translation, rotation, creation or destruction of molecules has been chosen.

The water sorption isotherm has been calculated for 300 K. Acknowledging the very restricted available space in between tobermorite layers, one should not expect capillary condensation to occur by contrast to larger pore systems such as vycor [123]. In our case, the adsorption/desorption process is expected to be close to that observed for microporous zeolite [124]. We did not calculate the entire water adsorption/desorption isotherm but perform a single GCMC simulation with the water chemical potential fixed to a value that corresponds to the bulk liquid phase with a density of 1 g/cm^3 at room temperature ($\mu = 0$ eV for the used core-shell water model).

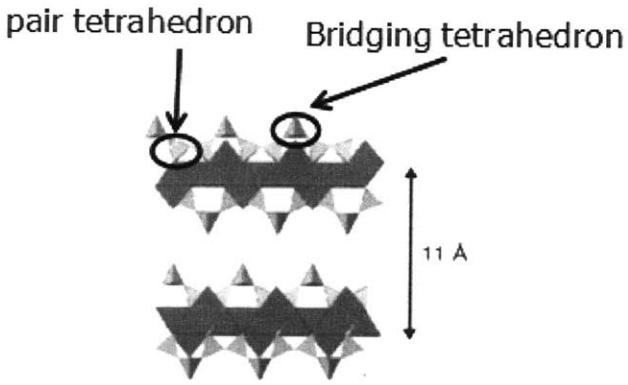

Figure 7-1: A view of tobermorite 11 Å crystal. Green ribbons represent Ca layers and pink pyramids symbolize silicon tetrahedra (silica chain).

7.2.2 Molecular Dynamics in the NPT Ensembles

Room temperature relaxation were carried out using Molecular Dynamics simulation in the NPT statistical ensembles integrating motion equation with the leapfrog Verlet algorithm with Nosé-Hoover thermostat and barostat (with corresponding parameters set to 0.05 eV). Finite temperature entropic effects are included in NPT-MD relaxations (with zero external pressure) on the resulting system obtained from energy minimization.

7.3 Model Construction

One of the key issues in designing a realistic C-S-H molecular model is the Ca/Si ratio. Indeed, confirming earlier measurements [56],[131] energy dispersive X-ray analyses of C-S-H in hardened Portland cement pastes aged 1 day to 3.5 years reveal a composition variation spanning Ca/Si from approximately 1.2 to 2.3 with a mean value of 1.7; this variation also depends on the water-to-cement (w/c) mass ratio at which cement is hydrated [135].

Given the shortfalls of the natural analogs, tobermorite and jennite, to meet this compositional constraint, Richardson proposed a two-fold classification to clarify C-S-H chemistry [135]. This classification references so-called tobermorite/jennite (T/J) models on one hand and tobermorite-calcium hydroxyl (T/CH) models on the other hand. The T/CH class considers models that are solid solutions of tobermorite layers sandwiching calcium hydroxide, hence

providing a means to achieve a higher Ca/Si ratio than the one of tobermorite. The T/J class considers C-S-H as an assembly of tobermorite regions followed by jennite domains. While the T/CH class was found to be relevant for hydrated KOH-activated metakaolin Portland cement, more common water activated Portland cement pastes can be only partly described by the T/J or the T/CH approaches.

A realistic model for C-S-H that predicts a realistic Ca/Si ratio thus remains a center piece of any model construction. Furthermore, quantitative information on the fractions of Si present in silicate tetrahedra with different connectivities is provided by ^{29}Si nuclear magnetic resonance (NMR) [10],[24]. Such studies have established that the dimer is the most predominant of all silicate species, with the linear pentamer as the second most abundant. Tetrahedral coordination measured by NMR is expressed in terms of the Q_n factor, denoting the fractional chemical shift of a silicon atom bound to n bridging oxygens. Thus Q_0 is the fraction of a single tetrahedron (a silicate monomer), Q_1 the fraction of tetrahedra at the end of a chain (a silicate dimer would have two Q_1), Q_2 the fraction of tetrahedra in the middle of a chain (a silicate pentamer would have three Q_2).

7.3.1 Removal of SiO_2 Units

To construct a molecular model of C-S-H that has a Ca/Si ratio consistent with small-angle neutron scattering measurements, we begin with a monoclinic periodic computational cell of dry tobermorite 11 Å with Ca/Si=1, with 2, 4, and 1 units along axes *a, b,* and c. Figure 7-1 shows a side view of tobermorite 11 Å. Note that with this value of Ca/Si, the tobermorite layers are not electroneutral and there are interlayer calcium ions to maintain electroneutrality. We then remove SiO_2 (neutral) groups in silica tetrahedra guided by the NMR results [38], $Q_0 \sim 10\%$, $Q_1 \sim 67\%$, and $Q_2 \sim 23\%$, obtaining a defective C-S-H structure that has a distribution of $Q_0 = 13\%$, $Q_1 = 67\%$, and $Q_2 = 20\%$, with a Ca/Si ratio of 1.65. Obviously there are many possible ways for creating a defected structure with the aforementioned NMR signatures. In Chapter 8, we discuss and explore a combinatorial approach to produce defected silicate chains. In this Chapter, we only focus on a single morphology.

Our procedure was carried out without the presence of any OH groups, so that a reasonable Ca/Si ratio could be obtained under the electroneutrality constraint [132]. After the silicate

chain modification, we relax the dry cell using the core-shell potential model at 0 K to find a density of 2.12 g/cm^3, the interlayer distance having shifted slightly to 11.3 Å. At this stage, one can observe significant distortion of the layer structure.

7.3.2 Adsorption of Water Molecules

In order to hydrate the defected unit cell, we performe Grand Canonical Monte Carlo simulation of water adsorption in the distorted anhydrous unit cell, coupling the system to an external reservoir at a chemical potential corresponding to liquid water at 300 K as implemented in GULP [47]. At equilibrium, the adsorbed water increases the density to 2.56 g/cm^3, which is close to the experimental value provided by neutron scattering of 2.6 g/cm^3 [4]. We regard this agreement, which was an outcome rather than an input or constraint to this model, to be a significant consistency check on our model development procedure. Further relaxation at 0 K of this hydrated C-S-H model yields a slight increase of the interlayer spacing from 11.3 Å to 11.9 Å, reducing the density by 4% to 2.45 g/cm^3; molecular dynamics simulations under constant pressure and temperature (NPT-MD) give the same result.

In the final model, one can observe water molecules adsorbed in cavities inside the calcium oxide layers as a result of relaxation. While the amount of water is similar to that present in the interlayer region of 14 Å tobermorite, the water in our model is adsorbed not only in the interlayer regions, but also in the distorted intralayer regions around the silica monomers. As a consequence of water adsorption the density increases to 2.56 g/cm^3, with the adsorbed water molecules being in an ultra-high confining environment. This water may be regarded as part of the structure, reminiscent of structural water or bound water in cement chemistry terminology. The overall chemical composition of the computational model of the hydrated C-S-H is thus found to be $(CaO)_{1.65}(SiO_2)(H_20)_{1.75}$, which is in reasonable agreement with the neutron scattering experiments $(CaO)_{1.7}(SiO_2)(H_20)_{1.8}$ [4]. The molecular configuration of this model is shown in Fig. 7-2; and its cell parameters and atomic positions are given in the Appendix C.

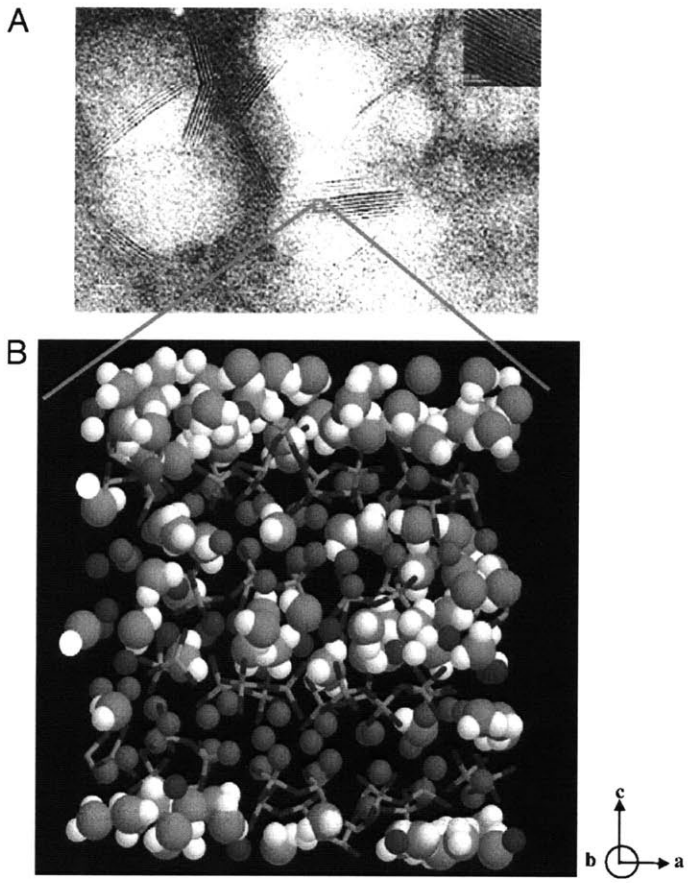

Figure 7-2: (a) TEM image of clusters of C-S-H (courtesy of A. Baronnet, CINaM, CNRS and Marseille Université, France), the inset is a TEM image of tobermorite 14 Å from [136] (b) the molecular model of C-S-H: the blue and white spheres are oxygen and hydrogen atoms of water molecules, respectively; the green and grey spheres are inter and intra-layer calcium ions, respectively; yellow and red sticks are silicon and oxygen atoms in silica tetrahedra.

7.4 Model Validation Against Experiments

7.4.1 Structural Validation Through EXAFS, XRD and IR Measurements

We validated the structure of our model by calculating several experimentally accessible properties. The results, summarized in Fig. 7-3, consist of extended X-ray absorption fine structure (EXAFS) spectroscopy signals measuring short-range order around Ca atoms (Fig. 7-3A), longer range correlations revealed in X-ray diffraction intensity (Fig. 7-3B) and vibrational density of states measured by infrared spectroscopy (Fig. 7-3E).

The various tests provide strong evidence of a short-range structural disorder, the hallmark of a glassy phase. For instance, the simulated and experimental Ca total pair distribution functions as measured in EXASF (Fig. 7-3A), agree well, showing peaks at the same interatomic distances with same relative intensities that allow discriminating C-S-H against all other calcio-silicate crystalline solids [89]. The fact that the first peak in the experimental EXAFS signal is broader than that obtained in simulation suggests that real C-S-H may exhibit an even larger volume fraction of short-range structural disorder. The X-ray diffractogram of our C-S-H model (Fig. 7-3B) clearly indicates the reduced degree of crystallinity as compared with tobermorite.

The suggestion that our C-S-H model can be seen as a glassy phase at short length scales is confirmed by a comparison of the partial pair distribution functions g(r) of our C-S-H model with that of a true non-porous calcio-silicate glass at room temperature with the same Ca/Si ratio and a density of 2.34 g/cm^3 (Fig. 7-3C and 7-3D): the structure of the second peaks in the g(r) for Si-O and Ca-O pairs in tobermorite show characteristic structural features that are absent for both the calcium-silicate glass and our C-S-H model. For the sake of consistency, the Ca-glass and crystalline tobermorite simulations were carried out with the same empirical potential model, with the Ca-glass potential obtained by following the method given in [50]. We may interpret this comparison to indicate that C-S-H should be considered as a glass on the short range of distances associated with the distorted intralayer structure, while retaining some layered crystal features at longer range of distances associated with the interlayer spacing.

The comparison between simulation and experimental infrared spectra (Fig. 7-3E), allows further characterization of our model. Note that calculated infrared intensities were obtained

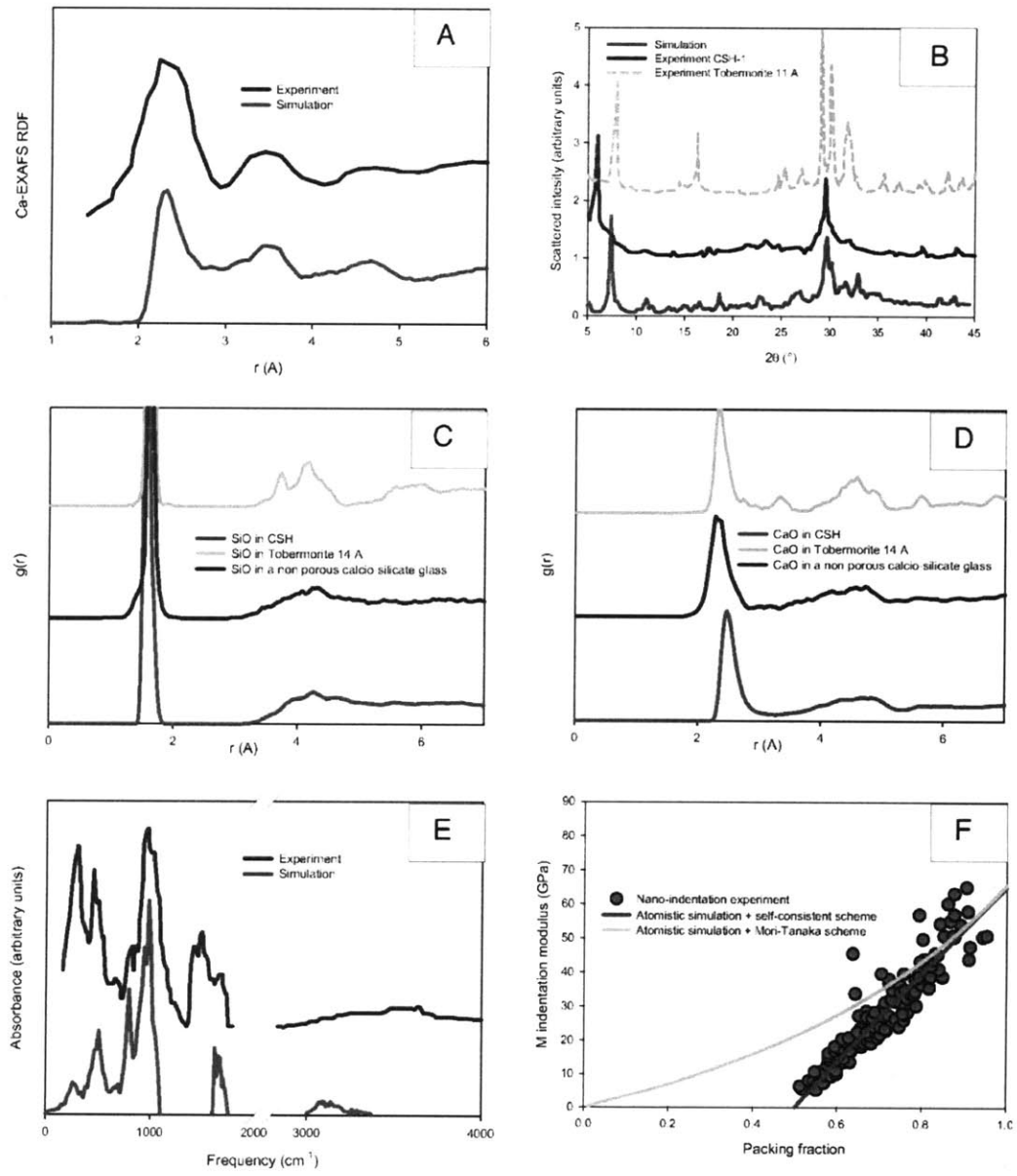

Figure 7-3: Characterization and validation of molecular model of C-S-H. (a) EXAFS Ca-radial distribution function, exp. [89] (phase shift of +0.3 Å, background subtracted); (b) XRD data, exp. [65] for C-S-H and [99] for Tobermorite 14 Å; X-ray diffraction patterns for cCSH are calculated with the CRYSTAL-DIFFRACT code at a wave length of 1.54 Å and an apparatus aperture broadening of 0.4 $Å^{-1}$[179] (c) SiO radial distribution function, comparison with that for a non porous calcio-silicate with Ca/Si=1.6 and with that for Tobermorite 14 Å; (d) idem for the CaO pair; (e) Infrared data, exp. [173]; (f) nanoindentation data, exp. [160], see text.

from the relaxed model C-S-H structure by performing a numerical integration over the sampled phonon modes [37]. All of the experimental bands are present in the calculated spectrum but the ones in the range 1,200–1,500 cm^{-1}; the absence of these bands is not surprising, as these correspond to experimental carbonation effects (Q_3 silicate stretching and vibrational mode of CO_3^{2-} ions) that can be avoided in a computational model.

The first low frequency band in the range 200–350 cm^{-1} corresponds to the vibration of Ca polyhedra including those of other hydration products, namely $Ca(OH)_2$ grains, that nucleate in the mesopores of the real cementitious material, in addition to C-S-H. Since our model only represents the C-S-H, this Ca polyhedra band is present in the model, but not of as high intensity as in experiment, more closely corresponding to that measured for tobermorite [173]. The band in the domain 440–450 cm^{-1} can be attributed to deformations of SiO_4^- tetrahedra. The band in the range 660–670 cm^{-1} is due to Si-O-Si bending while that at 810 and 970 cm^{-1} is attributed to Si-O stretching in silica tetrahedra (Q_1 and Q_2 environments, respectively).

Finally, infrared analysis provides some information on the nature of the water molecules: the band at approximately 1,600 cm^{-1} is characteristic of water H-O-H bending, while that at 3,300 cm^{-1} is attributed to O-H stretching. Interestingly, these band positions are lower than that of bulk liquid (bulk liquid water is also present in the mesopores of C-S-H) and are characteristic of a strong confining environment, as is also suggested from neutron quasi-elastic experiments [41].

7.4.2 Mechanical Validation Through Stiffness and Strength Measurements

We consider mechanical properties of the model C-S-H, computed by stretching the cell dimensions to calculate elastic constants (Tables 7.1 and 7.2) as well as the rupture strength. For a quantitative comparison, we use nanoindentation measurements that probe the stiffness and hardness of nanoscale clusters of randomly oriented C-S-H particles at the micrometer scale (Fig. 7-2), which have been characterized by isotropic stiffness and strength particle properties and particle packing density [27],[160]. Then, using micromechanics-based scaling relations pertaining to granular [59] and porous materials [109], of the indentation elastic modulus, $M = m_s \Pi_M (\eta, \nu)$, and indentation hardness, $H = h_s \Pi_H (\eta, \alpha)$, we correct for the effect of interparticle porosity, via particle packing density, η, and determine the C-S-H particle in-

Elastic properties	
Voigt bulk modulus in GPa	51
Reuss bulk modulus in GPa	47
Voigt shear modulus in GPa	24
Reuss shear modulus in GPa	22
Young modulus along the x-z plane in GPa	66-68
Young modulus along the y direction in GPa	55
Poisson's ratio	0.3
Indentation modulus in GPa	65
Strength in GPa	3

Table 7.1: Elastic Properties

C_{ij} /GPa	1	2	3	4	5	6
1	93.5	45.4	26.1	0.58	-0.05	3.46
2		94.9	30.01	-4.60	1.79	-3.00
3			68.5	-4.32	-2.72	-0.57
4				19.2	0.33	1.82
5					16.1	-0.4
6	Sym					31.2

Table 7.2: Elastic Tensor

dentation modulus, $m_s = E_s/\left(1-\nu_s^2\right)$, and the particle hardness, h_s, (where E_s is the Young's elastic modulus, ν_s is the Poisson's ratio, α is the friction coefficient). The extrapolation is shown in Fig. 7-3F.

The experimental values are in excellent agreement with the ones obtained from our computational C-S-H model, using for the elasticity constants the Reuss-Voigt-Hill average (m_s = 65 GPa, Table 7.1) calculated from the full elasticity tensor (Table 7.2) to compare with the elasticity properties of randomly oriented C-S-H particles; and for hardness the maximum negative isotropic pressure (h_s = 3 GPa, Table 7.1) that precedes rupture of the simulation cell perpendicular to the layer plane. These values are somewhat higher than those for tobermorite 14 Å and jennite, for which m_s = 56 GPa obtained from classical [118] and our *ab initio* plane-wave GGA-DFT calculations (Chapter 4).

This comparison underscores the importance of considering a realistic C-S-H structure for the prediction of elasticity and strength properties of cement-based materials. Moreover, combining the elastic properties determined from our C-S-H model with some micromechanics

models [59], [109] with no adjustable parameters, we can also probe the texture and extent of anisotropic structures within cement paste at micrometer length scales of randomly oriented C-S-H particles. Fig. 7-3F compares the prediction of two micromechanics models along with nano-indentation results; one is a porous bicontinuous matrix approach captured by the so-called Mori-Tanaka scheme [109], and the other a granular approach captured by the self-consistent scheme [59]. From this comparison, we observe first that the granular approach better describes the experimental data over the entire domain of C-S-H particle packing fractions. Second, both approaches give acceptable predictions at larger packing fractions. That is, at the micrometer-scale, Mori-Tanaka and self consistent micromechanics approaches, parameterized only with nanoscale derived elasticity constants, indicate that cement paste can be conceptualized as a cohesive granular material rather than a porous bicontinuous matrix.

7.5 Chapter Summary

In this Chapter, we provided an atomistic-level structural model for C-S-H, developed with the core-shell model and validated against several experimental analyses of structure and properties. By allowing for short silica chains distributed as monomers, dimers, and pentamers, this C-S-H archetype of a molecular description of interacting CaO, SiO_2, and H_2O units provides not only realistic values of the Ca/Si ratio and the density computed by Grand Canonical Monte Carlo simulation of water adsorption at 300 K. Our proposed model, with a chemical composition of $(CaO)_{1.65}(SiO_2)(H_2O)_{1.75}$ and density 2.6 g/cm^3 may serve as the first consistent molecular model of C-S-H, to which one may refer to as the DNA of concrete. Analogous to Watson and Crisk's discovery of DNA, which revolutionized biology, our model can greatly impact the cementitious materials landscape by enabling many opportunities for understanding fundamental deformation mechanisms, diffusive properties, electrical properties and many other characteristic material parameters. In the next Chapter, we show one example of how the concepts and methodologies used in this Chapter help decoding a set of C-S-H molecular phases across different Ca/Si ratios.

Chapter 8

Decoding Molecular C-S-H Phases by CSH-FF

The previous Chapter was focused on a single molecular phase of C-S-H with an average ratio of Ca/Si=1.7. In this Chapter, by leveraging from the efficiency and validated predictive capability of CSH-FF, along with statistical mechanics and a combinatorial approach, we aim to unravel the structure, chemical composition and mechanical features of several non-stoichiometric C-S-H phases spanning from Ca/Si=1.1 to Ca/Si=2.1. We present several physio-chemical properties that vary across C-S-H phases. Under shear computational experiments, we show how mechanical properties such as strength and hardness can be modulated with varying the molecular morphology and chemical composition of C-S-H phases.

8.1 Computational Approach

The computational strategy used in this Chapter is a combination of a combinatorial approach and different atomistic-scale classical simulation techniques including internal energy relaxation, GCMC for water adsorption and NPT/NVT Molecular Dynamics at room temperature. In this Chapter, all these simulations techniques rely on a consistent description of interatomic interactions based on the core-only force field potential, CSH-FF developed in Chapter 6. Such a force field is obviously far less computationally expensive than polarizable (core-shell) force field that have additional degrees of freedom.

While CSH-FF was calibrated based on our DFT results on tobermorite 11 Å (Chapter 4), its predictive capability was tested and confirmed in estimating the structure and elastic properties of a realistic C-S-H, cCSH (Chapter 6 and 7). Compared to tobermorite 11 Å mineral, cCSH can be distinguished by two major features: first, it has 70% larger Ca/Si ratio than tobermorite 11 Å, and second, it has a distorted layered structure composed of silica chains of various lengths (as opposed to infinite chains in tobermorite 11 Å mineral). Hence, we consider cCSH model as a full-scale validation for predictive capability of CSH-FF.

In developing combinatorial C-S-H models, aside from the random nature of the strategy, we use similar computational methods and codes (energy minimization, GCMC and NPT-MD) with identical parameters as presented in the previous Chapter. Note that we did not investigate the effect of temperature and as needed it was set to 300 K. We wrote several scripts to automatize the computational routines.

8.1.1 Combinatorial Model Construction

In the previous Chapter, cCSH was constructed to meet the Q_i valued measured by ^{29}Si NMR experiments on cement pastes, hence cCSH is, in fact, a model equivalent to an average composition of the nonstoichiometic C-S-H gel with Ca/Si=1.7 [4]. In this Chapter, we remove this constraint and aim at achieving various possible chemical compositions of the nonstoichiometric C-S-H across different Ca/Si ratios; thus covering the whole experimental spectrum of energy dispersive X-ray analyses of local Ca/Si ratios spanning from approximately 1.2. to 2.3 with a mean value of 1.7 [56], [131], [135] (see Fig. 8-1). Our approach is similar to what we employed earlier in the previous Chapter, thus we randomly remove SiO_2 entities from an anhydrous supercell of tobermorite 11 Å crystal until we achieve the targeted Ca/Si ratio.

8.1.2 Generating Different Ca/Si ratios

We employ our developed strategy in Chapter 7 to impose a given chemistry in terms of Ca/Si ratio. As for the cCSH initial model, we start from a periodic simulation box of tobermorite 11 Å (Hamid structure, Ca/Si=1) with 2, 3 and 1 units along cell axes a, b and c. At this stage, we considered an anhydrous version of this structure as we were only interested in creating the model itself; the addition of water was carried out at a second stage using Grand Canonical

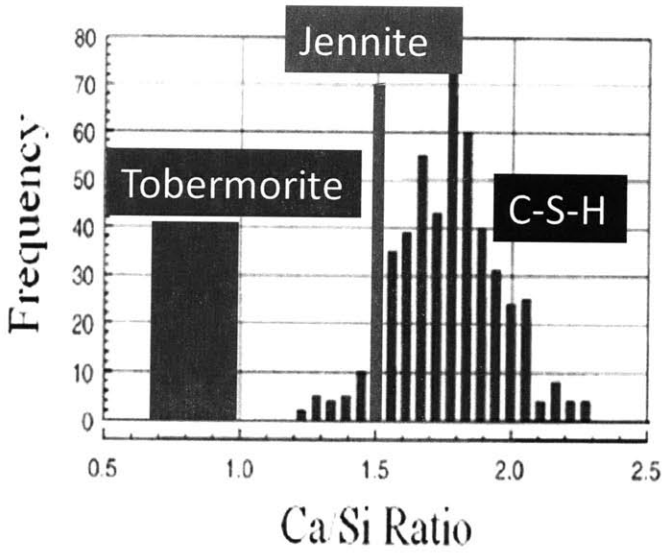

Figure 8-1: Ca/Si ratio frequency histogram in Portland cement pastes, measured by TEM micoanalyses of C-S-H free of admixtures with other phases [135]. For comparison, the Ca/Si ratios for tobermorite minerals and jennite are also shown with wide and narrow rectangular boxes respectively.

$$\begin{pmatrix} 2 & 1 & 1 & 2 & 1 & 1 & 2 & 1 & 1 \\ 2 & 1 & 1 & 2 & 1 & 1 & 2 & 1 & 1 \\ 1 & 2 & 1 & 1 & 2 & 1 & 1 & 2 & 1 \\ 1 & 2 & 1 & 1 & 2 & 1 & 1 & 2 & 1 \\ 1 & 1 & 2 & 1 & 1 & 2 & 1 & 1 & 2 \\ 1 & 1 & 2 & 1 & 1 & 2 & 1 & 1 & 2 \\ 1 & 2 & 1 & 1 & 2 & 1 & 1 & 2 & 1 \\ 1 & 2 & 1 & 1 & 2 & 1 & 1 & 2 & 1 \end{pmatrix}$$

Figure 8-2: The matrix of the backbone structure for a tobermorite crystal.

Monte-Carlo simulation implemented to describe adsorption/desorption processes.

Note that our simulation box is large enough to accommodate silica dimmers, pentamers and even octamers as these types of silica chain are known to be present in real cement paste. One can map out each silica initial infinite chain onto line that contains "1" for non-bridging tetrahedral and "2" for the bridging ones (in tobermorite, both types of silica tetrahedral form a so-called drierketten pattern that in this simple notation writes "-112-". Thus within our periodic simulation box, silica structure of tobermorite writes "–112112112–". Juxtaposing all the eight chains (2 per side of each layer, two layers), we can assemble the Hamid's structure of tobermorite in a matrix shown in Fig. 8-2

Note that for the given considered size of our model (in number of initial unit cells of Hamid's model of tobermorite), it contains 72 silicon species. Implementing a target Ca/Si ratio is achieved through the following steps. First, we developed a simple computer program that uses a random number generator to replace some elements of the above matrix by "0" with the constraint of matching a given Ca/Si ratio (within $\pm$ 0.25) and producing only dimmers "–11–" pentamers "–11211–" and octamers "–11211211–". For instance the "cutting" matrix for a Ca/Si=1.30 is shown in Fig. 8-3

The second step is to realize the combinatorial aspect of the approach as they are many ways to "cut" for a given Ca/Si ratio. In this report, for each Ca/Si ratio, we constructed 10 to 15 different samples. Finally, each "cutting matrix" is automated to be projected onto our

$$\begin{pmatrix} 0 & 1 & 1 & 0 & 1 & 1 & 0 & 1 & 1 \\ 2 & 1 & 1 & 2 & 1 & 1 & 2 & 1 & 1 \\ 1 & 2 & 1 & 1 & 0 & 1 & 1 & 2 & 1 \\ 1 & 0 & 1 & 1 & 2 & 1 & 1 & 0 & 1 \\ 1 & 1 & 0 & 1 & 1 & 0 & 1 & 1 & 0 \\ 1 & 1 & 2 & 1 & 1 & 2 & 1 & 1 & 0 \\ 0 & 0 & 1 & 1 & 0 & 1 & 1 & 0 & 1 \\ 1 & 2 & 1 & 1 & 0 & 0 & 1 & 0 & 1 \end{pmatrix}$$

Figure 8-3: The matrix of a backbone structure for a combinatorial C-S-H with Ca/Si=1.3.

simulation box. Each "0" corresponds to a silicon atom that has to be removed along with two of its neighboring oxygens. Since SiO_2 is a neutral entity, overall system electroneutrality is maintained. We also make sure that the silicons in sites that correspond to the chain ends (or Q_1 in the nomenclature of solid state NMR) have the necessary 4 oxygen neighbors. Figure 8-4 shows a schematic picture of the defected tobermorite along with cavities occurring inside the layers.

8.1.3 Calculation of Shear Strength and Hardness

Before investigating the strength response of combinatorial C-S-H models, all internal degrees of freedom and cell parameters and angles were relaxed using NPT-MD at 300K. Next, in order to predict strength and Hardness, we recourse to the Von-Mises pure solid case, for which $H \simeq 2.8Y$ from comprehensive analysis of conical indentation [49]. Here, H represents Hardness and Y is the uniaxial strength. It can be simply shown that for such Von-Mises solids $Y = \sqrt{3}c^s$ where c^s is the Von-Mises cohesion or the yield stress of the material in pure shear. Hence, to obtain Hardness we simulate the stress-strain behavior of all combinatorial C-S-H polymorphs in affine shear deformation (strain controlled).

A series of shear strains in increments of 0.005 is applied; after each increment the atomic configuration is relaxed at fixed volume by energy minimization and shear stress determined by calculating the derivative of the total energy density with respect to strain. Then c^s is taken

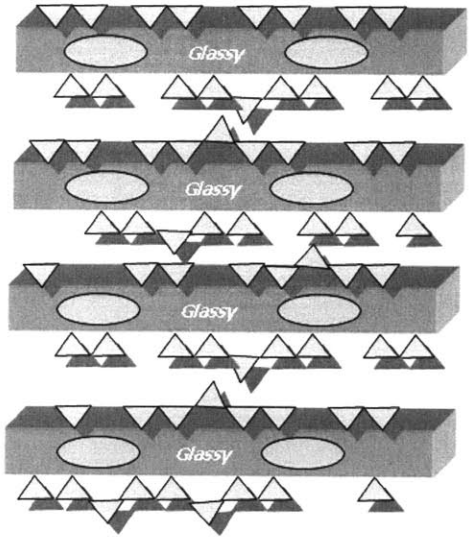

Figure 8-4: A schematic defected supercell of the tobermorite where some bridging silicon tetrahedra (triangles) are removed. Ellipsoid represent cavities inside the tobermorite layers, which arise from the tetrahedra removals.

as the yield stress of the shear stress-strain behavior. On average, each data point representing simulated hardness took about three days involving relaxation and energy minimization.

8.2 Variation of the C-S-H Backbone Structure

By following the above computational methodology, we decoded a variety of C-S-H phases (more than 130 polymorphs[1]) spanning from approximately Ca/Si=1.1 to 2.1. Each C-S-H polymorph creation took about 3-4 days of computational time on a single CPU. Figure 8-5 shows a few of these polymorphs for different Ca/Si ratios. For simplicity we only display the defected silica chains (water molecules and Ca ions are not shown). From the pool of combinatorial C-S-H polymorphs and their corresponding physical and mechanical properties including density, morphology, water contents, total energy, stiffness, and shear strength, a number of different cross-plots can be generated that each represents an interesting trend.

By increasing Ca/Si, more defects appear in the C-S-H structure. In Fig. 8-5, we have

[1]The actual number of attempted polymorphs was much more, however, not all of them converged.

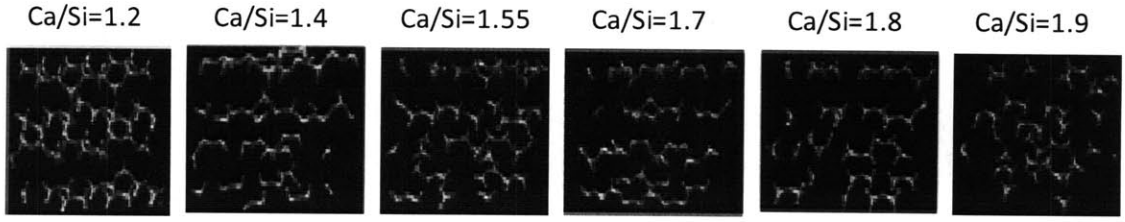

Figure 8-5: Sample combinatorial C-S-H models along with defects for different Ca/Si ratios. The yellow bars represent Si atoms and the red bars indicate Oxygen atoms. For clarity, water molecules and interlayer Ca ions are not shown.

shown a few snapshots of the defected structures. At low Ca/Si (less defects), the 2D backbone structure of the lamella is almost preserved. However, for large Ca/Si (more defects), the removal of several silicon tetrahedra results in changing the 2D layered structure to a (3D) glassy structure. In is interesting to note that more defects creates more empty sites in the (distorted) backbone structure, hence more water molecules can enter into the system.

Thus by increasing the Ca/Si, the density of water per Si atom increases (Fig 8-6a), which is consistent with the concept that each SiO_2 occupies the volume of approximately two H_2O molecules. This trend generally results in shrinking the interlayer distance (in which the water molecules and interlayer Ca ions are mostly located), hence increasing the density (Fig 8-6b and Fig 8-6c) due to the competence of several chemical interactions inside each single distorted C-S-H structure to find the minimum overall energy. Figure 8-6d compares the total energy of each unit cell normalized by their volume as a function of Ca/Si. In this figure, it appears that for a given Ca/Si ratio, there are concurrently different C-S-H polymorphs that are structurally equilibrated. This hints toward the presence of different stable morphologies (hereafter called C-S-H polymorphs) at a given composition, which are energetically distinct and competitive.

8.3 Modulation of Mechanical Properties of Combinatorial C-S-H Phases

Besides our DFT study in Chapter 4, there are scarce MD simulations of the elastic properties of distinct mineral analog phases of C-S-H such as tobermorite family and jennite as a function of

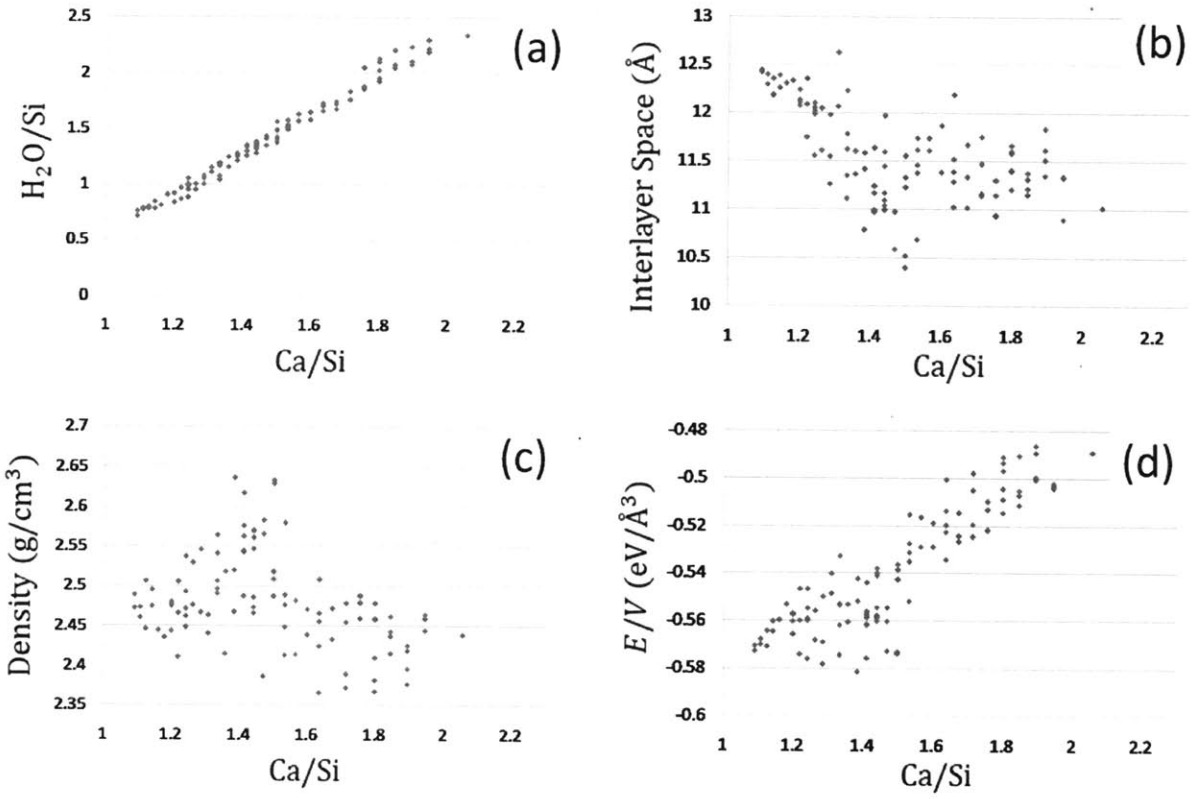

Figure 8-6: Effect of Ca/Si on a few physical properties of combinatortial C-S-H structures. (a) The number of water molecules per Si atom, (b) The interlayer spacing between adjacent C-S-H layers, (c) Density of the unit cell, (d) Total energy per volume in a final equilibrated unit cell.

Ca/Si [52],[96],[118],[119]. These studies are based on mineral phases that although seemingly are similar to C-S-H, whose backbone structures are significantly different within themselves and also from that of the C-S-H gel. Here, we show a set of attainable mechanical properties as a function of Ca/Si ratio within a fixed chemical framework (i.e. tobermorite supercell), in which all structures have similar backbone layers and interlayer distances.

Following the methods presented in Chapter 7, analyses of various cell deformations relates to VRH approximation for bulk modulus and shear modulus, which both are linked to in-plane stiffness, indentation modulus, M. Hardness values are predicted using shear stress-strain plots. Figure 8-7 shows how these two mechanical parameters, indentation modulus and hardness, varies as a function of Ca/Si. From these plots, it turns out that there are significant changes in mechanical properties as a function of defects or structural changes discussed in Fig. 8-6:

First, we note that the factor Ca/Si has a significant effect on stiffness and strength properties which can be up to 100%. This is particularly the case for structures with low Ca/Si, which in general show higher stiffness than those with larger Ca/Si ratios. Hardness shows a slightly wider spectrum as a function of Ca/Si. Thus as expected and analogous to many other compounds and alloys, the chemical specificity of a C-S-H system plays a major role in defining mechanical properties.

Second, in contrast to common intuition, the existence of different polymorphs at a given Ca/Si, results in significant variation in stiffness and strength properties of C-S-H systems. Thus it appears besides the chemical composition, there is another important degree of freedom, molecular morphology, which similarly has a profound effect on mechanical properties of C-S-H phases. For instance for Ca/Si=1.8, we note how stiffness and hardness varies between approximately 52-75 GPa and 3-7 GPa, respectively.

Thus, in summary, in view of Fig. 8-6 and Fig. 8-7 we showed by means of a combinatorial computational methodology, how Ca/Si ratio and molecular morphology as two controlling parameters can affect the structural disorder and hence mechanical properties of C-S-H phases. In what follows, we validate our predictions by chemomechanical characterization of real cement paste samples.

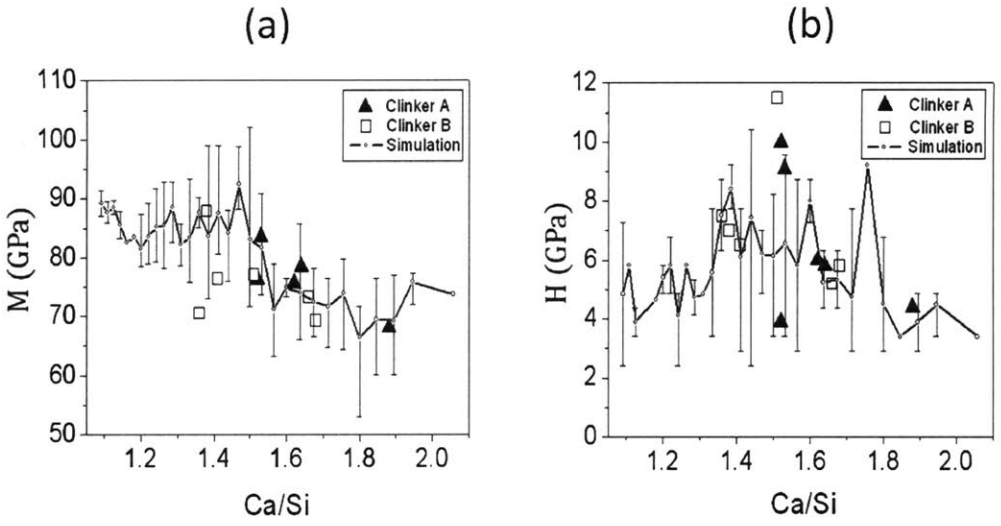

Figure 8-7: Comparison of experiments and simulations. a) Indentation modulus, M. Experimental indentation modulus data extrapolated to η=1 closely matches the average of several possible polymorphs of C-S-H from simulation data at each Ca/Si ratio. b) Indentation hardness, H. Hardness values predicted by computational shear experiments are in agreement with the experimental hardness data extrapolated to η=1. Solid blue lines represent the average M or H value of all the polymorphs. Error bars here indicate the maximum and minimum values at each Ca/Si. Some of the samples only had one data point and therefore have no data range. [Experimental data courtesy of Dr. Karen Stewart and Prof. Krystyn van Vleit, MIT].

8.4 Chemomechanical Validation of Combinatorial C-S-H Phases

Synthesized cement paste samples include two different clinkers, different additives, and different water:cement (w/c) ratios[2]. Clinker A is comprised of 65.3% C_3S, 13.5% C_2S, 7.1% C_3A and 8.6% C_4AF while clinker B is comprised of 6.3% C_3S, 71.2% C_2S, 9.1% C_3A and 11% C_4AF. With the exception of A2 and B2 (w/c = 0.4), all cement pastes have w/c = 0.3 using 100 g of cement. All cement paste samples contained 5 wt % gypsum and 95 wt % clinker. The 12 pastes were cured for 28 days at 20°C and 98% relative humidity.

After curing, the cement paste samples were prepared for *in situ* mechanical characterization (via nanoindentation) and chemical characterization (via Wavelength Dispersive X-ray Spectroscopy, WDS). Mechanical samples were sectioned with a diamond saw into slices of 15 mm x

[2]All experiments and characterizations in this Section are performed by Dr. Stewart and Prof. van Vliet at the Department of Material Science and Engineering of MIT.

Sample	Ca/Si	M (GPa)	H (GPa)
B3	1.36	70.5	7.5
B6	1.38	87.9	7
B4	1.41	76.4	6.5
B5	1.51	77.1	11.5
A5	1.52	76.4	10
A6	1.52	92.7	3.9
A4	1.53	83.6	9.1
A1	1.62	75.7	6
A3	1.64	78.5	5.8
B1	1.66	73.3	5.2
B2	1.68	69.3	5.8
A2	1.88	68.1	4.4

Table 8.1: Details of each cement paste sample and the corresponding Ca/Si ratio, extrapolated indentation modulus and hardness [Experimental data courtesy of Dr. Karen Stewart and Prof. Krystyn van Vleit, MIT].

5 mm x 5 mm thickness. Chemical samples from the same cured cement pasted were sectioned into 5 mm x 5 mm x 3 mm thickness; this smaller size reduced the time required for vacuum pumping within the WDS chamber. All samples were polished using silicon carbide sandpaper of decreasing grits (500, 1200, and 4000) in air, and cleaned within each polishing step via high pressure air flow. A final polish was employed via a diamond impregnated polishing pad of <1 μm grit diameter, to achieve a mirror-like finish on the cement sample surface.

The detailed procedure in nanoindentation experiments on porous cement paste samples is similar to the method presented in [27] and [163], and the values of M and H for fully dense C-S-H solids (i.e. packing density, η=1) was calculated from extrapolating packing density plots to η=1. The determination of Ca/Si and the chemical composition were performed using WDS by collecting 400 data points on each of the samples with 15 kV accelerating voltage. More details on the techniques and procedures used in both nanoindentation and WDS experiments on these cement paste samples will be published elsewhere [150]. The parameters for each samples is given in Table 8.1.

From the comparison of the experimental chemomechanical characterizations of cement paste samples with mechanical properties of combinatorial C-S-H phases (Fig. 8-7), it turns out that there is an excellent agreement between the two results. Thus confirming our earlier predictive approach in modulating cement hydrate via chemical composition and molecular

morphology. Here, two of the clinker B samples do not match with the simulation plot for indentation modulus. Clinker B samples may be flawed in that they are comprised of C_2S which needs a longer period of curing to reach hydration levels similar to C_3S, which were typically more porous.

Another reason for why some of the B samples do not match simulation is due to the fact that our combinatorial C-S-H models are developed based on a framework (tobermorite 11 Å, Hamid structure) whose precursors are validated and obtained from typical industrial samples, which are based on primarily C_3S clinkers. C_3S and C_2S have different crystal structures and therefore their clinker dissociation in water and eventual precipitation may result in different C-S-H products. Thus one may not expect a satisfactory match to B clinkers. Also, our models are comprised of only Ca and Si, and water whereas these real cement paste samples have various degrees of additives/impurities especially Na substitution.

8.4.1 Is the stiffest C-S-H polymorph the hardest ?

One interesting aspect of the mechanical properties of C-S-H is whether the stiffness polymorphs is the hardest polymorph ? This is important because if the stiffest is the hardest, then there is not much room for ductility; hence indicating very brittle behavior of C-S-H. This may not be appealing in terms of energy dissipation that is usually a concern in code designs. Figure 8-8 shows for simulated molecular C-S-H phase, hardness do not linearly increase with stiffness. For comparison, experimental values for clinker A and B are also shown, which together with simulation results indicate that the stiffest polymorphs are not the hardness. Hence, C-S-H shows ductility at the nano-scale. However, this is not the case at the higher hierarchical scales as other parameters such as porosity, materials boundary mismatch and sliding limit the ductility regime.

In view of Fig. 8-7, simulation data are denoted as a weighted average of each mechanical property at a given composition, which relates implicitly to the relative energy of each C-S-H polymorph. Figure 8-6d shows this total energy/volume of C-S-H varies over a narrow range for each Ca/Si. In other words, C-S-H polymorphs are energetically distinct. Interestingly, Fig. 8-6d indicates that C-S-H phase stability generally increases with decreasing Ca/Si; as expected, the crystalline tobermorite phase at low extreme approaching Ca/Si = 1 is most

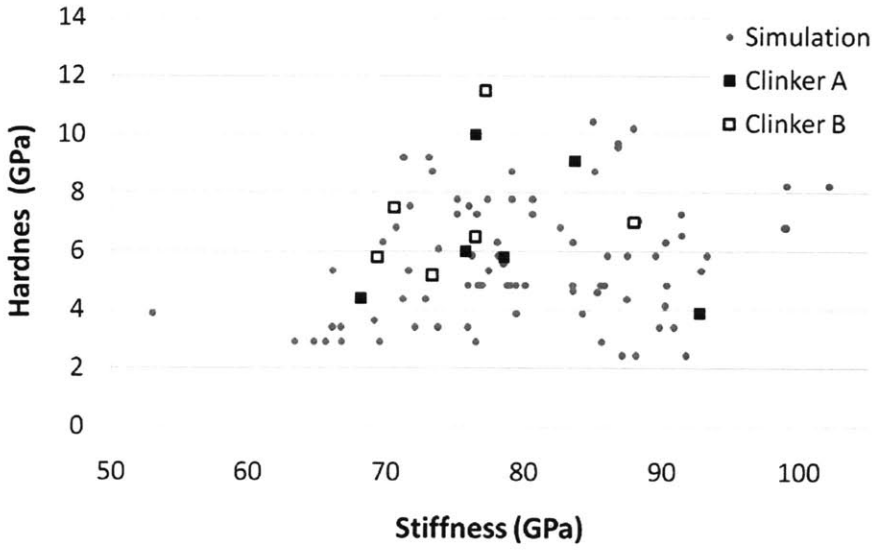

Figure 8-8: Hardness versus stiffness for C-S-H.

stable. Relevant to this notion, Fig. 8-9 cross-plots the total energy per atom and the elastic moduli and hardness of the C-S-H phases. From Fig 8-9a, it appears that by increasing the Ca/Si ratio (moving up), the stiffness and stability decrease (moving left and up respectively), whereas there is no correlation between stability and hardness. Further, for a polymorph family of a fixed composition, there is no correlation between the polymorph phase energy and these mechanical properties, hence these structures are being energetically competitive. Therefore, modulating to stiffer or harder phases cannot be achieved only by chemistry and relative phase stability, but may need altered reaction kinetics.

Considering the unsettled nature of C-S-H nucleation in actual cement pastes containing impurities that are unaccounted for in our current simulations, satisfactory level of agreement was found between experiments and simulations to validate our computational approach. Our results underscore potential to optimize stiffness and strength attainable via the modulating Ca/Si ratio of C-S-H.

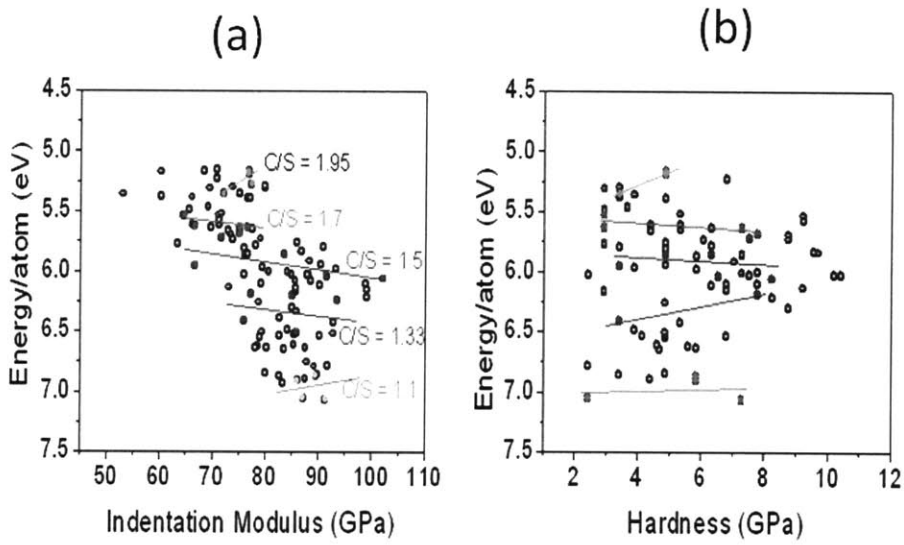

Figure 8-9: Relationship betweem the energy and mechanical properties a) Energy per atom decreases with an increase in indentation modulus. However, all polymorph family of a fixed composition are energetically very competitive. b) There is no correlation between energy per atom and the hardness of the C-S-H polymorph.

8.5 Hydraulic Shear Response

Probing atomic-level mechanisms to gain insights into structural deformation and failure at larger length scales is currently a central issue in the development of nanomechanics of hard crystalline materials [151],[176]. The formulation of molecular models of C-S-H presents an opportunity to initiate similar investigations of cementitious materials, thereby opening up a class of microstructures with unique chemistry-rich and spatially heterogeneous characteristics. A fundamental question common to all systems is the nucleation and evolution of a "unit process" in the constitutive response to tensile and shear loading, and the effects of specimen size, temperature, and strain-rate dependence.

In order to investigate the deformation and fracture mechanisms of the highly anisotropic C-S-H models, the uniaxial properties such as stiffness and strength may not provide a good reliable results. But shear deformation would engage more atomistic degrees of freedom, hence better representing the complex behavior of anisotropic C-S-H models. While we have simulated the shear stress-strain behavior of all combinatorial C-S-H models, in what follows, we focus

on a representative C-S-H model with Ca/Si=1.65 and elucidate the common characteristics of combinatorial C-S-H models such as deformation mechanisms and atomistic strength features.

8.5.1 Strength-Controlling Shear Localization

Here, we zoom at cCSH, as the most representative C-S-H model and discuss the shear stress-strain curves of both hydrated cCSH as well as a "dry" version of this model in which all water molecules have been removed (Fig. 8-10). The responses in both cases are a sequence of elastic loading under incremental strain, interspersed with discrete stress drops reminiscent of strain localization events. This type of intermittent or saw-tooth behavior is typical in all combinatorial C-S-H models and has been observed in deformation simulation of metallic glasses [7], glassy polymers [111] as well as nanoindentation-induced dislocation nucleation [90].

Here, we will discuss the first two stress drops in each response curve. These occur at stresses between 2.5 to 3 GPa in the dry sample and approximately 1 GPa in the hydrated sample; these values are lower than the ideal shear strength, or about 10% of the shear elastic modulus, due to the defected microstructure of this C-S-H phase. Moreover, it is not surprising that the presence of water lowers the strength.

On the other hand, inspection of Fig. 8-10a indicates a significant difference between the two response curves. If we take the elastic loading portion of the response after the first drop and extrapolate back to zero stress, we find a significant "residual" strain of approximately 0.1 in the dry sample, an indication of irreversible deformation associated with the first drop. In contrast, in the hydrated sample unloading after the first drop indicates essentially no residual strain, which suggests the deformation to be largely elastic. To observe the atomic displacements that correspond to these stress drops, we display in Fig. 8-10b the largest individual displacements associated with the four stress drops in Fig. 8-10a.

It is clear that in the dry sample local strains are distributed across the cell, with a slight degree of strain concentration within the layers rather than in the interlayer region, especially at stage (d). It is also quite clear that in the hydrated sample the strains are localized entirely in the interlayer region and are mostly associated with displacements of water molecules. Combining these observations with the characteristics of the stress-strain response in Fig. 8-10a we can conclude that the shear response of the C-S-H model is strain localization in the interlayer

region; this localization occurs in the form of sliding, ostensibly facilitated by the lubricating action of the water molecules. In the absence of water, strain localization appears to manifest as individual events of irreversible deformation.

The present results demonstrate the potential to gain insights into the effects of water on the deformation behavior of the C-S-H particle. This problem bears some analogy to the phenomenon of "hydrolytic weakening" in other crystalline and glassy silicates, where it is believed that hydration causes more than a five-fold reduction in the compressive strength of α-quartz [54].

8.6 Density as a Unified Parameter Governing Stiffness in C-S-H Phases

Classifying C-S-H mechanical properties under a single controlling parameter is a controversial subject. There are various experimental and computational results quantifying C-S-H stiffness as a function of several parameters including Ca/Si, w/Ca and so on. However, these results in many cases don't match with each other and even in some cases they clearly contradict the general pattern of each other! Our pool of combinatorial C-S-H models constructed under an unified computational umbrella by means of a bottom-up approach originating from DFT calculations provides a reliable and consistent databank to clarify many common ambiguities found in the literature.

While various cross-plots representing the combinatorial C-S-H data are possible, here we show the results of our investigation on the in-plane stiffness or indentation modulus M, which linearly scales with the density. This bears some analogy with the packing of C-S-H granular particles inside the porous matrix of a cement paste [27]. However, in this case the packing pattern occurs inside a single C-S-H particle with a fixed size by rearrangement of the atomistic species in favor of the minimum internal energy, hence most stability and stiffness.

8.7 Chapter Summary

In this Chapter, by leveraging from the computational efficiency of CSH-FF potential along with its unique capability of predicting structural and mechanical properties of the C-S-H family,

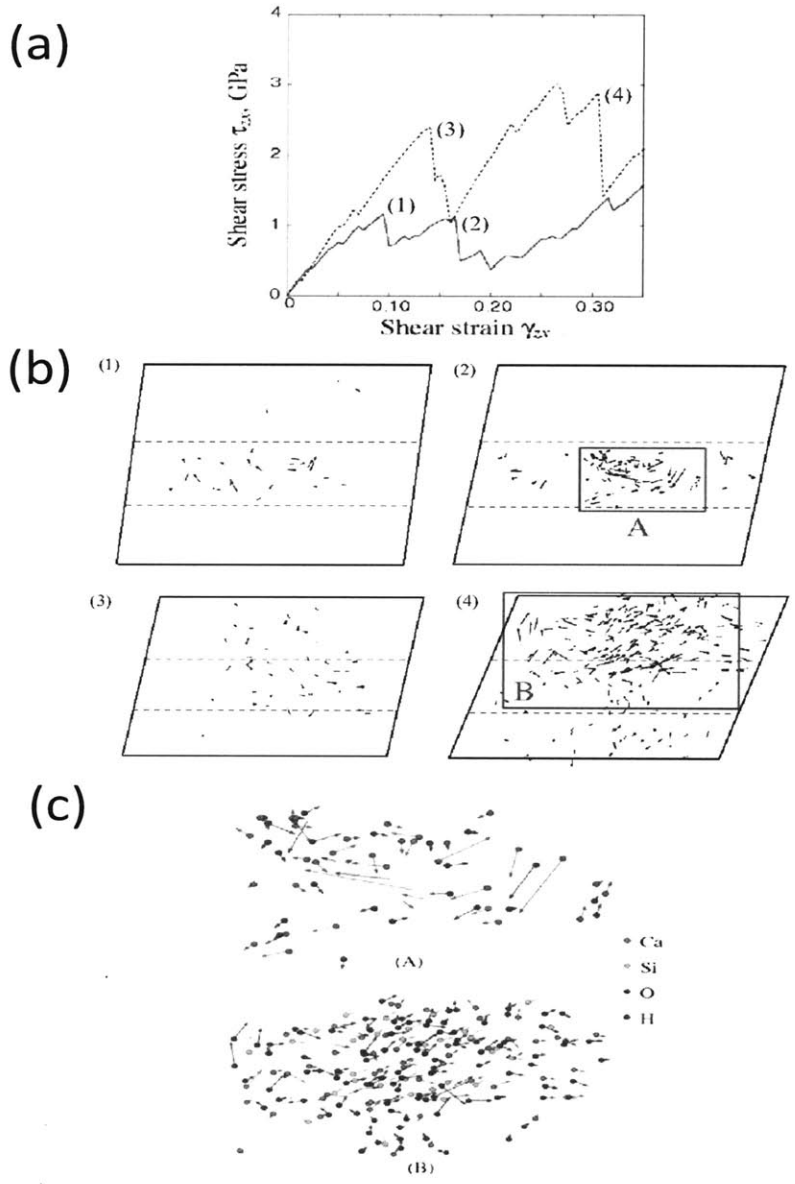

Figure 8-10: (a) Relationships between the shear stress τ_{zx} and the strain γ_{zx} for the cCSH model with (solid line) and without (dashed line) water molecules. (B) Atom displacements at the stress drops (1)–(4) in panel (a). Only atoms with displacement larger than 0.5 Å are shown, and the arrows indicate the displacements. Dashed lines correspond to the C-S-H layers. (c) Magnified view of regions (A) and (B) that are marked as red boxes in panel (b).

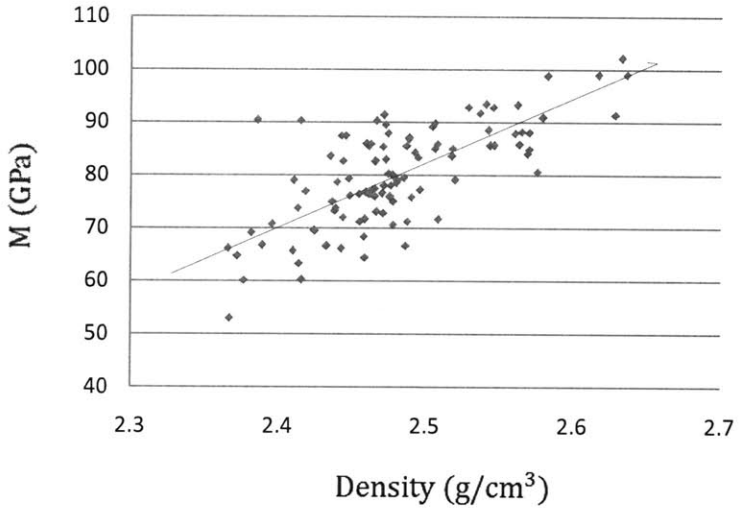

Figure 8-11: This figure shows how indentation modulus, M, of C-S-H models scales linearly with density.

we built an immense spectrum of C-S-H polymorphs spanning from approximately Ca/Si=1.1 to 2.1, hence covering all local values of experimental Ca/Si ratios. Our results were based on a combinatorial approach tailored to statistical mechanics to unravel the structure and morphology of more than 130 C-S-H atomistic models with realistic mechanical properties.

We showed the removal of SiO_2 units distorts the layered C-S-H structures by creation of defects (cavities), which may serve as a host for water molecules, hence shrinking the interlayer space and increasing the density. By analyses of deformation of C-S-H models, we showed mechanical properties such as stiffness and hardness vary significantly as a function of composition and molecular morphology. The trend and the magnitude of our computational predictions are in perfect agreements with experimental results of chemomechanical characterization of real cement paste samples. This demonstrates that CSH-FF is a powerful predictive potential for directing chemistry to achieve targeted mechanical properties.

From hundreds of affine shear tests, it was predicted that the hardness can significantly vary (up to 100%) by lowering the Ca/Si. Moreover, we showed that the stiffest C-S-H polymorphs are not the hardest polymorphs, hence suggesting a ductile behavior for the C-S-H at the

nano-scale. Finally, post-analyzing the pool of combinatorial C-S-H models, enabled us to draw the conclusion that under similar chemical conditions, the density is the unified governing parameter controlling stiffness; simply the denser, the stiffer. In the next Part, we summarize all the results of this thesis and suggest some future directions towards building the C-S-H mesotexture at the next higher scale.

Part V

Conclusions

Chapter 9

Summary of Results and Perspectives

The ultimate goal of this study was the implementation of the shift of paradigms in computational materials science for cement-based materials, that is, the bottom-up multi-scale approach to unravel the link between structure, composition and mechanical properties of cement hydrate across different scales. This Chapter presents a summary of this implementation for the C-S-H gel. Based on findings and contributions some future research is proposed.

9.1 Summary of Main Contributions

This research led the following scientific findings and contributions about the hierarchical structure of the non-stoichiometric C-S-H gel and its link with mechanical properties:

- Structure and mechanical properties of several mineral analogs of C-S-H gel are characterized based on DFT calculations. This provides the first ever benchmark DFT calculations on the C-S-H crystalline models. In contrast to common intuition that layered materials are soft in the interlayer direction, a class of hydrated oxides, C-S-H crystals, were shown that this is not the case. The reason lies in the strong coulombic interactions between the charged lamella, which become comparable to iono-covalent intalayer chemical interactions. The former interactions becomes important at interlayer distances of 11 Å and

9 Å, which lead to new (hinge-type) deformation mechanisms within the crystals affecting both elastic and strength/fracture properties.

- Using acoustic tensor analyses, fundamental wave velocities and particle-motion directions are obtained for C-S-H crystals in any random directions. This information hints towards identifying critical softest and stiffest planes in lattice structures, and assessing the stability of each crystal as a whole cluster in 3D space. Based on these findings, a novel statistical method is derived to average the bulk and shear moduli (K, G) for anisotropic materials. This simple averaging method is superior than the classic averaging schemes in mechanics such as Voigt-Reuss-Hill approach or Molinary approach in that i) it considers all the 21 elastic components of an anisotropic material, ii) it is frame-indifference (objective) meaning that it is invariant under any random transformation of the coordinates system, and iii) it is a physically perceivable method as it clearly shows the contributions of the softest and/or stiffest regions.

- A systematic methodology for comparison of empirical force fields is presented, which shows that in regards to transferability of empirical force fields, second order properties such as elasticity are of crucial importance. For a particular case of C-S-H systems, ClayFF model predictions proved to be computationally faster but less reliable than the core-shell model. To avoid the shortfalls of ClayFF, a new force-field potential, CSH-FF, is developed that is well customized and substantiated for the C-S-H family. This re-parametrized version of ClayFF potential is based on core-only representation and includes both structural data and full elasticity tensor from DFT calculations to parametrize the potential functional forms.

- The efficiency and the validated predictive capability of CSH-FF potential in conjunction with the statistical mechanics enabled decoding the structure and molecular morphology of series of molecular C-S-H models. Our simulation results predict a range of C-S-H compositions and corresponding mechanical properties that are consistent with real cement paste samples. Upon applying hundreds of affine shear deformations to these molecular models, it was shown that the hardness can significantly vary (up to 100%) by lowering the Ca/Si. Moreover, it was predicted that the stiffest C-S-H polymorphs are

not the hardest polymorphs, hence suggesting a ductile behavior for the C-S-H at the nano-scale. Together, these findings and developments set up a modeling toolbox that allows improving cement core properties with a predictive computational design strategy.

9.2 Industrial Benefit

Since concrete is ubiquitous material, scientific contributions have a potential for great industrial benefits. The new CSH-FF potential in conjunction with the statistical physics enabled decoding a variety of C-S-H phases at the molecular level. The investigation of strength properties of these molecular C-S-H phases shows that it is possible to lessen the Ca/Si ratio to achieve nano level C-S-H phases with much higher strengths. The benefit of this is threefold: i) low Ca/Si ratio can reduce the energy consumption and CO_2 footprint of cement, ii) in addition to (i) higher strength requires less volume for construction, hence cement manufacturers save energy and release less CO_2, iii) end-users can have more efficient, streamlined structures.

9.3 Perspectives for Future Research

The CSH-FF potential was developed based on fitting to DFT data at 0 K. Although k_bT was shown to have negligible effects in predicting lattice parameters and bond distances, it is necessary to rigorously analyze the effect of temperature on higher order properties such as elastic constants (which pertains to the curvature of binding energies) and strength/fracture properties. This issue is crucial for force field development especially for C-S-H since most of its functionality is based on its mechanical performances at room temperature.

All MD simulations in this work were based on nonreactive force field potentials. Simulations of water-silica interactions have identified three distinct competing mechanisms in the water attack on the siloxane bridging bond, Si-O-Si [177]. Considerations of this mechanism in regards to (un)confined water in C-S-H gel, and also other reactive processes that may happen under shear and stretch need to be explained via either first-principles MD studies or reactive force fields.

This thesis provided an atomistic modeling framework to build several molecular C-S-H models. These models together represent the solid phase of the C-S-H gel as infinite matrices

with variable Ca/Si ratios. It is possible to bridge these infinite matrices to the C-S-H meso-texture for a hardened cement hydrate. Under pulling computational experiments, one can identify the uniaxial strength boundaries of the C-S-H mediums along each of the X, Y and Z directions. These strength boundaries mechanistically define C-S-H particles as encapsuled volumes surrounded by the larger periodic cells. With distinct compositions and/or internal molecular morphologies, these particles form the C-S-H mesotexture, which can be simulated using Monte Carlo method and coarse-grain modeling. The parameters of this coarse-graining are crucial in determining any mesotexture properties, and can be obtained based on all-atom MD simulation of C-S-H particles interacting in a water solution via CSH-FF potential. To provide representative averaged functionals for coarse-grain modeling, all-atom MD simulation are necessary for several pair-particles in various orientations. This coarse graining rooted in MD, which is subsequently rooted in DFT calculations, will present a modeling path that on one end relates to electronic and nuclear properties at the atomistic scale, and on the other end can be directly tested with typical laboratory measurements on C-S-H samples; hence providing a bottom-up approach from electrons to the C-S-H mesotexture.

To summarize, concrete as the king of construction materials continues to be the world's dominating manufacturing materials on the future horizon. There is an urgency to curb its energy consumption and environmental footprint for a sustainable progress of our societies. However, for such a heterogenous multi-physics material, there are several scientific enigma to suppress concrete footprint and improve its core properties. This study suggests that the shift of paradigms in materials from macro to nano is now ripe to rethink concrete as an assembly of atoms that build cement paste and bulk concrete at other end. Our bottom-up computational techniques showed that intelligently tuning materials chemistry at the nanoscale can result in improved strength and ultimately less carbon footprint. Given the global potential impact of such an approach and the complexity of the material in hand, we hope that this study will incite consideration of predictive atomistic modeling as the next frontier in construction material design and other complex materials such as colloids, protein gels, and nanocomposites.

Appendix A

Interaction Parameters of ClayFF and Core-shell Potentials

Bond species	k_1 (eV Å^{-2})	R_0 (Å)
Hw-Ow-Hw	48.0574	1
Oh-Ho	48.0574	1

Table A.1: Bonded species potential parameters for harmonic terms (ClayFF).

Angle species	k_2 (eV Rad^{-2})	θ_0 (deg)
Ow-Hw	3.9694	109.47
Oh-Ca-Ho	3.9694	109.47

Table A.2: Three-body potential parameters for harmonic terms (ClayFF).

		R_{ij} (Å)	D_{ij} (eV)
Ca	Oh	4.898	3.83E-05
Ca	Ow	4.898	3.83E-05
Ca	O	4.898	3.83E-05

Table A.3: Non-bonded Lennard Jones parameters for different oxygens and Ca (ClayFF).

		R_{ij} (Å)	D_{ij} (eV)
Si	Oh	3.6298	2.32E-05
Si	O	3.6298	2.32E-05
Si	Ow	3.6298	2.32E-05

Table A.4: Non-bonded Lennard Jones parameters for different oxygens and Si (ClayFF).

		R_{ij} (Å)	D_{ij} (eV)
Ow	Ow	3.5532	0.00673854
Ow	Oh	3.5532	0.00673854
Ow	O	3.5532	0.00673854
O	O	3.5532	0.1554
O	Oh	3.5532	0.1554
Oh	Oh	3.5532	0.1554

Table A.5: Non-bonded Lennard Jones parameters for different oxygens (ClayFF).

		R_{ij} (Å)	D_{ij} (eV)
Ca	Ca	6.2428	2.18E-07
Si	Si	3.7064	7.98E-08
Ca	Si	4.9746	1.32E-07

Table A.6: Non-bonded Lennard Jones parameters for calcium and silicon (ClayFF).

Form	Inter/intra	species 1	species 2	A (eV)	ρ (Å)	C_6 (eV Å^6)	R_{min}(Å)	R_{max}(Å)
Buck	inter	Ca core	O shell	1090.4	0.343	0	0	12
Buck	inter	Ca core	Oh shell	777.27	0.343	0	0	12
Buck	inter	Si core	O shell	1283.9	0.320	10.66158	0	12
Buck	inter	Si core	Oh shell	983.5	0.320	10.66158	0	12
Buck	inter	O shell	O shell	22764	0.149	27.879	0	12
Buck	inter	O shell	Oh shell	22764	0.149	13.94	0	12
Buck	inter	Oh shell	Oh shell	22764	0.149	6.97	0	12
Buck	inter	H core	O shell	311.97	0.25	0	0	12

Table A.7: short range interaction parameters for tobermorite (core-shell model).

Form	Inter/intra	species 1	species 2	D (eV)	α (Å^{-1})	R_0(Å)	R_{min}(Å)	R_{max}(Å)
Morse	inter	H core	Oh shell	7.0525	3.1749	0.9428	1	1.4

Table A.8: short range interaction parameters for tobermorite (core-shell model).

Form	inter	species 1	species 2	species 3	K_2(eVRad^{-2})	θ_0(deg)	R_{min}^{1-2}	R_{max}^{1-3}	R_{max}^{2-3}
Three	inter	Si core	O shell	O shell	2.0972	109.47	1.8 Å	1.8 Å	3.2 Å
Three	inter	Si core	O shell	Oh shell	2.0972	109.47	1.8 Å	1.8 Å	3.2 Å

Table A.9: short range interaction parameters for tobermorite (core-shell model).

Form	Inter/intra	species 1	species 2	A (eV)	ρ (Å)	C_6 (eV Å^6)	R_{min} (Å)	R_{max} (Å)
Buck	inter	Cw core	Ow shell	777.27	0.343	0	0	12

Table A.10: short range interaction parameters for water and interlayer Ca (core-shell model).

Form	Inter/intra	species 1	species 2	A (eV)	ρ (Å)	C_6 (eV Å^6)	R_{min} (Å)	R_{max} (Å)
Buck	inter	Cw core	O shell	1090.4	0.343	0	0	12
Buck	inter	Cw core	Oh shell	1090.4	0.343	0	0	12

Table A.11: short range interaction parameters for oxygen and interlayer Ca (core-shell model).

Form	inter	species 1	species 2	A (eV)	B (Å)	R_{min}	R_{max}		
Lennard	inter	Ow shell	Ow shell	39344.9	42.15	0	12 Å		
Form	inter	species 1	species 2	A (eV)	ρ (Å)	C_6	R_{min}	R_{max}	
Buck	inter	Hw core	Ow shell	396.27	0.25	0	0	12 Å	
Form	inter	species 1	species 2	D (eV)	α (Å^{-1})	R_0	R_{min}	R_{max}	
Morse	intra	Hw core	Ow shell	6.2033	2.22003	0.92 Å	1 Å	1.4 Å	
Form	Inter	species 1	species 2	species 3	K_2	θ_0(deg)	R_{min}^{1-2}	R_{max}^{1-3}	R_{max}^{2-3}
Three	intra	Ow shell	Hw core	Hw core	4.1 eV/rad^2	108.69	1.2 Å	1.2 Å	1.8 Å

Table A.12: short range interaction parameters for water molecules (core-shell model).

Form	Inter/intra	species 1	species 2	A (eV)	ρ (Å)	C_6 (eV Å^6)	R_{min}(Å)	R_{max}(Å)
Buck	inter	Ca core	Ow shell	777.27	0.34	0	0	12
Buck	inter	Si core	Ow shell	983.55	0.32	10.66158	0	12
Buck	inter	H core	Ow shell	311.97	0.25	0	0	12
Buck	inter	O shell	Ow shell	22764	0.14	13.94	0	12
Buck	inter	Oh shell	Ow shell	22764	0.14	6.97	0	12
Buck	inter	O shell	Hw core	311.97	0.25	0	0	12
Buck	inter	Oh shell	Hw core	311.97	0.25	0	0	12

Table A.13: short range interaction parameters for water molecule and tobermorite (core-shell model).

Appendix B

Developed In-House Codes

B.1 Matlab Code to Develop A New Averaging Scheme for (K, G) and 3D Visualizations of Directional Wavespeeds and Eigenvectors

```
function Averaging

    whitebg('w')
    clc
    % options = optimset('LargeScale','off');
    clay=load('clay.txt'); %case -1
    port=load('port.txt'); %case 0
    A9=load('9A.txt'); %case 1
    Mer11=load('11AMer.txt'); %case2
    CS6=load('CS.6.txt'); %case3
    CS8=load('CS.8.txt'); %case4
    CSDFT=load('CS1.txt'); %case5
    CS1F=load('CS1-ClayFF.txt'); %case5
    CS1C=load('CS1-CoreShell.txt'); %case5
    CS1FF=load('CSH-FF.txt'); %case5
    A14=load('14A.txt'); %case6
    A14F=load('14A-ClayFF.txt'); %case6
    A14C=load('14A-CoreShell.txt'); %case6
    A14FF=load('14ACSH-FF.txt'); %case6
    Jen=load('iso'); %case7
    %%%%%%%%%%%%%%%% choosing CSH type
    p=6;
    pp=0;
    ww=1;
    function waves(pp)
    if pp >2
```

```
ww=3;
end
switch p
case -1
x=clay;
ro=2700;
coef=1.7;
V1=coef*[0.99238769 0 0];
V2=coef*[-0.496193845      0.859431288      0];
V3=coef*[0      0      1.346973585];
case 0
x=port;
ro=2230;
coef=1.7;
V1=coef*[0.99238769 0 0];
V2=coef*[-0.496193845      0.859431288      0];
V3=coef*[0      0      1.346973585];
case 1
x=A9;
ro=3120; %density N/m^3
coef=1.7;
V1=coef*[0.999963962      0.000259621      0.000555471];
V2=coef*[0.002694942      0.659053311      -0.001115162];
V3=coef*[-0.039157313      -0.188093934      0.844505952];
case 2
x=Mer11;
ro=2387;
coef=1.5;
V1=coef*[1.000488808      0.000162553      0.002170952];
V2=coef*[-0.609035527      0.922044214      0.00078827];
```

```
V3=coef/2.5*[0.047337414      0.040248776      3.317554388];
case 3
x=CS6;
ro=2352;
coef=1.5;
V1=coef*[1.01004133      0.000901124      0.000024242];
V2=coef*[-0.614369463      0.887436274      0.000036492];
V3=coef/2.5*[0.000320447      -0.000042568      3.243603668];
case 4
x=CS8;
ro=2487;
coef=1.5;
V1=coef*[0.999371818      0.000171098      -0.000009816];
V2=coef*[-0.609844657      0.913597842      0.000045232];
V3=coef/2.5*[0.000050042      -0.000195319      3.357958431];
case 5
switch pp
case 1
%CS1=load('Beryllium'); %case5
CS1=load('CS1.txt'); %case5
case 2
CS1=load('CS1-ClayFF.txt'); %case5
case 3
CS1=load('CS1-CoreShell.txt'); %case5
case 4
CS1=load('CSH-FF.txt'); %case5
end
x=CS1;
ro=2589;
coef=1.5;
```

```
V1=coef*[1.006519982      0.002025859      -0.00011813];
V2=coef*[-0.626866678      0.938468288      0.000273757];
V3=coef/2.5*[0.000426699      -0.000771729      3.529424491];
case 6
switch pp
case 1
A14=load('14A.txt'); %case5
case 2
A14=load('14A-ClayFF.txt'); %case5
case 3
A14=load('14A-CoreShell.txt'); %case5
case 4
A14=load('14ACSH-FF.txt'); %case5
end
x=A14;
ro=2381;
coef=1.5;
V1=coef*[0.999160411      -0.000082475      -0.000377643];
V2=coef*[-0.617859499      0.886871685      0.000742269];
V3=coef/3.5*[0.001259076      0.004428587      4.141870737];
case 7
x=Jen;
ro=2275;
coef=1.8;
V1=coef*[1.011791615      -0.001387144      0.019152881];
V2=coef*[-0.23457857      0.653408744      -0.004083587];
V3=coef*[-0.109043032      -0.262542403      0.989806484];
end
function wall
tr=.2; %transparency
```

```
Ver=[0 0 0;V1(1) 0 0;V1(1)+V2(1) V2(2) 0;V2(1) V2(2) 0; V3(1) V3(2) V3(3);V1(1)+V3(1)
V3(2) V3(3);V1(1)+V2(1)+V3(1) V2(2)+V3(2) V3(3);V2(1)+V3(1) V2(2)+V3(2) V3(3)];
epsi=1.05;
text(V1(1)*epsi^4,V1(2)*epsi^4,V1(3)*epsi^4,' a','FontSize',16);
text(V2(1)*epsi, V2(2)*epsi,V2(3)*epsi,' b','FontSize',16);
text(V3(1)*epsi,V3(2)*epsi,V3(3)*epsi,' c','FontSize',16);
Face=[1 2 6 5; 4 1 5 8;1 2 3 4];
hold on;
patch('Vertices',Ver,'Faces',Face);
alpha(tr);
end
%%%%%%%%%%%%% next box
Ver(:,1)=Ver(:,1)-V1(1);
Face=[1 2 6 5;2 3 7 6; 3 4 8 7;4 1 5 8;1 2 3 4;5 6 7 8];
Face=[1 2 6 5; 4 1 5 8;1 2 3 4];
hold on;
patch('Vertices',Ver,'Faces',Face);
alpha(tr);
%%%%%%%%%%%%% next box
Ver(:,2)=Ver(:,2)-V2(2);
Ver(:,1)=Ver(:,1)-V2(1);
Face=[1 2 6 5;2 3 7 6; 3 4 8 7;4 1 5 8;1 2 3 4;5 6 7 8];
Face=[1 2 6 5; 4 1 5 8;1 2 3 4];
hold on;
patch('Vertices',Ver,'Faces',Face);
alpha(tr);
%%%%%%%%%%%%% next box
Ver(:,1)=Ver(:,1)+V1(1);
Face=[1 2 6 5;2 3 7 6; 3 4 8 7;4 1 5 8;1 2 3 4;5 6 7 8];
Face=[1 2 6 5; 4 1 5 8;1 2 3 4];
```

```
hold on;
patch('Vertices',Ver,'Faces',Face);
alpha(tr);
%%%%%%%%%%%%%%%%%%%%%%%%%%%%%%%%%%%%%%%%%%%%%%%%%
C11=x(1,1);
C22=x(2,2);
C33=x(3,3);
C44=x(4,4);
C55=x(5,5);
C66=x(6,6);
C12=x(1,2);
C13=x(1,3);
C16=x(1,6);
C23=x(2,3);
C26=x(2,6);
C36=x(3,6);
C45=x(4,5);
m=[C11 C12 C13 0 0 C16;C12 C22 C23 0 0 C26;C13 C23 C33 0 0 C36; 0 0 0 C44 C45 0; 0 0 0 C45 C55 0;C16 C26 C36 0 0 C66];
m=x;
S=x^-1;
%%%%%working with log-Euclodian metric %%%%%%%%
x=logm(CSDFT)-logm(CS1);
error=mean2(x);
stdv=std2(x);
norm=(trace(transpose(x)*x))^.5;
%%%%%%%%%%%%%%%%%%%%%%%%% end fot Log-Euclodian
%%%%% Viot bounds
F=fopen('bounds','wt');
Kv=1/9*(C11+C22+C33+2*(C12+C13+C23))
```

```
Kr=(S(1,1)+S(2,2)+S(3,3)+2*(S(1,2)+S(1,3)+S(2,3)))^-1
Kh=(Kv+Kr)/2
Gv=1/15*(C11+C22+C33+3*(C44+C55+C66)-C12-C13-C23)
Gr=15/(4*(S(1,1)+S(2,2)+S(3,3)-S(1,2)-S(1,3)-S(2,3))+3*(S(4,4)+S(5,5)+S(6,6)))
Gh=(Gv+Gr)/2
Mh=4*Gh*(3*Kh+Gh)/(3*Kh+4*Gh)
%%%%%%% Molinary bounds
C=C33*(C11+C12)-2*C13^2;
Km=C/(C11+2*C33+C12-4*C13)
Gm=3*C/2/(2*C11+C33+2*C12+4*C13)
Mmoli=4*Gm*(3*Km+Gm)/(3*Km+4*Gm)
fprintf(1,'%%%%%%%%%%%%%%%%%%%%%%%%%%%%%%%%%%%%%%% \n');
fprintf(1,' \n');
fprintf(1,'%f\n',Kv);
fprintf(1,'%f\n',Kr);
fprintf(1,'%f\n',Kh);
fprintf(1,'%f\n',Gv);
fprintf(1,'%f\n',Gr);
fprintf(1,'%f\n',Gh);
fprintf(1,'%f\n',Mh);
fprintf(1,'%f\n',Km);
fprintf(1,'%f\n',Gm);
fprintf(1,'%f\n',Mmoli);
fclose(F);
%%%%%%%%%% finding maximum Young modulus
l1=0:.1:1;
l2=0:.1:1;
x = rand(500,1)*16 - 8;
y = rand(500,1)*16 - 8;
r = sqrt(x.^2 + y.^2) + eps
```

```
z = sin(r)./r;
h=1;
function maxspeed(h,q)
l1=X(h,q);
l2=Y(h,q);
l3=Z(h,q);
D=[l1 0 0 0 l3 l2;0 l2 0 l3 0 l1;0 0 l3 l2 l1 0];
%%%%%%%%%%%% stiffness
Wave=1/ro*D*x*10^9*transpose(D);
[eigvec,eigval]=eig(Wave);
speed1(h,q)= (abs(eigval(1,1)))^.5;
speed2(h,q)= (abs(eigval(2,2)))^.5;
speed3(h,q)= (abs(eigval(3,3)))^.5;
[speedm,pos]=max(diag(eigval));
speedmax(h,q)=speedm^.5;
[speedmini,pos]=min(diag(eigval));
speedmin(h,q)=speedmini^.5;
%%%%%%% cheking only one direction to see if K,G can be compared
%%%%%%% with I3-I3* of the povolo1987
fprintf(F,'just one direction')
aveCL=speed3(h,q)
aveCT1=speed2(h,q)
aveCT2=speed1(h,q)
Vs=(aveCT1+aveCT2)/2;
G=ro*Vs^2
K=((aveCL)^2*3*ro-4*ro*Vs^2)/3
M=4*G*(3*K+G)/(3*K+4*G)
%%%%%%%%%%%%%%%%%%end of cheking I3-I3
% %%%%%%%%%%%% for compliance
Wave=ro*D*(x^-1)*10^(-9)*transpose(D);
```

```
[eigvec,eigval]=eig(Wave);
speed1(h,q)= 1/(abs(eigval(1,1)))^.5;
speed2(h,q)= 1/(abs(eigval(2,2)))^.5;
speed3(h,q)= 1/(abs(eigval(3,3)))^.5;
%speed(h,q)=speed1(h,q);
% speedmax(h,q)=max([ speed1(h,q); speed2(h,q); speed3(h,q)]);
%speedmin(h,q)=min([ speed1(h,q); speed2(h,q); speed3(h,q)]);
[speedm,pos]=min(diag(eigval));
speedmax(h,q)=1/speedm^.5;
[speedmini,pos]=max(diag(eigval));
speedmin(h,q)=1/speedmini^.5;
%%%%%%%%%%%%%%%%%%%%%%%%%%%%%%%%%%%%%%%%%%%%%%%%%%%%%%%%%%%%%%%%%%%%%%%%%%%%%%%
end
n=50;
[X,Y,Z]=sphere(n);
[XX,YY,ZZ]=sphere(n);
[XXX,YYY,ZZZ]=sphere(n); %min
[XXXX,YYYY,ZZZZ]=sphere(n); %med
maxim=70;
mini=70;
for h=1:n+1
for q=1:n+1
maxspeed(h,q);
if eigvec(1,pos) < 0
eigvec(1,:)=-eigvec(1,:);
end
if eigvec(2,pos) < 0
eigvec(2,:)=-eigvec(2,:);
end
if eigvec(3,pos) < 0
```

```
eigvec(3,:)=-eigvec(3,:);
end
XX(h,q)=(eigvec(1,pos));
YY(h,q)=(eigvec(2,pos));
ZZ(h,q)=(eigvec(3,pos));
%
[speedmini,pos]=min(diag(eigval));
speedmin(h,q)=speedmini^.5;
if X(h,q) >=0 & Y(h,q) >=0 & Z(h,q) >=0
maxspeed(h,q)
XX(h,q)=abs(eigvec(1,pos));
YY(h,q)=abs(eigvec(2,pos));
ZZ(h,q)=abs(eigvec(3,pos));
end
if X(h,q) >=0 & Y(h,q) >=0 & Z(h,q) <=0
maxspeed(h,q)
XX(h,q)=abs(eigvec(1,pos));
YY(h,q)=abs(eigvec(2,pos));
ZZ(h,q)=-abs(eigvec(3,pos));
end
if X(h,q) <=0 & Y(h,q) >=0 & Z(h,q) >=0
maxspeed(h,q)
XX(h,q)=-abs(eigvec(1,pos));
YY(h,q)=abs(eigvec(2,pos));
ZZ(h,q)=abs(eigvec(3,pos));
end
if X(h,q) <=0 & Y(h,q) >=0 & Z(h,q) <=0
maxspeed(h,q)
XX(h,q)=-abs(eigvec(1,pos));
YY(h,q)=abs(eigvec(2,pos));
```

```
ZZ(h,q)=-abs(eigvec(3,pos));
if eigvec(3,pos) > 0
eigvec(:,pos)=- eigvec(:,pos);
end
XXX(h,q)=(eigvec(1,pos));
YYY(h,q)=(eigvec(2,pos));
ZZZ(h,q)=(eigvec(3,pos));
if speedmax(h,q) ~= speed1(h,q)
if speedmin(h,q) ~= speed1(h,q)
speedmed(h,q)=speed1(h,q);
XXXX(h,q)=(eigvec(1,1));
YYYY(h,q)=(eigvec(2,1));
ZZZZ(h,q)=(eigvec(3,1));
end
end
if speedmax(h,q) ~= speed2(h,q)
if speedmin(h,q) ~= speed2(h,q)
speedmed(h,q)=speed2(h,q);
XXXX(h,q)=(eigvec(1,2));
YYYY(h,q)=(eigvec(2,2));
ZZZZ(h,q)=(eigvec(3,2));
end
end
if speedmax(h,q) ~= speed3(h,q)
if speedmin(h,q) ~= speed3(h,q)
speedmed(h,q)=speed3(h,q);
XXXX(h,q)=(eigvec(1,3));
YYYY(h,q)=(eigvec(2,3));
ZZZZ(h,q)=(eigvec(3,3));
end
```

```
end
%
E(h,q)=0;
E(h,q)=l1.^4*S(1,1)+2*l1.^2.*l2.^2*S(1,2)+2*l1.^2.*l3.^2*S(1,3)+
2*l1.^2.*l2.*l3*S(1,4)+2*l1.^3.*l3*S(1,5)+2*l1.^3.*l2*S(1,6);
E(h,q)=E(h,q)+ l2.^4*S(2,2)+2*l2.^2.*l3.^2*S(2,3)+
2*l2.^3.*l3*S(2,4)+2*l1.*l2.^2.*l3*S(2,5)+2*l1.*l2.^3*S(2,6);
E(h,q)=E(h,q)+ l3.^4*S(3,3)+ 2*l2.*l3.^3*S(3,4)+
2*l1.*l3.^3*S(3,5)+2*l1.*l2.*l3.^2*S(3,6) ;
E(h,q)=E(h,q)+ l2.^2.*l3.^2*S(4,4)+
2*l1.*l2.*l3.^2*S(4,5)+ 2*l1.*l2.^2.*l3*S(4,6) ;
E(h,q)=E(h,q)+ l1.^2.*l3.^2*S(5,5)+ 2*l1.^2.*l2.*l3*S(5,6);
E(h,q)=E(h,q)+ l1.^2.*l2.^2*S(6,6);
CC(h,q)=0;
CC(h,q)=l1.^4*x(1,1)+2*l1.^2.*l2.^2*x(1,2)+2*l1.^2.*l3.^2*x(1,3)+
2*l1.^2.*l2.*l3*x(1,4)+2*l1.^3.*l3*x(1,5)+2*l1.^3.*l2*x(1,6);
CC(h,q)=CC(h,q)+ l2.^4*x(2,2)+2*l2.^2.*l3.^2*x(2,3)+
2*l2.^3.*l3*x(2,4)+2*l1.*l2.^2.*l3*x(2,5)+2*l1.*l2.^3*x(2,6);
CC(h,q)=CC(h,q)+ l3.^4*x(3,3)+ 2*l2.*l3.^3*x(3,4)+
2*l1.*l3.^3*x(3,5)+2*l1.*l2.*l3.^2*x(3,6) ;
CC(h,q)=CC(h,q)+ l2.^2.*l3.^2*x(4,4)+
2*l1.*l2.*l3.^2*x(4,5)+ 2*l1.*l2.^2.*l3*x(4,6) ;
CC(h,q)=CC(h,q)+ l1.^2.*l3.^2*x(5,5)+ 2*l1.^2.*l2.*l3*x(5,6);
CC(h,q)=CC(h,q)+ l1.^2.*l2.^2*x(6,6);
Young(h,q)=E(h,q)^(-1);
if maxim < Young(h,q)
maxim =Young(h,q);
l11max=l1;
l22max=l2;
l33max=l3;
```

```
end
if mini > Young(h,q)
mini =Young(h,q);
l11min=l1;
l22min=l2;
l33min=l3;
end
end
end
subplot(2,3,3*(pp-ww)+1)
wall
surf(X,Y,Z,abs(speedmax),'FaceColor','interp','EdgeColor','none','FaceLighting','phong');
daspect([5 5 5])
xlabel('x')
ylabel('y')
colorbar('vertical','FontSize',16)
%colorbar
axis off
axis tight
view(160,30)
view(90,0)
camlight left
subplot(2,3,3*(pp-ww)+2)
wall
surf(X,Y,Z,abs(speedmed),'FaceColor','interp','EdgeColor','none','FaceLighting','phong');
daspect([5 5 5])
xlabel('x')
ylabel('y')
colorbar('vertical','FontSize',16)
%colorbar
```

```
axis off
axis tight
view(160,30)
view(90,0)
camlight left
subplot(2,3,3*(pp-ww)+3)
wall
surf(X,Y,Z,abs(speedmin),'FaceColor','interp','EdgeColor','none','FaceLighting','phong');
daspect([5 5 5])
xlabel('x')
ylabel('y')
hold on
colorbar('vertical','FontSize',16)
ylabel(colorbar,'Hello')
colorbar
axis off
axis tight
view(160,30)
view(90,0)
camlight left
minE=min(speedmin(:));
maxE=max(speedmax(:));
%maxim
% mini
E11=1/S(1,1);
%average directional speeds %%%%%%%%%%%%%%%%%%%%%%%%%%%%%
aveCL=mean2(speedmax);
aveCT1=mean2(speedmed);
aveCT2=mean2(speedmin);
Vs=(aveCT1+aveCT2)/2;
```

```
G=ro*Vs^2
K=((aveCL)^2*3*ro-4*ro*Vs^2)/3
M=4*G*(3*K+G)/(3*K+4*G)
waves(1)
waves(2)
waves(3)
waves(4)
speedmax(5,5)
speedmed(5,5)
speedmin(5,5)
end
```

B.2 Script to Deform the Molecular C-S-H Phases for Elasticity and Strength Calculations

```
import os,sys,string,math
    import time
    from string import *
    #from Numeric import *
    def break_line(s):
    copy = s[:]
    return string.split(copy)
    def print_help():
    print '\nUsage syntax: python xxx.py direction increment(A)'
    sys.exit()
    args = sys.argv[:]
    #print "length", len(args),args[1]
    if len(args) != 2: print_help()
    # get the necessary files
    #Dir = args[1]
    template = 'out'
    #newfile = args[2]
    newfile = 'input'
    e = float (args [1]) # Deformation (A)
    f = open(template,'r')
    T = f.readlines()
    f.close()
    template1='model'
    f1 = open(template1,'r')
    T1 = f1.readlines()
    f1.close()
    newlines = []
```

```
print "************************************************
#if (string.find(T[ii-1],'DL_Poly') == 0):
newlines.append ('opti conv conjugate molecule nosys nonrepulsive_cutoff\n')
newlines.append ('maxcyc opt 49\n')
#newlines.append ('supercell\n')
#newlines.append ('1 1 2\n')
newlines.append ('#rspeed 0.25\n')
newlines.append ('#lbfgs_order 50\n')
newlines.append ('vectors\n')
R11=1
R12=0
R13=0
R21=0
R22=1
R23=0
R31=0
R32=0
R33=1
i=1
nat=10
while i < (len(T)):
if (string.find(T[i],' Dimensionality = 3 : Bulk') == 0):
nn=split(T[i-2])
nat=int(nn[4])
# print nat
if (string.find(T[i],' Cartesian lattice vectors (Angstroms)') == 0):
i=i+2
# print T[i]
v1=split(T[i])
i=i+1
```

```
v2=split(T[i])
i=i+1
v3=split(T[i])
i=i+1
R22=float(1+e/float(v2[1]))
newlines.append ('%10f %10f %10f\n'%(float(v1[0]),float(v1[1]),float(v1[2])))
newlines.append ('%10f %10f %10f\n'%(float(v2[0])*R22,float(v2[1])*R22,float(v2[2])))
newlines.append ('%10f %10f %10f\n'%(float(v3[0]),float(v3[1]),float(v3[2])))
if (string.find(T[i],' Fractional coordinates of asymmetric unit :') == 0):
print T[i]
h=i+6
# cha=[]
# cha=cha+[2]
# for j in range(1+h,nat+h):
# gg=split(T[j])
# print gg
# cha=cha+[float(gg[9])]
if (string.find(T[i],' Final fractional coordinates of atoms :') == 0):
newlines.append ('frac\n')
i =i+6
for j in range(1,nat+1):
#print T1[j+17]
#print T[i]
#so=split(T1[j+16])
sn=split(T[i])
#print T[i], cha[j-1]
#newlines.append ('%s %s %5.8f %5.8f %5.8f %2.7f %1.4f %1.4f %d %d %d \n'%
(sn[1],sn[2],float(sn[3]),float(sn[4]),float(sn[5]),float(cha[j-1]),1.000,0.000, 1,1,1))
newlines.append ('%s %s %5.8f %5.8f %5.8f %2.7f %1.4f %1.4f %d %d %d \n'%
(sn[1],sn[2],float(sn[3]),float(sn[4]),float(sn[5]),1,1.000,0.000, 1,1,1))
```

```
i=i+1
ff=int(nat/2.0)+7
i=i+1
while ff < len(T1) :
newlines.append (T1[ff])
ff=ff+1
f = open(newfile,'w')
f.writelines(newlines)
f.close()
print "rescaling DONE**************************************************
```

B.3 Script to Analyze Bond Strain and Three-Body Strains

```
import os,sys,string,math
    import time
    from string import *
    #from Numeric import *
    def break_line(s):
    copy = s[:]
    return string.split(copy)
    def print_help():
    print '\nUsage syntax:  python xxx.py initialREVCON finalREVCOn x.xyz number-of-
atoms '
    sys.exit()
    args = sys.argv[1:]# [1: means 1 not included
    #if len(args) != 4: print_help()
    # get the necessary parameters/files
    ############ calculating bonds for the Eq state ############
    #just 3 important steps for this whole script:1-adjust the alat 2-create a
    OutO file form in1 with right cellpara (K-POINTs should be attached to
    positions without space) 3-adjust the bond lengths particularly OH
    newfile = 'bondseq'
    #a=args[3]
    newlines = []
    alat=21.187*0.529177249
    bCaO=2.7
    bSiO=1.8
    bOH=1.11
    for j in range(1,2):
    template ='Out0'
    f = open(template,'r')
```

```
T = f.readlines()
f.close()
ii=6
n=0.
for ii in range(1,len(T)):
if (string.find(T[ii],'CELL_PARAMETERS') ==0):
print "foundcell"
V1=split(T[ii+1])
V2=split(T[ii+2])
V3=split(T[ii+3])
print V1[0]
if (string.find(T[ii],'ATOMIC_POSITIONS') ==0):
start=ii+1
    print "found",start
if (string.find(T[ii],'K_POINTS') == 0):
finish=ii-1
print "finish",finish
i=1;
for ii in range(start,finish+1):
s=split (T[ii])
k=i #print s[:]
for jj in range(ii,finish+1):
u=split(T[jj])
X1car=float(s[1])*float(V1[0])+float(s[2])*float(V2[0])+float(s[3])*float(V3[0])
X2car=float(u[1])*float(V1[0])+float(u[2])*float(V2[0])+float(u[3])*float(V3[0])
Y1car=float(s[1])*float(V1[1])+float(s[2])*float(V2[1])+float(s[3])*float(V3[1])
Y2car=float(u[1])*float(V1[1])+float(u[2])*float(V2[1])+float(u[3])*float(V3[1])
Z1car=float(s[1])*float(V1[2])+float(s[2])*float(V2[2])+float(s[3])*float(V3[2])
Z2car=float(u[1])*float(V1[2])+float(u[2])*float(V2[2])+float(u[3])*float(V3[2])
cutoff=.5
```

```
#print X1car
if (s[0]=='Ca') and (u[0]=='O'):
cutoff=bCaO
if (s[0]=='O') and (u[0]=='Ca'):
cutoff=bCaO
if (s[0]=='Si') and (u[0]=='O'):
cutoff=bSiO
if (s[0]=='O') and (u[0]=='Si'):
cutoff=bSiO
if (s[0]=='O') and (u[0]=='H'):
cutoff=bOH
if (s[0]=='H') and (u[0]=='O'):
cutoff=bOH
dis=((X2car-X1car)**2+(Y2car-Y1car)**2+(Z2car-Z1car)**2)**.5*float(alat)
if (dis <cutoff) and (dis>0):
    print i,k,s[0],u[0],dis
n=n+1
inter = '%d %d %s %s %f %f %f %f\n' % (i,k,s[0],u[0],dis,(float(alat)*
(X2car-X1car)/dis)**2,(float(alat)*(Y2car-Y1car)/dis)**2,(float(alat)*
(Z2car-Z1car)/dis)**2)
    newlines.append(inter)
k=k+1
i=i+1
f = open(newfile,'w')
f.writelines(newlines)
f.close()
bonds=n
print finish-start+1
print "bonds",n
print "************************************************
```

```
################ calculating bonds for the Out files ##########
#newfile = args[2]
newfile = 'allbonds'
#a=args[3]
newlines = []
for j in range(1,13):
template ='Out'+str(j)
template1 ='bondseq'
f = open(template,'r')
T = f.readlines()
f.close()
f = open(template1,'r')
Eq= f.readlines()
f.close()
#newlines.append ('%d \n'%int(a))
#newlines.append ('MESO\n')
ii=6
n=0
for ii in range(0,len(T)):
if (string.find(T[ii],'CELL_PARAMETERS') ==0):
print "Out",j
V1=split(T[ii+1])
V2=split(T[ii+2])
V3=split(T[ii+3])
#print V1[0]
if (string.find(T[ii],'ATOMIC_POSITIONS') ==0):
start=ii+1
    #print "found",T[ii+1]
if (string.find(T[ii],' number of atoms/cell') == 0):
atoms=split(T[ii])
```

```
finish=int(atoms[4])
print "found nat",finish
i=1
newlines.append ( 'Out %d\n'%j)
for ii in range(start,start+finish):
s=split (T[ii])
k=i#print s[:]
for jj in range(ii,start+finish):
u=split(T[jj])
X1car=float(s[1])*float(V1[0])+float(s[2])*float(V2[0])+float(s[3])*float(V3[0])
X2car=float(u[1])*float(V1[0])+float(u[2])*float(V2[0])+float(u[3])*float(V3[0])
Y1car=float(s[1])*float(V1[1])+float(s[2])*float(V2[1])+float(s[3])*float(V3[1])
Y2car=float(u[1])*float(V1[1])+float(u[2])*float(V2[1])+float(u[3])*float(V3[1])
Z1car=float(s[1])*float(V1[2])+float(s[2])*float(V2[2])+float(s[3])*float(V3[2])
Z2car=float(u[1])*float(V1[2])+float(u[2])*float(V2[2])+float(u[3])*float(V3[2])
cutoff=.5
#print X1car
if (s[0]=='Ca') and (u[0]=='O'):
cutoff=bCaO
if (s[0]=='Si') and (u[0]=='O'):
cutoff=bSiO
if (s[0]=='O') and (u[0]=='H'):
cutoff=bOH
if (s[0]=='O') and (u[0]=='Ca'):
cutoff=bCaO
if (s[0]=='O') and (u[0]=='Si'):
cutoff=bSiO
if (s[0]=='H') and (u[0]=='O'):
cutoff=bOH
dis=((X2car-X1car)**2+(Y2car-Y1car)**2+(Z2car-Z1car)**2)**.5*float(alat)
```

```
if (dis <cutoff) and (dis>0):
    #print i,k, s[0],u[0],dis
#print "n",n
e=split(Eq[n])
if (s[0]==e[2]) and (u[0]==e[3]) and (i==int(e[0])) and (k==int(e[1])):
n=n+1
    inter = '%d %d %s %s %10.5f %d %d %s %s %10.5f %10.5f %
10.5f %10.5f %10.5f\n' % (i,k,s[0],u[0],dis,int(e[0]),int(e[1]),e[2],e[3],
float(e[4]),float(dis-float(e[4]))/float(e[4]),float(e[5]),float(e[6]),float(e[7]))
    newlines.append(inter)
k=k+1
i=i+1
print "bonds",n
f = open(newfile,'w')
f.writelines(newlines)
f.close()
# avergaing distnces
template='allbonds'
f = open(template,'r')
T= f.readlines()
f.close()
aveCaO=[]
aveSiO=[]
aveOH=[]
for i in range(0,len(T)):
s=split(T[i])
if (s[0]=='Out'):
print "found",s[1]
CaO=0
nCaO=0
```

```
SiO=0
nSiO=0
OH=0
nOH=0
cos=1.
temp=int(s[1])-1
for j in range(i+1,i+1+n):
s=split(T[j])
if (temp==0) or (temp==6):
cos=abs(float(s[11]))
#print "found cos",cos
if temp==1 or temp==7:
cos=abs(float(s[12]))
if temp==2 or temp==8:
cos=abs(float(s[13]))
if (s[2]=='Ca') and (s[3]=='O') and (s[7]=='Ca') and (s[8]=='O'):
CaO=CaO+abs(float(s[10]))*cos
nCaO=nCaO+cos
if (s[2]=='O') and (s[3]=='Ca') and (s[7]=='O') and (s[8]=='Ca'):
CaO=CaO+abs(float(s[10]))*cos
nCaO=nCaO+cos
if (s[2]=='Si') and (s[3]=='O') and (s[7]=='Si') and (s[8]=='O'):
SiO=SiO+abs(float(s[10]))*cos
nSiO=nSiO+cos
if (s[2]=='O') and (s[3]=='Si') and (s[7]=='O') and (s[8]=='Si'):
SiO=SiO+abs(float(s[10]))*cos
nSiO=nSiO+cos
if (s[2]=='H') and (s[3]=='O') and (s[7]=='H') and (s[8]=='O'):
OH=OH+abs(float(s[10]))*cos
nOH=nOH+cos
```

```
if (s[2]=='O') and (s[3]=='H') and (s[7]=='O') and (s[8]=='H'):
OH=OH+abs(float(s[10]))*cos
nOH=nOH+cos
aveCaO=aveCaO+[float(CaO/nCaO)]
aveSiO=aveSiO+[float(SiO/nSiO)]
aveOH=aveOH+[float(OH/nOH)]
print "aveCaO",CaO,nCaO,CaO/nCaO
print "ave-SiO",SiO,nSiO,SiO/nSiO
print "ave-OH",OH,nOH,OH/nOH
print "vector",aveCaO[0]
#print finish-start+1
############ calculating stdev
newlines1=[]
newfile1='ave.std'
for i in range(0,len(T)):
s=split(T[i])
if (s[0]=='Out'):
print "found",s[1]
newlines1.append('Out %d\n'% int(s[1]))
cos=1.
CaO=0
nCaO=0
SiO=0
nSiO=0
OH=0
nOH=0
temp=int(s[1])-1
for j in range(i+1,i+1+n):
s=split(T[j])
if (temp==0) or (temp==6):
```

```
cos=abs(float(s[11]))
#print "found cos",cos
if temp==1 or temp==7:
cos=abs(float(s[12]))
if temp==2 or temp==8:
cos=abs(float(s[13]))
if (s[2]=='Ca') and (s[3]=='O') and (s[7]=='Ca') and (s[8]=='O'):
CaO=CaO+(abs(float(s[10]))*cos-aveCaO[temp])**2
nCaO=nCaO+cos
if (s[2]=='O') and (s[3]=='Ca') and (s[7]=='O') and (s[8]=='Ca'):
CaO=CaO+(abs(float(s[10]))*cos-aveCaO[temp])**2
nCaO=nCaO+cos
if (s[2]=='Si') and (s[3]=='O') and (s[7]=='Si') and (s[8]=='O'):
SiO=SiO+(abs(float(s[10]))*cos-aveSiO[temp])**2
nSiO=nSiO+cos
if (s[2]=='O') and (s[3]=='Si') and (s[7]=='O') and (s[8]=='Si'):
SiO=SiO+(abs(float(s[10]))*cos-aveSiO[temp])**2
nSiO=nSiO+cos
if (s[2]=='H') and (s[3]=='O') and (s[7]=='H') and (s[8]=='O'):
OH=OH+(abs(float(s[10]))*cos-aveOH[temp])**2
nOH=nOH+cos
if (s[2]=='O') and (s[3]=='H') and (s[7]=='O') and (s[8]=='H'):
OH=OH+(abs(float(s[10]))*cos-aveOH[temp])**2
nOH=nOH+cos
#stdCaO=stdCaO+[CaO/nCaO]
#stdSiO=stdSiO+[SiO/nSiO]
#stdOH=stdOH+[OH/nOH]
#print "stdCaO",CaO,nCaO,(float(CaO/nCaO))**.5
#print "std-SiO",SiO,nSiO,float(SiO/(nSiO))**.5
#print "std-OH",OH,nOH,float(OH/(nOH))**.5
```

```
inter = 'Ca-O %f %10.5f %10.5f \n' % (nCaO,aveCaO[temp],
float(CaO/(nCaO))**.5)
newlines1.append(inter)
inter = 'Si-O %f %10.5f %10.5f \n' % (nSiO,aveSiO[temp],float(SiO/(nSiO))**.5)
newlines1.append(inter)
inter = 'O-H %f %10.5f %10.5f \n' % (nOH,aveOH[temp],float(OH/(nOH))**.5)
newlines1.append(inter)
f1 = open(newfile1,'w')
f1.writelines(newlines1)
f1.close()
print "*****************************************************************
```

B.4 Script to Analyze Energy and Calculate Stess

```
import os,sys,string,math
    import time
    from string import *
    #from Numeric import *
    def break_line(s):
    copy = s[:]
    return string.split(copy)
    def print_help():
    print '\nUsage syntax: python xxx.py x/y/z initialOUT LastOUT'
    sys.exit()
    args = sys.argv[:]
    #print "length", len(args),args[1]
    if len(args) != 4: print_help()
    # define outpit file
    ini=int(args[2])
    f=int(args[3])
    newfile = 'plotinput'
    newlines = []
    print "*************************************************************************"
    for i in range(ini,f+1):
    template ='out'+str(i)
    #print os.path.isfile(template)
    f = open(template,'r')
    T = f.readlines()
    f.close()
    #definig the line number where lattice parameter is
    j=1
    while j< len(T):
    # if i==1000000 and (string.find(T[j],' Final Cartesian lattice vectors') == 0):
```

```
# if (args[1]=='x' or args[1]=='X'):
# t=split(T[j+2])
# cell=float(t[0])
# elif (args[1]=='y' or args[1]=='Y'):
# t=split(T[j+3])
# cell=float(t[1])
# elif (args[1]=='z' or args[1]=='Z'):
# t=split(T[j+4])
# cell=float(t[2])
#else:
# print "Please specify a direction using this format:python xxx.py x/y/z
initial_OUTPUT last_OUTPUT"
# sys.exit()
if (string.find(T[j],' Cartesian lattice vectors') == 0):
    if (args[1]=='x' or args[1]=='X'):
        t=split(T[j+2])
        cell=float(t[0])
    elif (args[1]=='y' or args[1]=='Y'):
        t=split(T[j+3])
        cell=float(t[1])
    elif (args[1]=='z' or args[1]=='Z'):
        t=split(T[j+4])
        cell=float(t[2])
    else:
    print "Please specify a direction using this format:python xxx.py x/y/z
initial_OUTPUT last_OUTPUT"
    sys.exit()
j=j+1
j=1
while j < len(T):
```

```
if (string.find(T[j],' Final energy') == 0):
s=split(T[j])
    newlines.append ('%f %f\n'%(cell,float(s[3])))
j=j+1
f = open(newfile,'w')
f.writelines(newlines)
f.close()
template ='plotinput'
f = open(template,'r')
T = f.readlines()
f.close()
newline1 = []
j=0
#print T[j]
while j <len(T)-1:
t1=split(T[j])
t2=split(T[j+1])
delta=float(t2[0])-float(t1[0])
diff=float(t2[1])-float(t1[1])
stress=float(diff)/float(delta)
newline1.append ('%f %f\n'%(float(t1[0]),float(stress)))
j=j+1
f = open('stress','w')
f.writelines(newline1)
f.close()
print "writing DONE"
print "*************************************************************************"
```

Appendix C

Molecular Configuration of the Consistent C-S-H Model

C.1 Cell Parameters and Atomic Positions of cCSH

All length units are in Å.

Number of Atoms: 672

C.1.1 Cell Parameters

a =26.618

b =29.521

c =23.691

α =92.02 deg

β =88.52 deg

γ =123.58 deg

C.1.2 Atomic Positions in Cartesian Coordinates

Ca	9.0248822	2.489555	6.9455407
Ca	0.2314494	13.5005146	6.7084888
Ca	4.9693745	7.8895264	6.2373611
Ca	-3.5958435	18.9610178	8.6885592
Ca	21.632521	2.3347079	7.833785
Ca	14.1899251	13.7676501	5.6965703
Ca	17.8188456	7.2286737	6.2814971
Ca	9.1704938	19.7533586	6.7801312
Ca	2.4622424	-0.2118658	15.8655833
Ca	-3.6925914	11.9216108	14.1112502
Ca	1.3789855	6.7426245	14.2041509
Ca	-8.7301849	17.2976727	14.4705676
Ca	-1.2210967	22.1316093	13.8951489
Ca	10.0394601	11.9128905	14.4350234
Ca	15.1495054	6.9397873	15.5421889
Ca	5.760837	17.6498568	15.230708

Ca	8.2002221	2.3250477	18.5309981
Ca	0.2790733	14.4241146	16.7310351
Ca	3.7239289	8.3119493	18.1758216
Ca	-5.7203013	20.9469943	18.1229446
Ca	15.1234129	0.5469502	15.7499896
Ca	13.3171626	14.5773871	16.9714087
Ca	17.9043855	8.6511572	18.5410508
Ca	1.8330511	18.3189162	21.2373836
Ca	0.3003985	4.9255589	4.0744062
Ca	-8.0294249	17.1157769	4.2246492
Ca	-3.334589	10.9209441	4.2587752
Ca	-12.6631702	23.0839023	3.5599545
Ca	13.4592603	4.6225404	3.4155997
Ca	5.5038157	17.1465521	4.6036362
Ca	10.0626691	11.0708357	3.7419985
Ca	0.9114894	23.2774546	4.2875931
Ca	2.9561668	2.0735705	3.8033799
Ca	-5.076671	14.0433099	4.208268
Ca	-1.3526566	8.027336	3.7591231
Ca	-9.7533537	20.5447532	5.4665524
Ca	15.7990923	1.7554645	3.0285819
Ca	8.4058581	14.3252515	4.0129444
Ca	11.8322414	8.179123	2.30641
Ca	3.8697993	20.3467255	5.250631
Ca	6.3635341	5.4215991	18.4773753
Ca	-1.4248983	17.4182461	17.1263133
Ca	2.5809648	11.3109039	16.3502416
Ca	11.7901971	-0.1309444	19.770889
Ca	20.2475052	5.9880973	17.3804732
Ca	11.8313821	17.7031082	17.0403425

Ca	16.0136678	11.6574862	16.7463935
Ca	7.4207821	23.6189439	18.03141
Ca	1.9342798	3.6088223	14.6347294
Ca	-5.1285622	14.8061037	12.7408359
Ca	-0.9605833	9.2687791	13.0940899
Ca	-8.5518088	22.9560211	14.097007
Ca	16.7593667	3.4957177	14.5944857
Ca	8.0465204	14.889843	14.6795757
Ca	12.1696234	8.9128236	14.1519154
Ca	4.1111031	21.2052379	15.7093575
Ca	5.6920534	4.8109375	6.860704
Ca	-1.4289851	16.5231444	7.1195587
Ca	3.200849	10.8252223	6.2973787
Ca	-4.6788024	22.1904418	7.6394155
Ca	20.8077787	4.6963854	5.5572181
Ca	12.0148961	16.8336295	6.5515173
Ca	16.2982018	10.6056856	5.6483928
Ca	6.4858598	23.1262558	7.8464657
Si	8.580958	1.3310624	3.7003934
Si	1.4648659	13.9992264	3.30065
Si	5.3593399	7.76959	2.8863295
Si	-3.2984816	20.0244098	5.1926708
Si	22.2194284	1.7562108	4.3331544
Si	15.4146396	13.9899997	2.5218982
Si	18.5767017	7.6851453	3.0198574
Si	10.55464	20.0777546	3.553323
Si	-0.4591382	4.9670538	17.2455152
Si	-7.8810231	17.5814181	17.5256022
Si	-3.9971803	11.5691814	17.8915417
Si	-11.9651923	23.6392356	18.8901593

Si	13.7627422	5.354826	18.70651
Si	4.7852005	16.9204195	18.3739674
Si	9.3604551	11.1869262	17.7209827
Si	0.2577343	23.209873	17.8987651
Si	18.7203209	0.8603213	12.7652004
Si	14.5049611	14.4814851	12.9815196
Si	18.6144873	8.5678235	12.7576361
Cw	8.2924698	20.116778	17.5332116
Si	6.7011008	0.1335596	11.4606066
Si	1.8424653	14.9606136	13.3741674
Si	6.3280679	9.140821	12.6003544
Cw	-8.0190751	19.9907602	12.539366
Si	-0.2800382	5.3923767	7.7635088
Si	-8.7506482	16.1266813	7.6222957
Si	-4.1947468	10.1976419	7.5428357
Cw	-11.8458035	22.9909355	8.4076246
Si	16.2404399	4.0611813	8.1509362
Si	5.6248186	16.4369661	7.8882863
Si	10.4628919	10.6352874	7.2343238
Cw	17.9339681	-0.1855523	9.8718417
Cw	4.2694324	0.9065142	0.5792329
Cw	0.6605465	16.611599	1.0371828
Si	2.5126498	9.2061304	0.8952949
Cw	-7.7893596	20.1319074	2.3274008
Cw	-4.3039494	7.5289179	0.0045339
Cw	11.614763	15.1695896	0.0138786
Si	17.3644875	9.2108449	0.5121055
Cw	8.0098895	22.167959	1.2274469
Cw	10.3216441	23.62439	21.717134
Si	-4.4787084	13.5490967	20.2505233

Cw	2.3236599	10.1032656	21.4753446
Cw	18.2172319	12.8121318	23.2426401
Cw	21.6124419	1.9469794	18.3195704
Si	8.449965	12.7141116	20.2476467
Cw	13.3251688	7.9093794	21.2914989
Cw	2.4835008	15.3348916	21.3065329
Cw	6.679168	3.5327129	10.4658292
Cw	1.4659401	17.4936339	10.8545256
Cw	6.8212967	11.5121493	9.9828873
Cw	3.7795935	21.0336069	11.8377777
Cw	19.1220961	3.7864989	10.8613678
Cw	6.2861627	15.5577737	10.958871
Cw	11.6683492	9.7395467	10.3988272
Cw	10.0048775	20.956857	14.0030788
Cw	-7.2203459	11.1797124	10.4697143
Cw	5.4825578	6.8545889	9.8700471
Cw	15.2312816	17.1446155	10.7096546
Cw	10.397875	23.004007	10.7771608
Cw	13.9613752	13.6936619	9.4880603
Cw	16.1999996	7.0981108	9.7843509
Cw	9.2885786	18.9821062	10.4529046
Si	-5.8437558	23.3084467	4.1430939
Si	3.3662536	11.4176365	3.0788286
Si	6.9370188	5.1205141	3.3031051
Si	-1.1806673	17.5449385	4.1755271
Si	7.4791598	23.6211115	4.3788318
Si	17.1656898	11.3462762	2.5027967
Si	20.4246503	5.1675683	2.3529586
Si	12.1652675	17.4089919	2.9542808
Si	1.6406213	2.3723188	17.6432534

Si	-6.7404738	14.8956554	18.0349518
Si	-1.7696133	9.1127202	18.4269392
Si	-11.8027984	21.5104737	16.7017863
Si	15.2509286	2.7012691	18.2110438
Si	6.5993701	14.4068729	17.9111498
Si	11.2357044	8.5458423	17.79553
Si	1.8211861	20.576376	18.6015135
Cw	-4.2127581	23.3866578	11.3193154
Si	3.4847592	12.2893172	13.0447405
Si	7.0314639	6.1810214	12.7614384
Si	-3.6819509	18.4550248	11.9974009
Cw	6.7122693	23.578172	13.8066258
Si	15.9611978	11.7747633	13.0032419
Si	20.6327889	6.1915902	13.681756
Si	11.545592	17.9538045	13.0717615
Cw	3.4189578	1.1389194	8.6129962
Si	-7.1304072	13.4103239	7.5570647
Si	-2.0109978	7.7733559	7.0064556
Si	-12.1029879	19.9292739	8.4589912
Cw	11.5677108	0.8824484	8.8632898
Si	7.8531688	13.9124009	7.528242
Si	11.2176432	7.8205259	7.7066069
Si	3.6815456	19.9761987	8.8675396
O	6.1348267	0.7651836	2.5796832
O	0.1967809	14.7032023	2.1922155
O	4.2850169	8.1867146	1.4426533
O	-6.3165535	19.8244577	4.4629961
O	19.9939491	1.400985	3.1328421
O	15.0683285	14.5512422	1.0741238
O	16.7377636	8.2995368	1.9519367

O	10.6332294	21.2245329	2.4606944
O	-9.3415966	23.8898216	19.895915
O	-3.3428824	12.7880587	19.0114398
O	2.0075969	6.0171666	18.0726813
O	-10.9140671	16.9804017	16.7455861
O	19.4727293	-0.422478	18.5120624
O	9.7058603	11.6956928	19.319509
O	13.8621842	5.8551636	20.215777
O	4.0682669	17.379291	19.8080241
O	5.3610388	1.3053125	11.051194
O	2.6798661	16.080286	12.2333992
O	7.4759013	9.9335288	11.2373552
O	19.5925862	1.7364658	11.3973975
O	13.9228329	14.9501378	11.5099867
O	18.2872046	8.848915	11.1966095
O	-4.0246321	10.7997579	8.9981081
O	3.1481235	6.0348257	7.8862999
O	15.6173759	16.2169418	8.7357825
O	11.0056859	11.227768	8.7380175
O	16.3904194	5.0640915	9.4280592
O	5.7827713	17.0197595	9.38483
O	-7.5375154	24.4541555	4.2739939
O	2.2955691	12.6809636	2.5875766
O	6.3488543	6.4551005	2.4989991
O	-2.9822518	18.5093209	4.8808585
O	22.3704057	0.2357898	4.8447887
O	17.0834999	12.8570436	2.0651202
O	19.7001202	6.6431975	2.0870154
O	10.9435503	18.7424692	2.7586209
O	-0.1576341	3.439566	17.48895

O	-7.2290542	16.3585101	18.4372428
O	-2.6184418	10.5354376	18.6656862
O	-12.6357565	22.1529069	18.0998324
O	15.7409186	4.2866653	18.5939894
O	5.1969443	15.4362569	18.6819798
O	11.2746198	10.1563768	17.6334067
O	-0.0536601	21.6278703	18.3223854
O	3.1941622	13.8158383	12.7338113
O	6.8044293	7.6659497	12.2410346
O	14.2884888	12.8910514	12.7053603
O	19.1802911	7.0616426	12.7088785
O	-9.2081618	14.4714791	7.5831742
O	-3.4368708	8.7369103	7.865115
O	7.547655	15.3920985	7.9982949
O	12.0533656	9.4187723	7.1520369
O	-1.190383	2.6169913	3.9653967
O	-9.0137997	14.9495408	3.5515757
O	-5.422077	8.7883762	3.6290352
O	-13.4700282	20.7890612	4.5379128
O	11.6263385	2.2746083	3.2204844
O	4.3091344	14.934871	4.0026337
O	8.1810859	8.8794912	3.3372548
O	-0.5094459	21.0782175	4.539563
O	5.1987787	0.1909972	17.7450513
O	-2.2935777	12.1840521	16.5524809
O	-0.0930542	5.1236349	15.6535802
O	-7.7237979	18.7940505	18.5085679
O	0.1746688	23.4072086	16.2892841
O	11.0334796	12.3435424	16.693694
O	15.7077499	6.4668066	17.6688372

O	7.5477014	17.8950188	17.6294221
O	21.3518647	0.6126167	13.4899837
O	-9.0726598	15.3201762	13.5567181
O	-5.2376245	9.6790043	13.3826954
O	11.2412721	19.4309513	12.836284
O	10.0015283	0.4273566	11.0616799
O	3.5997455	15.4673578	14.7370222
O	8.4188862	9.7636646	13.8303961
O	-5.9242982	18.5643008	10.8455265
O	7.2160937	0.4768388	7.941161
O	-1.7504585	11.1394273	6.5710899
O	-1.0559634	4.9710899	6.2433179
O	-5.4882484	16.8612283	7.9169266
O	21.2168997	0.2686171	8.4259827
O	12.1772589	11.5637059	6.0209093
O	17.2394118	4.9168507	6.7816819
O	7.4076734	17.4837631	6.7784786
O	7.2533016	1.9868122	4.8748994
O	-0.9369124	13.315189	4.4344836
O	2.9395361	7.3856623	4.0059293
O	-3.4912762	20.3328771	6.7635677
O	21.0754572	2.4329297	5.5592376
O	12.5580617	13.3365815	3.3860739
O	16.3971244	6.8118632	4.0918954
O	7.7562063	19.5583804	4.4763065
O	23.0303517	4.7929725	17.7572561
O	-5.5322416	17.9401746	16.3654224
O	19.3483008	10.8451671	17.6503868
O	-14.9486988	23.4518753	19.5992338
O	10.5759259	4.6119055	18.2326004

O	2.3207668	16.6591415	17.270564
O	6.1948942	10.4805623	17.3086296
O	-2.7155214	23.2703027	18.496124
O	6.5046595	-0.0228002	13.1028475
O	-1.4409317	14.2721274	13.6863041
O	3.0425564	8.7700996	12.9507579
O	-5.5295758	22.138283	13.173441
O	16.9262139	1.4785817	13.8259143
O	12.0637133	14.3602282	14.0932852
O	15.9331525	8.2854691	13.7260838
O	6.5457064	19.819471	15.3842656
O	-1.5303379	4.1621284	8.754813
O	-10.0244187	16.4215745	6.2001999
O	19.4240684	9.7024644	6.7777826
O	11.8306741	20.5029373	8.6507469
O	13.0240332	3.0396062	8.0690328
O	2.4359046	15.6978355	7.402759
O	7.1669558	10.0363349	6.8671816
O	3.3355168	21.4169925	9.3270592
O	-6.3003069	12.5666304	21.3511827
O	5.7153819	11.9035521	21.0392639
O	-0.6630678	8.480789	1.317445
O	14.9182097	8.1879691	23.5463672
O	2.5901271	17.0097864	22.7707097
O	20.4641004	8.3672454	23.3847812
O	10.7511009	23.845564	0.0571032
O	3.7142182	8.8524326	23.0347234
O	-2.0059835	14.7503882	20.820125
O	10.7402445	13.6269364	21.2303141
O	5.9822826	3.8642916	2.3202957

O	-1.3335889	17.5814701	2.5949042
O	3.8817466	10.654741	1.7092689
O	-7.5186871	22.2809373	3.0103375
O	21.3781918	4.9251551	0.8845865
O	10.8881725	16.3735945	1.7777861
O	18.0772551	10.7889457	1.0687565
O	5.9067542	22.9644078	3.0213585
O	25.92392	1.149276	18.3412501
O	-6.7597246	14.2431608	19.5375115
O	0.404989	8.9825364	19.565534
O	12.7112079	20.012757	16.6362759
O	17.5808538	2.2169483	18.9455459
O	7.6724671	13.6559525	19.0948442
O	13.3832403	8.5590457	18.9856169
O	1.5833745	20.1425756	20.1325502
O	7.0025491	5.476853	11.3182002
O	-3.1557182	17.0006917	12.0318513
O	3.4554872	11.6507703	11.601455
O	19.9859583	4.7196115	13.014341
O	10.0008587	17.0863632	11.773998
O	14.7501326	10.6475649	11.8940522
O	8.3078802	22.1173764	12.5322255
O	18.1213746	12.4882489	8.7980967
O	-1.6029574	6.6646875	8.1256175
O	-12.1117413	19.0056414	9.7249607
O	9.1626161	13.3884232	8.7882003
O	9.9548987	7.830988	9.1935075
O	5.3220275	19.5821099	10.1526555
O	4.8494366	4.7392064	4.6091456
O	-2.8810628	16.1344864	4.8562406

O	1.0227879	10.4510333	4.0326851
O	-6.2357918	22.5965078	5.5857638
O	17.6461792	4.0957223	2.9949649
O	10.8768284	16.6977993	4.3507028
O	14.1754221	10.4502311	3.0659609
O	6.3321316	22.5749355	5.582757
O	2.520666	2.073306	16.1210832
O	17.3080444	14.0141234	17.155091
O	-4.7279516	7.9324308	18.486945
O	-12.4543463	22.34003	15.404378
O	12.1669488	1.8155067	18.7781216
O	4.1799396	13.4563685	17.0100899
O	8.0401785	7.6472649	18.0656165
O	0.6869443	19.4797081	17.476634
O	4.3580375	5.4759018	13.6866261
O	-5.0433413	18.7947725	13.3913512
O	0.842318	11.4216651	13.9750351
O	-11.5227403	23.3150004	10.7945482
O	18.8538702	5.8540076	15.1044769
O	10.0575074	17.2782788	14.4862479
O	14.8910883	11.234991	14.4939236
O	2.7271046	21.765984	13.8311916
O	10.7777052	23.6805825	8.7289426
O	-8.0109593	12.7996295	6.080006
O	-4.2023794	7.0809205	5.867823
O	13.994674	19.1053862	7.0263597
O	-2.7934238	23.8256191	9.1314348
O	4.732843	12.9315964	7.1597267
O	8.7683251	6.9391375	6.7315678
O	0.708251	18.7401135	8.7084917

O	-15.7641959	24.2321421	4.2762407
O	-7.1116246	11.587774	3.6394714
O	22.9248179	5.5017917	3.4506609
O	-11.0297022	18.0115035	2.9610709
O	-2.5756134	24.1041859	3.8270697
O	6.3025543	11.97234	3.8503168
O	10.2414828	5.7056533	3.5972247
O	1.9241976	18.0741797	4.8173866
O	4.4349278	3.0570677	18.5072373
O	-3.766439	15.2051333	17.3021709
O	-0.191913	9.2368486	17.0045948
O	-8.5240116	21.633587	16.6826896
O	15.5265458	2.5426713	16.5996545
O	9.2425819	15.2180721	16.9643107
O	12.3720306	8.222642	16.3507767
O	5.1111012	21.3548892	18.1631007
O	8.2479466	23.2062022	15.8601379
O	-7.3064293	12.411001	12.7468873
O	-2.7189398	7.0386221	13.8023169
O	-11.7298397	18.0190512	12.9832503
O	0.211744	24.0036706	12.2123398
O	6.3332151	12.6032674	13.9166084
O	9.9385503	6.5219721	13.5604044
O	-0.6275444	19.5256893	11.6753371
O	6.0413233	3.2737907	8.2170408
O	-3.7930926	14.1935851	7.5911765
O	0.9996828	8.5762839	6.3969085
O	-9.3897234	21.2897437	8.2497486
O	18.2831624	3.168987	8.5480682
O	10.0369802	14.3222631	6.2615457

O	14.0510968	7.3788389	7.7133142
O	5.3886513	20.2559455	7.4520327
Ow	4.4323539	21.6861352	23.4131399
Hw	2.1555537	21.6132143	0.0445054
Hw	3.7952132	22.3532453	23.0038551
Ow	8.7598954	8.2348873	23.1915126
Hw	6.8556919	8.1847146	0.0637229
Hw	7.7270197	8.8242039	22.953715
Ow	9.0012215	5.8924721	21.0376042
Hw	7.8795219	5.409592	21.7594281
Hw	10.2210352	5.3944894	20.7534876
Ow	8.6158724	2.8410194	0.4598392
Hw	10.2883384	2.8936811	23.5122199
Hw	8.3461537	3.3097999	1.2502844
Ow	8.2208215	17.9147173	21.6939532
Hw	6.6316013	17.5548079	22.2764296
Hw	7.4615751	17.8641864	20.8107021
Ow	3.4574626	19.0030312	13.1592238
Hw	4.4147298	19.4315655	13.9443941
Hw	1.5524178	19.0296561	13.2349621
Ow	21.7692416	3.9110093	20.1246994
Hw	19.8738535	3.6800287	19.8117412
Hw	22.8019691	4.6146436	19.5437287
Ow	-1.5252729	21.4719253	10.1928472
Hw	0.1334959	21.5283875	9.6829199
Hw	-1.623873	20.7753678	10.8190998
Ow	6.6364881	14.6183375	22.0665668
Hw	5.9625613	13.6629886	22.1476534
Hw	8.3245955	14.8047896	21.5469183
Ow	5.4615196	8.1518575	15.6852605

Hw	6.4622424	9.0301559	15.3749682
Hw	6.7854174	7.8308921	16.1516436
Ow	-4.7178099	23.1414286	22.0734446
Hw	-2.8918781	23.1186056	22.326513
Hw	-5.9480177	22.7821004	22.8036851
Ow	19.5793403	2.2459555	0.6222112
Hw	19.8715057	3.1812549	0.5230601
Hw	20.618489	2.1822964	1.4087901
Ow	-12.4852442	23.677189	6.1128535
Hw	-13.9296794	24.0478105	5.8560893
Hw	-10.7960131	24.4144333	6.2800387
Ow	6.2827631	22.0853992	20.671106
Hw	6.5783759	21.6028944	19.9138966
Hw	4.3961989	21.612374	20.906387
Ow	7.8738041	5.7071196	15.9639885
Hw	9.2131884	6.565332	16.1130737
Hw	7.5653646	5.6962378	15.033147
Ow	-2.2714129	7.1945442	21.2197998
Hw	-3.5271002	7.3976429	20.6061355
Hw	-0.6039502	7.4159764	20.6980205
Ow	-0.8345513	15.3426618	9.6201559
Hw	0.7157043	15.2059202	9.1475555
Hw	-2.4338982	14.6519505	9.2996902
Ow	0.6135489	5.4297719	11.0425524
Hw	-0.7850293	5.7195247	11.4814624
Hw	-0.3748914	4.8391854	10.3536921
Ow	3.222945	13.639704	9.7878525
Hw	3.4387558	13.2165892	8.9689303
Hw	3.0043282	12.983087	10.4827075
Ow	13.8013909	15.4529961	19.4400652

Hw	12.4866568	15.0983938	20.1473924
Hw	15.4853852	16.0370694	19.8210623
Ow	21.1721906	1.2141344	15.9448421
Hw	21.7178149	1.4982823	15.0561739
Hw	20.4247483	0.2638338	15.8662604
Ow	0.2936171	13.738976	23.3424493
Hw	-0.7035852	12.958826	22.8498288
Hw	-0.1185257	14.0358084	0.5529932
Ow	-1.3887269	19.935291	22.338687
Hw	-3.21976	20.0281819	22.4190609
Hw	-0.7146932	20.2497926	21.4597164
Ow	8.6293311	13.983852	11.5894042
Hw	8.8089694	13.5584325	12.4067283
Hw	10.4762366	14.547043	11.3720811
Ow	9.9594727	20.5010403	19.825376
Hw	10.2778113	20.1374139	20.6552126
Hw	11.0889463	21.4246924	19.8275896
Ow	-2.6597778	10.1171917	21.5466224
Hw	-4.180611	9.6535426	22.1269751
Hw	-3.4276936	10.3954003	20.7680316
Ow	-4.0393033	22.165231	1.0105193
Hw	-4.5377704	22.7317239	1.6518461
Hw	-2.0563829	22.5435167	0.8846196
Ow	-1.8806276	3.4487319	22.6100401
Hw	23.4884433	3.636149	21.9785126
Hw	24.1470894	3.6844233	23.4598116
Ow	6.6670646	3.0420932	13.1613641
Hw	8.3732247	3.3656077	13.659527
Hw	6.4752589	2.1407113	12.8990267
Ow	-8.3784205	18.7344667	7.9331042

Hw	-9.0940455	18.5721158	7.0525568
Hw	-9.8650795	18.2275602	8.5034326
Ow	2.1944474	1.3773837	20.6587142
Hw	1.4960508	0.9709635	19.8188889
Hw	2.8181298	2.3027207	20.4535486
Ow	12.8975656	8.0134605	4.8714759
Hw	10.9884987	7.7095305	5.1814225
Hw	13.2640884	7.2238863	4.5600376
Ow	23.4222147	0.3255137	22.4606494
Hw	21.5511759	0.1708008	22.7792661
Hw	24.3113381	1.2695309	22.5235863
Ow	1.0359999	2.7597115	10.0115371
Hw	0.8712884	3.3219671	9.2874807
Hw	-0.4320795	2.7914233	10.6005551
Ow	-9.557577	19.9091501	14.8586248
Hw	-8.3250589	20.4252955	15.5214585
Hw	-11.4078928	19.6634047	15.2292591
Ow	5.1252397	19.7571813	0.4428188
Hw	3.5273602	19.5647901	1.0257427
Hw	5.3334342	18.3897295	23.5637806
Ow	16.0861219	1.4120983	21.4852955
Hw	17.0314961	1.8357323	20.6865307
Hw	17.496933	1.3913787	22.1170455
Ow	12.7593842	1.3195972	0.7639096
Hw	11.6122874	1.7733094	1.2101046
Hw	13.3718486	0.929885	23.5134794
Ow	23.9518931	3.7563373	13.669144
Hw	23.7247847	4.2353933	14.4557822
Hw	22.4188794	3.7532594	13.1201307
Ow	-6.710428	15.354545	10.3203592

Hw	-6.188432	16.2408128	10.6768947
Hw	-5.8831999	15.4776077	9.4533542
Ow	1.6415167	0.5949068	13.0719887
Hw	2.120593	1.1249419	12.2839301
Hw	3.2387964	0.2929735	13.1655902
Ow	0.6379741	5.4303544	1.390219
Hw	-1.3287018	5.2953393	1.2511959
Hw	1.6356513	6.2883608	1.0293911
Ow	22.0302065	6.0206202	10.4504897
Hw	-3.8878783	6.3105613	9.5760388
Hw	21.844697	6.7729941	10.9286254
Ow	17.7210007	10.278222	20.8984675
Hw	19.307765	10.8245363	21.3652981
Hw	17.2736168	10.919923	20.3551908
Ow	-2.9477683	8.9631561	10.6013388
Hw	-4.5655588	9.2446532	10.6915049
Hw	-2.7298568	8.968944	9.6603523
Ow	-7.7003401	18.6198516	21.34703
Hw	-6.8191161	17.9906108	21.6571187
Hw	-7.4948005	18.6671386	20.3904745
Ow	7.7017882	5.7623585	0.2491288
Hw	7.3650661	4.9241554	0.685953
Hw	6.4329167	6.1342681	0.6918742
Ow	19.2119412	4.9791935	22.6078595
Hw	19.5303945	4.3565338	23.2417688
Hw	18.243125	4.4783904	21.867358
Ow	0.7216383	23.9808991	6.7943034
Hw	-0.2498631	24.3716571	7.4119238
Hw	2.6568951	24.3304709	7.0450563
Ow	2.5321526	8.1993297	9.8872592

Hw	0.8286033	7.9589782	9.3855971
Hw	2.2984133	8.7107629	10.6404438
Ow	11.2021835	5.043012	6.1203066
Hw	12.2929882	5.5962077	6.8094581
Hw	10.7084632	5.6352522	5.5119385
Ow	12.9179851	16.6719812	22.3936309
Hw	14.7006259	17.3587387	22.3760826
Hw	11.5330939	17.0726055	22.1383228
Ow	-4.4148392	15.1039119	23.2317753
Hw	-4.7517712	15.9377346	23.1082148
Hw	-3.2431561	15.0170185	22.4946405
Ow	1.7843709	10.8388627	9.3063975
Hw	-0.0113802	10.7700418	8.9547841
Hw	1.4745527	10.8350296	10.2548252
Ow	-2.3356512	12.3775411	11.0421476
Hw	-0.6399548	13.0034683	11.3599758
Hw	-1.8938596	12.0098056	10.21921
Ow	1.6123662	13.0011879	20.3986236
Hw	3.1512339	12.6678452	20.2293597
Hw	0.1014229	12.5186677	19.8335748
Ow	13.6266825	18.4459502	19.5194186
Hw	-11.0044224	18.6452362	19.3681008
Hw	13.406386	18.7636033	20.3879057
Ow	6.1416868	17.1660149	1.5715977
Hw	7.6542736	17.9849625	1.5327437
Hw	7.0786568	16.5073703	1.5134789
Ow	1.2614693	23.1377926	21.1142634
Hw	0.5260174	22.3330946	20.6097413
Hw	2.249754	23.7880087	20.4683056
Ow	-3.6059132	16.9904635	20.5891861

Hw	-3.3921582	16.1190607	20.564367
Hw	-5.1306952	16.9279051	19.9985203
Ow	4.907981	8.082916	20.7731621
Hw	6.6642083	7.906112	20.7491337
Hw	4.25331	7.9240554	21.6744801
Ow	15.9459987	9.9461003	8.8736384
Hw	15.9354843	10.7804034	8.492369
Hw	16.5154924	9.4867529	8.1633446
Ow	-9.2590754	23.4459817	1.0018682
Hw	-8.7079788	22.7612507	1.4346534
Hw	-8.3134	24.2334946	1.4995955
Ow	16.0567479	14.1004211	21.7028387
Hw	-9.2506475	14.4405614	20.9892752
Hw	14.2398225	13.8190337	21.2919298
Ow	-0.4656766	1.0090459	1.7302858
Hw	24.632707	1.3306921	1.9713199
Hw	25.4597422	0.2824644	1.1159728
Ow	12.191694	0.5647876	6.4337904
Hw	10.2793625	0.0537714	6.2209208
Hw	13.3444225	0.4094825	5.7369017
Ow	14.102064	10.8329312	23.3103665
Hw	12.2754442	10.5834127	22.9281927
Hw	14.370354	10.015319	23.5949874
Ow	11.8268089	3.3340308	21.2765265
Hw	12.7329705	4.2777121	21.1870375
Hw	12.8118909	2.9337889	20.6722022
Ow	8.4790522	3.0445883	15.9975558
Hw	6.4880088	2.9109762	16.0292337
Hw	9.401102	3.9087148	16.3838444
Ow	-12.1129345	20.2274136	1.000952

Hw	13.0675506	19.3831886	1.0371401
Hw	-13.1031476	20.8305346	1.2526449
Ow	-13.4437056	21.4280229	22.4069129
Hw	-13.5738287	22.1012406	23.031146
Hw	-12.0577406	21.0635108	22.743381
Ow	12.6433152	6.8500146	11.2803406
Hw	10.7569487	6.4781843	10.9750059
Hw	12.5356879	6.9814755	12.2152732
Ow	-8.9026257	21.5315844	10.9114559
Hw	-8.8747891	21.2125435	10.0241444
Hw	-10.3331088	21.950148	10.9159732
Ow	20.602984	8.7051009	15.9407722
Hw	20.6408336	9.1852284	15.1304703
Hw	-4.1074834	8.748447	16.1098183
Ow	13.2438364	4.9560627	13.5538889
Hw	14.6311483	5.4916735	12.9462382
Hw	11.6574601	5.2712764	13.4514209
Ow	-1.5677268	17.4294952	14.5709213
Hw	-2.890859	17.9178149	14.5204781
Hw	-1.4366716	17.1260648	13.6857359
Ow	-6.4588889	24.1676207	16.5306117
Hw	-6.623534	23.3314316	16.9523096
Hw	8.5918751	-0.0728236	16.9943598
Ow	-3.0710809	20.2449376	15.7657575
Hw	-2.268829	19.8590396	16.4537182
Hw	-4.1413218	19.4838501	15.2687618
Ow	11.1741045	1.4843732	14.250941
Hw	9.9030328	1.1587166	13.528601
Hw	10.1238648	1.7653367	14.9250324
Ow	0.2786879	1.9221106	6.4996583

Hw	25.4844206	1.1295368	6.1972665
Hw	-0.1813034	2.6409926	6.0717835
Ow	18.1559993	7.509192	20.9837162
Hw	19.1639065	7.6520755	21.8058843
Hw	17.3111934	6.5646896	20.8620047
Ow	2.579396	5.0128889	20.549011
Hw	1.5890864	5.3806651	19.9119671
Hw	1.2366184	4.5116797	21.1803396
Ow	-4.1632731	19.1616453	1.5336339
Hw	-3.3415624	18.5711546	1.9695655
Hw	-2.8793015	19.5365292	0.8293868
Ow	14.3478423	2.406989	11.7217152
Hw	12.4136649	2.0349109	11.4972351
Hw	14.6380458	1.8096542	12.3802376
Ow	-9.253895	21.3877879	19.9218777
Hw	-10.9601437	21.1515092	19.4212928
Hw	-9.297403	22.1523711	20.4131723
Ow	13.7341456	5.5541356	0.811552
Hw	15.7006999	6.0362932	0.7307803
Hw	12.7951705	5.9150385	0.1579683
Ow	7.7745404	12.9343685	0.0852345
Hw	6.6619332	12.1679274	0.5645303
Hw	7.8149383	12.1703179	22.8452523
Ow	11.4579613	4.0338041	10.2250223
Hw	11.8005919	3.9522621	9.3031918
Hw	13.3024448	4.307654	10.5549299
Ow	15.1786706	12.1362697	19.2909563
Hw	13.4825121	12.2151982	19.6632053
Hw	16.6999436	12.8335024	19.6610839
Ow	0.7684769	11.7548588	0.0826278

Hw	2.0135411	12.3209529	0.7102938
Hw	-0.8684262	11.2836446	0.5831748
Ow	1.7051848	20.8084774	2.291608
Hw	0.1302943	20.478959	2.8785899
Hw	2.8994705	21.6047989	2.6990271
Ow	-6.4571616	13.7362596	15.2318303
Hw	-8.0114807	14.0692879	15.3307469
Hw	-5.1086909	14.2596242	15.8416899
Ow	23.5109313	0.0521721	10.8787197
Hw	23.134109	0.7068458	11.4552796
Hw	23.3971577	0.3475632	9.9742836
Ow	2.2397381	23.9066926	1.6802782
Hw	19.1023122	0.2516124	1.8274101
Hw	3.8971838	23.6788981	1.8971892
Ow	2.8792926	3.1228055	0.003047
Hw	3.5305389	3.5872935	0.8278076
Hw	2.3581048	2.9903149	23.2720215
Ow	11.1568532	9.8072278	20.7030018
Hw	9.9095339	10.2998924	20.5177
Hw	12.383153	9.9787506	19.9410289
Ow	6.3574072	-0.0366707	22.0382958
Hw	-9.9379579	23.7334496	21.6792033
Hw	6.7857589	0.5134855	21.2759085
Ow	-9.4895546	17.0896814	0.4882262
Hw	-9.2694114	16.2477805	0.7197759
Hw	-10.372776	17.333586	1.253362

Bibliography

[1] Allen AJ, Thomas JJ (2007). "Analysis of C-S-H gel and cement paste by small-angle neutron scattering." Cement and Concrete Research, 37: 319-324.

[2] Alder BJ, Wainwright TE (1956). "Molecular dynamics by electronic computers." International Symposium on Statistical Theory of Transport Processes, Brussels: Interscience.

[3] Allen MP, Tildesley TJ (1987). *Computer Simulation of Liquids*, Clarendon Press, Oxford.

[4] Allen AJ, Thomas JJ and Jennings HM (2007). "Composition and density of nanoscale calcium-silicate-hydrate in cement." Nature Material,.6: 311-316.

[5] Anderson HC (1980). "Molecular dynamics simulations at constant pressure and/or temperature." Journal of Chemical Physics, 72: 2384.

[6] Anderson OL (1965), *In Physical Acoustics*. New York, Academic Press.

[7] Argon AS, Demkowicz M (2008) "What can plasticity of amorphous silicon tell us about plasticity of metallic glasses?" Metallurgical and Materials Transactions A, 39:1762.

[8] Arsigney A, Filared P, Pennec X and Ayache N (2005). Research Report 5584, INRIA.

[9] Auzende AL, Pellenq RJM, Devouard B, Baronnet B and Grauby O (2006). "Atomistic calculations of structural and elastic properties of serpentine minerals: the case of lizardite." Physics and Chemistry of Minerals. 33: 266-275

[10] Ayuela A, Dolado JS, Campillo I, de Miguel YR, Erkizia E, Sánchez-Portal D, Rubio A, Porro A, Echenique PM.(2007). "Silicate chain formation in the nanostructure of cement-based materials." Journal of Chemical Physics, 127:164710.

[11] Baroni S, Dal Corso A,de Gironcoli S and Giannozzi P, http://www.pwscf.org.

[12] Berendsen HJC, Grigera JR, Straatsma TP (1987). "The missing term in effective pair potentials." Journal of Physical.Chemistry 91: 6269-6271.

[13] Bernal JD, Jffrey JW, Taylor HFW (1952). "Crystallographic research on the hydration of Portland cement: A first report investigation in progress." Magazine of Concrete Research 4: 5.

[14] Bonnacorsi E and Merlino S (2005). "The crystal structure of tobermorite 14 Å (Plombierite), a C-S-H phase." Journal of American Ceramic Society, 88: 505-512.

[15] Bonnacorsi E and Merlino S (2005). "Modular microporous minerals: cancrinite-davyne group and C-S-H phases." Reviews in Mineralogy and Geochemistry, 57: 241-290.

[16] Bonnacorsi E, Merlino and Taylor HFW (2004). "The crystal structure of jennite $Ca_9Si_6O_{18}(OH)_6.8H_2O$." Cement and Concrete Research, 34: 1481-1488.

[17] Born M, Oppenheimer R (1927)."Zur Quantetheorie der molekule." Annalen der Physik, 84:27.

[18] Car R, Parrinello M (1985). "Unified approach for molecular dynamics and density-functional theory." Physical Review Letters, 55: 2471–2474.

[19] Carbovzi EJ,. Bentz DP (2001). "The effect of statistical fluctuations, finite sizes, error, and digital resolution on the phase percolation and transport properties of the NIST cement hydration model." Cement and Concrete Research, 31:1501-1514.

[20] Chatterj S, Jeffrey JW (1966). "3-dimensional arrangement of hydration products in set cement paste." Nature,209:1233-1236.

[21] Chen JJ, Thomas JJ, Taylor HFW, Jennings HM (2004). "Solubility and structure of calcium silicate hydrate." Cement and Concrete Research, 34:1499-1519.

[22] Collins DR, Catlow CRA (1992). ") Computer simulation of structures and cohesive properties of micas." American Mineralogists, 77:1172-1181.

[23] Colombet P, Grimmer AR, Zanni H and Sozzani P (1998). *Nuclear magnetic resonance spectroscopy of cement based materials,* Springer, Berlin.

[24] Cong X and Kirkpatrick RJ (1996). "^{29}Si and ^{17}O NMR investigation of the structure of some crystalline calcium silicate hydrates." Advances in Cement Based Materials, 3: 133-143.

[25] Constantinides G, Ulm FJ (2004). "The effect of two types of C-S-H on the elasticity of cement-based materials: Results from nanoindentation and micromechanical modeling." Cement and Concrete Research, 34: 67-80.

[26] Costantinides G, Ulm FJ (2006). "Invariant mechanical properties of calcium -silicate-hydrate (C-S-H) in cement-based materials: Instrumented indentation and micromechanical modeling." Ph.D. Thesis. MIT, Cambridge.

[27] Constantinides G and Ulm FJ (2007). "The nanogranular nature of C-S-H." Journal of Mechanics and Physics of Solids, 55: 64-90.

[28] Corno M, Busco C, Civalleri B and Ugliengo P (2006). "Periodic ab initio study of structural and vibrational features of hexagonal hydroxyapatite $Ca_{10}(PO_4)_6(OH)_2$." Physical Chemistry Chemical Physics 8: 2464-2472.

[29] Coussy O (1995). *Mechanics of Porous Continua.* Chichester, John Wiley & Sons.

[30] Cygan RT, Liang JJ, Kalinichev AG (2004). "Molecular models of hydroxide, oxyhydroxide, and clay phases and the development of a general force field." Journal of. Physical Chemistry, 108: 1255-1266.

[31] Daimon M, Abo-el-enein SA, Rosara G, Goto S and Kondo R (1977). "Pore Structure of Calcium Silicate Hydrate in hydrated tricalcium silicate." Journal of American Ceramic Society, 60:110-114.

[32] Dejon MJ, Ulm FJ (2007). "The nanogranular nature of C-S-H at elevated temperatures.(up to 700 °C)." Cement and Concrete Research, 37:1-12.

[33] De leeuw NH, Watson JW, Parker SC (1995). "Atomistic Simulation of the Effect of Dissociative Adsorption of Water on the Surface Structure and Stability of Calcium and Magnesium Oxide." Journal of Physical Chemistry, 99: 17219-17225.

[34] de Leeuw NH, Parker SC (1998). "Molecular-dynamics simulation of MgO surfaces in liquid water using a shell-model potential for water." Physical Review B, 58: 13901.

[35] Donev A, Cisse I, Sachs D, Variano E, Stillinger FH, Connelly R, Torquato S, Chaikin PM (2004). "Improving the density of jammed disordered packing using ellipsoids." Science 303: 990-993.

[36] Dove MT, Cool T, Palmer DC, Putnis A, Salje EKH and Winkler B (1993). "On the role of A1- Si ordering in the cubic-tetragonal phase transition of leucite." American Mineralogists, 78: 486-492.

[37] Dowty E (1987). "Fully automated microcomputer calculation of vibrational spectra." Physics and Chemistry of Minerals, 14:67-79.

[38] d'Espinose de la Caillerie JB, Lequeux N (2008). *Lecture on the structure of CSH, AFm and AFt phases in Physique.* Chimie et Mécanique des Matériaux Cimentaire, ed Ecole ATILH-CNRS 3rd Ed.

[39] Ewald PP (1921). "The calculation of optical and electronic grid potential." Annalen Der Physik, 64:253-287.

[40] Feldman A (1970). "A new model for hydrated Portland cement and its practical implications." Eng. J. Can, 1970, 53: 53-59.

[41] Fratini E, Chen S-H, Baglioni P, Bellissent-Funel M-C (2001). "Age-dependent dynamics of water in hydrated cement paste." Physical Review E, 64:020201.

[42] Frenkel D, Smit B (1996). *Understanding molecular simulation: from algorithms to applications.* Academic press, San Diego.

[43] Frenkel D, Smit B (2002) *Understanding Molecular Simulations*, Academic Press, New York, 2nd Ed.

[44] Fujii K, Kondo W (1983). "Estimation of thermomechanical data for calcium silicate hydrate (C-S-H)." Communication for American Ceramic Society, 220.

[45] Gale JD (1997). "A computer program for the symmetry adapted simulation of solids." Journal of Chemical Society, Faraday Transactions 93: 629-637.

[46] Gale JD (1996). "Empirical potential derivation for ionic materials." Philosophical Magazine B, 73:3-19.

[47] Gale JD and Rohl AL (2003). "The General Utility Lattice Program." Molecular Simulations, 29: 291.

[48] Galin LA (1953) *Contact problems in theory of elasticity,* Gostekhizdat, Moscow.

[49] Ganneau FP, Constantinides G, Ulm FJ (2006). "Dual-indentation technique for the assessment of strength properties of cohesive-frictional materials." International Journal of Solids and Structures, 43: 1727-1745.

[50] Ganster P, Benoit M, Kob W, Delaye JM (2004). "Structural properties of a calcium aluminosilicate glass from molecular-dynamics simulations: A finite size effects study." Journal of Chemical Physics, 120:10172-10181.

[51] Gay JG, Berne BJ (1981). "Modification of the overlap potential to mimic a linear site–site potential." Journal of Chemical Physics 74: 3316-3322.

[52] Gmira A (2003). Etude texturale et thermodynamique d'hydrates modeles du ciment, Universite D Orleans. Ph.D Thesis, France.

[53] Goto S, Daimon M, Kondo R (1976). "Composition and morphology of hydrated tricalcium silicate." Journal of. American Ceramic Society, 9: 281-284.

[54] Griggs D (1974). "A model of hydrolytic weakening in quartz." Journal of Geophysical. Research, 79:1653.

[55] Grimvall G (1986). *Thermophysical Properties of Materials.* Amsterdam, North-Holland.

[56] Groves GW, Le Sueur PJ, Sinclair W (1986). "Transmission electron microscopy and microanalytical studies of ion-beam-thinned sections of tricalcium silicate paste." Journal of American Ceramic Society, 69:353–356.

[57] Grudemo A (1986) ."The crystal structure of cement hydration-A review and a new gel model." S.C.a.C.R. Institute,3-16.

[58] Hamid SA (1981)."The crystal structure of the 11 Å natural tobermorite." Zeitschrift fur kristallographie 154, 189-198.

[59] Hershey AV (1954). "The elasticity of an isotropic aggregate of anisotropic cubic crystals." Journal of Applied Mechanics, 21:135-144.

[60] Hill R (1952) "The elastic behavior of a crystalline aggregate." Proceedings of the Physical Society of London, 65, 350.

[61] Hohenberg P and Kohn W (1964). "Inhomogeneous electron gas." Physical Review B, 136, 84-71.

[62] Holleman AF, Wyberg E (1985) *In Lehrbuch der anorganischen Chemie*, Walter Gruyter Verlag, Berlin, New York.

[63] Hoover WG (1985). "Canonical dynamics: Equilibrium phase-space distributions." Physical Review A, 31: 1695–1697.

[64] Jaeger HM, Nagel SR (1992). "Physics of the gnanular state." Science, 255: 1523-1531.

[65] Janika JA, Kurdowsk W, Podsiadey R, Samset J (2001). "Fractal Structure of CSH and Tobermorite Phases." Acta Physica Polonica, 100: 529-537.

[66] Jennings HM (2000). "A model for the microstructure of calcium silicate hydrate in cement paste." Cement and Concrete Research, 30: 101-116.

[67] Jennings HM (2004). "Colloid model of C-S-H and implications to the problem of creep and shrinkage." Materials and Structures, 37: 59-70.

[68] Jennings HM (2008). "Refinements to colloid model of C-S-H in cement: CM-II." Cement and Concrete Research, 38: 275-289.

[69] Jennings HM and Tennis PD (1994). "Model for the developing microstructure in Portland-cement pastes." Journal of the American Ceramic Society, 77: 3161-3172.

[70] Jennings HM and Tennis PD (1995). "Model for the developing microstructure in Portland-cement pastes (Vol 77, Pg 3161, 1994)." Journal of the American Ceramic Society, 78: 2575-2575.

[71] Jennings HM, Thomas JJ, Gevrenov JS, Constantinides G and Ulm FJ (2007). "A multi-technique investigation of the nanoporosity of cement paste." Cement and Concrete Research, 37: 329-336.

[72] Jennings HM, Thomas JJ, Gevrenov JS, Constantinides G, Ulm FJ (2007). "A multi-technique investigation of the nanoporosity of cement paste." Cement and Concrete Research, 37: 329-336.

[73] Jenning HM, Dalgleish BJ, Pratt PL (1981). "Morphological development of hydrating tricalcium silicate as examined by electron microscopy techniques." Journal of American Ceramic Society, 64: 567-572.

[74] Jennings HM, Bullard JW, Thomas JJ, Andrade JE, Chen JJ, Scherer GW (2008). "Characterization and modeling of pores and surfaces in cement paste: correlations to processing and properties." Journal of Advanced Concrete Technology, 6:5-29.

[75] Jmol: an open-source Java viewer for chemical structures in 3D. http://www.jmol.org/

[76] Kantro DL, Brunauer S, Weise CH (1962). "Development of surface in the hydration of calcium silicate: Extension of investuigation to earlier and later stages of hydration." Journal of Physical Chemistry, 66: 1804-1809.

[77] Kohn W, Meir Y, Makarov DE (1998). "Van der Waals energies in density functional theory." Physical Review Letters, 80, 4153.

[78] Kohn W and Sham LJ (1965). "Self-consistent equations including exchange and correlation effects." Physical Review A, 140: 1133-1138.

[79] Kokalj A (1999). " XCrySDen—A New Program for Displaying Crystalline Structures and Electron Densities." Journal of Molecular Graphics Modelling, 17: 176-179.

[80] Komarneni S, Roy DM, Fyfe CA, and Kennedy GJ (1987). "Naturally occurring 1.4nm tobermorite and synthetic jennite: characterization by Al and Si MASNMR spectroscopy and cation Exchange properties." Cement and Concrete Research, 17, 891-895.

[81] Kosmatka SH, Kerkhoff B and Panarese WC (2002). *Design and control of concrete mixtures.* Skokie, Illinois.

[82] Kreher W, Molinari A (1993). "Residual stresses in polycrystals as influenced by grain shape and texture." Journal of Mechanics and Physics of Solids, 41, 1955-1977.

[83] Kurczyk HG, Schwiete HE (1960). "Concerning the hydration products of C_3S and $\beta-C_2S$." 4th international Symposium on the Chemistry of Cement, Washington, National Bureau of Standards (NIST).

[84] Lea FM and Hewlett PC (1998) Lea's chemistry of cement and concrete, 4th Ed, Oxford: Elsevier Butterworth-Heinemann.

[85] Leach AR (2001). *Molecular Modelings: principles and applications.* 2nd Ed, Harlow England; New York: Prentice Hall.

[86] Le Chatelier H, Mack JL (1905). *Experimental Researches on the constitution of hydraulic mortars*, New York, McGraw Hill.

[87] Levine IN (1991). *Quantum chemistry*, 4th. Ed, 1991, Englewood Cliffs, NJ: Prentice Hall.

[88] Le Page Y and Saxe P (2002). "Symmetry-general least-square extraction of elastic data for strained materials from *ab initio* calculations of stress." Physical Review B, 65, 104104.

[89] Lequeux N, Moreau A, Philippot S (1999). "Extended X-ray absorption fine structure investigation of calcium silicate hydrates." Journal of American Ceramic Society, 8: 1299-1306.

[90] Li J, Van Vliet KJ, Zhu T, Yip S, Suresh S (2002). "Atomistic mechanisms governing elastic limit and incipient plasticity in crystals." Nature 418:307.

[91] London F (1930). "Some characteristic and uses of molecular force." Zeitschrift fur physikalische chemie-abteilung B-chemie der elementarprozesse aufbau der materie, 11, 222-251.

[92] Long JVP, McConell JC (1958). "A mineral application of X-ray absorption microspectroscopy: the hydration of larnite." Mineralogical Magazine, 32:10.

[93] Love AEH (1944). *Mathematical Theory of Elasticity.* New York, Dover Publications.

[94] Maeshima T, Noma N, Sakiyama S, T. Mitsuda T (1978). "Natural 1.1 and 1.4nm tobermorites from Fuka, Okayama, Japan: chemical analysis, cell dimensions, Si NMR and thermal behavior." Cement and Concrete Research, 42, 229-235.

[95] Manzano H (2009) Atomistic Simulation Studies of Cement Paste Components." Ph.D Thesis, Labein Tecnalia, Spain.

[96] Manzano H, Dolado JS, Ayuela A (2009). "Elastic properties of the main species present in Portland cement pastes." Acta Materials, 57: 1666-1674.

[97] Manzano H, Dolado JS, Guerrero A, Ayuela A (2007). "Mechanical properties of crystalline calcium-silicate-hydrates:comparison with cementitious C-S-H gels." Physica Status Solidi A, 204: 1775.

[98] Martin RM (2004). *Electronic strucutre, basic theory and practical methods,* Cambridge, Cambridge University Press.

[99] Martin SI (1994). "Synthesis of tobermorite: a cement phase expected under repository conditions." Lawrence Livermore National Laboratory Report.

[100] McConnell JDC (1954) ."The hydrated calcium silicates riversideite, tobermorite, and plombierite." Minerallogists Magazine, 30: 293-305.

[101] Mehta, PK, Monteiro P (1993). *Concrete: structure, properties, and materials.* 2nd Ed., Englewood Cliffs, NJ, Prentice Hall.

[102] Merlino S, Bonnacorsi E, and Armbruster T (2000). "The real structure of clinotobermorite and tobermorite 9 Å: OD character, polytypes, and structural relationships." European Journal of Mineralogy, 12: 411-429.

[103] Merlino S, Bonnacorsi E, and Armbruster T (2001). "The real structure of tobermorite 11 Å: normal and anomalous forms, OD character and polytyptic modifications." European Journal of Mineralogy, 13: 577-590.

[104] Metropolis N, Rosenbluth AW, Rosenbluth MN (1953). "Equations of state calculations by fast computing machines." Journal of chemical physics, 21: 1087-1092.

[105] Michaelis W (1909). "The hardening of cement under water." Chicago, Cement and Engineering News.

[106] Miller M, Bobko C, Vandamme M. and Ulm FJ (2008). "Surface roughness criteria for cement paste nanoindentation." Cement and Concrete Research, 38: 467-476.

[107] Monkhorst HJ and Pack JD (1976). "Special points for brillouin-zone integrations." Physical Review B, 13, 5188.

[108] Moakher M (2006). "On the averaging of symmetric positive-definite tensors." Journal of Elasticity, 82: 273.

[109] Mori T. and Tanaka K. (1973). "Average stress in matrix and average elastic energy of materials with misfitting inclusions." Acta Metallurgica, 21: 571-574.

[110] Moruzzai VL, Janak JP, Schwarz K (1988). "Calculated Thermal Properties of Metals." Physical Review B, 37: 790-799.

[111] Mott PH, Argon AS, Suter UW (1993). "Atomistic modeling of cavitation of glassy polymers." Philosophical Magazine A, 68:537.

[112] Nicholson D, Parsonage NG (1982). *Computer Simulation and the Statistical Mechanics of Adsorption,* Academic Press, New York.

[113] Nielson H and Martin RM (1983). "First-principle calculations of stress." Physical Review Letters, 50: 697-700.

[114] Nonat A. (2004). "The structure and stoichiometry of C-S-H." Cement and Concrete Research, 34: 1521-1528.

[115] Nose S (1984). "A molecular dynamics method for simulations in the canonical ensemble." Molecular Physics, 52: 255-268.

[116] Nye JF (1957) *Physical properties of crystals.* Oxford University Press. London.

[117] Paci E, Vendruscolo M, Karplus M (2002). "Validity of Go Models: Comparison with a Solvent-Shielded Empirical Energy Decomposition." Biophysical Journal, 83: 3032–3038.

[118] Pellenq RJM and van Damme H (2004). "Why does concrete set?: the nature of cohesion forces in hardened cement based materials," Materials Research Bulletin, 319-323.

[119] Pellenq RJM, Lequrux N, van Damme H (2008). "Engineering the bonding scheme in C-S-H: the iono-covalent framework." Cement and Concrete Research, 38: 159.

[120] Pellenq RJM, Nicholson DA (1998). "A simple method for calculating dispersion coefficients for isolated and condensed-phase species." Molecular Physics, 95, 549.

[121] Povolo F, Bolmaro RE (1987). "Average Elastic Constants and Tensor Invariants." Physica Status Solidi, 99, 423.

[122] Powers TC, Brownyard TL (1948) Studies of the physical properties of hardened portland cement paste, PCA Bulletin, Portland Cement Association 22, p 22.

[123] Puibasset J, Pellenq RJM (2005) ."Water adsorption in disordered mesoporous silicaVycor at 300 K and 650 K: A Grand Canonical Monte Carlo simulation study of hysteresis." Journal of Chemical Physic, 122: 094704.

[124] Puibasset J, Pellenq RJM (2008). "Grand canonical Monte Carlo simulation study of water adsorption in silicalite at 300 K." Journal of Physical Chemistry B, 112: 6390–6397.

[125] Ramachandran VS, Beaudoin JJ (2001). *Handbook of analytical techniques in concrete science and technology*, William Andrew Publishing.

[126] Ramachandran VS, Feldman RF and Beaudoin JJ (1981). *Concrete Science*, Heyden, London.

[127] Rapaport DC (1995). *The art of molecular dynamics simulation*, Cambridge, New York, Cambridge University Press.

[128] Rarick R, Bhatty J and Jennings HM (1995). "Surface area measurement using gas sorption: applications to cement paste." Materials Science of Concrete IV, edited by John Skalny and Sidney Mindess, The American Ceramic Society, Westerville, OH, 1-39.

[129] Reid N (1973). *Deformation Geometry for Materials Scientists.* Oxford, Pergamon.

[130] Reuss A and Angew Z (1929) ."Berchung der fiessgrenze von mischkristallen auf grund der plastiziatsbedingung fur einkristalle" Applied Mathematical.and Mechanics, 9: 55.

[131] Richardson IG and Groves GW (1992). "Models for the composition and structure of calcium silicate hydrate (C–S–H) gel in hardened tricalcium silicate pastes." Cement and Concrete Research, 22: 1001-1010.

[132] Richardson IG (2004) ."Tobermorite/jennite- and tobermorite/calcium hydroxide-based models for the structure of C–S–H: applicability to hardened pastes of tricalcium silicate, β-dicalcium silicate, portland cement, and blends of portland cement with blast-furnace slag, metakaolin, or silica fume" Cement and Concrete Research 34: 1733-1777.

[133] Richardson IG (2000). "The nature of hydration products in hardened cement pastes." Cement and Concrete Research, 22: 97-113.

[134] Richardson IG, Groves GW (1993). "Microstructure and microanalysis of hardened ordinary portland cement pastes." Journal of Material Science, 28: 265-277.

[135] Richardson IG (1999). "The nature of C-S-H in hardened cements." Cement and Concrete Research, 29:1131–1147.

[136] Richardson IG (2008). "The calcium silicate hydrates." Cement and Concrete Research, 38:137-158.

[137] Richardson IG, Caberera JG (2000). "The nature of C-S-H in model slag-cements." Cement and Concrete Composites, 22, 259-266.

[138] Roberts AP, Garboczi EJ (2002). "Computation of the linear elastic properties of random porous materials with a wide variety of microstructure." Proceedings of the Royal Society of London A, 458: 1033.

[139] Rodger SA, Groves GW, Clayden NJ and Dobson CM (1987). "Microstructural development during the hydration of cement." In: L.J. Struble and P.W. Brown, Editors, Symposia Proceedings, 85, Materials Research Society, Pittsburgh, 213–222.

[140] Rydberg H, Dion M, Jacobson N, Schroder E, Hyldgaard P, Simak SI, Langreth DC, and Lundqvist BI (2003). "Van der Waals density functional for layered structures." Physical Review Letters, 91: 126402.

[141] Saint-Diaz CI, Laguna-Hernandez A and Dove MT (2001). "Modeling of dioctahedral 2:1 phyllosilicates by means of transferable empirical potentials." Physics and Chemistry of Minerals, 28, 130-141.

[142] Sanchez JM, Stark KP, Moruzzi VL (1991). "First-principles calculation of the Ag-Cu phase diagram." Physical Review B, 44: 5411-5418.

[143] Schlick T (1996). "Pursuing Laplace's Vision on Modern Computers". in J. P. Mesirov, K. Schulten and D. W. Sumners. Mathematical Applications to Biomolecular Structure and Dynamics, IMA Volumes in Mathematics and Its Applications. 82. New York: Springer-Verlag. 218–247.

[144] Shrodinger E (1926). "An undulatory theory of the mechanics of atoms and molecules,." Physical Review, 28:1049-1070.

[145] Shypnova LG, Nabitovich A, Belov NV (1967) ."Microstructure of alite cement stone." Soviet Physics Crystallography, 11: 4.

[146] Sloane NJA (1998). "Kepler's conjecture confirmed." Nature, 395: 435-436.

[147] Smith A, Hall CK (2001). "Alpha-Helix Formation: Discontinuous Molecular Dynamics on an Intermediate-Resolution Protein Model." Proteins 44: 344–360.

[148] Sneddon IN (1965). "The relation between load and penetration in the axisymmetric boussinesq problem for a punch of arbitrary profile." International Journal of Engineering Science, 3, 47-57.

[149] Stade VH (1980). "Uber eine aus poly-und disilicat bstehende phase.". Zeitschrift Fur Anorganic Chemistry, 470: 69-83.

[150] Stewart K, Shahsavari R, Qu M, Lebreiro S, Yip S, Ulm FJ, Pellenq RJM, van Vliet K (2010). "Designing liquid Stone: Modulating cement mechanics via computation and physical chemistry." Manuscript in preparation.

[151] Suresh S, Li J (2008). "Deformation of the ultra-strong." Nature, 456:756.

[152] Taylor HFW (1986). "Proposed structure for calcium silicate hydrate gel." Journal of Americal Ceramic Society, 69: 464-467.

[153] Taylor HFW (1964) *Chemistry of cement,* Academic Press, New York.

[154] Taylor HFW, Howison JW (1956). "Relationships between calcium silicate and clay minerals." Clay Minerals Bulletin, 3: 98-111.

[155] Tennis PD, Jennings HM (2000). "A model for two types of calcium silicate hydrate in the microstructure of Portland cement pastes." Cement and Concrete Research 30: 855-863.

[156] Thomas J. Grey (1999). "A coordinated approach to modeling zeolite structure and adsorption", Ph.D Thesis, Imperial College.

[157] Thomas JJ, FitzGerlad RA, Nuemann DA, Livingston RA (2001). "State of water in hydrating tricalcium silicate and portland cement pastes as measured by quasi-elastic neutron scattering." Journal of American Ceramic Society, 84, 1811-1816.

[158] Thomas JJ, Jennings HM, Allen AJ (1998). "The surface area of ceemnt paste as measured by neutron scattering: Evidence for two C-S-H morphologies."Cement and Concrete Research, 28: 897-905.

[159] Ugliengo P, Zicovitch-Wilson CM, Tosconi S, Civalleri B (2009). "Role of dispersive interactions in layered materials: a periodic B3LYP and B3LYP-D* study of $Mg(OH)_2$, $Ca(OH)_2$ and kaolinite." Journal of Material Chemistry,19: 2564-25772.

[160] Ulm FJ, VanDamme M, Bobko C, Ortega JA, Tai K, Ortiz C (2007). "Statistical indentation techniques for hydrated nanocomposites: concrete, none, and shale." Journal of American Ceramic Society, 90: 2677-2692.

[161] Van Beest BWH, Kramer GJ and van Santen RA (1990). "Force fields for silicas and aluminophosphates based on ab initio calculations." Physical Review Letters, 64: 1955.

[162] Van Damme M (2008). "The nanogranular origin of concrete creep: A nanoindentation investigation of microstructure ad fundamental properties of calcium-silicate-hydrate, Ph.D. Thesis. MIT, 2008.

[163] Vandamme M, Ulm FJ (2009). "Nanogranular origin of concrete creep." Proceedings of the National Academy of Sciences of the United States, 106:10552–10557.

[164] Vanderbilt D (1990). "Self-consistent pseudopotentials in a generalized eigenvalue formalism." Physical Review B, 41: 7892-7895.

[165] Verlet L (1967). "Computer Experiments on Classical Fluids. I. Thermodynamical Properties of Lennard-Jones Molecules." Physical Review, 159: 98–103.

[166] Viehland LJ, Yaun LJ, Xu Z, Cong X, and Kirkpatrick RJ (1997). "Structural studies of jennite and 1.4nm tobermorite: distorted layering along the [100] of jennite." Journal of American Ceramic Society, 80:3021-3028.

[167] Voigt W (1928) *Lehrbuch der kristallphysik.* Taubner, Leipzig.

[168] Wallance DC (1972). *Thermodynamics of Crystals.* New York, John Wiley & Sons.

[169] Wieker W, Grimmer AR, Winkler A, Magi M, Tarmak M, and Lippmaa E (1982). "Solid-state high resolution ^{29}Si NMR spectroscopy of synthetic 14 Å, 11 Å and 9 Å tobermorites." Cement and Concrete Research 12: 333-339.

[170] Winkler B (1999). "An introduction to Computational Crystallography." Z. Kristallogr, 212: 506-11.

[171] Winkler B, Dove MT and Leslie M (1991). "Static lattice energy minimization and lattice dynamics calculations on aluminosilicate minerals." American Mineralogist,76: 313.

[172] Yao HL, Ouyang L and Ching WY (2007). "*Ab initio* calculation of elastic constants of ceramic crystals." Journal of American Ceramic Society, 90, 3194-3204.

[173] Yu P, Kirkpatrick RJ, Poe B, McMillan PF, Cong X (1999). "Structure of calcium silicate hydrate (C-S-H): Near-, mid-, and far-infrared spectroscopy." Journal of American Ceramic Society, 82: 742-748.

[174] Yu P and Kirkpatrick RJ (1999). "Thermal dehydration of tobermorite and jennite." Concrete Science and Engineering, 1: 185-191.

[175] Zhang X, Chang W, Zhang T, and Ong CK (2000). "Nanostructure of calcium silicate hydrate gels in cement paste." Journal of American Ceramic Society, 83, 2600-4.

[176] Zhu T, Li J, Ogata S, Yip S (2009). "Mechanics of ultra-strength materials." Materials Research Bulletin, 34: 167-172.

[177] Zhu T, Li J, Lin X, Yip S (2005). "Stress-dependent molecular pathways of silica-water reaction." Journal of Mechanics and Physics of Solids 53: 1597.

[178] http://www.crystal.unito.it

[179] www.crystalmaker.com/crystaldiffract/